Cytochrome P450 family 4 enzymes in cancer: Leveraging bioactivation for therapeutic potential

John P. Kowalski

A dissertation submitted in partial fulfillment of the requirements for the degree of

Doctor of Philosophy

University of Washington

2020

Reading Committee:

Allan E. Rettie, Chair

Rheem A. Totah

Abhinav Nath

Program Authorized to Offer Degree:

Medicinal Chemistry

University of Washington

Abstract

Cytochrome P450 family 4 enzymes in cancer: Leveraging bioactivation for therapeutic potential

John P. Kowalski

Chair of the Supervisory Committee:

Allan E. Rettie

Department of Medicinal Chemistry

Cytochrome P450 (CYP) enzymes are a critical family of hemoproteins that are involved in the metabolism of both xenobiotic and endogenous molecules. The CYP4 family constitutes thirteen enzymes in humans that are typically involved in fatty acid and eicosanoid oxidation. CYP4 enzymes are known to play roles in hypertension, stroke, and cancer so modulation of the enzyme activity may be of therapeutic benefit. CYP4B1 and CYP4Z1 are two orphan isozymes in the family, with relatively unknown endogenous substrate selectivities. Therefore, these two enzymes potentially offer new paradigms as CYP drug targets, particularly with regard to anticancer applications, which is a common theme of the research presented herein.

The CYP-mediated metabolism of certain substrates can result in the formation of electrophilic, and highly reactive, metabolites. This process is termed bioactivation, and while the resultant species can wreak havoc on biological systems, under certain circumstances the chemistry can be harnessed to achieve a desired beneficial effect. Consequently, the unique catalytic abilities of CYP4B1 and CYP4Z1 were manipulated to design, synthesize, and characterize pro-toxicants and mechanism-based inhibitors for these enzymes, thus leveraging bioactivation for therapeutic potential.

Over the past 20 years, CYP4B1 has been explored as a candidate enzyme in suicide gene systems for its ability to bioactivate the natural product 4-ipomeanol (IPO) to a reactive species that causes cytotoxicity. However, metabolic limitations of IPO necessitate discovery of new pro-toxicant substrates for CYP4B1. We examined a series of synthetically facile *N*-alkyl-3-furancarboxamides for cytotoxicity in HepG2 cells that express CYP4B1. This compound series maintains the furan warhead of IPO while replacing its alcohol group with alkyl chains of varying length (C1 - C8). Compounds with C3 – C6 carbon chain lengths showed similar potency to IPO (LD_{50} ~5 μM). Short chain analogs (<3 carbons) and long chain analogs (>6 carbons) exhibited reduced toxicity, resulting in a parabolic relationship between alkyl chain length and cytotoxicity. A similar parabolic relationship was observed between alkyl chain length and reactive intermediate formation upon trapping of the putative ene-dial as a stable pyrrole adduct in incubations with purified recombinant rabbit CYP4B1 and common physiological nucleophiles. These parabolic relationships reflect the lower affinity of shorter chain compounds for CYP4B1 and increased ω-hydroxylation of the longer chain compounds by the enzyme. Furthermore, modest time-dependent inhibition of CYP4B1 by *N*-pentyl-3-furancarboxamide was completely abolished when trapping agents were added, demonstrating escape of reactive intermediates from the enzyme after bioactivation. An insulated CYP4B1 active site may explain the rarely observed direct correlation between adduct formation and cell toxicity reported here.

Mammary tissue restricted CYP4Z1 has garnered interest for its potential role in breast cancer progression. CYP4Z1-dependent metabolism of arachidonic acid preferentially generates 14,15-epoxyeicosatrienoic acid (14,15-EET), a metabolite known to influence cellular proliferation, migration, and angiogenesis. We developed mechanism-based inhibitors (MBIs) of CYP4Z1 designed as fatty acid mimetics linked to the bioactivatable pharmacophore, 1-aminobenzotriazole (ABT). The most potent analog, 8-[(1H-benzotriazol-1-yl)amino]octanoic acid (8-BOA), showed a 60-fold lower shifted IC_{50} for CYP4Z1 compared to ABT**,** efficient

mechanism-based inactivation of the enzyme evidenced by a K_I = 2.2 μM, k_{inact} = 0.15 min^{-1} and a partition ratio of 14. Furthermore, 8-BOA exhibited low off-target inhibition of other CYP isozymes. Finally, low micromolar concentrations of 8-BOA inhibited 14,15-EET production in T47D breast cancer cells transfected with CYP4Z1. This first-generation, selective MBI will be a useful molecular tool to probe the biochemical role of CYP4Z1 and its association with breast cancer.

Due to the favorable inhibitory activity of 8-BOA *in vitro,* an *in vivo* characterization of this inhibitor was performed. The pharmacokinetics and metabolism of 8-BOA in rats was examined after a single IV bolus dose of 10 mg/kg. A biphasic time-concentration profile indicated relatively low clearance and distribution to a peripheral compartment. The major circulating metabolites identified in plasma were products of *β*-oxidation; bis- and tetra-demethylenated congeners accounted for >50% of metabolites by peak area. The bis-demethylenated product was characterized previously as a CYP4Z1 MBI and so represents an active metabolite that may contribute to the desired pharmacological effect. *Ex vivo* analysis of total CYP content in rat liver and kidney microsomes showed that off-target CYP inactivation was minimal; liver microsomal probe substrate metabolism also demonstrated low off-target inactivation. Standard clinical chemistries provided no indication of acute toxicity and *in silico* simulations using the free concentration of 8-BOA in plasma suggested that the *in vivo* dose used here may effectively inactivate CYP4Z1 in a xenografted tumor.

As such, the studies reported in the Chapters of this dissertation provide two excellent examples of leveraging the bioactivation potential of human CYP4 enzymes for use in anticancer settings.

Table of Contents

List of Figures, Schemes, and Tables

Summary of Supporting Information

Acknowledgements

My sincerest thanks and appreciation to:

My advisor Allan Rettie, for your excellent mentoring, research expertise, true friendship, jovial competitiveness, and extensive knowledge of Scottish proverbs.

My committee members Rheem Totah, Abhinav Nath, Kent Kunze, and Edward Kelly for your guidance through the years and the motivation to keep pushing the envelope.

Wendel Nelson, for introducing me to medicinal chemistry and always asking the hard (and necessary) questions.

Matt McDonald, for your excellent tutelage and contributions. Someday I will learn how to clean up my glassware.

Robert Pelletier, for teaching me to be game theory optimal, both at the table and in the lab.

Dale Whittington and Scott Edgar, for the mass spectrometry assistance at all hours of the day and night. They are instruments, not machines.

My classmates Ben Maldonato and Mark Benhaim, for all the shared experiences – the good, the bad, and the ugly.

Chris Burtner, for believing I could be a scientist. The skiff adventures await.

Daniel Gross, for being a brother and an endlessly supportive teammate.

Paul Kowalski, for always reminding me to keep my eye on the ball, in all aspects of life.

Alice Grette and Jeff Hay, for all the laughter and music you brought into my life.

Sophia and Sylvia Kowalski, my sisters, for your enthusiasm and encouragement.

Roscoe and Pepper, for your unwavering protection, endless cuddles, and keeping me awake.

Finally, my partner Amber Jackson, I could not have done this without you (hopefully this settles my coffee debt).

Dedication

To Amber Jackson,

For inspiring greatness and always believing in me

Chapter 1

Introduction

1.1 Cytochrome P450 enzymes in cancer progression and treatment strategies

1.1.1 Cytochrome P450 enzymes

Cytochrome P450 (CYP) enzymes are a critical family of hemoproteins that are involved in the metabolism of both xenobiotic and endogenous molecules (Ortiz de Montellano, 2005). From the initial spectral observation in the early 1960's (Omura and Sato, 1962), of pigment-450 ('P450'), the wavelength at which reduced and carbon monoxide-bound CYPs have maximal absorbance, to the conclusion of the Human Genome Project, which established 57 *CYP* genes (https://drnelson.uthsc.edu/CytochromeP450.html), the history behind the study of these enzymes is as rich as their isoform diversity. In humans, these 57 *CYP* genes are divided into 18 families, and 41 subfamilies based on sequence identity, and encode for 58 CYP enzymes, one due to a splice variant (Nebert et al., 2013). Predominantly localized to the endoplasmic reticulum, CYPs are expressed in practically all tissues but chiefly in the clearance organs, namely the liver, lung, and kidney. CYPs require the coenzyme cytochrome P450 reductase (CPR), and sometimes also cytochrome b5, for electron transport. These ancillary enzymes work in concert with the cofactor nicotinamide adenine dinucleotide phosphate (NADPH) as an electron donor to provide the reducing power for oxidation (Ortiz de Montellano, 2005). The canonical CYP reaction cycle, outlined in **Figure 1.1**, is regarded as the basic mechanism of catalysis for this enzyme superfamily (Guengerich, 2008). The plurality of the CYP reaction profile is expansive and includes (but is not limited to) aliphatic and aromatic hydroxylation, olefin epoxidation, *O-, S-,* and *N*-dealkylations, *S*- and *N*-oxidations, oxidative and reductive dehalogenations, and desaturation (Ortiz de Montellano, 2005).

1.1.2 The diverse roles of CYP enzymes in cancer

CYPs metabolize many important endogenous molecules and so it is not surprising that the role of these enzymes in human disease, including cancer, has been studied extensively (Nebert et al., 2013). In 2020, the United States will see an estimated 1.8 million new cases of cancer (American Cancer Society, 2020), the all-encompassing term for disease caused by the unrestrained division and growth of aberrant cells. CYPs play many diverse roles in both the progression of cancer and in the development of therapeutics to combat this array of diseases (**Figure 1.2**). In total, CYP enzymes remove and produce signaling ligands, drugs, or reactive metabolites, which can then cause a myriad of downstream effects.

CYP-mediated metabolism leading to deactivation and clearance of anticancer agents is crucial to understanding the efficacy of drugs currently used in the clinic and those in therapeutic development. Much of the hepatic metabolism of anticancer drugs may be attributed to CYP1, CYP2, and CYP3 family enzymes. Genetic polymorphisms of these enzymes plays an influential role in determining effective treatment strategies (McFadyen et al., 2004). Numerous profiling studies have found cancer-specific expression of CYP1B1, CYP2W1, CYP2S1, CYP2R1, CYP2U1, and CYP4Z1 (Rodriguez-Antona and Ingelman-Sundberg, 2006; Szaefer et al., 2013; Yang et al., 2017). These enzymes may prove successful as biomarkers and/or in the development of therapies targeted specifically towards the tissues in which they are expressed.

The CYP-mediated activation of pro-carcinogenic compounds has been studied for its link to cancer and has also ushered in a new understanding of chemical toxicology (Guengerich, 2008). The xenobiotics that have been extensively investigated for their role as substrates in this process are the polycyclic aromatic hydrocarbons (PAHs) that are commonly found in grilled meats and tobacco smoke. For example, through sequential epoxidation, CYP1A1 and CYP1B1 convert the PAH benzo[*a*]pyrene to the reactive benzo[*a*]pyrene-7,8-dihydrodiol-9,10-epoxide,

which can subsequently form mutagenic DNA adducts to guanine residues (Sims et al., 1974; Reed et al., 2018).

Many members of the CYP4 family are capable of metabolizing polyunsaturated fatty acids to active compounds that then participate in intricate networks of signaling events (Edson and Rettie, 2013). Metabolites of arachidonic acid that are produced by CYP4 enzymes, notably 20-hydroxeicosatetraenoic acid and 14,15-epoxyeicosatrienoic acid, are thought to play roles in human cancer progression, by influencing angiogenesis, tumor growth, and metastasis (Johnson et al., 2015; McDonald et al., 2017). The roles of CYP4 enzymes in cancer are discussed in further detail in section **1.2**.

Two tactics, mechanism-based inhibition and pro-drug activation for specific cytotoxicity, both harness CYP-mediated 'bioactivation' to combat cancer progression. The underlying phenomena surrounding these strategies with relevant clinical and pre-clinical examples are described in detail below, as these approaches were fundamental to the research presented in this dissertation. While considered a relatively mature field of study, new and exciting scientific opportunities emerge constantly to reveal novel facets about CYPs in cancer progression and therapeutics.

1.1.3 Mechanism-based inhibition of CYPs

Mechanism-based inhibitors (MBIs) may be thought of as "suicide substrates" or "booby trap substrates" for the target enzyme. Typically, an unreactive compound that is structurally related to an enzyme's substrate, is bioactivated to a reactive species which then covalently modifies the active site thus inactivating the enzyme (Silverman, 1988). The reaction pathway is presented below in **Equation 1.1**, where E, I, I', I'' and P represent enzyme, inhibitor, activated inhibitor, covalently bound inhibitor and product, respectively. The micro-rate constants (*k*) for each step in the process that govern the kinetics of inactivation are also shown.

(1.1)

$$E + I \underset{k_{-1}}{\overset{k_1}{\rightleftharpoons}} E \cdot I \xrightarrow{k_2} E \cdot I' \xrightarrow{k_4} E - I''$$
$$\downarrow k_3$$
$$E + P$$

Two kinetic constants are used to characterize MBIs: K_I; the concentration that results in the half-maximal inactivation rate, and k_{inact}; the rate of inactivation at an infinite concentration of the MBI. The micro-rate constants shown in **Equation 1.1** are used in combination to define K_I and k_{inact} as depicted in **Equations 1.2 and 1.3,** and the inactivation half-life ($t_{1/2}$) is calculated according to **1.4** (Silverman, 1988)**.**

(1.2) $$\boldsymbol{K_I = [(k_{-1} + k_2)/k_1][(k_3 + k_4)/(k_2 + k_3 + k_4)]}$$

(1.3) $$\boldsymbol{k_{inact} = k_2 k_4/(k_2 + k_3 + k_4)}$$

(1.4) $$\boldsymbol{t_{1/2} = 0.693/k_{inact}}$$

In drug development, mechanism-based inactivation is typically undesirable because the enzymes affected by this process are frequently off-target CYPs. When this occurs, drug-drug interactions (DDIs) are common liabilities since these enzymes are rendered catalytically incompetent and must then be newly biosynthesized (Obach et al., 2007). Furthermore, MBIs are also present in foods, environmental toxins, herbal supplements and recreational drugs. A well-recognized dietary MBI in grapefruit juice is bergamottin, a furanocoumarin that has been shown to inactivate CYP2B1, CYP2B4, CYP2B6, and CYP3A4/5. This constituent causes the 'grapefruit juice effect', which requires occasional DDI warnings on product data sheets (Lin et al., 2005; Kent et al., 2006b).

Several compound functional groups are recognized for their propensity to undergo CYP-mediated bioactivation and cause enzyme inactivation. These include acetylenes, isothiocyanates, thiophenes, arylamines, quinones, furans, and cyclic tertiary amines that,

through oxidative processes, form highly reactive electrophilic species that can irreversibly incapacitate the catalyzing CYP (Hollenberg et al., 2008); nucleophilic trapping agents are frequently used to identify these reactive metabolites. Reactive metabolites can lead to three modes of CYP inactivation: covalent binding to the apoprotein, binding to the prosthetic heme and heme destruction (frequently with associated apoprotein modification from heme fragments) (Hollenberg et al., 2008). For some MBIs the pathway(s) have been elucidated, as exemplified by the seminal work of Ortiz de Montellano and coworkers. This group determined that rat liver microsomal bioactivation of 1-aminobenzotriazole generates the reactive metabolite benzyne, which adds across the heme cofactor of rat liver CYPs to form an *N*-*N*-bridged benzyne-protoporphyrin IX adduct (Ortiz de Montellano and Mathews, 1981). In another example, the oral contraceptive 17-α-ethynylestradiol has been shown to inactivate CYPs through both heme and apoprotein modification. The exposed acetylene is oxidized by CYP2B1 and CYP2B6 to a ketene intermediate that leads to apoprotein adduction *via* esterification with an active site serine residue (Kent et al., 2006a). CYP3A4 primarily oxidizes this acetylene to an α-ketocarbene intermediate, which leads to heme adduction (Lin et al., 2002). Unfortunately, the mode of covalent modification/inactivation for many CYP MBIs is still unknown as frequently these experiments yield either inconclusive results or are impractical to perform without a radiolabeled inhibitor, purified enzyme, or the necessary instrument sensitivity (e.g. mass spectrometer).

Beyond being a liability, mechanism-based inactivation has also been exploited for its therapeutic potential. Drugs tailored as MBIs exhibit biochemical efficiency, a longer duration of action, efficient inactivation of the target and the potential to avoid some resistance mechanisms (Johnson et al., 2010). MBIs of CYP19, an enzyme critical in the biosynthesis of estrogen, have proved to be highly successful for the treatment of breast cancer (Brueggemeier et al., 2005).

1.1.4 Case study of CYP19 aromatase MBIs

The malignant growth and development of hormone-dependent breast cancer is driven largely by the interaction of estrogen with the estrogen receptor, which leads to gene transcription for tumor cell proliferation (Brodie et al., 2009). Inhibiting the ability of estrogen to bind to the estrogen receptor with the drug tamoxifen has been a relatively effective treatment option for many years. However, the drawbacks of tamoxifen include both resistance and partial estrogen-receptor agonism that can lead to endometrial cancer (Fornander et al., 1993; Baum et al., 2002). In humans, it is estimated that steroidogenesis is the main function of 14 out of the 58 CYP enzymes (Ortiz de Montellano, 2005). CYP19 (aromatase) is expressed throughout the body and catalyzes the rate-limiting step in the biosynthesis of estrogens such as estrone. This is accomplished through two sequential oxidations of the C-19 methyl group of androstenedione, followed by A-ring aromatization through loss of formic acid containing the C-19 carbon atom (Bruno and Njar, 2007); the structures of estrone and androstenedione are shown in **Figure 1.3A** and **B**. The third step of this process may, or may not, involve an intermediate that is enzyme-bound; however, this is beyond the scope of the discussion here. Given its role in estrogen production, it was postulated that aromatase was a druggable target in breast cancer treatment strategies.

In 1973, the androstane steroid mimetic 4-hydroxy-androst-4-ene-3,17-dione (formestane, **Figure 1.3C**) was identified by Brodie and colleagues as a potent aromatase inhibitor (Schwarzel et al., 1973). Although not designed as an MBI, *in vitro* studies indicated that time-dependent CYP19 inhibition was occurring. Considered a second-generation aromatase inhibitor, the potency of formestane is characterized by an IC_{50} ranging from 44 – 80 nM (Di Salle et al., 1990; Wiseman and Goa, 1996), with a k_{inact}, of 0.27 min^{-1} (Brodie et al., 1981). In clinical trials, formestane response rates were near 30% and the drug was approved for use in Europe. However, due to its poor bioavailability and rapid glucuronidation at the C-4 hydroxyl position (necessitating intramuscular administration), formestane is no longer in use

(Lombardi, 2002). Nevertheless, it helped to usher in a highly successful third generation aromatase MBI.

Efforts to improve upon inhibitors such as formestane resulted in the design, synthesis, and characterization of 6-methyleneandrost-1,4-diene-3,17-dione (exemestane, **Figure 1.3D**) in the late 1980's (Giudici et al., 1988). Comparative experiments to those performed with formestane showed an equipotent IC_{50} of 42 nM, whereas the inactivation of aromatase by exemestane is characterized by a K_I of 26 nM and a k_{inact} of 0.05 min^{-1} (Di Salle et al., 1990). Although not determined experimentally, the hypothesized mechanism for aromatase inactivation by exemestane involves the sequential oxidation of the C-19 methyl group, followed by peroxy-anion attack, akin to the enzyme's normal metabolic pathway. Next, the C4 position of the 3,4-double bond of exemestane is targeted by a nucleophilic active site amino acid. However, the additional 1,2-double bond that is in place for exemestane allows for aromatization and loss of formic acid, while maintaining covalent attachment to the apoprotein of aromatase (**Figure 1.3E**) (Lombardi, 2002).

In humans, it was observed that following a single dose of exemestane, the levels of circulating estrogens were significantly lowered for 4 – 5 days, and this sustained effect is attributed to the inactivation of aromatase rather than an extended drug half-life *in vivo* (Brueggemeier et al., 2005). Success in clinical trials throughout the 1990's resulted in FDA approval in 1999 of exemestane ('Aromasin') for advanced breast cancer treatment, specifically for postmenopausal women where tamoxifen treatment was no longer efficacious (Lombardi, 2002). Additional aromatase MBIs have been explored in pre-clinical settings and have also showed promising efficacy. Exemestane remains in use for breast cancer treatment and demonstrates the utility of mechanism-based inhibition of CYPs as a therapeutic paradigm. In addition to this inhibitory mode already showing success in the clinic, mechanism-based

inhibition may be the strategy of choice for future research regarding direct inhibition of CYPs to probe their roles in cancer.

1.1.5 Prodrug bioactivation

In contrast to the undesirable result that occurs from CYP-mediated bioactivation of procarcinogens, prodrug bioactivation takes advantage of the catalytic ability of CYPs to generate active metabolites from a therapeutic agent, with the goal of controlled and/or heightened cytotoxicity in cancerous cells (McFadyen et al., 2003). Whereas the reactive metabolite(s) generated from an MBI partition towards inactivation of the enzyme, the reactive metabolites generated from a pro-cytotoxic drug, perhaps more aptly named a pro-toxicant, escape the enzyme active site to produce toxicity in the host cell, while also potentially eliciting a 'bystander' effect on neighboring cells (Schwartz et al., 2002). Many factors, including the reactivity of the escaped metabolite, vulnerable tissue nucleophiles in the vicinity, and enzyme structure likely contribute to the outcome of the observed cytotoxicity instead of mechanism-based enzyme inhibition.

Numerous reactive pharmacophores, sometimes termed chemical warheads, have been explored for CYP-mediated bioactivation of pro-toxicants (Ortiz de Montellano, 2013). Insight into their use as therapeutics no doubt derived in part from the study of procarcinogen bioactivation and moieties that cause mechanism-based inhibition. The most widely recognized drug used, the alkylating agent cyclophosphamide, has a particularly gruesome history in that its mechanism of action was derived from mustard gases used for chemical warfare (although technically only the sulfur mustards, and not the nitrogen mustards, were ever used in combat, Centers for Disease Control and Prevention). The mechanism of cyclophosphamide bioactivation involves CYP-mediated hydroxylation of the carbon adjacent to the cyclic nitrogen and (reversible) ring opening to form an unstable aldophosphamide. This intermediate

spontaneously decomposes leading to the phosphoramide mustard with subsequent aziridinium cation formation. The guanine residues of DNA, particularly the N-7 position, act as nucleophiles towards this electrophile, resulting in cross-linked DNA and cell death (Ortiz de Montellano, 2013); this mechanism is presented in **Figure 1.4**. Cyclophosphamide was approved by the FDA in 1959 and is still in use today, effectively treating multiple types of cancer (Emadi et al., 2009).

In addition to DNA, the *in vivo* targets of bioactivated pro-toxicants can also be proteins. Although not related to any therapeutic application, an *in vivo* study of rat liver CYP-mediated menthofuran bioactivation identified enzymes involved with maintaining cellular homeostasis as the targets for the reactive epoxide and γ-ketoenal metabolites (Khojasteh et al., 2012). It is plausible that similar enzymes are adducted by other furan-containing substrates that have been explored for their pro-toxicant potential (Roellecke et al., 2017).

Pro-toxicant bioactivation *via* endogenously expressed CYPs occurs in both normal healthy tissue and more selectively in tumors with high specific expression of the bioactivating CYP. The aforementioned cyclophosphamide undergoes bioactivation predominantly by CYP2B6, however, CYP2A6, CYP2C9, CYP2C18, CYP2C19, and CYP3A4/5 are also partially responsible (Ortiz de Montellano, 2013). Although very useful in general cancer treatment regimes, without more specific targeting, cyclophosphamide causes undesirable off-target cytotoxicity. A number of pro-toxicants have been designed for tumor specific CYP activation; these include CYP1A1-mediated bioactivation of Phortress and aminoflavone, CYP1B1-mediated bioactivation of DMU-135, and the multiple CYP-mediated bioactivation of AQ4N (a reduction process, only under hypoxic conditions) (Bruno and Njar, 2007).

CYP2W1 has emerged as a prognostic marker in colon cancer, with high level, tumor-specific, expression in ~30% of cases (Stenstedt et al., 2012). Duocarmycins are antitumor natural products, derived from *Streptomyces* bacteria, containing a cyclopropane moiety that

results in DNA adduction leading to highly potent cytotoxicity (Boger and Johnson, 1995). Recently, a promising study reported on a deactivated congener that takes advantage of tumor-specific CYP1A1 and CYP2W1-mediated hydroxylation that results in a spirocyclization reaction to generate the electrophilic cyclopropane (Sheldrake et al., 2013). In theory, this may be effective for tumor-specific action with low off-target consequences.

1.1.6 Gene-directed enzyme prodrug therapy

The exogenous introduction of an activating enzyme, termed gene-directed enzyme pro-drug therapy (GDEPT, **Figure 1.5**), builds on the prior discussed efficacy of CYP-mediated bioactivation (Waxman et al., 1999). Additionally, GDEPT features localized drug bioactivation in (theoretically) any specific cancerous tissue with presumably lowered systemic toxicity. While initial GDEPT success was achieved with the herpes simplex virus thymidine kinase (HSV-TK) and ganciclovir combination (Fillat et al., 2003), the use of mammalian enzymes (especially of human origin) such as CYPs, may be desirable to limit potential immune responses to the products of a viral gene like HSV-TK (Waxman et al., 1999).

The first instance of a CYP-based GDEPT can be traced to studies using rat CYP2B1-expressing glioma cells and cyclophosphamide to selectively eradicate brain tumors in rats (Wei et al., 1994). Subsequently, the use of rat CYP2B1-expressing HEK293 cells injected into pancreatic cancer tumors with cyclophosphamide treatment showed relatively favorable results in a phase I/II clinical trial (Lohr et al., 2001). CYP-based GDEPT was improved upon through using human CYP2B6, delivered specifically to cancerous tissue *via* the encoding MetXia retroviral vector. The subsequent administration of cyclophosphamide showed enhanced cytotoxicity localized to the tumor in a promising phase I/II trial for treatment of advanced breast cancer (Braybrooke et al., 2005).

Still, off-target toxicities may arise in GDEPT using CYP enzymes. CYP2B6, for example, is also expressed in healthy human tissues and unwanted bioactivation also occurs in that locale. How might one accomplish the seemingly paradoxical task of utilizing a human enzyme to reduce potential immunogenicity in GDEPT, while at the same time ensuring that enzyme is not functionally expressed elsewhere? This has been achieved with the re-engineering of human CYP4B1 to render the enzyme catalytically competent (Wiek et al., 2014). While normally only animal orthologs, such as cow or rabbit CYP4B1, exhibit high enzyme activity (Baer and Rettie, 2006; Parkinson et al., 2016) this newly engineered mutant form of human CYP4B1 efficiently bioactivates furan-containing pro-toxicants, thereby causing potent cytotoxicity that may be useful in adoptive cellular therapies (Roellecke et al., 2016 and 2017). In the next section, general CYP4 family biochemistry is summarized and the specific attributes of CYP4B1 and CYP4Z1 that make them attractive targets for cancer therapeutics are outlined.

1.2 Cytochrome P450 family 4 (CYP4) enzymes in cancer: From B to Z

1.2.1 CYP4 enzymes

It is postulated that the CYP4 family evolved approximately 1.25 billion years ago, making it one of the oldest CYP families (Simpson, 1997). In humans, the CYP4 family constitutes thirteen enzymes, divided into six subfamilies. The majority of these isozymes are particularly well-recognized for their terminal (ω)-hydroxylase activity towards fatty acid and eicosanoid substrates (Edson and Rettie, 2013). Furthermore, several CYP4 enzymes metabolize numerous drugs such as tacrolimus, erythromycin, benzphetamine and terfenadine (Jarrar and Lee, 2019), placing them at the interface between endobiotic and xenobiotic metabolism (**Figure 1.6**) (Baer and Rettie, 2006). Structurally, CYP4 enzymes fall into two categories, those that uniquely possess a covalently attached heme: CYP4A11, CYP4A22,

CYP4B1, CYP4V2, CYP4F2, CYP4F3A/B, CYP4F11 and CYP4F22, and those that do not: CYP4F8, CYP4F12, CYP4X1, and CYP4Z1 (Edson and Rettie, 2013). Based on the recently solved crystal structure of CYP4B1, covalent attachment of the heme is an important determinant of CYP4-mediated ω-hydroxylation of aliphatic substrates (Hsu et al., 2017).

The CYP4 family enzymes most-associated with cancer are CYP4A11, CYP4F2, and CYP4F3B. While normally expressed in the liver and kidney, elevated transcript levels have been observed in thyroid, ovarian, breast, colon, and pancreatic cancers (Alexanian et al., 2012; Gandhi et al., 2013). The ω-hydroxylase activity of these enzymes towards the polyunsaturated fatty acid (PUFA) substrate arachidonic acid (AA) has been considered to be a causative pathway leading to cancer progression. Although other PUFAs such as eicosapentaenoic acid (EPA) and docosahexaenoic acid (DHA) also act as substrates for CYP enzymes with downstream signaling effects (Fer et al., 2008), this is beyond the scope of the current discussion.

The metabolism of AA results in the generation of three main categories of eicosanoids: the prostaglandins, hydroperoxides, and hydroxyl/epoxide-products (Kaspera and Totah, 2009). This last category is formed mainly by CYP enzymes, specifically, CYP4A11, CYP4F2, and CYP4F3B are known to produce substantial amounts of 20-hydroxyeicosatetraenoic acid (20-HETE), while CYP2C, CYP2J, and CYP3A family enzymes are largely responsible for generating the epoxyeicosatriencoic acids (EETs) (Sausville et al., 2019). 20-HETE has been shown in numerous studies to function in tandem with vascular endothelial growth factor (VEGF) to promote the necessary neovascularization (angiogenesis) and cell proliferation/migration for tumor progression and metastasis (Roman et al., 2002; Johnson et al., 2015). Increasing, or inhibiting, CYP4-mediated 20-HETE production in a number of *in vivo* brain, kidney, and breast cancer models can markedly modulate tumor size (Guo et al., 2006; 2008). In addition to VEGF, and the attendant mitogen-activated protein kinase (MAPK)

signaling cascades, 20-HETE is also implicated in the activation of the PI3K/Akt pathway for cellular proliferation and survival (Chen et al., 2012). EETs also promote cell proliferation, angiogenesis, and metastasis in tumors (Tacconelli and Patrignani, 2014). Cheranov et al. showed that angiogenesis stimulated by 14,15-EET is likely due proto-oncogene tyrosine-protein kinase (Src)-dependent signal transducer and activator of transcription-3 (STAT-3)-mediated generation of VEGF (Cheranov et al., 2008). This pathway has also been associated specifically with CYP3A4-mediated production of 14,15-EET that results in increased breast cancer cell growth (Mitra et al., 2011). Furthermore, the pro-tumorigenic signaling pathways of VEGF, MAPK, and PI3K/Akt also appear to be regulated, in part, by EETs as well (Sausville et al., 2019). The contribution of CYP4 enzymes, namely CYP4X1 and CYP4Z1, to 14,15-EET production has also been reported (Stark et al., 2008; McDonald et al., 2017). A simplified scheme of CYP-mediated AA metabolism to pro-tumorigenic metabolites has been provided in **Figure 1.7.**

The complexity of PUFA metabolism by the CYP4 family, and the interconnectedness of these enzymes and substrates, should not be understated. Both CYP4F3A and CYP4F11 have shown the ability to produce 20-HETE (Fer et al., 2008; Tang et al., 2010). However, CYP4F3A is localized to myeloid tissues and is largely associated with leukotriene B4 ω-hydroxylation to mediate inflammation (Johnson et al., 2015) whereas CYP4F11 is predominantly a liver enzyme most connected to ω-hydroxylation of long chain fatty acids such as vitamin K (Edson et al., 2013). CYP4F12 preferentially produces 18-HETE from AA (Bylund et al., 2001), although its physiological role may be more closely tied to other PUFA metabolism and signaling or even the metabolism of xenobiotics (Eksterowicz et al., 2014). CYP4F8 is a seminal vesicle enzyme and also generates 18-HETE from AA, however, it is most commonly associated with the hydroxylation of prostaglandin endoperoxides (Bylund et al., 2000). CYP4V2 is an ocular ω-hydroxylase associated with Bietti's crystalline dystrophy (Nakano et al., 2009; 2012), and

CYP4F22, an ω-hydroxylase of ultra-long-chain fatty acids (≥28 carbons), is a key enzyme in acylceramide production with links to hyperkeratotic skin disease (Ohno et al., 2015). Although some (minimal) AA metabolism has been reported with these latter two enzymes (Kelly et al., 2011), neither appear likely to contribute to cancer progression. CYP4A22 was recently categorized as a fatty acid hydroxylase, metabolizing both lauric and myristic acids at the ω-position, however, no metabolism of AA was observed, and biochemical characterization of this enzyme is limited (Durairaj et al., 2019).

Recently recognized potential roles for CYP4B1 and CYP4Z1 in cancer treatment and progression have stimulated interest in the biochemical properties of these enzymes. CYP4B1 is a unique ω-hydroxylase that is well-known for its ability to bioactivate small molecular size substrates for site-specific toxicity. This enzyme's journey towards gene-directed enzyme prodrug therapy (GDEPT) is presented in section **1.2.2**. The endogenous mammary-specific expression of CYP4Z1, with upregulation in breast cancer, suggests this enzyme may generate pro-tumorigenic metabolites from substrates such as AA. The new avenues of research presented by CYP4Z1 are detailed in section **1.2.3.**

1.2.2 CYP4B1: From inscrutability to GDEPT

CYP4B1 was first partially isolated from rabbit lung microsomes in the 1970's, with the preparation showing 7-ethoxycoumarin *O*-deethylation and benzphetamine *N*-demethylation activity (Arinc and Philpot, 1976). At the time, this pulmonary CYP was termed $P450_{II}$ and estimated to account for ≥35% of the CYP content in this organ (Wolf et al., 1978). The enzyme was placed in the newly identified subfamily 4B in 1989 from analysis of cDNAs comparing rabbit and rat CYP4B1 to rabbit P-450p2 and rat P-450LAω (~50% identity) (Gasser and Philpot, 1989). CYP4B1 is predominantly localized to the lung, with very little hepatic expression in most of the species that have been interrogated including human, monkey, rabbit, guinea pig,

hamster and rat (Robertson et al., 1981; Vanderslice et al., 1987). The rabbit, historically the archetypal species with which to study this enzyme, also shows relatively high expression in the bladder (Vanderslice et al., 1985). An exception to pulmonary-selective expression has been observed in mice, as CYP4B1 is localized to the kidney of males (but not in females). Both sexes of mice show some CYP4B1 expression in the bladder and lung (Imaoka et al., 1995).

While it has been suggested that an endogenous role for CYP4B1 exists due to sequence preservation and developmental expression in human and mouse fetal tissues (Choudhary et al., 2005), its metabolic capabilities towards physiologically relevant substrates remains uncertain. Lauric acid (LA) is an endogenous medium-chain fatty acid that is the principal component of multiple natural oil sources such as in coconuts (McCarty and DiNicolantonio, 2016). Although a physiological role for LA as a signaling ligand has been mooted (Lappano et al., 2017), its widest use is as a substrate to probe ω-hydroxylation capabilities for CYP enzymes. CYP4B1-mediated metabolism of LA results in preferential ω-hydroxylation over the ω-1 position with a ratio of ~1.5/1 (Williams et al., 1984; Cheesman et al., 2003). The ω-hydroxylation preference is more pronounced for the simple aliphatic substrates *n*-octane and *n*-heptane, with ratios of ~7 and 22, respecetively (Hsu et al., 2017). As mentioned above, terminal hydroxylation can function to activate fatty acid ligands for downstream processes, but oxidation at this position can also deactivate them, hence the importance of deducing the contribution of specific CYPs (Kikuta et al., 2002). However, the ω-hydroxylation capability of CYP4B1 apparently does not extend to several PUFA substrates that have been interrogated, as no prostaglandin E_1 or A_1 metabolism has been detected for rabbit and rat CYP4B1, respectively (Williams et al., 1984; Imaoka and Funae, 1990). Furthermore, in incubations with rabbit lung microsomes, no AA metabolism could be attributed to CYP4B1 as CYP2B4 was determined to be the solely responsible enzyme; this was confirmed with purified CYP4B1 in a reconstituted system as well (Zeldin et al., 1995). In contrast, rabbit cornea-

derived CYP4B1, transfected into rabbit corneal epithelial cells, was observed to produce a ~5-fold increase in the AA metabolite 12-hydroxyeicosatrienoic acid (Mezentsev et al., 2005). However, to date, follow up experiments were not performed to further investigate arachidonate metabolism by this enzyme. Although discussed in more detail later, it is important to note that human CYP4B1 has been determined to be catalytically incompetent (Baer and Rettie, 2008).

Recently, rabbit CYP4B1 was co-crystallized with *n*-octane, providing structural insight for the preferential ω-hydroxylase activity over other more energetically favored internal positions (Hsu et al., 2017). The CYP4B1 active site shows a narrow hydrophobic cavity, that restricts the terminal position of substrates like octane above the heme for ω-hydroxylation. This is due, in part, to a highly conserved helix I motif that contains the amino acid Glu310 covalently bound to the heme through an ester bond (Hsu et al., 2017). The structural characteristics of CYP4B1 may be extended, potentially, to other CYP4 family enzymes that display similar ω-hydroxylase activity, since crystal structures for other CYP4s have not yet been solved. Lastly, this view of the enzyme has provided some explanation for the structure-activity relationships that have been observed for CYP4B1 metabolism of pro-toxicant substrates.

CYP4B1 has become particularly well-known for its role in the metabolism of numerous xenobiotics to generate reactive metabolites that alkylate susceptible DNA and protein nucleophiles. This bioactivation pathway is known to cause tissue-specific toxicity at sites where the enzyme is expressed, most notably the lung, but also in the bladder (Baer and Rettie, 2008). Mechanistically, the bioactivation of most xenobiotics appears unrelated to the ω-hydroxylase products of CYP4B1, but instead may emanate from a common initial abstraction of a hydrogen atom at this oxidizable site. As deduced from seminal studies by Rettie and coworkers, structural constraints for this enzyme that lead to terminal oxidation are likely responsible for the CYP4B1-mediated metabolism of valproic acid to the terminal olefin, a metabolite that can cause toxicity after further biotransformation (Rettie et al., 1988; Rettie et al., 1995). Other

xenobiotic examples include the CYP4B1-mediated bioactivation of 3-methylindole to 3-methyleneindolenine that can form DNA/protein-adducts and the bioactivation of 2-aminofluorene, 2-aminoanthracene, and 2-acetylaminofluorene to *N*-hydroxy metabolites with the capability of forming DNA adducts; although additional downstream mechanisms may also be involved (Beland and Kadlubar, 1990; Baer and Rettie, 2008). The furan-containing natural product 4-ipomeanol (IPO) represents another class of bioactivatable substrates for CYP4B1 and has a particularly interesting history.

In 1974, Boyd published a report detailing the pulmonary edema and frequent deaths observed in cattle after they had consumed sweet potatoes (*Ipomoea batatas*) that had become infected by a common mold (*Fusarium solani*) (Boyd, 1974). The culprit was IPO, biosynthesized by the sweet potato as a possible defense mechanism against the mold infection; IPO also proved fatal to rabbits (Dutcher and Boyd, 1979). Using radiolabeled IPO, it was found subsequently that the reactive metabolites derived from bioactivation could covalently bind to both proteins and DNA in the lung. Studies with anti-CYP4B1 indicated the effect was largely due to CYP4B1, thus providing a molecular mechanism for the observed cytotoxicity (Boyd, 1977; Boyd, 1980; Slaughter et al., 1983; Czerwinski et al., 1991). The identity of the IPO reactive metabolite generated by rabbit CYP4B1 was proposed to be an electrophilic ene-dial. Mechanistically, this may be generated through epoxidation of IPO, followed by sigmatropic rearrangement to the ene-dial species. This intermediate may either go on to elicit toxicity through binding to tissue nucleophiles or, in the case described by Baer et al., trapped with exogenously added nucleophiles, such as *N*-acetyl cysteine (NAC) and *N*-acetyl lysine (NAL), thus enabling analysis of a stable pyrrole adduct (Baer et al., 2005). The proposed mechanism for this process is shown in **Figure 1.8**.

The ability of animal CYP4B1 orthologs to bioactivate IPO stimulated interest in its use as pro-toxicant to fight lung cancer in humans. In fact, a clinical trial with non-small and small

cell lung cancer patients was attempted using IPO, in the hopes that endogenous pulmonary CYP4B1 in humans would effectively generate site-specific cytotoxicity. Unfortunately, no beneficial outcome was observed, and hepatotoxicity was dose-limiting (Rowinsky et al., 1993). The latter observation is explained by other, hepatic, CYPs bioactivating IPO (Baer et al., 2005), while the lack of CYP4B1-mediated cytotoxicity can be rationalized by the finding that human CYP4B1 is catalytically incompetent (Zheng et al., 1998). In 1990, Yokotani and coworkers identified that human CYP4B1 cDNA contained a serine at position 427, located in the meander region near the heme, normally occupied by a proline residue in other species (Yokotani et al., 1990). However, it was not until 1998 that this substitution was probed for its effect on catalysis when the human S427P mutant was generated and expressed in a baculovirus system, resulting in human CYP4B1 regaining a degree of activity (Zheng et al., 1998). This would prove to be highly influential in future studies that more extensively re-engineered human CYP4B1 for optimal catalytic activities (Wiek et al., 2015).

While the lack of functional endogenous CYP4B1 in humans removes the possibility of site-specific bioactivation (e.g. for lung cancer), it opens up new opportunities for use in GDEPT. The first to pioneer CYP4B1 in this role was Rainov in 1998, who used rat 9L gliosarcoma and human U87 glioblastoma cells modified to express rabbit CYP4B1, in tandem with the arylamine substrate 2-aminoanthracene (Rainov et al., 1998). Subsequently, the same group showed that tumor growth in immunocompromised mice, consisting of CYP4B1-expressing 9L gliosarcoma cells, could be significantly slowed after two 200 µg administrations of IPO (Rainov in 1998).

More recent studies have explored the use of CYP4B1 in more complex GDEPT settings. Specifically, as part of a molecular switch system to inactivate (kill) T-cells that have been administered for the treatment of blood cancers, the first non-solid tumor application (Wiek et al., 2015; Roellecke et al., 2016). This could be an important safety feature since adverse immunological responses pose serious safety issues and limit T-cell doses (Bonini et al., 2015;

Ciceri et al., 2005). An exciting advance reported by Wiek et al. detailed the re-engineering of human CYP4B1 to include not only the requisite S427P mutation, but 12 additional amino acids (termed P+12). This resulted in a stable enzyme with IPO bioactivating capabilities equal to that of rabbit CYP4B1 (Wiek et al., 2015). In such a sensitive setting as T-cell therapy, it is clear that a human enzyme would be desirable as part of an inactivation system to avoid further immunological responses that may arise from the presence of a foreign bioactivating enzyme. Studies by Roellecke and coworkers optimized a lentiviral vector for high level expression of P+12 in T-cells that can effectively be eliminated after IPO treatment (Roellecke et al., 2016). Further work by this group characterized various furan-containing compounds as substrates for CYP4B1-mediated bioactivation that result in cytotoxicity. The natural product perilla ketone, which is produced by the purple mint plant, was identified as another promising pro-toxicant. However, non-productive oxidation of the aliphatic tail appeared to be a limiting factor (Roellecke et al., 2017).

Although both the rabbit and human versions of CYP4B1 seem primed for use in GDEPT, the pro-toxicant IPO (or other candidates such as perilla ketone) requires optimization. As mentioned before, several hepatic CYPs can bioactivate IPO. It was reported by Baer and coworkers that while recombinantly expressed CYP4B1 in a reconstituted system produces NAC/NAL-trapped IPO adduct at a rate of ~700 nmol/nmol CYP/30 min, CYP1A2 Supersomes can produce this adduct at a rate of ~530 nmol/nmol CYP/30 min (Baer et al., 2005). Potentially then, administration of IPO might cause unwanted hepatotoxicity via hepatic CYP1A2-mediated bioactivation, such as that observed in the failed clinical trial for lung cancer patients (Rowinsky et al., 1993). Additionally, rodent studies have shown that IPO becomes rapidly glucuronidated (Statham et al., 1982; Parkinson et al., 2016), and IPO is also a substrate for human uridine 5'-diphosphoglucuronosyl transferases (Teitelbaum et al., 2019). Therefore, circulating

concentrations of IPO may prove to be too low *in vivo* to achieve pharmacodynamic efficacy in GDEPT utilizing CYP4B1.

In summary, CYP4B1 is a rather enigmatic enzyme with unknown endogenous substrate selectivities that has been studied in many species, notably the rabbit. The ω-hydroxylase ability of CYP4B1 has been scrutinized with multiple probe substrates such as LA and simple straight-chain hydrocarbons, with the recently solved crystal structure providing structural insights to terminal oxidation. Although recent research was explicitly performed to investigate CYP4B1 playing a role in a molecular switch for T-cell inactivation, this enzyme would clearly also have utility in more classical GDEPT scenarios. The efficacy of CYP4B1 as a candidate enzyme in GDEPT stems from i) the relatively unique ability to bioactivate substrates such as IPO, and, ii) given the right pro-toxicant, off-target cytotoxicity would be minimized as there is no functional human CYP4B1 endogenously expressed to bioactivate the substrate. Finding the optimal 'chemical bullet,' however, is a continuing process as the on-target potency, off-target bioactivation (by other CYP members), and metabolic stability have proved difficult to balance. Structure-activity relationships surrounding this search for more optimal CYP4B1-bioactivatable pro-toxicants is discussed in Chapter 2 of this dissertation.

1.2.3 Mammary tissue-associated CYP4Z1: A potential driver of malignant breast cancer

The human CYP4Z subfamily consists of the genes *CYP4Z1* and the truncated pseudogene *CYPZ2P* (Rieger et al., 2004). The human CYP4Z1 enzyme is the only member of this subfamily (in all species) with confirmed functional activity (Yang et al., 2017). In 2004, Rieger et al. identified and cloned CYP4Z1, a previously unrecognized CYP that was highly localized to mammary tissue and elevated in breast carcinoma. Their analysis of CYP4Z1 mRNA showed that levels in the normal breast were ~60-fold higher than in other tissues, with a ~4-fold increase observed in breast carcinoma compared to normal breast tissue. A cancer

profiling array with cDNA derived from 50 paired normal/breast cancer specimens showed that over half of the cancer samples had CYP4Z1 expression 2 – 111-fold higher than that observed for normal samples (Rieger et al., 2004). Additional expression profiling studies also consistently showed that elevated CYP4Z1 transcript levels were associated with an increased tumor grade and aggressiveness (Murray et al., 2010; Al-Esawi et al., 2020). It has been reported that CYP4Z1 mRNA levels in cell culture may be induced 10 – 14-fold by progesterone and dexamethasone, suggesting progesterone and glucocorticoid receptors play roles in gene regulation (Savas et al., 2005). However, the consequences of this observation in relation to increased CYP4Z1 expression in breast cancer have not been further studied. Also, it should be noted that CYPZ1 is upregulated to some degree in ovarian cancer (Downie et al., 2005), although the enzyme's association with breast cancer remains at the forefront of current research.

In collaboration with Dr. Shreeram Akilesh (Department of Pathology, University of Washington), we performed our own analysis of The Cancer Genome Atlas (TCGA) to determine differential CYP4 transcript levels in the breast from 1000 cancer and 100 control samples. We observed that CYP4Z1 is the most highly upregulated CYP4 in breast cancer (**Figure 1.9**). In combination with the number of expression profiling studies that have been published, these data support a strong connection between *CYP4Z1* gene regulation and breast cancer.

The over-expression and high-grade tumor association of CYP4Z1 inspired both *in vitro* and *in vivo* studies to interrogate this enzyme's effect on cell and tumor growth. Yu et al. reported that conditioned medium, derived from cells over-expressing CYP4Z1, increased proliferation, migration and tube formation of human umbilical vein endothelial cells. These are common assays for angiogenesis (the formation of new blood vessels), a necessary function for tumor growth and metastasis (Reimer et al., 2002; Schneider et al., 2005). This supports the

hypothesis that CYP4Z1 expression may be linked to increased metastasis. Furthermore, angiogenesis was also significantly increased in both zebrafish and chick embryo models when CYP4Z1 was expressed compared to controls (Yu et al., 2012). Additionally, this group showed that in mouse xenograft studies, T47D breast cancer cells that were modified to express CYP4Z1 resulted in an approximately tripling of tumor size compared to that of control T47D cells. Lastly, they found that the ω-hydroxylated metabolite of AA, 20-HETE, was elevated approximately 4-fold in CYP4Z1-expressing T47D cells compared to vector control (Yu et al., 2012). As 20-HETE may be involved in signaling pathways related to mitogenesis and vascular endothelial growth factor-stimulated angiogenesis (Guo et al., 2007; Dhanasekaran et al., 2009), this provided a potential molecular mechanism for CYP4Z1-driven breast cancer progression.

However, the production of 20-HETE appears somewhat at odds with the first study to characterize the catalytic activity of CYP4Z1, which utilized the fission yeast *Schizosaccharomyces pombe* in whole-cell biotransformation assays (Zollner et al., 2009). In this, the saturated fatty acids caprylic, decanoic, lauric, myristic, palmitic, stearic, and arachidic acid, corresponding to 8, 10, 12, 14, 16, 18, and 20 carbons, respectively, were assessed as substrates for CY4Z1 metabolism. The unsaturated oleic and linoleic acids (both with 18 carbons) were also tested. Mass spectrometric fragmentation analysis showed that the major metabolite of lauric acid (LA) was the ω-4 hydroxyl product, and the major metabolite of myristic acid was the ω-2 hydroxyl product. No CYP4Z1-mediated metabolites of any of the other substrates that were tested were detected (Zollner et al., 2009). This indicates that CYP4Z1 acts as an internal oxidase, distinct from the tendency for oxidation at the terminal position that is observed for CYP4A and some CYP4F enzymes (Johnson et al., 2015).

Whereas most CYP4 family enzymes possess a covalently attached heme, CYP4F8, CYP4F12, CYP4X1, and CYP4Z1 do not (Yang et al., 2017). Additionally, it has been reported

that both CYP4F8 and CYP4F12 produce 18-HETE from AA (Bylund et al., 2000; 2001), and CYP4X1 produces 14,15-EET (Stark et al., 2008). Therefore, it seems plausible that CYP4 enzymes without a covalently attached heme lack this apparent structural requirement for ω-hydroxylation (Hsu et al., 2017), and thus would not necessarily produce 20-HETE as a major metabolite of AA. This prompted McDonald et al. to perform a thorough assessment of the catalytic activity of CYP4Z1 to confirm the preference for internal hydroxylation of LA as observed by Zollner et al. and evaluate the CYP4Z1 metabolite profile of AA. CYP4Z1, expressed in *Saccharomyces cerevisiae*, efficiently metabolized LA to a similar array of metabolites as observed by Zollner et al. Importantly, the preference to generate the ω-4 hydroxylated metabolite (8-hydroxy-LA) was also confirmed, at a rate of ~40 pmol/pmol CYP/min. The AA metabolite 20-HETE was not detected, however, a clear preference for 14,15-EET generation, at a rate of ~2 pmol/pmol CYP/min, was seen (McDonald et al., 2017). Therefore, CYP4Z1 acts as an internal oxidase of all of its currently known fatty acid substrates. It is tempting to speculate that a role for CYP4Z1 in breast cancer may then arise from its production of 14,15-EET, a ligand confirmed to promote angiogenesis and breast cancer cell growth (Cheranov et al., 2008; Mitra et al., 2011).

This result prompted further TCGA analysis to determine the transcript levels of other EET-producing CYPs in breast cancer samples. CYP2C8, CYP2C9, CYP2C18, CYP2C19, CYP2J2, CYP3A4, CYP4X1, and the recently identified CYP4Z1, are all known to produce some amount of EETs (Kaspera and Totah, 2009; Stark et al., 2008). These enzymes were further categorized based on Prediction Analysis of Microarray 50 (PAM50) profiling, which generates a ‘molecular portrait’ of breast cancer and aids in the projection of metastasis (Perou et al., 2000; Chia et al., 2012). Across the four major molecular subtypes of Luminal A/B, Basal (also known as triple negative), and Her2, high CYP4Z1 expression was observed (**Figure 1.10**). Although a preliminary finding, the transcript level comparison between these EET-

producing CYPs clearly shows additional evidence for a strong association between CYP4Z1 expression and breast cancer.

Additional biochemical characterization of CYP4Z1, expressed in permeabilized fission yeast cells, revealed that luciferin benzyl ether (Luc-BE) is an excellent substrate for this enzyme (Yan et al., 2017). Although the kinetics of CYP4Z1-mediated Luc-BE *O*-debenzylation were not evaluated, activity was significantly higher than in control yeast cells. Using chemiluminescence to determine CYP4Z1 activity in diverse settings such as in whole cells, microsomal incubations, and when assessing inhibitor potency is a considerable boon for future biochemical studies, since the cumbersome nature of extraction and derivatization of fatty acid metabolites precludes their use in higher-throughput assays. Lastly, recent mutagenesis studies performed by this same group determined key amino acids that may be involved with substrate binding. In particular, the polar amino acid Asn381 in the active site of CYP4Z1 was identified as the most important residue for catalytically competent binding (Du et al., 2020). Asn381 may be involved with positioning fatty acid substrates for metabolism, which matches what was observed in docking performed with AA/LA and a CYP4Z1 homology model in prior work (McDonald et al., 2017).

In summary, CYP4Z1 has emerged as a potential driver of malignant breast cancer. Expression profiling studies have shown that CYP4Z1 transcript levels are highly localized to mammary tissue and elevated in breast carcinoma. Overexpression of CYP4Z1 has been shown to promote angiogenesis and cell proliferation *in vitro*, and enhanced tumor growth *in vivo*. The molecular mechanism for this may be explained by the ability of CYP4Z1 to metabolize AA to the pro-tumorigenic metabolite, 14,15-EET. Further biochemical characterization of CYP4Z1 has broadened our knowledge of current substrates and inhibitors of this enzyme, but questions remain as to the significance of CYP4Z1 in metastatic breast cancer and whether it is a druggable target. Therefore, a selective inhibitor of CYP4Z1 would be

a much-desired chemical tool to enable further characterization of this enzyme's possible role in breast cancer progression. Efforts to design, synthesize, and characterize a new mechanism-based inhibitor of CYP4Z1 are detailed in Chapters 3 and 4 of this dissertation.

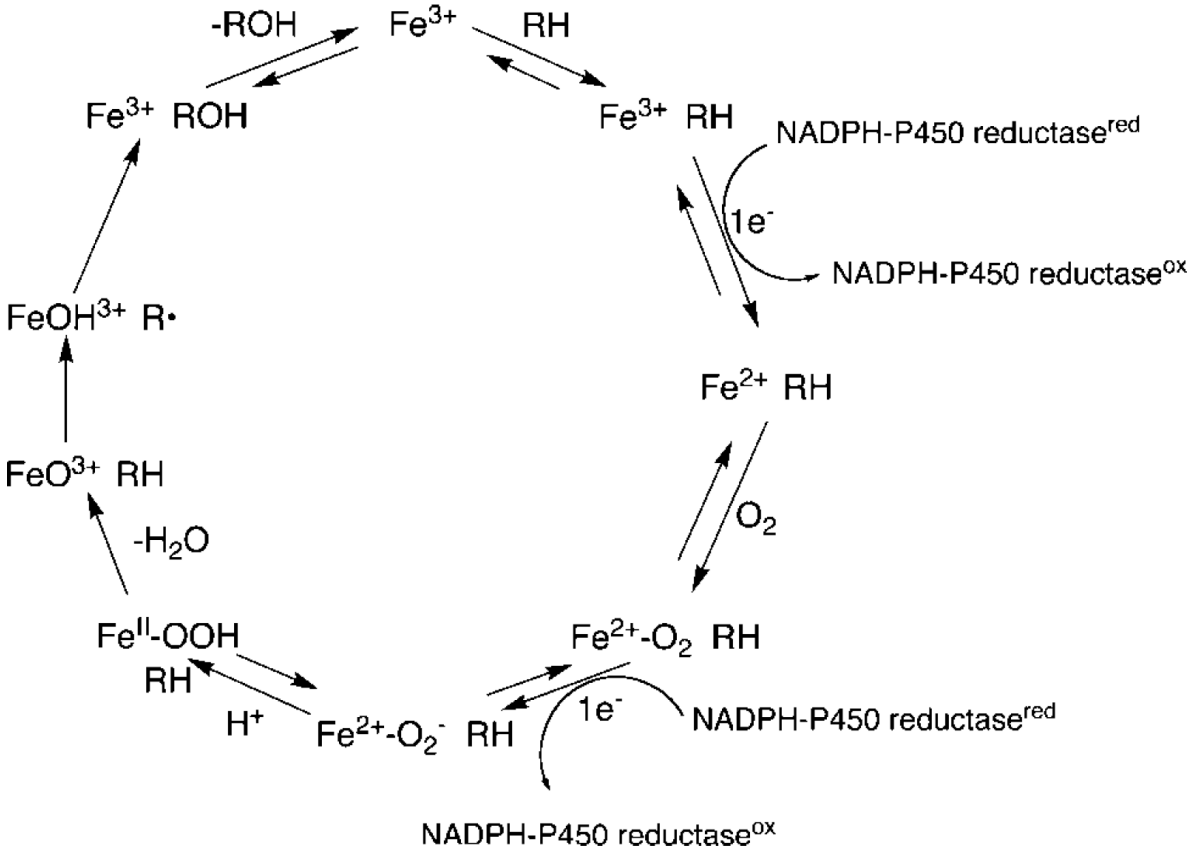

Figure 1.1 The canonical cytochrome P450 catalytic cycle (from Guengerich, 2008).

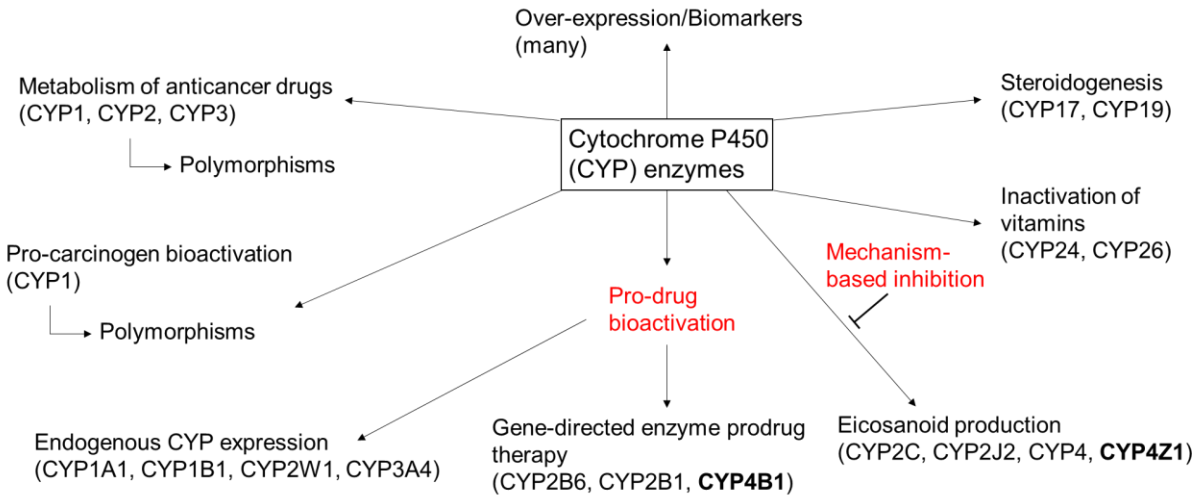

Figure 1.2 The diverse roles of CYP enzymes in cancer. Red denotes the strategies that were employed in the research presented in the chapters of this dissertation. The enzymes in bold were utilized for their bioactivation abilities for these respective strategies.

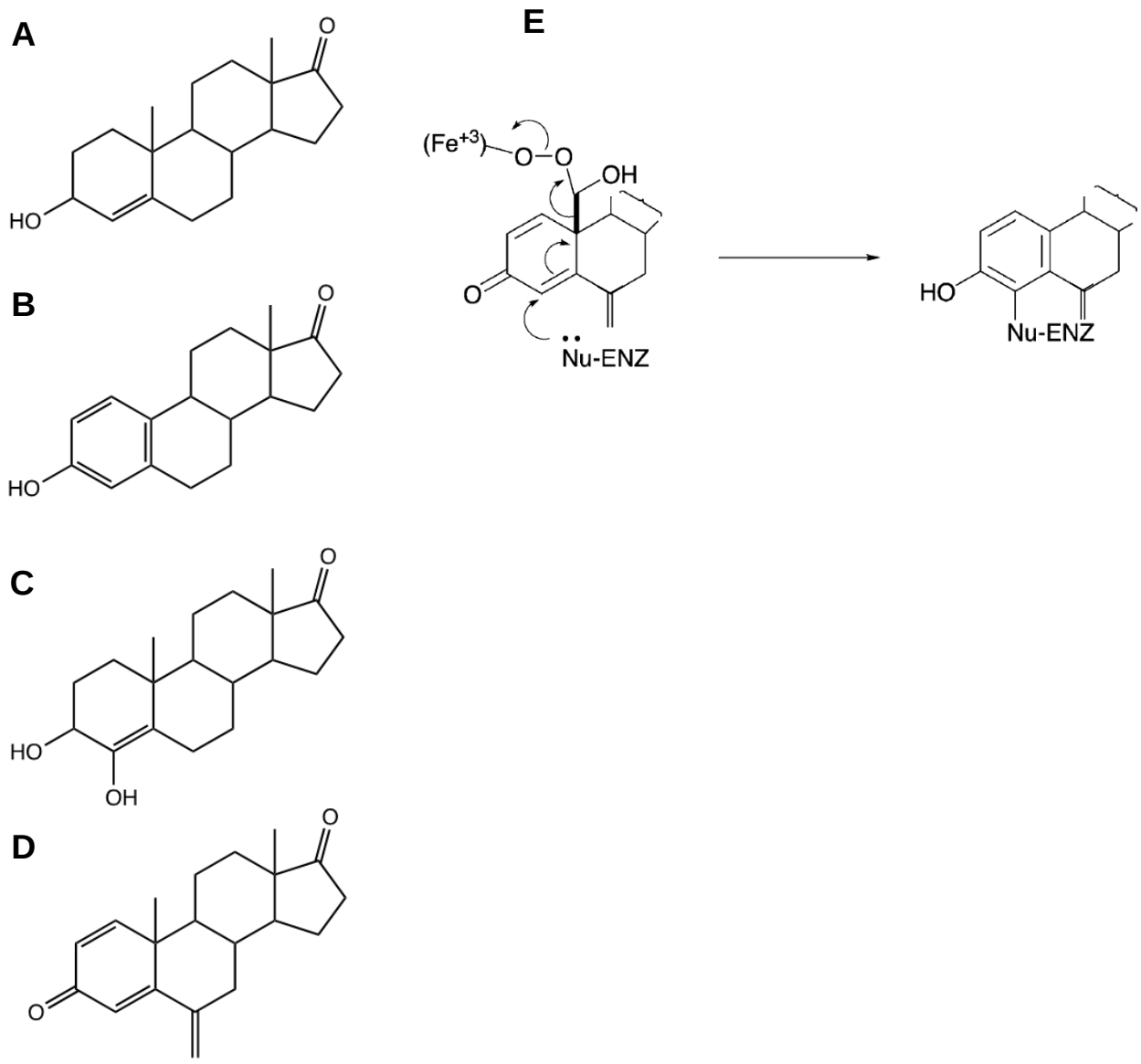

Figure 1.3 Chemical structures of androstenedione (**A**), estrone (**B**), formestane (**C**), and exemestane (**D**). Note the similarities between exemestane, a successful breast cancer drug, and androstenedione/estrone. The hypothesized mechanism for aromatase inactivation by exemestane, following the enzyme-bound intermediate (**E**) (from Lombardi, 2002).

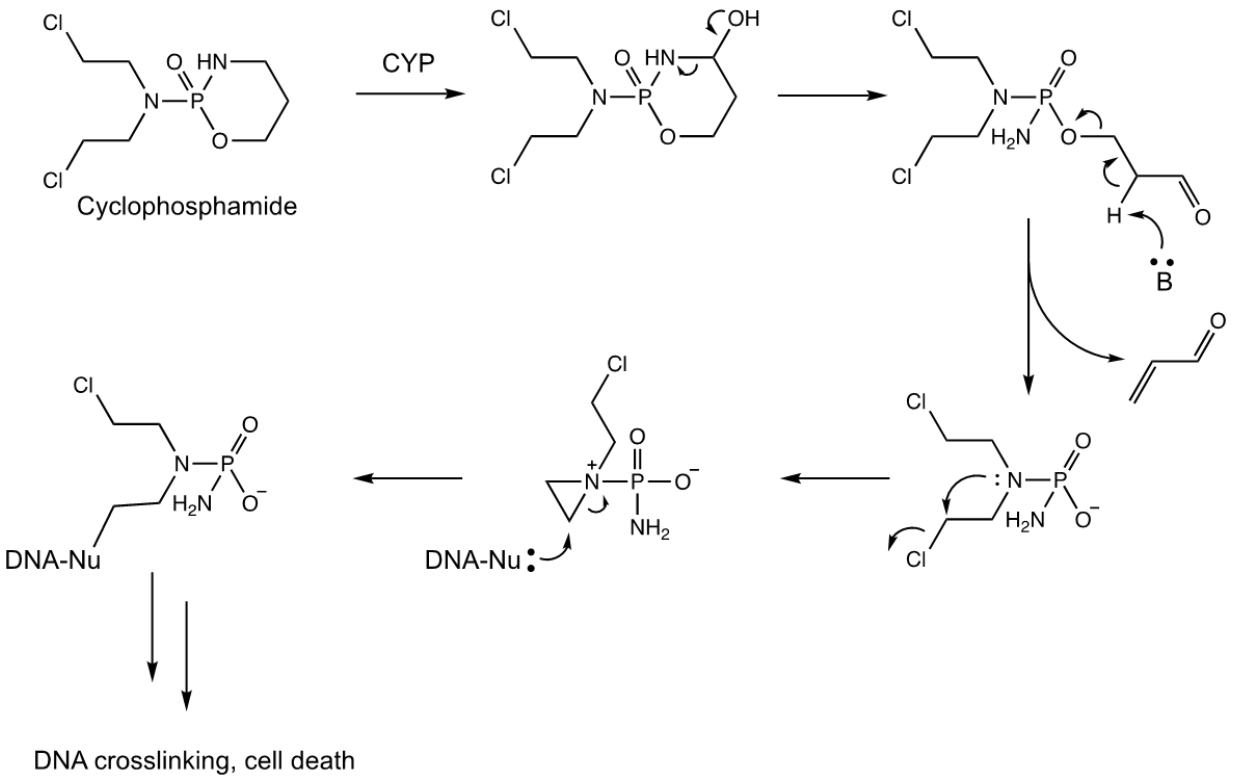

Figure 1.4 CYP-mediated bioactivation and subsequent DNA adduction of cyclophosphamide (adapted from Ortiz de Montellano, 2013).

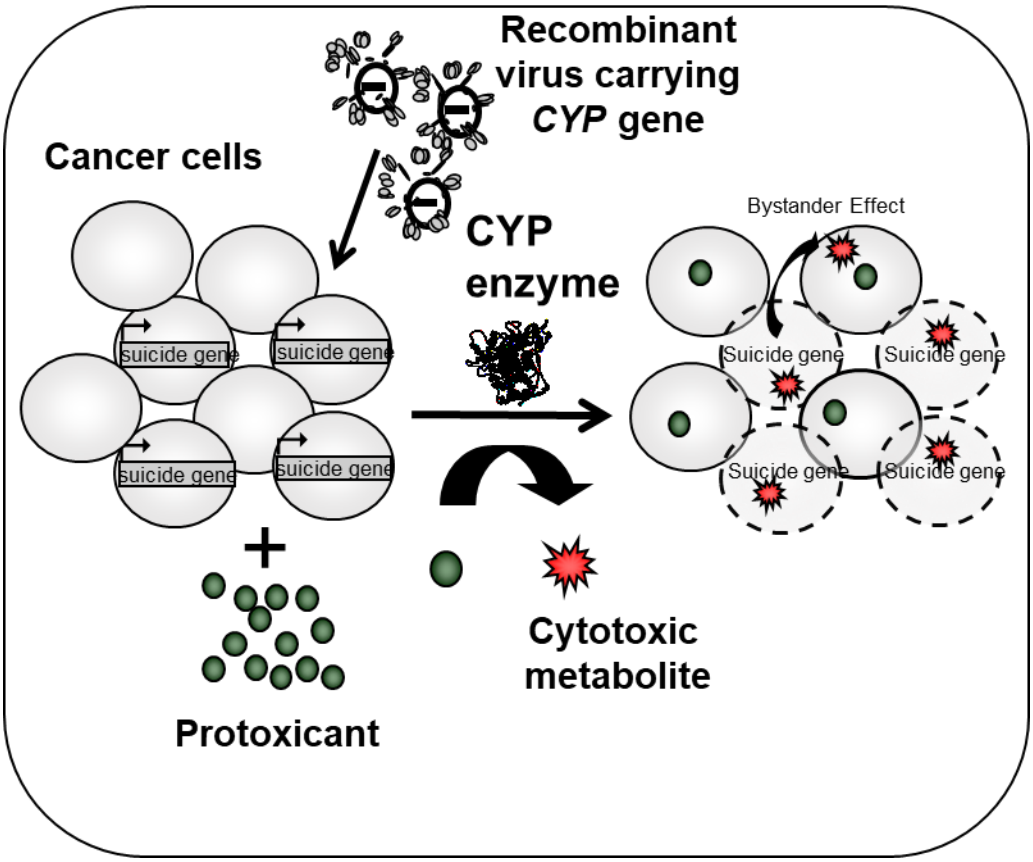

Figure 1.5 Gene-directed enzyme prodrug therapy (GDEPT).

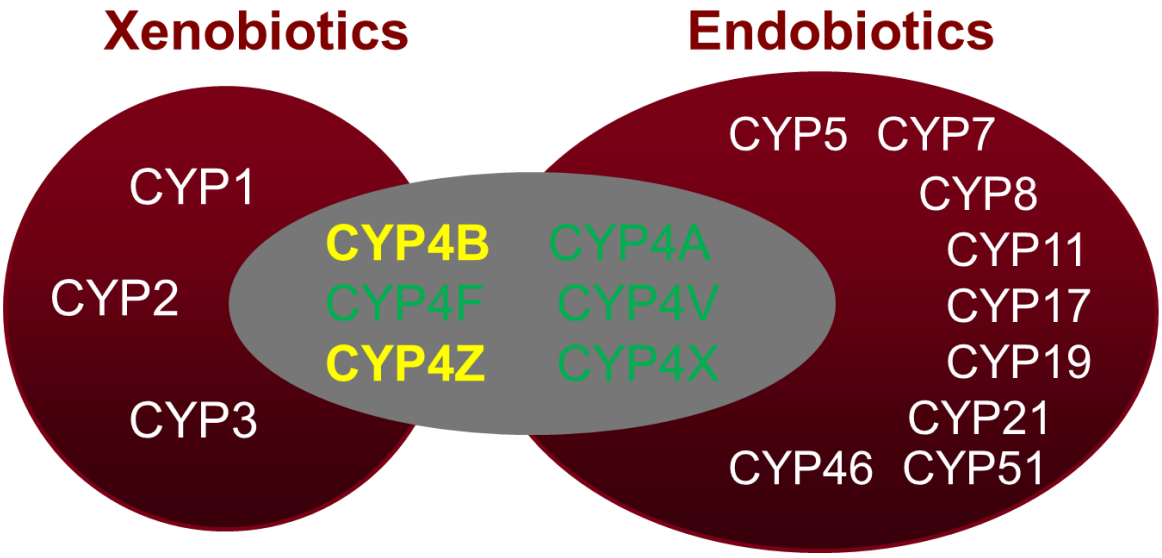

Figure 1.6. The CYP4 family enzymes reside at the interface of xenobiotic and endobiotic metabolism. CYP4B and CYP4Z (yellow) enzymes are the focus of the research presented in this dissertation and their bioactivation capabilities have been leveraged for potential cancer treatment strategies (adapted from Baer and Rettie, 2006).

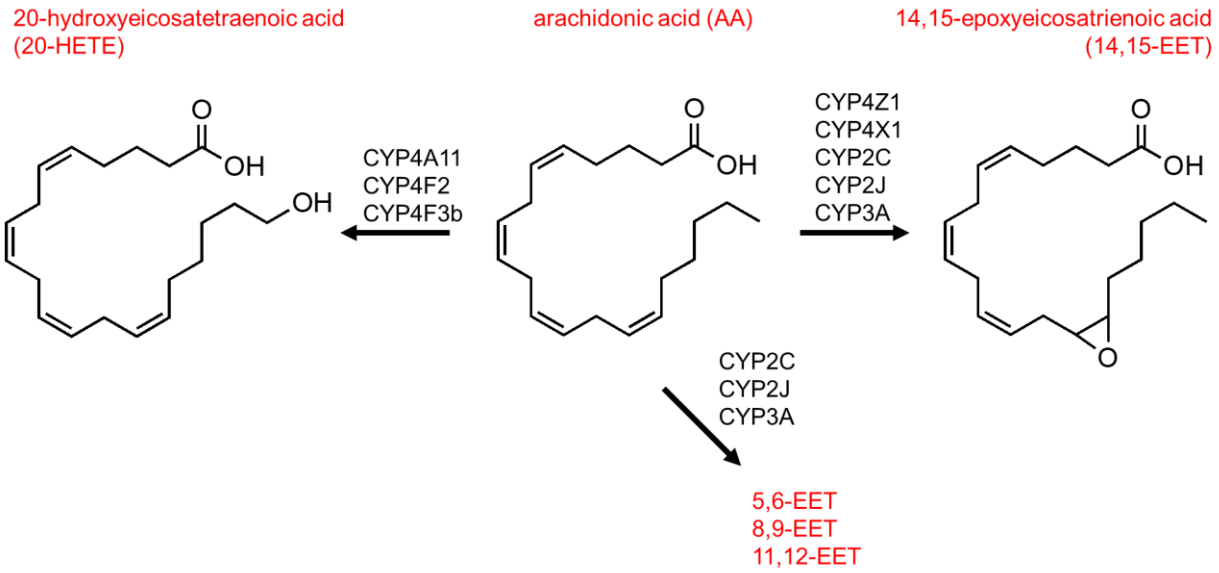

Figure 1.7. A simplified scheme of CYP-mediated AA metabolism to (potential) pro-tumorigenic metabolites (adapted from Johnson et al., 2015, with data also derived from Stark et al., 2008; McDonald et al., 2017).

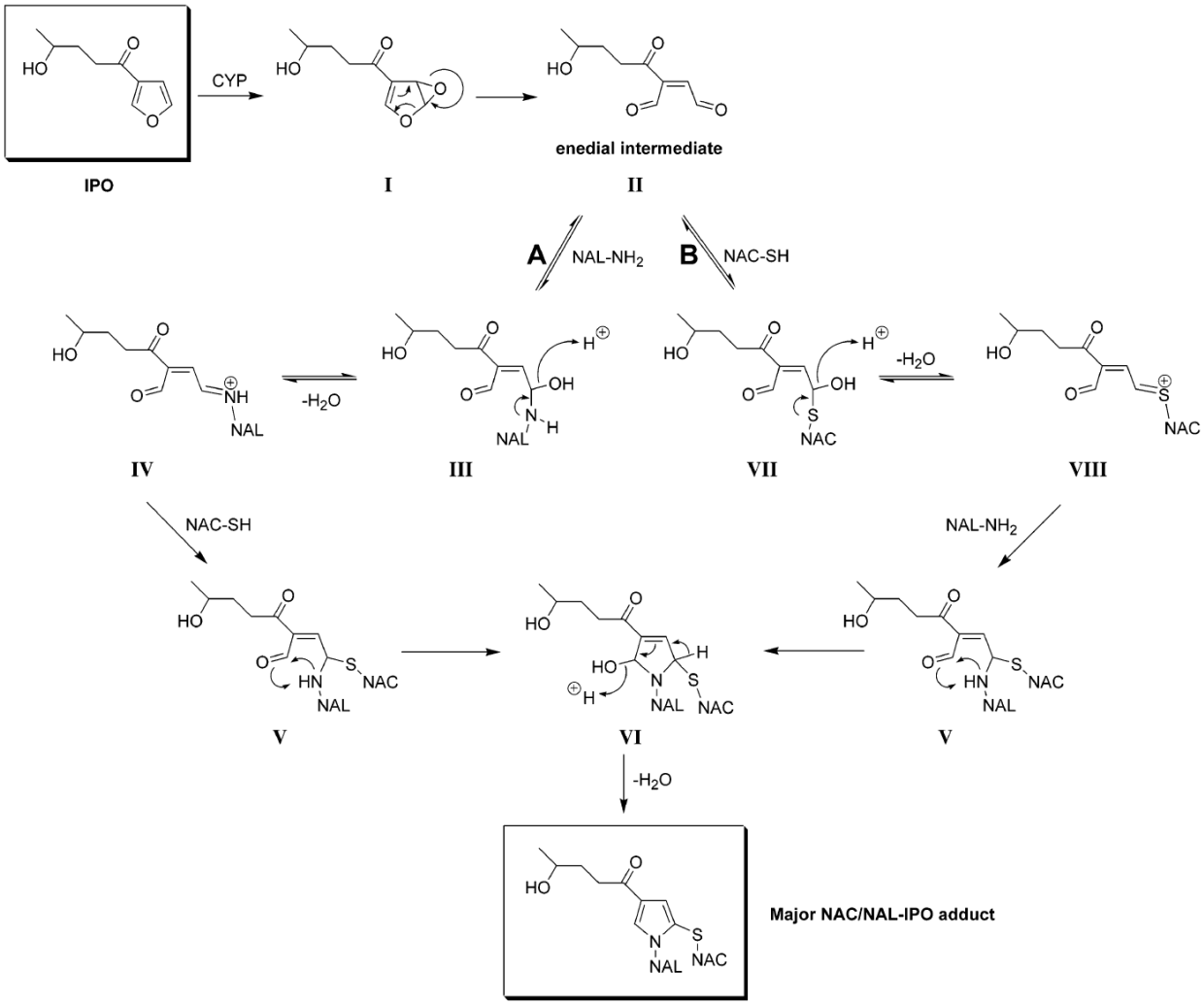

Figure 1.8. The proposed mechanism for CYP-mediated bioactivation of IPO and subsequent trapping with NAC/NAL to form the pyrrole adduct; other trapping experiments with oxidized furans indicate pathway B is most likely (from Baer et al., 2005).

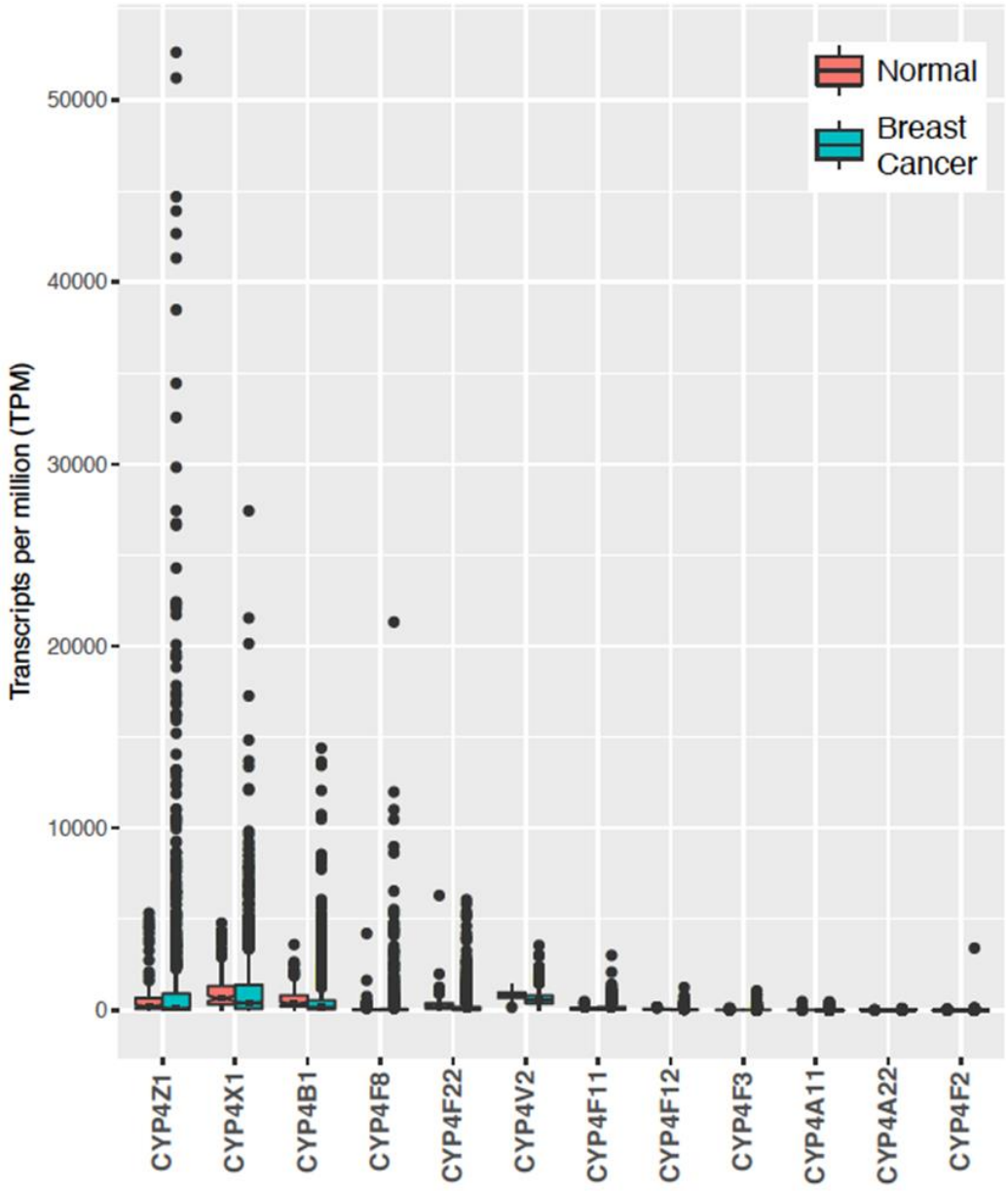

Figure 1.9. TCGA analysis of 1000 breast cancer and 100 normal samples indicate that CYP4Z1 is the most highly upregulated CYP4 in breast cancer (in collaboration with Dr. Shreeram Akilesh, UW Dept. of Pathology).

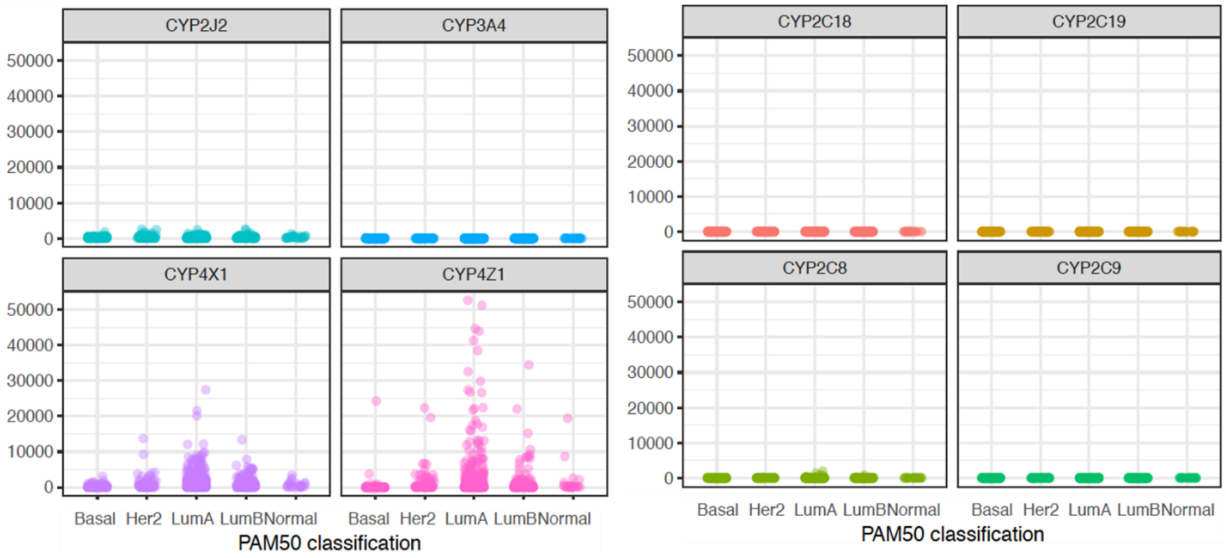

Figure 1.10. Further TCGA analysis indicates that among the EET-generating CYPs expressed in breast cancer, there is a primacy of CYP4Z1 across PAM50 classifications (in collaboration with Dr. Shreeram Akilesh, UW Dept. of Pathology).

References

Al-Esawi NSE, Geeran ARM, Alajeely MHJ, Al-Isawi AOJ. (2020). Expression of CYT4Z1 in breast carcinoma; Correlating with clinicopathological parameters. Biomed Pharmacol J, 13, 1.

Alexanian A, Miller B, Roman RJ, Sorokin A. (2012). 20-HETE-producing enzymes are up-regulated in human cancers. Cancer Genomics Proteomics, 9, 163-9.

American Cancer Society. https//www.cancer.org (accessed May 2020)

Angelastro MR, Laughlin ME, Schatzman GL, Bey P, Blohm TR. (1989). 17 beta-(cyclopropylamino)-androst-5-en-3 beta-ol, a selective mechanism-based inhibitor of cytochrome P450(17 alpha) (steroid 17 alpha-hydroxylase/C17-20 lyase). Biochem Biophys Res Commun, 162, 1571-7.

Arinç E, Philpot M. (1976). Preparation and properties of partially purified pulmonary cytochrome P-450 from rabbits. J Biol Chem, 251, 3213-20.

Baer BR, Rettie AE. (2006). CYP4B1: an enigmatic P450 at the interface between xenobiotic and endobiotic metabolism. Drug Metab Rev, 38, 451-76.

Baer BR, Rettie AE, Henne KR. (2005). Bioactivation of 4-ipomeanol by CYP4B1: adduct characterization and evidence for an enedial intermediate. Chem Res Toxicol, 18, 855-64.

Baum M, Budzar AU, Cuzick J, Forbes J, Houghton JH, Klijn JG, Sahmoud T, ATAC Trialists' Group (2002). Anastrozole alone or in combination with tamoxifen versus tamoxifen alone for adjuvant treatment of postmenopausal women with early breast cancer: first results of the ATAC randomised trial. The Lancet, 359, 2131-9.

Beland, F., Kadlubar, F. (1990). Metabolic acitvation and DNA adducts of aromatic amines and

nitroaromatic hydrocarbons. In: Couper, C., Grover, P., eds*.,* Chemical Carcinogenesis and Mutagenesis I. New York: Springer, pp. 267–325.

Boger DL, Johnson DS. (1995). CC-1065 and the duocarmycins: unraveling the keys to a new class of naturally derived DNA alkylating agents. Proc Natl Acad Sci U S A, 92, 3642-9.

Bonini C, Mondino A. (2015). Adoptive T-cell therapy for cancer: The era of engineered T cells. Eur J Immunol, 45, 2457-69.

Boyd MR. (1977). Evidence for the Clara cell as a site of cytochrome P450-dependent mixed-function oxidase activity in lung. Nature, 269, 713-5.

Boyd MR. (1980). Biochemical mechanisms in chemical-induced lung injury: roles of metabolic activation. Crit Rev Toxicol, 7, 103-76.

Boyd MR, Burka LT, Harris TM, Wilson BJ. (1974). Lung-toxic furanoterpenoids produced by sweet potatoes (Ipomoea batatas) following microbial infection. Biochim Biophys Acta, 337, 184-95.

Braybrooke JP, Slade A, Deplanque G, Harrop R, Madhusudan S, Forster MD, Gibson R, Makris A, Talbot DC, Steiner J and others. (2005). Phase I study of MetXia-P450 gene therapy and oral cyclophosphamide for patients with advanced breast cancer or melanoma. Clin Cancer Res, 11, 1512-20.

Brodie A, Njar V, Macedo LF, Vasaitis TS, Sabnis G. (2009). The Coffey Lecture: steroidogenic enzyme inhibitors and hormone dependent cancer. Urol Oncol, 27, 53-63.

Brueggemeier RW, Hackett JC, Diaz-Cruz ES. (2005). Aromatase inhibitors in the treatment of breast cancer. Endocr Rev, 26, 331-45.

Bruno RD, Njar VC. (2007). Targeting cytochrome P450 enzymes: a new approach in anti-cancer drug development. Bioorg Med Chem, 15, 5047-60.

Bylund J, Bylund M, Oliw EH. (2001). cDna cloning and expression of CYP4F12, a novel human cytochrome P450. Biochem Biophys Res Commun, 280, 892-7.

Bylund J, Hidestrand M, Ingelman-Sundberg M, Oliw EH. (2000). Identification of CYP4F8 in human seminal vesicles as a prominent 19-hydroxylase of prostaglandin endoperoxides. J Biol Chem, 275, 21844-9.

Cheesman MJ, Baer BR, Zheng YM, Gillam EM, Rettie AE. (2003). Rabbit CYP4B1 engineered for high-level expression in Escherichia coli: ligand stabilization and processing of the N-terminus and heme prosthetic group. Arch Biochem Biophys, 416, 17-24.

Centers for Disease Control and Prevention.

https://emergency.cdc.gov/agent/nitrogenmustard/basics/facts.asp (accessed May 2020)

Chen L, Ackerman R, Guo AM. (2012). 20-HETE in neovascularization. Prostaglandins Other Lipid Mediat, 98, 63-8.

Cheranov SY, Karpurapu M, Wang D, Zhang B, Venema RC, Rao GN. (2008). An essential role for SRC-activated STAT-3 in 14,15-EET-induced VEGF expression and angiogenesis. Blood, 111, 5581-91.

Chia SK, Bramwell VH, Tu D, Shepherd LE, Jiang S, Vickery T, Mardis E, Leung S, Ung K, Pritchard KI and others. (2012). A 50-gene intrinsic subtype classifier for prognosis and prediction of benefit from adjuvant tamoxifen. Clin Cancer Res, 18, 4465-72.

Choudhary D, Jansson I, Stoilov I, Sarfarazi M, Schenkman JB. (2005a). Expression patterns of mouse and human CYP orthologs (families 1-4) during development and in different adult tissues. Arch Biochem Biophys, 436, 50-61.

Choudhary D, Jansson I, Stoilov I, Sarfarazi M, Schenkman JB. (2005b). Expression patterns of mouse and human CYP orthologs (families 1-4) during development and in different adult tissues. Arch Biochem Biophys, 436, 50-61.

Ciceri F, Bonini C, Gallo-Stampino C, Bordignon C. (2005). Modulation of GvHD by suicide-gene transduced donor T lymphocytes: clinical applications in mismatched transplantation. Cytotherapy, 7, 144-9.

Czerwinski M, McLemore TL, Philpot RM, Nhamburo PT, Korzekwa K, Gelboin HV, Gonzalez FJ. (1991). Metabolic activation of 4-ipomeanol by complementary DNA-expressed human cytochromes P-450: evidence for species-specific metabolism. Cancer Res, 51, 4636-8.

DeSantis CE, Ma J, Gaudet MM, Newman LA, Miller KD, Goding Sauer A, Jemal A, Siegel RL. (2019). Breast cancer statistics, 2019. CA Cancer J Clin, 69, 438-51.

Dhanasekaran A, Bodiga S, Gruenloh S, Gao Y, Dunn L, Falck JR, Buonaccorsi JN, Medhora M, Jacobs ER. (2009). 20-HETE increases survival and decreases apoptosis in pulmonary arteries and pulmonary artery endothelial cells. Am J Physiol Heart Circ Physiol, 296, H777-86.

di Salle E, Giudici D, Briatico G, Ornati G. (1990). Novel irreversible aromatase inhibitors. Ann N Y Acad Sci, 595, 357-67.

Downie D, McFadyen MC, Rooney PH, Cruickshank ME, Parkin DE, Miller ID, Telfer C, Melvin WT, Murray GI. (2005). Profiling cytochrome P450 expression in ovarian cancer: identification of prognostic markers. Clin Cancer Res, 11, 7369-75.

Du W, Machalz D, Yan Q, Sorensen EJ, Wolber G, Bureik M. (2020). Importance of asparagine-381 and arginine-487 for substrate recognition in CYP4Z1. Biochem Pharmacol, 174, 113850.

Durairaj P, Fan L, Machalz D, Wolber G, Bureik M. (2019). Functional characterization and mechanistic modeling of the human cytochrome P450 enzyme CYP4A22. FEBS Lett, 593, 2214-25.

Dutcher JS, Boyd MR. (1979). Species and strain differences in target organ alkylation and toxicity by 4-ipomeanol. Predictive value of covalent binding in studies of target organ toxicities by reactive metabolites. Biochem Pharmacol, 28, 3367-72.

Edson KZ, Prasad B, Unadkat JD, Suhara Y, Okano T, Guengerich FP, Rettie AE. (2013). Cytochrome P450-dependent catabolism of vitamin K: omega-hydroxylation catalyzed by human CYP4F2 and CYP4F11. Biochemistry, 52, 8276-85.

Edson KZ, Rettie AE. (2013). CYP4 enzymes as potential drug targets: focus on enzyme multiplicity, inducers and inhibitors, and therapeutic modulation of 20-hydroxyeicosatetraenoic acid (20-HETE) synthase and fatty acid omega-hydroxylase activities. Curr Top Med Chem, 13, 1429-40.

Eksterowicz J, Rock DA, Rock BM, Wienkers LC, Foti RS. (2014). Characterization of the active site properties of CYP4F12. Drug Metab Dispos, 42, 1698-707.

Emadi A, Jones RJ, Brodsky RA. (2009). Cyclophosphamide and cancer: golden anniversary. Nat Rev Clin Oncol, 6, 638-47.

Fer M, Dreano Y, Lucas D, Corcos L, Salaun JP, Berthou F, Amet Y. (2008). Metabolism of eicosapentaenoic and docosahexaenoic acids by recombinant human cytochromes P450. Arch Biochem Biophys, 471, 116-25.

Fillat C, Carrió M, Cascante A, Sangro B. (2003). Suicide gene therapy mediated by the Herpes Simplex virus thymidine kinase gene/Ganciclovir system: fifteen years of application. Curr Gene Ther, 3, 13-26.

Fornander T, Hellström AC, Moberger B. (1993). Descriptive clinicopathologic study of 17 patients with endometrial cancer during or after adjuvant tamoxifen in early breast cancer. J Natl Cancer Inst, 85, 1850-5.

Gandhi AV, Saxena S, Relles D, Sarosiek K, Kang CY, Chipitsyna G, Sendecki JA, Yeo CJ, Arafat HA. (2013). Differential expression of cytochrome P450 omega-hydroxylase isoforms and their association with clinicopathological features in pancreatic ductal adenocarcinoma. Ann Surg Oncol, 20 Suppl 3, S636-43.

Gasser R, Philpot RM. (1989). Primary structures of cytochrome P-450 isozyme 5 from rabbit and rat and regulation of species-dependent expression and induction in lung and liver: identification of cytochrome P-450 gene subfamily IVB. Mol Pharmacol, 35, 617-25.

Giudici D, Ornati G, Briatico G, Buzzetti F, Lombardi P, di Salle E. (1988). 6-Methylenandrosta-1,4-diene-3,17-dione (FCE 24304): a new irreversible aromatase inhibitor. J Steroid Biochem, 30, 391-4.

Guengerich FP. (2008). Cytochrome p450 and chemical toxicology. Chem Res Toxicol, 21, 70-83.

Guo AM, Arbab AS, Falck JR, Chen P, Edwards PA, Roman RJ, Scicli AG. (2007). Activation of vascular endothelial growth factor through reactive oxygen species mediates 20-hydroxyeicosatetraenoic acid-induced endothelial cell proliferation. J Pharmacol Exp Ther, 321, 18-27.

Guo AM, Sheng J, Scicli GM, Arbab AS, Lehman NL, Edwards PA, Falck JR, Roman RJ, Scicli AG. (2008). Expression of CYP4A1 in U251 human glioma cell induces hyperproliferative phenotype in vitro and rapidly growing tumors in vivo. J Pharmacol Exp Ther, 327, 10-9.

Guo M, Roman RJ, Fenstermacher JD, Brown SL, Falck JR, Arbab AS, Edwards PA, Scicli AG. (2006). 9L gliosarcoma cell proliferation and tumor growth in rats are suppressed by N-hydroxy-N'-(4-butyl-2-methylphenol) formamidine (HET0016), a selective inhibitor of CYP4A. J Pharmacol Exp Ther, 317, 97-108.

He K, Iyer KR, Hayes RN, Sinz MW, Woolf TF, Hollenberg PF. (1998). Inactivation of cytochrome P450 3A4 by bergamottin, a component of grapefruit juice. Chem Res Toxicol, 11, 252-9.

Hollenberg PF, Kent UM, Bumpus NN. (2008). Mechanism-based inactivation of human cytochromes p450s: experimental characterization, reactive intermediates, and clinical implications. Chem Res Toxicol, 21, 189-205.

Hsu MH, Baer BR, Rettie AE, Johnson EF. (2017). The Crystal Structure of Cytochrome P450 4B1 (CYP4B1) Monooxygenase Complexed with Octane Discloses Several Structural Adaptations for omega-Hydroxylation. J Biol Chem, 292, 5610-21.

Imaoka S, Funae Y. (1990). Purification and characterization of rat pulmonary cytochrome P-450. J Biochem, 108, 33-6.

Imaoka S, Hiroi T, Tamura Y, Yamazaki H, Shimada T, Komori M, Degawa M, Funae Y. (1995). Mutagenic activation of 3-methoxy-4-aminoazobenzene by mouse renal cytochrome P450 CYP4B1: cloning and characterization of mouse CYP4B1. Arch Biochem Biophys, 321, 255-62.

Jarrar YB, Lee SJ. (2019). Molecular Functionality of Cytochrome P450 4 (CYP4) Genetic Polymorphisms and Their Clinical Implications. Int J Mol Sci, 20.

Johnson AL, Edson KZ, Totah RA, Rettie AE. (2015). Cytochrome P450 omega-Hydroxylases in Inflammation and Cancer. Adv Pharmacol, 74, 223-62.

Johnson DS, Weerapana E, Cravatt BF. (2010). Strategies for discovering and derisking covalent, irreversible enzyme inhibitors. Future Med Chem, 2, 949-64.

Kaspera R, Totah RA. (2009). Epoxyeicosatrienoic acids: formation, metabolism and potential role in tissue physiology and pathophysiology. Expert Opin Drug Metab Toxicol, 5, 757-71.

Kelly EJ, Nakano M, Rohatgi P, Yarov-Yarovoy V, Rettie AE. (2011). Finding homes for orphan cytochrome P450s: CYP4V2 and CYP4F22 in disease states. Mol Interv, 11, 124-32.

Kent UM, Lin HL, Mills DE, Regal KA, Hollenberg PF. (2006a). Identification of 17-alpha-ethynylestradiol-modified active site peptides and glutathione conjugates formed during metabolism and inactivation of P450s 2B1 and 2B6. Chem Res Toxicol, 19, 279-87.

Kent UM, Lin HL, Noon KR, Harris DL, Hollenberg PF. (2006b). Metabolism of bergamottin by cytochromes P450 2B6 and 3A5. J Pharmacol Exp Ther, 318, 992-1005.

Khojasteh SC, Hartley DP, Ford KA, Uppal H, Oishi S, Nelson SD. (2012). Characterization of rat liver proteins adducted by reactive metabolites of menthofuran. Chem Res Toxicol, 25, 2301-9.

Kikuta Y, Kusunose E, Kusunose M. (2002). Prostaglandin and leukotriene omega-hydroxylases. Prostaglandins Other Lipid Mediat, 68-69, 345-62.

Kowalski JP, McDonald MG, Whittington D, Guttman M, Scian M, Girhard M, Hanenberg H, Wiek C, Rettie AE. (2019). Structure-Activity Relationships for CYP4B1 Bioactivation of 4-Ipomeanol Congeners: Direct Correlation between Cytotoxicity and Trapped Reactive Intermediates. Chem Res Toxicol, 32, 2488-98.

Lakhanpal S, Donehower RC, Rowinsky EK. (2001). Phase II study of 4-ipomeanol, a naturally occurring alkylating furan, in patients with advanced hepatocellular carcinoma. Invest New Drugs, 19, 69-76.

Lappano R, Sebastiani A, Cirillo F, Rigiracciolo DC, Galli GR, Curcio R, Malaguarnera R, Belfiore A, Cappello AR, Maggiolini M. (2017). The lauric acid-activated signaling prompts apoptosis in cancer cells. Cell Death Discov, 3, 17063.

Lin HL, Kent UM, Hollenberg PF. (2002). Mechanism-based inactivation of cytochrome P450 3A4 by 17 alpha-ethynylestradiol: evidence for heme destruction and covalent binding to protein. J Pharmacol Exp Ther, 301, 160-7.

Lin HL, Kent UM, Hollenberg PF. (2005). The grapefruit juice effect is not limited to cytochrome P450 (P450) 3A4: evidence for bergamottin-dependent inactivation, heme destruction, and covalent binding to protein in P450s 2B6 and 3A5. J Pharmacol Exp Ther, 313, 154-64.

Lombardi P. (2002). Exemestane, a new steroidal aromatase inhibitor of clinical relevance. Biochim Biophys Acta, 1587, 326-37.

Luo J, Feng XX, Luo C, Wang Y, Li D, Shu Y, Wang SS, Qin J, Li YC, Zou JM and others. (2016). 14,15-EET induces the infiltration and tumor-promoting function of neutrophils to trigger the growth of minimal dormant metastases. Oncotarget, 7, 43324-36.

Löhr M, Hoffmeyer A, Kröger J, Freund M, Hain J, Holle A, Karle P, Knöfel WT, Liebe S, Müller P and others, (2001). Microencapsulated cell-mediated treatment of inoperable pancreatic carcinoma. Lancet. England. 1591-2.

Mathews JM, Bend JR. (1986). N-alkylaminobenzotriazoles as isozyme-selective suicide inhibitors of rabbit pulmonary microsomal cytochrome P-450. Mol Pharmacol, 30, 25-32.

McCarty MF, DiNicolantonio JJ. (2016). Lauric acid-rich medium-chain triglycerides can substitute for other oils in cooking applications and may have limited pathogenicity. Open Heart, 3, e000467.

McDonald MG, Ray S, Amorosi CJ, Sitko KA, Kowalski JP, Paco L, Nath A, Gallis B, Totah RA, Dunham MJ and others. (2017). Expression and Functional Characterization of Breast Cancer-Associated Cytochrome P450 4Z1 in Saccharomyces cerevisiae. Drug Metab Dispos, 45, 1364-71.

McFadyen MC, Melvin WT, Murray GI. (2004). Cytochrome P450 enzymes: novel options for cancer therapeutics. Mol Cancer Ther, 3, 363-71.

Mezentsev A, Mastyugin V, Seta F, Ashkar S, Kemp R, Reddy DS, Falck JR, Dunn MW, Laniado-Schwartzman M. (2005). Transfection of cytochrome P4504B1 into the cornea increases angiogenic activity of the limbal vessels. J Pharmacol Exp Ther, 315, 42-50.

Mitra R, Guo Z, Milani M, Mesaros C, Rodriguez M, Nguyen J, Luo X, Clarke D, Lamba J, Schuetz E and others. (2011). CYP3A4 mediates growth of estrogen receptor-positive breast cancer cells in part by inducing nuclear translocation of phospho-Stat3 through biosynthesis of (+/-)-14,15-epoxyeicosatrienoic acid (EET). J Biol Chem, 286, 17543-59.

Murray GI, Patimalla S, Stewart KN, Miller ID, Heys SD. (2010). Profiling the expression of cytochrome P450 in breast cancer. Histopathology, 57, 202-11.

Nakano M, Kelly EJ, Rettie AE. (2009). Expression and characterization of CYP4V2 as a fatty acid omega-hydroxylase. Drug Metab Dispos, 37, 2119-22.

Nakano M, Kelly EJ, Wiek C, Hanenberg H, Rettie AE. (2012). CYP4V2 in Bietti's crystalline dystrophy: ocular localization, metabolism of omega-3-polyunsaturated fatty acids, and functional deficit of the p.H331P variant. Mol Pharmacol, 82, 679-86.

Nebert DW, Wikvall K, Miller WL. (2013). Human cytochromes P450 in health and disease. Philos Trans R Soc Lond B Biol Sci, 368, 20120431.

Nelson DR. The cytochrome P450 homepage. http://drnelson.ut-mem.edu/

CytochromeP450.html., 2003. (accessed May 2020)

Obach RS, Walsky RL, Venkatakrishnan K. (2007). Mechanism-based inactivation of human cytochrome p450 enzymes and the prediction of drug-drug interactions. Drug Metab Dispos, 35, 246-55.

Ohno Y, Nakamichi S, Ohkuni A, Kamiyama N, Naoe A, Tsujimura H, Yokose U, Sugiura K, Ishikawa J, Akiyama M and others. (2015). Essential role of the cytochrome P450 CYP4F22 in the production of acylceramide, the key lipid for skin permeability barrier formation. Proc Natl Acad Sci U S A, 112, 7707-12.

Omura T, Sato R. (1962). A new cytochrome in liver microsomes. J Biol Chem, 237, 1375-6.

Ortiz de Montellano PR. (2013). Cytochrome P450-activated prodrugs. Future Med Chem, 5, 213-28.

Ortiz de Montellano PR, Mathews JM. (1981). Autocatalytic alkylation of the cytochrome P-450 prosthetic haem group by 1-aminobenzotriazole. Isolation of an NN-bridged benzyne-protoporphyrin IX adduct. Biochem J, 195, 761-4.

Ortiz de Montellano, P. R. Cytochrome P450: Structure, 999 Mechanism, and Biochemistry;

Kluwer Academic Publishers: New 1000 York, NY, 2005.

Panigrahy D, Greene ER, Pozzi A, Wang DW, Zeldin DC. (2011). EET signaling in cancer. Cancer Metastasis Rev, 30, 525-40.

Parkinson OT, Teitelbaum AM, Whittington D, Kelly EJ, Rettie AE. (2016). Species Differences in Microsomal Oxidation and Glucuronidation of 4-Ipomeanol: Relationship to Target Organ Toxicity. Drug Metab Dispos, 44, 1598-602.

Rainov NG, Sena-Esteves M, Fraefel C, Dobberstein KU, Chiocca EA, Breakefield XO. (1998). A chimeric fusion protein of cytochrome CYP4B1 and green fluorescent protein for detection of pro-drug activating gene delivery and for gene therapy in malignant glioma. Advances in experimental medicine and biology, 451, 393.

Reed L, Arlt VM, Phillips DH. (2018). The role of cytochrome P450 enzymes in carcinogen activation and detoxication: an in vivo-in vitro paradox. Carcinogenesis, 39, 851-9.

Reimer CL, Agata N, Tammam JG, Bamberg M, Dickerson WM, Kamphaus GD, Rook SL, Milhollen M, Fram R, Kalluri R and others. (2002). Antineoplastic effects of chemotherapeutic agents are potentiated by NM-3, an inhibitor of angiogenesis. Cancer Res, 62, 789-95.

Rettie AE, Boberg M, Rettenmeier AW, Baillie TA. (1988). Cytochrome P-450-catalyzed desaturation of valproic acid in vitro. Species differences, induction effects, and mechanistic studies. J Biol Chem, 263, 13733-8.

Rettie AE, Sheffels PR, Korzekwa KR, Gonzalez FJ, Philpot RM, Baillie TA. (1995). CYP4 isozyme specificity and the relationship between omega-hydroxylation and terminal desaturation of valproic acid. Biochemistry, 34, 7889-95.

Rieger MA, Ebner R, Bell DR, Kiessling A, Rohayem J, Schmitz M, Temme A, Rieber EP, Weigle B. (2004). Identification of a novel mammary-restricted cytochrome P450, CYP4Z1, with overexpression in breast carcinoma. Cancer Res, 64, 2357-64.

Robertson LG, Philpot RM, Zeiger E, Wolf CR. (1981). Specificity of rabbit pulmonary cytochrome P-450 isozymes in the activation of several aromatic amines and aflatoxin B1. Mol Pharmacol, 20, 662-8.

Rodriguez-Antona C, Ingelman-Sundberg M. (2006). Cytochrome P450 pharmacogenetics and cancer. Oncogene, 25, 1679-91.

Roellecke K, Jager VD, Gyurov VH, Kowalski JP, Mielke S, Rettie AE, Hanenberg H, Wiek C, Girhard M. (2017). Ligand characterization of CYP4B1 isoforms modified for high-level expression in Escherichia coli and HepG2 cells. Protein Eng Des Sel, 30, 205-16.

Roellecke K, Virts EL, Einholz R, Edson KZ, Altvater B, Rossig C, von Laer D, Scheckenbach K, Wagenmann M, Reinhardt D and others. (2016). Optimized human CYP4B1 in combination with the alkylator prodrug 4-ipomeanol serves as a novel suicide gene system for adoptive T-cell therapies.

Roman RJ. (2002). P-450 metabolites of arachidonic acid in the control of cardiovascular function. Physiol Rev, 82, 131-85.

Rowinsky EK, Noe DA, Ettinger DS, Christian MC, Lubejko BG, Fishman EK, Sartorius SE, Boyd MR, Donehower RC. (1993). Phase I and pharmacological study of the pulmonary cytotoxin 4-ipomeanol on a single dose schedule in lung cancer patients: hepatotoxicity is dose limiting in humans. Cancer Res, 53, 1794-801.

Sausville LN, Williams SM, Pozzi A. (2019). Cytochrome P450 epoxygenases and cancer: A genetic and a molecular perspective. Pharmacol Ther, 196, 183-94.

Savas U, Hsu M-H, Griffin KJ, Bell DR, Johnson EF. (2005). Conditional regulation of the human CYP4X1 and CYP4Z1 genes. Archives of biochemistry and biophysics, 436, 377-85.

Silverman, R. B. Mechanism-Based Enzyme Inactivation: 1182 Chemistry and Enzymology;

CRC Press: Boca Raton, FL, 1988.

Schneider BP, Miller KD. (2005). Angiogenesis of Breast Cancer. Journal of Clinical Oncology, 23, 1782-90.

Schwartz PS, Chen CS, Waxman DJ. (2002). Enhanced bystander cytotoxicity of P450 gene-directed enzyme prodrug therapy by expression of the antiapoptotic factor p35. Cancer Res, 62, 6928-37.

Schwarzel WC, Kruggel WG, Brodie HJ. (1973). Studies on the mechanism of estrogen biosynthesis. 8. The development of inhibitors of the enzyme system in human placenta. Endocrinology, 92, 866-80.

Sheldrake HM, Travica S, Johansson I, Loadman PM, Sutherland M, Elsalem L, Illingworth N, Cresswell AJ, Reuillon T, Shnyder SD and others. (2013). Re-engineering of the duocarmycin structural architecture enables bioprecursor development targeting CYP1A1 and CYP2W1 for biological activity. J Med Chem, 56, 6273-7.

Simpson AE. (1997). The cytochrome P450 4 (CYP4) family. Gen Pharmacol, 28, 351-9.

Sims P, Grover PL, Swaisland A, Pal K, Hewer A. (1974). Metabolic activation of benzo(a)pyrene proceeds by a diol-epoxide. Nature, 252, 326-8.

Slaughter SR, Statham CN, Philpot RM, Boyd MR. (1983). Covalent binding of metabolites of 4-ipomeanol to rabbit pulmonary and hepatic microsomal proteins and to the enzymes of the pulmonary cytochrome P-450-dependent monooxygenase system. J Pharmacol Exp Ther, 224, 252-7.

Stark K, Dostalek M, Guengerich FP. (2008). Expression and purification of orphan cytochrome P450 4X1 and oxidation of anandamide. Febs j, 275, 3706-17.

Statham CN, Dutcher JS, Kim SH, Boyd MR. (1982). Ipomeanol 4-glucuronide, a major urinary metabolite of 4-ipomeanol in the rat. Drug Metab Dispos, 10, 264-7.

Stenstedt K, Hallstrom M, Johansson I, Ingelman-Sundberg M, Ragnhammar P, Edler D. (2012). The expression of CYP2W1: a prognostic marker in colon cancer. Anticancer Res, 32, 3869-74.

Szaefer H, Cichocki M, Majchrzak-Celinska A. (2013). [New cytochrome P450 isoforms as cancer biomarkers and targets for chemopreventive and chemotherapeutic agents]. Postepy Hig Med Dosw (Online), 67, 709-18.

Tacconelli S, Patrignani P. (2014). Inside epoxyeicosatrienoic acids and cardiovascular disease. Front Pharmacol, 5, 239.

Tang Z, Salamanca-Pinzon SG, Wu ZL, Xiao Y, Guengerich FP. (2010). Human cytochrome P450 4F11: heterologous expression in bacteria, purification, and characterization of catalytic function. Arch Biochem Biophys, 494, 86-93.

Teitelbaum AM, McDonald MG, Kowalski JP, Parkinson OT, Scian M, Whittington D, Roellecke K, Hanenberg H, Wiek C, Rettie AE. (2019a). Influence of Stereochemistry on the Bioactivation and Glucuronidation of 4-Ipomeanol. J Pharmacol Exp Ther, 368, 308-16.

Teitelbaum AM, McDonald MG, Kowalski JP, Parkinson OT, Scian M, Whittington D, Roellecke K, Hanenberg H, Wiek C, Rettie AE. (2019b). Influence of Stereochemistry on the Bioactivation and Glucuronidation of 4-Ipomeanol. J Pharmacol Exp Ther, 368, 308-16.

Turtle CJ, Hanafi LA, Berger C, Gooley TA, Cherian S, Hudecek M, Sommermeyer D, Melville K, Pender B, Budiarto TM and others. (2016a). CD19 CAR-T cells of defined CD4+:CD8+ composition in adult B cell ALL patients. J Clin Invest.

Turtle CJ, Riddell SR, Maloney DG. (2016b). CD19-targeted chimeric antigen receptor-modified T cell immunotherapy for B cell malignancies. Clin Pharmacol Ther.

Vanderslice RR, Boyd JA, Eling TE, Philpot RM. (1985). The cytochrome P-450 monooxygenase system of rabbit bladder mucosa: enzyme components and isozyme 5-dependent metabolism of 2-aminofluorene. Cancer Res, 45, 5851-8.

Vanderslice RR, Domin BA, Carver GT, Philpot RM. (1987). Species-dependent expression and induction of homologues of rabbit cytochrome P-450 isozyme 5 in liver and lung. Mol Pharmacol, 31, 320-5.

Waxman DJ, Chen L, Hecht JE, Jounaidi Y. (1999). Cytochrome P450-based cancer gene therapy: recent advances and future prospects. Drug Metab Rev, 31, 503-22.

Wei MX, Tamiya T, Chase M, Boviatsis EJ, Chang TK, Kowall NW, Hochberg FH, Waxman DJ, Breakefield XO, Chiocca EA. (1994). Experimental tumor therapy in mice using the cyclophosphamide-activating cytochrome P450 2B1 gene. Hum Gene Ther, 5, 969-78.

Wiek C, Schmidt EM, Roellecke K, Freund M, Nakano M, Kelly EJ, Kaisers W, Yarov-Yarovoy V, Kramm CM, Rettie AE and others. (2015). Identification of amino acid determinants in CYP4B1 for optimal catalytic processing of 4-ipomeanol. Biochem J, 465, 103-14.

Williams DE, Hale SE, Okita RT, Masters BS. (1984). A prostaglandin omega-hydroxylase cytochrome P-450 (P-450PG-omega) purified from lungs of pregnant rabbits. J Biol Chem, 259, 14600-8.

Wiseman LR, Goa KL. (1996). Formestane. A review of its pharmacological properties and clinical efficacy in the treatment of postmenopausal breast cancer. Drugs Aging, 9, 292-306.

Wolf CR, Szutowski MM, Ball LM, Philpot RM. (1978). The rabbit pulmonary monooxygenase system: characteristics and activities of two forms of pulmonary cytochrome P-450. Chem Biol Interact, 21, 29-43.

Yan Q, Machalz D, Zollner A, Sorensen EJ, Wolber G, Bureik M. (2017). Efficient substrate screening and inhibitor testing of human CYP4Z1 using permeabilized recombinant fission yeast. Biochem Pharmacol, 146, 174-87.

Yang X, Hutter M, Goh WWB, Bureik M. (2017). CYP4Z1 - A Human Cytochrome P450 Enzyme that Might Hold the Key to Curing Breast Cancer. Current pharmaceutical design, 23, 2060-4.

Yokotani N, Sogawa K, Matsubara S, Gotoh O, Kusunose E, Kusunose M, Fujii-Kuriyama Y. (1990). cDNA cloning of cytochrome P-450 related to P-450p-2 from the cDNA library of human placenta. Gene structure and expression. Eur J Biochem, 187, 23-9.

Yu W, Chai H, Li Y, Zhao H, Xie X, Zheng H, Wang C, Wang X, Yang G, Cai X and others. (2012). Increased expression of CYP4Z1 promotes tumor angiogenesis and growth in human breast cancer. Toxicol Appl Pharmacol, 264, 73-83.

Zeldin DC, Plitman JD, Kobayashi J, Miller RF, Snapper JR, Falck JR, Szarek JL, Philpot RM, Capdevila JH. (1995). The rabbit pulmonary cytochrome P450 arachidonic acid metabolic pathway: characterization and significance. J Clin Invest, 95, 2150-60.

Zheng YM, Fisher MB, Yokotani N, Fujii-Kuriyama Y, Rettie AE. (1998). Identification of a meander region proline residue critical for heme binding to cytochrome P450: implications for the catalytic function of human CYP4B1. Biochemistry, 37, 12847-51.

Zollner A, Dragan CA, Pistorius D, Muller R, Bode HB, Peters FT, Maurer HH, Bureik M. (2009). Human CYP4Z1 catalyzes the in-chain hydroxylation of lauric acid and myristic acid. Biol Chem, 390, 313-7.

Chapter 2

Structure-activity relationships for CYP4B1 bioactivation of 4-ipomeanol congeners: Direct correlation between cytotoxicity and trapped reactive intermediates

This is adapted, with permission, from the following publication:

Kowalski JP, McDonald MG, Whittington D, Guttman M, Scian M, Girhard M, Hanenberg H, Wiek C, Rettie AE. (2019) Structure-activity relationships for CYP4B1 bioactivation of 4-ipomeanol congeners: Direct correlation between cytotoxicity and trapped reactive intermediates. Chemical Research in Toxicology.

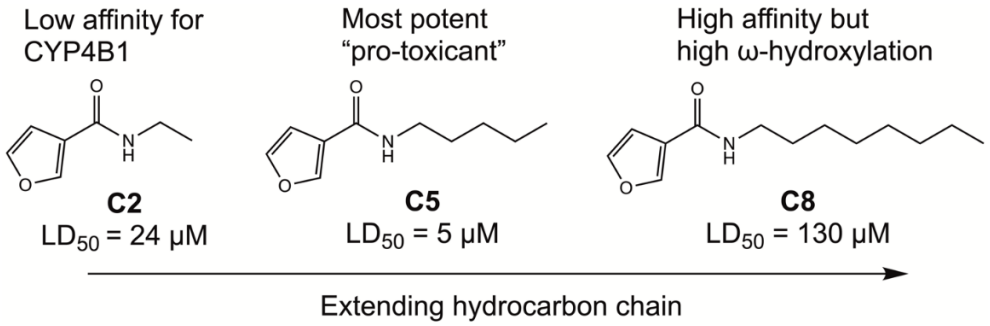

2.1 Introduction

The cytochrome P450 4 (CYP4) family consists of thirteen enzymes in humans that are typically involved in fatty acid and eicosanoid oxidation (Edson and Rettie, 2013). CYP4B1 is considered an orphan isozyme in the family, with unknown endogenous substrate selectivity (Baer and Rettie, 2006). In humans, CYP4B1 is catalytically deficient due to low stability caused, in part, by a Pro-to-Ser change in the meander region of the enzyme (Zheng et al., 1998; Wiek et al., 2015). However, other mammalian orthologs, present in cattle and rabbit,

exhibit good stability and bioactivate several protoxins that induce toxicological effects in expression-specific tissues (Baer and Rettie, 2006).

4-Ipomeanol (IPO), produced by the common sweet potato in response to stress, is a 3'-substituted furan-containing natural product, which is bioactivated by pulmonary CYP4B1 to an electrophilic species that binds tissue nucleophiles to elicit its organ toxicity (Baer et al., 2005). Consequently, IPO and related furans, like perilla ketone (PK), have been suggested as cytotoxic prodrugs in a novel CYP4B1 suicide gene system in humans. Introduction of exogenous and functional (e.g. rabbit) CYP4B1 could theoretically allow for controlled cytotoxicity relegated to where this bioactivating enzyme is newly expressed. Specifically, this may have utility in an anticancer setting as a molecular switch for T-cell inactivation (Roellecke et al., 2016), since adverse immunological responses pose serious safety issues that can limit T-cell therapy (Bonini and Mondino, 2015; Ciceri et al., 2005; Turtle et al., 2016). Use of mammalian CYP4B1 as a suicide gene could potentially reduce the immunogenicity that arises from other systems like the herpes simplex virus thymidine kinase and ganciclovir tandem (Roellecke et al., 2016).

However, IPO and PK possess structural features that could negatively impact their metabolism thereby limiting their duration of action and/or effectiveness. Rodent studies suggest rapid clearance of IPO by glucuronidation (Statham et al., 1982; Parkinson et al., 2016) and several human uridine 5'-diphosphoglucuronosyl transferases (UGTs) are known to conjugate IPO (Teitelbaum et al., 2019). While PK lacks this alcohol moiety, replacement by a methyl group confers extensive CYP4B1-mediated oxidation to non-reactive products (Roellecke et al., 2017). This latter observation suggests that CYP4B1 can bind alkyl furans in distinct catalytic orientations that influence the bioactivation versus inactivation processes.

The goal of this study is to clarify the relationship between 3'-substituted furan sub-structure and CYP4B1-mediated metabolism to either reactive intermediates (derived from oxidation of the furan group) or non-reactive metabolites (derived from oxidation of the alkyl group). In preliminary studies, we probed the CYP4B1 permissible chemical space for furan-containing substrates using a high-throughput cytotoxicity screen performed with CYP4B1-transfected HepG2 cells and a mini-library of >400 IPO-like compounds (data not shown). Although no compounds proved as potent as IPO, *N*-alkyl-3-furancarboxamides emerged as a common motif in the hits from this library. Therefore, we adopted a simple synthetic approach to generate a homologous series of eight *N*-alkyl-3-furancarboxamides and evaluated their CYP4B1-mediated cytotoxicity. Structure-metabolism relationships are discussed and the lack of mechanism-based inhibition of CYP4B1 by 3'-substituted furans identified as a key determinant of the efficiency of the cytotoxic process.

2.2 Experimental procedures

2.2.1 General reagents

Chloroform-d ($CDCl_3$) and deuterium oxide (D_2O) used for NMR experiments were purchased from Cambridge Isotope Laboratories, Inc. (Andover, MA). Reduced β-nicotinamide-adenine dinucleotide phosphate (NADPH) for CYP4B1 incubations was purchased from OYC Americas (Vista, CA). 1,2-dilauroyl-sn-glycero-3-phosphocholine (DLPC) for CYP4B1 incubations was purchased from Avanti Polar Lipids (Alabaster, AL). Tissue culture supplies (Gibco) and organic solvents were purchased from Thermo-Fisher Scientific (Pittsburgh, PA), and all other chemicals were obtained from Sigma Aldrich (St. Louis, MO). Recombinant rabbit CYP4B1 was expressed in *Escherichia coli* and purified using an established protocol (Cheesman et al.,

2003). The cytochrome P450 reductase (CPR) and cytochrome b5 coenzymes used in CYP4B1 incubations were expressed and purified according to previously published methods (Chen et al., 1998).

2.2.2 Whole cell measurement of CYP4B1-mediated toxicity

A cell proliferation assay was used to assess the cytotoxicity of compounds **C1 - C8**. HepG2 cells were modified by lentiviral transduction to express rabbit CYP4B1, or a control vector, as previously described (Wiek et al., 2015; Roellecke et al., 2016; Parkinson et al., 2016; Schmidt et al., 2015). Western blot analysis of the cell lines showed ~130 pmol CYP4B1/mg lysate protein, and no detectable enzyme in the control vector line. Enzyme levels were quantitated using recombinantly expressed purified rabbit CYP4B1 as a standard (**Fig. S2.1**). Stably transduced cells were grown in tissue culture media (DMEM, 10% FBS, 1% Pen/Strep, and 10 mM HEPES) and selected with puromycin treatment (2 µg/mL) over a 7-day period. Cells were seeded into white-walled 96-well plates at 10,000 cells/well and grown for 24 hours. Both cell lines were then treated with **C1 - C8** at 8 doses spanning the following concentrations: **C1** 0.55 – 1200 µM, **C2** 0.14 – 300 µM. **C3 - C6** 0.4 – 50 µM, **C7** 0.14 – 300 µM, **C8** 1.6 – 150 µM (DMSO did not exceed 0.1%). Cells were incubated for 72 hours and the viability was determined with the CellTiter-Glo Luminescent Assay (Promega, Madison, WI). Vehicle-treated wells were set to 100% viability and Lethal Dose 50% (LD_{50}) values were calculated from dose-response curves using nonlinear regression curve fitting with GraphPad Prism 7.00.

2.2.3 Chemical synthesis

General method for *N*-alkyl-3-furancarboxamides: A solution containing 1 equivalent (eq) of 3-furoic acid, 2 eq thionyl chloride, and a catalytic amount of DMF in anhydrous dichloromethane (DCM) was refluxed for 3 hours to generate a crude batch of 3-furoyl chloride.

Solvent and excess thionyl chloride were evaporated, and the 3-furoyl chloride was used in the following step without further work-up. A solution of 3-furoyl chloride in DCM was next cooled over ice and 2 eq of the aliphatic amine (ethyl-, through octyl-amine), along with a catalytic amount of pyridine, was added dropwise. Reactions were stirred overnight at room temperature, quenched with water, extracted with ethyl acetate and dried over magnesium sulfate. Compounds were isolated *via* flash chromatography using a hexane/ethyl acetate gradient. Purity assessed by LC-MS/UV and ^{1}H NMR was >95% for all compounds. ^{1}H NMR experiments were performed at 25 °C on a 499.73 MHz Agilent DD2 spectrometer. For characterization and spectral assignment purposes, the samples were ~30 mM solutions in $CDCl_3$ (99.96% D, Cambridge Isotopes). Chemical shifts are reported below relative to the solvent peak in $CDCl_3$ at 7.26 ppm, and the coupling constants (*J*) are noted in hertz (Hz). All annotated ^{1}H NMR spectra has been provided in Supporting Information. Accurate mass analyses of the compounds were determined *via* LC-MS on a Thermo LTQ-Orbitrap mass spectrometer.

N-Ethyl-3-furancarboxamide**, C2**: exact mass [M+H] calculated 140.0712, observed 140.0698, δ ppm 9.7. ^{1}H NMR ($CDCl_3$), 7.91 (s, 1H), 7.42 (s, 1H), 6.59 (s, 1H), 5.75 (bs, 1H), 3.46-3.42 (m, 2H), 1.22 (t, *J* = 7.5 Hz, 3H). Yield 58%.

N-Propyl-3-furancarboxamide, **C3**: exact mass [M+H] calculated 154.0868, observed 154.0871, δ ppm 1.9. ^{1}H NMR ($CDCl_3$), 7.94 (s, 1H), 7.39 (s, 1H), 6.67 (s, 1H), 6.51 (bs, 1H), 3.31 (q, *J* = 7 Hz, 2H), 1.56 (sx, *J* = 7.5 Hz, 2H), 0.92 (t, *J* = 7 Hz, 3H). Yield 56%.

N-Butyl-3-furancarboxamide, **C4**: exact mass [M+H] calculated 168.1025, observed 168.1022, δ ppm 1.5. ^{1}H NMR ($CDCl_3$), 7.95 (s, 1H), 7.36 (s, 1H), 6.88 (bs, 1H), 6.70 (s, 1H), 3.31 (q, *J* = 7 Hz, 2H), 1.50 (p, *J* = 7.5 Hz, 2H), 1.31 (sx, *J* = 7.5 Hz, 2H), 0.86 (t, *J* = 7.5 Hz, 3H). Yield 65%.

N-Pentyl-3-furancarboxamide, **C5**: exact mass [M+H] calculated 182.1181, observed 182.1170, δ ppm 6.1. ^{1}H NMR ($CDCl_3$), 7.94 (s, 1H), 7.46 (s, 1H), 6.62 (s, 1H), 5.76 (bs, 1H), 3.43 (q, *J* = 7 Hz, 2H), 1.62 (p, *J* = 7.5 Hz, 2H), 1.39 (m, 4H), 0.94 (t, *J* = 7 Hz, 3H). Yield 70%.

N-Hexyl-3-furancarboxamide, **C6**: exact mass [M+H] calculated 196.1338, observed 196.1333, δ ppm 2.3. ^{1}H NMR ($CDCl_3$), 7.94 (s, 1H), 7.39 (s, 1H), 6.66 (s, 1H), 6.41 (bs, 1H), 3.35 (t, *J* = 7 Hz, 2H), 1.54 (p, *J* = 7.5 Hz, 2H), 1.29 (m, 6H), 0.86 (t, *J* = 7 Hz, 3H). Yield 64%.

N-Heptyl-3-furancarboxamide, **C7**: exact mass [M+H] calculated 210.1494, observed 210.1484, δ ppm 4.8. ^{1}H NMR ($CDCl_3$), 7.94 (s, 1H), 7.46 (s, 1H), 6.62 (s, 1H), 5.76 (bs, 1H), 3.43 (q, *J* = 7 Hz, 2H), 1.61 (p, *J* = 7 Hz, 2H), 1.34 (m, 8H), 0.91 (t, *J* = 7 Hz, 3H). Yield 69%.

N-Octyl-3-furancarboxamide, **C8**: exact mass [M+H] calculated 224.1651, observed 224.1643, δ ppm 3.4. ^{1}H NMR ($CDCl_3$),7.94 (s, 1H), 7.38 (s, 1H), 6.67 (s, 1H), 6.52 (bs, 1H), 3.34 (q, *J* = 7 Hz, 2H), 1.54 (p, *J* = 7.5 Hz, 2H), 1.27 (m, 10H), 0.85 (t, *J* = 7 Hz, 3H). Yield 48%.

N-(2-hydroxyethyl)-3-furancarboxamide, **C2-OH**: exact mass [M+H] calculated 156.0655, observed 156.0652, δ ppm 1.9. ^{1}H NMR ($CDCl_3$), 7.95 (s, 1H), 7.43 (s, 1H), 6.63 (s, 1H), 6.33 (bs, 1H), 3.82 (s, 2H), 3.59 (s, 2H). Yield 42%.

N-(2-hydroxypentyl)-3-furancarboxamide, **C5-OH**: exact mass [M+H] calculated 198.1125, observed 198.1126, δ ppm 0.6. ^{1}H NMR ($CDCl_3$), 7.93 (s, 1H), 7.43 (s, 1H), 6.61 (s, 1H), 5.94 (bs, 1H), 3.67 (t, *J* = 6.5 Hz, 2H), 3.43 (q, *J* = 7 Hz, 2H), 1.74 (bs, 1H), 1.64 (sx, *J* = 7 Hz, 4H), 1.47 (m, 2H). Yield 46%.

N-(2-hydroxyoctyl)-3-furancarboxamide, **C8-OH**: exact mass [M+H] calculated 240.1594, observed 240.1595, δ ppm 0.4. ^{1}H NMR ($CDCl_3$), 7.92 (s, 1H), 7.43 (s, 1H), 6.61 (s, 1H), 5.84

(bs, 1H), 3.64 (t, *J* = 6.5 Hz, 2H), 3.4 (q, *J* = 7 Hz, 2H), 1.67 (bs, 1H), 1.58 (sx, *J* = 7.5 Hz, 4H), 1.35 (m, 8H). Yield 35%.

N-Methyl-3-furancarboxamide, **C1:** Synthesis of C1 was performed as previously described (Hyster and Rovis, 2010). Briefly, 1 eq of 3-furoic acid, 1.2 eq EDC-HCl, 0.3 eq HOBt and 1.05 eq $MeNH_3Cl$ were placed in a sealed flask flushed with nitrogen. MeCN was added and the solution was stirred for 5 min, followed by addition of 1.05 eq Et_3N. The reaction was stirred for 1.5 hours and water was added prior to workup. The mixture was extracted thrice with ethyl acetate followed by a brine wash, then dried over magnesium sulfate and purified *via* flash chromatography with a hexane/ethyl acetate gradient. Exact mass [M+H] calculated 126.0550, observed 126.0553, δ ppm 2.4. ^{1}H NMR, 7.92 (s, 1H), 7.43 (s, 1H), 6.60 (s, 1H), 2.96 (s, 3H). Yield 65%.

Glutathione (GSH) / N-α-acetyl-l-lysine (NAL) C5 adduct standard, **C5-GSH/NAL**: A modified synthesis procedure that has been published was utilized (Li et al., 2015). To a mixture of 1 eq compound **C5** in a 1:1 solution of saturated aqueous $NaHCO_3$/acetone was added 1.1 eq of potassium peroxymonosulfate. The *in situ* generation of dimethyldioxirane and oxidation of **C5** was allowed to proceed for 30 min at room temperature with stirring. Subsequently, 1.1 eq of GSH and 2 eq of NAL were added, and the reaction allowed to proceed for 1 hour at 70°C. Upon cooling, the precipitates were filtered out and the crude mixture was subjected to semi-preparative HPLC purification on a Phenomenex (Torrance, CA) Luna C18 column (10 x 250 mm, 5 µm, 100 Å), starting with 95% mobile phase A (0.1% formic acid in H_2O) and 5% mobile phase B (0.1% formic acid in acetonitrile) at a flow rate of 5 ml/min. After holding for five min, B was increased linearly from 5 to 30% between 5 and 30 min, then B was increased linearly from 30 to 50% between 30 and 35 min. At 35.01 min, B was increased to 95% and held for 5 min; total run time was 45 min following a 5-min equilibration period. The synthetic standard was

characterized by high resolution LC-MS/MS and 2D-NMR techniques (**Fig. S2.3 and S2.4**). Exact mass [M+H] calculated 657.2912, observed 657.290 (δ ppm 1.3). Yield 16%.

2.2.4 GSH/NAL trapping and adduct comparison of CYP4B1-generated reactive intermediates from compounds C1 - C8

Metabolic incubations contained 25 pmol purified rabbit CYP4B1, 50 pmol CPR, 25 pmol cytochrome b5, 2.5 µg DLPC, 100 U catalase, 50 µg superoxide dismutase, 5 mM NAL**,** and 5 mM GSH in 50 mM potassium phosphate buffer (KPi), pH 7.4, in a final volume of 100 µL; similar to as reported previously (Roellecke et al., 2017). Compounds **C1 - C8** were added to achieve a final concentration of 100 µM. After 30 min reconstitution on ice, metabolic reactions were initiated by the addition of NADPH (1 mM final concentration) and allowed to progress for 30 min at 37°C. Reactions were quenched with an equal volume of acetonitrile containing 2 µM furafylline as the internal standard and centrifuged at 16,000 x g for 5 min. A supernatant aliquot (10 µL) was analyzed by UPLC-MS/MS on a Waters Acquity UPLC (Milford, MA) connected to a Xevo TQ-S instrument in ESI+ mode, with the following settings: capillary 3.50 kV, cone 30.0 V, collision 10.0 V, source offset 60.0 V, source temperature 150°C, desolvation temperature 350°C, cone gas flow 150 L/hour, desolvation gas flow 800 L/hour, and collision gas flow 0.15 mL/min. Analytes were separated chromatographically using a Waters HSS T3 column (2.1 × 100 mm, 1.8 µm), starting with 95% mobile phase A (0.1% formic acid in H_2O) and 5% mobile phase B (0.1% formic acid in acetonitrile) at a flow rate of 0.3 ml/min. After holding for 1 min, B was increased linearly from 5 to 95% between 1 and 7 min and held at 95% between 7 and 10 min; total run time was 12 min following a 2-min equilibration period. Under these conditions, the 8 different GSH/NAL adducts eluted at 3.2, 3.4, 3.6, 3.8, 4.0, 4.2, 4.5, and 4.7 min for **C1 - C8**, respectively, and were detected with neutral loss scanning of 129 Da (NL129). Windows spanning 5 Da were set for each compound, surrounding the parent *m/z* for each adduct. The

internal standard, furafylline, eluted at 4.1 min and was detected by multiple reaction monitoring (MRM) at *m/z* 261.3 > 81.0. Peak area ratios (PAR) for each adduct were determined by dividing the peak areas of the analytes by that of furafylline, and metabolite analysis was performed with MassLynx V4.1.

2.2.5 Kinetics of metabolite formation by CYP4B1

Metabolic incubations contained the same reconstituted enzyme mixture as outlined above. Concentrations of **C2**, **C5**, and **C8** spanned 50 – 3000, 1 – 300, and 1 – 100 μM, respectively. The reactions were initiated by the addition of NADPH (1 mM final concentration) and allowed to progress for 15 min at 37° C, followed by the same workup described above in the GSH/NAL trapping experiments. Chromatographic separation of **C5-OH**, **C5-Adduct**, and **C8-OH** utilized the same instrument, column, and LC method as described above. A Xevo TQ-S instrument was set to ESI+ mode with the following settings: capillary 3.50 kV, cone 30.0 V, collision 10.0 V, source offset 60.0 V, source temperature 150° C, desolvation temperature 350 ° C, cone gas flow 150 L/hour, desolvation gas flow 800 L/hour, and collision gas flow 0.15 mL/min. Using these conditions **C5-OH**, **C5-Adduct**, and **C8-OH** eluted at 3.7, 4.1, and 4.7 min and were detected, respectively, in the following channels by MRM: *m/z* 198.1 > 95.1, 657.2 > 528.1, and 240.2 > 95.1. **C5-Adduct** was also detected *via* NL129 with results practically identical to that obtained with MRM. Separation of **C2-OH** was also achieved with a gradient of 0.1% formic acid in H_2O (solvent A) and 0.1% formic acid in acetonitrile (solvent B) at a flow rate of 0.3 ml/min. After holding at 2% for 3 min, B was increased linearly to 95% between 3 and 9 min and held at 95% between 9 and 10 min. The total run time was 12 min following a 2-min equilibration period. **C2-OH** eluted at 4.9 min and was detected by MRM at *m/z* 156.1 > 95.1. Calibration standards for **C2-OH**, **C5-OH**, **C5-Adduct**, and **C8-OH** were prepared in blank

incubation matrix from DMSO stocks and metabolite analysis was performed with MassLynx V4.1.

2.2.6 Characterization of C5-Adduct isomers

Metabolic incubations contained 50 pmol purified rabbit CYP4B1, 100 pmol CPR, 50 pmol cytochrome b5, 5 µg DLPC, 100 U catalase, 50 µg superoxide dismutase, 5 mM NAL, and 5 mM GSH in 50 mM KPi, pH 7.4, in a final volume of 100 µL. Compound **C5** was added to achieve a final concentration of 200 µM and then the same incubation and work-up procedure described above in the GSH/NAL trapping experiments was used. A supernatant aliquot (10 µL) was analyzed by UPLC-MS/MS on a Waters Acquity UPLC connected to an AB Sciex Triple TOF 5600 (Framingham, MA) set to ESI+ mode with the following settings: Ion source gas 1 60 arbitrary units (au), ion source gas 2 60 au, curtain gas 35 au, temperature 600℃, ionspray voltage 4500 V, declustering potential 100 V, collision energy 35 V, collision energy spread 20 V, ion release delay 67 au, and ion release width 25 au. Isomers were separated chromatographically using a Tosoh Biosciences (Tokyo, Japan) TSKgel ODS-100V column (2.0 x 150 mm, 3 µm), starting with 100% mobile phase A (0.2% acetic acid in H_2O) at a flow rate of 0.2 mL/min. After a 2-min hold, mobile phase B (0.2% acetic acid in methanol) was increased linearly from 0 to 60% between 2 and 50 min, then ramped to 100% B rapidly and held at 100% B from 50.1 to 56 min. Total run time was 60 min following a 4-min equilibration period. Using these conditions, isomers numbered 1, 2, 3, and 4 eluted at retention times (RT) of 40.0, 40.8, 41.9 and 42.4 min, respectively. Analytes were detected by both TOF MS positive mode using a 50-1000 Da window, and positive mode product ion scanning from the parent ion of *m/z* 657.29 Da.

2.2.7 CYP4B1 substrate docking

Substrate docking was performed in AutoDock Vina (Trott and Olson, 2010) using the crystal structure of rabbit CYP4B1 (Hsu et al., 2017, PDB 5T6Q). Models of **C2**, **C5**, and **C8** were generated in Open Babel (O'Boyle et al., 2011) at pH 7.4 and the substrate and protein files were processed using AutoDock tools. Docking was restrained to the active site area of the enzyme above the heme moiety and used default settings. Multiple simulations were performed for each substrate with consistent results for the preferred pose directionality and docking scores. Visualization of docked **C2, C5,** and **C8** in the active site was performed in Chimera (Pettersen et al., 2004).

2.2.8 Time-dependent inhibition (TDI) assays

Inhibition reactions contained 100 pmol purified rabbit CYP4B1, 200 pmol CPR, 100 pmol cytochrome b5, 10 µg DLPC, 100 U catalase and 50 µg superoxide dismutase, in 50 mM KPi, pH 7.4, in a final volume of 125 µL. Compound **C5** or 1-aminobenzotriazole (ABT) was added from concentrated DMSO stocks to achieve a final concentration of 100 μM, and DMSO alone was also utilized as a vehicle control. DMSO concentration did not exceed 0.2%. Reactions were set up with and without 5 mM NAL and GSH to examine the effect of trapping agents on time-dependent inhibition. After 30 min on ice for reconstitution, the reactions were initiated by the addition of NADPH (1 mM final concentration). Aliquots of the inhibition reaction (25 μL) were taken at times ~0 and 30 min, diluted 20-fold into a 0.5 mL probe substrate reaction containing lauric acid, at 10x the reported K_m for CYP4B1 (350 μM, Baer et al., 2005), in 50 mM KPi buffer with 1 mM NADPH. The probe substrate reactions progressed for 10 min at 37 °C and were quenched with 50 μL of 10% HCl. Subsequently, 10 nmol of 15-hydroxypentadecanoic acid was added as internal standard, and the solutions were extracted twice with 1 mL of ethyl acetate. The organic solvent was evaporated under a nitrogen stream, and the residues were redissolved in 50 μL of ethyl acetate. 50 μL of BSTFA reagent (Sigma)

was added and the silylation reactions were heated to 90 °C for 180 min. After cooling, the samples were analyzed by gas chromatography-mass spectrometry (GC-MS) on a Shimadzu QP2010 Gas Chromatograph Quadrupole mass spectrometer (Columbia, MD) with electron impact (EI) ionization using a previously reported method (McDonald et al., 2017).

2.3 Results

2.3.1 CYP4B1-mediated cytotoxicity of *N*-alkyl-3-furancarboxamide analogs C1 - C8

Previously, we demonstrated the utility of HepG2 cells stably transfected with CYP4B1 as a tool for investigating the potency of bioactivatable furan substrates that elicit cytotoxicity (Teitelbaum et al., 2019; Roellecke et al., 2017). A series of *N*-alkyl-3-furancarboxamides (**C1 - C8**, **Fig. 2.1A**) were chosen to establish the optimal aliphatic chain-length for CYP4B1 furan substrate bioactivation. Dose-dependent toxicity was observed in CYP4B1-HepG2 cells with all eight compounds. A representative dose-response curve is shown for **C5** in **Fig. 2.1B.** Compounds **C3**, **C4**, **C5**, and **C6** were the most potent cytotoxins exhibiting LD_{50} values 6 ± 1, 5 ± 1, 5 ± 1, and 5 ± 1 μM, respectively. CYP4B1-mediated cytotoxicity was greatly attenuated (one to two log-fold) when chain-length was shortened to <**C3** or lengthened beyond **C6**. LD_{50} values of 680 ± 40 and 24 ± 3 μM were measured for the short-chain compounds **C1** and **C2**, respectively, while LD_{50} values of 26 ± 3 and 130 ± 3 μM were measured for the long-chain compounds **C7** and **C8** (**Fig. 2.1A)**. No toxicity was observed in the control-HepG2 cells for any of the compounds, up to doses allowed by limits of aqueous solubility.

2.3.2 Relative CYP4B1-mediated reactive intermediate formation from compounds C1 - C8

The nucleophile tandem of GSH and NAL was originally chosen for our studies due to: (i) the stable pyrrole formation that occurs when a thiol and amine combination are added to oxidized furans (Baer et al., 2005; Li et al., 2015; Peterson, 2013), and (ii) the facile ability to track GSH-trapped reactive metabolites *via* neutral loss 129 scanning from different parent furan-containing compounds (Li et al., 2015). Preliminary work, performed with the same instrument settings as detailed in *Experimental Procedures*, showed that all eight parent compounds had ionization levels within ~2-fold of each other. Presumably, the neutral loss of 129 is not greatly influenced by the species with which GSH reacts. Therefore, the combination of labile GSH fragmentation and similar parent ionization efficiency should enable semi-quantitative comparisons between GSH/NAL-trapped adducts for the different compounds **C1 - C8**. Although structurally more divergent homologues might be trapped with different efficiencies, we reasoned that the simple aliphatic modifications located away from the furan pharmacophore likely does not cause a serious quantitative complication.

Therefore, we could monitor CYP4B1-dependent bioactivation of compounds **C1 - C8** by measuring the relative amounts of GSH/NAL-trapped pyrrole adduct generated from their respective reactive intermediates. **C1 - C8-Adducts** were detected by neutral loss scanning and had base peak *m/z* values that matched a proposed pyrrole adduct structure with one each of GSH and NAL, and LC retention times that increased according to parent substrate chain length, as expected (**Fig. 2.2A, B**). The relative amount of adduct formation was measured *via* PAR, with respect to the internal standard furafylline, and then normalized such that PAR was set to 100 for the **C5-Adduct**. The respective amounts generated from each substrate (average from three replicates ± SD) are shown in **Fig. 2.2B**. Adduct PAR showed an elevated value for

compounds **C3** through **C6** that inversely mirrored the LD_{50} values reported in **Fig. 2.1A**. Short-chain compounds **C1** and **C2**, as well as long-chain compounds **C7** and **C8**, generated ~10- to >100-fold less GSH/NAL-adduct than their mid-length chain homologs.

2.3.3 MS/MS Characterization of CYP4B1-mediated formation of isomeric C5-Adducts

For the simple comparative experiment above, we did not separate all isomeric products that were formed and could be detected with much longer chromatography runs. A detailed characterization was carried out on the pyrrole adducts formed from a fortified CYP4B1 incubation with compound **C5**. In the presence of GSH, NAL, and NADPH, CYP4B1 produced four isobaric metabolite peaks identified through an extended chromatographic separation followed by MS/MS analysis. These analytes eluted at retention times of 40.0, 40.8, 41.9 and 42.4 min and are numbered 1, 2, 3, and 4, respectively (**Fig. 2.3A**). Each of these metabolites had an [M+H] peak at *m/z* 657.29 and likely represent different regio-isomers of a pyrrole adduct structure containing one NAL and one GSH moiety. Tandem MS of each analyte showed a fragment ion at *m/z* 528, indicative of a neutral loss of 129, as well as other diagnostic ions that are common fragments observed with GSH adducts (**Fig. 2.3B**: isomer 1, **Fig. S2.2A and C**: isomers 2 and 4). Isomer 3 lacked the characteristic GSH-adduct [M+H – 75] fragment ion that was present in each of the other three isomers at *m/z* 582. Therefore, 3 was suggested to be the result of a cyclization reaction, perhaps resulting from the free acid of the GSH-glycine moiety attacking a cyclic iminium intermediate. A possible structure, along with assigned fragmentation data, is shown in **Fig. S2.2B and D**.

2.3.4 Characterization of the synthesized C5-GSH/NAL adduct standard

As a means of confirming our mass spectral evidence for the **C5-Adduct**, we synthesized a chemical standard of a **C5-GSH/NAL** adduct. Our synthesis produced a dominant

species that matched the CYP4B1 incubation-derived **C5-Adduct** 1 by LC-MS at retention time 40.0 min (**Fig. 2.3A**). The synthesized compound had an [M+H] peak at *m/z* 657.292 and exhibited the same MS/MS fragmentation pattern as observed for isomer 1 (**Fig. 2.3B, C**). ^{1}H NMR analysis of the **C5-GSH/NAL** standard showed the presence of a pyrrole substructure and aliphatic protons consistent with side chain NAL and GSH moieties. Additional structural validation was performed *via* multiplicity-edited HSQC NMR (**Fig. S2.3**). ROESY was used to characterize the GSH thiol attachment site to the pyrrole adduct from through-space proton interactions (**Fig. S2.4**). The assignments specified the pyrrole protons as straddling the carboxamide with the GSH moiety attached adjacent to the NAL side chain. When tested with the aforementioned NL129 LC-MS/MS method, the synthesized **C5-GSH/NAL** adduct displayed a linear response from ~1 nM to 10 μM. This broad range of linearity provided additional confidence in comparing relative adduct amounts deriving from compounds **C1 – C8**. Of note, a very minor second peak that matched the retention time of adduct 2 was also present in the LC-MS chromatogram of the synthetic standard, but insufficient material was available for further NMR analysis.

2.3.5 Kinetics of CYP4B1-mediated ω-hydroxylation for C2, C5, and C8 and Adduct formation for C5 of the 3-furancarboxamide series

Preliminary experiments suggested that the major hydroxylation (+16) metabolite of the N-alkyl-3-furancarboxamides, produced by CYP4B1, occurs at the ω-position of the alkyl tail, although metabolism of both **C5** and **C8** produced additional mono-oxygenated products that were tentatively assigned as the ω_{-1}-OH analogs (**Fig. S2.5**). Therefore, compounds **C2**, **C5**, and **C8** were chosen (spanning the homologous series) as substrates for a kinetic analysis of CYP4B1-dependent ω-hydroxylation, following synthesis of the respective **C2**, **C5** and **C8** ω-OH metabolites (**Fig. 2.4A-D**). CYP4B1 exhibited kinetics consistent with the Michaelis–Menten

model for a single-substrate reaction for **C2**-, **C5**-, and **C8-ω-OH** formation, with K_m values of 2.7 mM, 51 μM, and 15 μM along with V_{max} values of 0.03, 7.4, and 10 pmol/pmol enzyme/min, respectively. Due to the fact that we were unable to achieve full apparent saturation with **C2**, the kinetic parameters calculated for this substrate should be treated as an approximation. The catalytic efficiencies for ω-hydroxylation of **C2**, **C5**, and **C8** by CYP4B1 increased substantially with increasing alkyl tail length, *viz*, 1.2e-5, 0.15, and 0.67 μM^{-1} min^{-1}, respectively.

With a characterized **C5-GSH/NAL** adduct standard (isomer 1) in hand, CYP4B1-mediated flux between reactive intermediate and ω-hydroxylation could be directly compared for compound **C5**. Metabolism of **C5** by CYP4B1 to the trapped **C5-Adduct** exhibited kinetics again consistent with the Michaelis–Menten model of a single-substrate reaction and apparent saturation by substrate was achieved. The K_m, V_{max}, and catalytic efficiency values for **C5** were calculated to be 48 μM, 11 pmol/pmol enzyme/min, and 0.23 μM^{-1} min^{-1} respectively.

2.3.6 Investigation of time-dependent inhibition of CYP4B1 by C5

A single concentration point, time-dependent inhibition assay was used to determine if the reactive electrophilic intermediates generated from compound **C5** (chosen due to the high amount of trapped reactive intermediate formation) were causing inactivation of CYP4B1. A 30-min inhibition preincubation (t_{30}) with compound **C5** showed a 44% reduction in CYP4B1 activity, as measured by the rate of lauric acid metabolism to the 11- and 12-OH metabolites (**Fig. 2.5**). The 0-min preincubation (t_0) did not show any change relative to the vehicle control, indicating lack of both reversible and time-dependent inhibition after the dilution step for the probe substrate turnover. Incubation with the pan-CYP mechanism-based inhibitor 1-aminobenzotriazole (ABT) (Ortiz de Montellano, 2018) resulted in 78% loss of activity for t_{30}, with minimal inactivation observed at t_0. Addition of the trapping agent combination, GSH and NAL, had no significant effect on t_0 CYP4B1 activity, however, this condition completely

abrogated the **C5** TDI for t_{30}. Upon bioactivation, a true mechanism-based inactivator reacts in the active site of the catalyzing enzyme and isn't significantly affected by the addition of trapping agents. It is therefore possible that bioactivated **C5** causes its low amount of CYP4B1 TDI through reaction with nucleophilic surface amino acid residues belonging to CYP4B1 or CPR. TDI of CYP4B1 by ABT was not affected by the addition of GSH and NAL.

2.3.7 Docking of compounds C2, C5, C8 into the CYP4B1 crystal structure

The rabbit CYP4B1 crystal structure shows a narrow and hydrophobic active site, with residues Phe309, Leu485, Val375, and Val378 acting to confine aliphatic substrates, like *n*-octane (Hsu et al., 2017). The Gln218 and Tyr379 residues at the mouth of the boot-like binding pocket may participate in hydrogen-bonding to the carboxylate moiety of fatty acids or other electron-rich functionalities, such as the furan in the 3-furancarboxamide series. As the carbon chain is lengthened for compounds **C2**, **C5**, and **C8**, docking studies predict increased affinity towards CYP4B1, generating scores that are approximations of ΔG values of -5.7, -6.7, and -7.4 kcal/mol, respectively. The top poses for **C2** and **C5** (**Fig. 2.6**; colored yellow and green, respectively) position the furan ring above the heme for epoxidation, with the 4' and 5' carbons of the furan at 3.8 and 3.3 Å from the heme iron for both **C2** and **C5**. The top pose for **C8** (**Fig. 2.6**; colored plum) reoriented the substrate with the aliphatic tail positioned over the heme for ω-hydroxylation, situating the terminal carbon 3.1 Å away from the heme iron. Additionally, the furan moiety oxygen of **C8** is located 3.3 and 3.6 Å from residues Gln218 and Tyr379, respectively. This is consistent with hydrogen-bonding contacts that may aid in terminal tail positioning for **C8**, which could explain the observed CYP4B1 preference for ω-hydroxylation of this substrate over epoxidation. The positions of these substrates in the CYP4B1 active site should not be considered as atomically exact, but as representative computational models consistent with our experimental data.

2.4 Discussion

Of the known xenobiotics that undergo CYP4B1-mediated bioactivation, the natural products IPO and PK have been most extensively studied, both *in vitro* and *in vivo*, including the use of IPO in humans (Rowinsky et al., 1993). Given the potential liabilities of rapid glucuronidation and metabolism to inactivated products for IPO and PK, respectively, it seemed advantageous to investigate other structurally related compounds to identify new bioactivatable substrates for CYP4B1. The current study was begun with the principal goal of elucidating alkyl furan structure-activity relationships to better define elements of protoxicant potency and metabolism by the enzyme. Rabbit CYP4B1 is the most commonly studied form of the enzyme and its use as a suicide gene was first suggested in the 1990s (Rainov et al., 1998). In contrast to native human CYP4B1, rabbit CYP4B1 is both highly stable and efficiently bioactivates furan protoxicants to cytotoxic species. Although a re-engineered form of CYP4B1 with improved stability has been described recently (Wiek et al., 2015), we used rabbit CYP4B1 for all studies conducted here.

Substrates **C1 – C8** were readily synthesized and proved to be an effective set of analogs to explore structure-metabolism relationships for CYP4B1. Upon testing in our assay, compounds **C3 - C6** were the most potent cytotoxins in the CYP4B1-HepG2 cells, with LD_{50} values approximating that seen with IPO and PK of ~5 μM (Teitelbaum et al., 2019; Roellecke et al., 2017). From this we conclude that clearly (i) an alcohol (*i.e.* such as present in IPO) is not necessary for protoxicant effectiveness with CYP4B1, (ii) a 3' positioned amide between the furan and tail substructure is an effective linker for preserving the chemical reactivity of furan metabolites, and (iii) an intermediary degree of aliphatic character is ideal for bioactivation. Additionally, compounds **C2**, **C5**, **C8** were shown to be stable to hydrolysis in complete tissue culture media, because no significant decline in concentration was observed after 72 hours (**Fig.**

S2.6). Consequently, conclusions drawn from studying this series is not confounded by undesirable hydrolytic reactions.

Because lipophilicity undoubtedly plays an important role in cellular permeability of the compounds, one might have surmised that **C8** would have been the most potent congener based on accumulated intracellular concentration. Therefore, the distinctive cytotoxicity profile we obtained prompted a biochemical analysis of the CYP4B1-dependent metabolism of **C1 - C8** homologs. Congeneric pyrrole adducts derived from furan bioactivation were easily detected for **C1 - C8** utilizing NL129 scanning. Upon investigating the relative amounts generated, normalized PAR for the adduct species were strikingly proportional to the cytotoxicity-dose response curve observed in whole HepG2 cells. The parabolic relationship seen between relative adduct amount and alkyl chain length strongly mirrored the relationship observed between cytotoxicity and alkyl chain length (**Fig. 2.7A**), thereby demonstrating a tight relationship between furan bioactivation and cell death.

While clearly a useful tool in the analysis of xenobiotic metabolic liability, attempts to demonstrate a direct link between covalent binding and hepatotoxicity have been elusive. Historically, there are convincing examples showing the correlation between the covalent binding of reactive metabolites and liver necrosis (Gillette, 1974). However, as shown from metabolic analysis of hepato- and nonhepato-toxins, *in vitro* covalent binding studies, when analyzed alone, are not predictive of liver toxicity at least (Obach et al., 2008). To our knowledge, the data presented here are unique in demonstrating a highly quantitative association between a covalent binding event (in this case the trapped reactive species formed), and cytotoxicity.

This strong correlation facilitates construction of a simple association model; a log-log plot of adduct PAR versus the LD_{50} results in a linear relationship (**Fig. 2.7B**). If a power

function does indeed model the dependency of cytotoxicity on reactive intermediate formation in this HepG2 system, then furan-containing congeners bioactivated by CYP4B1 that result in even higher quantities of electrophilic species would only show a nominal increase in potency. This is a unique finding that illustrates the robust association between these two variables that has not been observed to this degree before, and thus could have implications for future toxicological studies. A caveat is that the current research has not explored covalent binding of radiolabeled versions of these compounds, although we suggest a similar differential effect would be observed between amount of covalent binding generated *in vitro* and whole cell toxicity.

In general, trapping systems for reactive intermediates typically produce multiple adduct species (Peterson, 2013). Therefore, the **C5** furan was utilized for an in-depth interrogation of different conceivable pyrrole isomers that could be trapped from a CYP4B1 incubation. Previously, published research performed with the GSH/NAL system had either not investigated the possibility of multiple isomers formed or provided definitive structural assignments of the bioactivated and trapped furan-containing products (Li et al., 2015). Using an extended chromatography method with the GSH/NAL system, we detected two major and two minor isobaric **C5-Adducts** formed in an NADPH-dependent manner (**Fig. 2.3A, upper**). MS/MS analysis for three of the isomers provided a rationale for the generation of the pyrrole adduct, while a fourth showed evidence for a cyclized variant, akin to that reported for GSH trapping of IPO (Chen et al., 2006). The fragmentation data could not definitively assign the thiol attachment of GSH for these isomers. Therefore, we attempted to synthesize **C5**-**GSH/NAL** adduct standards to allow for their structural characterization. Interestingly, only one pyrrole adduct isomer could be isolated in abundance (potentially due to elevated temperature, differential stoichiometry of trapping agents, or solvents in the synthetic reaction compared to the biological incubation), which had the same LC-MS/MS profile as the metabolically-generated

isomer 1 (**Fig. 2.3A, lower**). 2D NMR techniques enabled unambiguous determination of GSH attachment to the 5' position of the pyrrole. We were thus able to assign a structure for the CYP4B1-generated isomer 1 which shows that **C5** is bioactivated and trapped by GSH/NAL in the same manner as IPO (Baer et al., 2005). However, for **C5** it is likely that both 1,2-addition and 1,4-addition by GSH, followed by NAL attack and condensation, contribute to the adducts formed (**Fig. 2.8**). Note that all of these products are represented in the single peaks analyzed in a shorter chromatography run performed across all **C1 - C8** analogs (**Fig. 2.2A**). While other trapped species were also detected in CYP4B1 incubations with **C5** and GSH/NAL (a potential limitation with this nucleophile tandem), these were not explored in depth for this study.

Given the proclivity of CYP4B1 to ω-hydroxylate fatty acid substrates (Fisher et al., 1998), and the recent publication on PK metabolism by CYP4B1 (Roellecke et al., 2017), we hypothesized that as the aliphatic tail is lengthened for these compounds, substrate reorientation may occur in the active site of CYP4B1. This could result in a switching of metabolism from furan bioactivation to hydroxylation at the terminal end of the carbon chain, and thus lower the cytotoxic potency. A kinetic analysis of CYP4B1-dependent metabolism to the ω-hydroxyl metabolites of compounds **C2**, **C5**, and **C8** (chosen to span the series) indeed showed that catalytic efficiencies (V_{max}/K_m) for ω-hydroxylation increased substantially with tail length, peaking for **C8** at 0.67 μM^{-1} min^{-1} (**Fig. 2.4D**).

Additional kinetic studies were performed for **C5** metabolism by CYP4B1, in order to compare the relative rates of furan bioactivation *versus* ω-hydroxylation. Although most likely an underestimation of the total reactive metabolite amount generated, the V_{max} for the adduct was only 1.5-fold higher than that for the ω-hydroxylation process for **C5**. This is a key finding regarding future optimization of potency for CYP4B1 protoxicants since extensive (inactivating) hydroxylation may be a pharmacokinetic liability. Non-productive metabolism to hydroxy

metabolites could then render these compounds substrates for glucuronidation. We suggest further that potent protoxicants that undergo CYP4B1-mediated bioactivation with optimal length may benefit from fluorine substitution on the aliphatic moiety to block oxidation at terminal carbon positions.

In order to investigate differences in substrate binding to CYP4B1, compounds **C2**, **C5**, and **C8** were docked into the recently published CYP4B1 crystal structure (Hsu et al., 2017). The results indicated increased affinity as the carbon chain was lengthened, from a comparatively loosely bound **C2** to a much more tightly bound **C8**. Interestingly, the increased binding affinity for **C8** paralleled a preference for substrate reorientation, with the **C8** aliphatic tail, rather than its furan moiety, now oriented above the heme iron (**Fig. 2.6**). This modelling matched extremely well to the trends we saw in the kinetic and metabolic data we acquired and bolsters the use of the CYP4B1 crystal structure for future substrate design work. Given our metabolic data and docking models that describe the interactions between CYP4B1 and *N*-alkyl-3-furancarboxamide analogs, the parabolic relationship between alkyl chain length and cytotoxicity may be rationalized by poorer binding of the shorter-chain compounds to CYP4B1 and increased oxidative metabolism for the longer chain compounds at sites distant from the furan warhead.

Numerous furan-containing compounds act as mechanism-based inactivators of CYPs (Peterson, 2013). The reactive intermediates that are generated in the CYP4B1-HepG2 system could partition between quenching by active site nucleophiles, and escape from the CYP4B1 active site to cause cytotoxicity. To evaluate this potential flux, a TDI investigation was performed that showed a 44% loss of activity from **C5** treatment of CYP4B1 in the presence of NADPH. However, the addition of trapping agents *completely* nullified the small degree of enzyme inactivation observed (k_{obs} ~0.02 min^{-1} at 100 μM). This indicates that bioactivated **C5** is

not a true mechanism-based inhibitor of CYP4B1 as assessed by the criteria given by Silverman (Silverman, 1988). In the absence of GSH and NAL, escaped reactive intermediate may cause some minimal time-dependent loss of enzyme activity through attachment to exterior amino acid residues on either CYP4B1 or CPR in this reconstituted system. We posit this would play a marginal role if the enzyme is expressed in target cells dosed with similar furan-containing congeners, when excess biological nucleophiles, like GSH are present in high concentration. Therefore, the CYP4B1 active site architecture likely insulates the enzyme from self-inactivation and contributes to its efficient cytotoxic action.

In summary, we have undertaken an in-depth characterization of the structural elements required for potent IPO-like congeners that undergo CYP4B1 bioactivation to elicit whole cell toxicity. *N*-alkyl-3-furancarboxamides are stable, easily synthesized for analog and library generation, and possess a similar cytotoxicity and reactivity profile as their ketone counterparts. When these congeners are affixed with 3-6 tail carbons they are highly toxic in HepG2 cells expressing CYP4B1 and elicit no observed effect in control vector cells. Reducing aliphatic character lowers the affinity of these substrates for the enzyme, while extending the tail increases ω-hydroxylation rates; both of which lower the potency for CYP4B1-mediated cytotoxicity. Relative amounts of trapped reactive intermediates formed from CYP4B1 metabolism of these substrates with GSH and NAL is strikingly correlated to cytotoxicity; to our knowledge, a comparison like this has never been shown to this high degree. This effect may be explained, due in large part, to the efficient nature by which the reactive intermediates are able to escape the CYP4B1 active site without causing measurable mechanism-based inactivation. These studies further demonstrate the utility of CYP4B1 for use in suicide gene systems, especially in settings requiring highly controlled cytotoxicity. Future studies will investigate the utility of fluorinated congeners and probe the specificity of bioactivation by hepatic CYPs, particularly CYP1A2.

Abbreviations

CYP4B1, cytochrome P450 4B1; IPO, 4-ipomeanol; PK, perilla ketone; UGT, uridine 5'-diphosphoglucuronosyl transferase; CPR, cytochrome P450 reductase; LD_{50}, lethal dose 50%; GSH, reduced glutathione; NAL, *N*-α-acetyl-L-lysine; KPi, potassium phosphate buffer; NL129, neutral loss scanning of 129 Da; MRM, multiple reaction monitoring; PAR, peak area ratio; TDI, time-dependent inhibition; ABT, 1-aminobenzotriazole; C1–C8, *N*-alkyl-3-furancarboxamide compounds with aliphatic tails of one through eight carbons; C5-Adduct, GSH/NAL trapped adduct(s) from CYP4B1 bioactivation of C5.

A

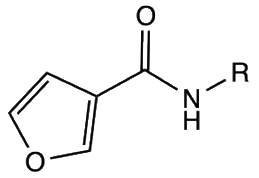

R	ID	LD_{50} (μM)
methyl	**C1**	680 ± 40
ethyl	**C2**	24 ± 3
propyl	**C3**	6 ± 1
butyl	**C4**	5 ± 1
pentyl	**C5**	5 ± 1
hexyl	**C6**	5 ± 1
heptyl	**C7**	26 ± 3
octyl	**C8**	130 ± 3

B

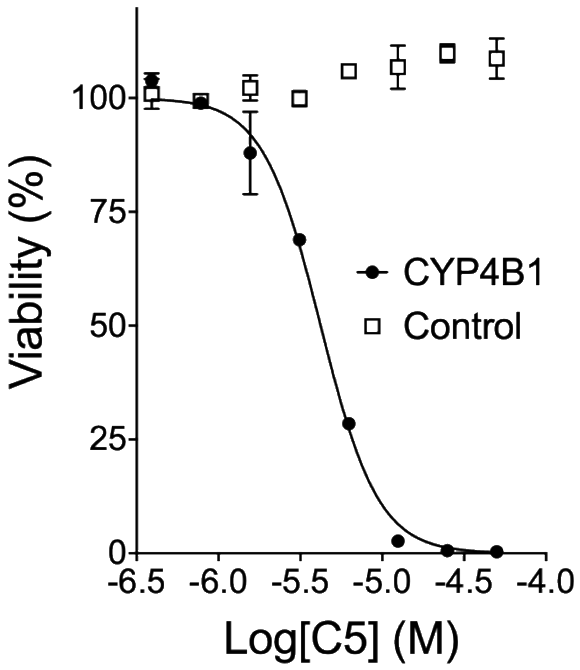

Figure 2.1. *N*-alkylated 3-furancarboxamides (**C1 – C8**) were synthesized to establish optimal aliphatic tail length for CYP4B1-mediated bioactivation, compounds were utilized for cytotoxicity and metabolism assays. (**A**) The LD_{50} values from CYP4B1-HepG2 cells dosed substrates **C1 – C8,** and assayed for viability 72 hours later, showed that **C3 – C6** were the most potent congeners. Values presented are means ± SD from three to six replicates. (**B**) The representative dose-response curve for substrate **C5** illustrates the 5 μM LD_{50} detected in the CYP4B1-HepG2 cell line. No toxicity was observed in the control vector HepG2 cell line from exposure to **C5**, nor from any of the analogs up to doses outlined in the *Experimental Procedures* section.

A

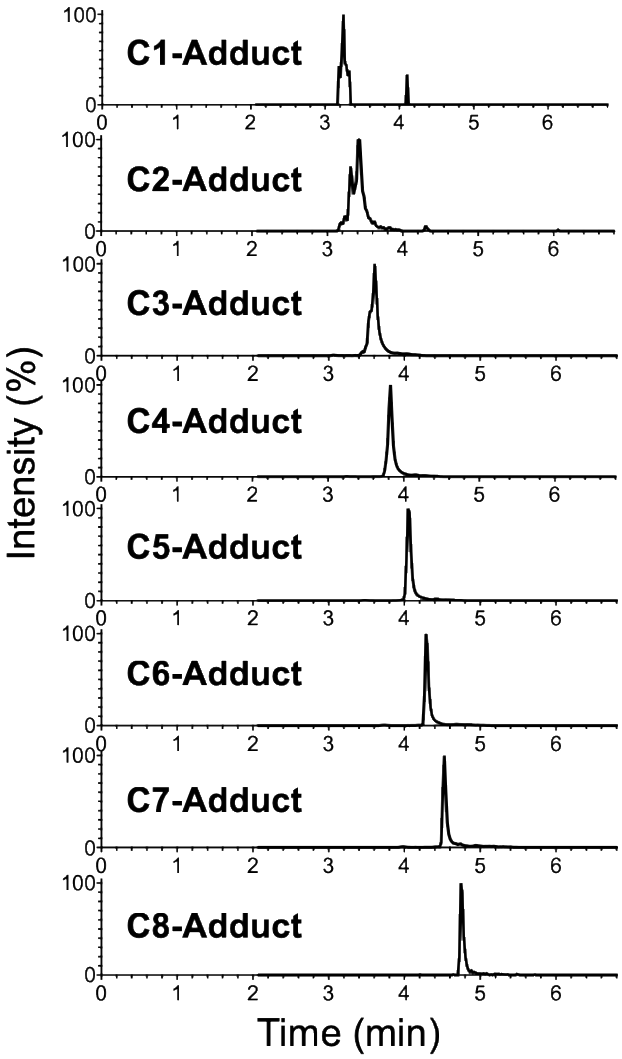

B

Product	*m/z*	PAR (± SD)
C1-Adduct	601.2	0.03 ± 0.002
C2-Adduct	615.2	2 ± 0.03
C3-Adduct	629.2	43 ± 2
C4-Adduct	643.2	78 ± 4
C5-Adduct	657.3	100 ± 7
C6-Adduct	671.3	76 ± 5
C7-Adduct	685.3	7 ± 0.6
C8-Adduct	699.3	1 ± 0.2

Figure 2.2. Assessment of GSH/NAL trapped reactive intermediates derived from substrates **C1 - C8**. (**A**) Separate CYP4B1 incubations with **C1 - C8**, in the presence of GSH (5 mM) and NAL (5 mM), each produced an NADPH-dependent metabolite adduct with a parent mass corresponding to a pyrrole structure containing one GSH and one NAL moiety (termed **C1 – C8-Adduct**). Relative amounts of the adducts were evaluated *via* NL129 scanning and eluted according to parent chain length. Peak sizes have been normalized for viewing. Due to the short chromatographic separation, any different isomers present could not be resolved. (**B**) Average PAR values of the **C1 – C8-Adduct** products with corresponding adduct *m/z*. Shown is the normalized average ± SD derived from three replicates. Compounds **C3 - C6** produced substantially more trapped adduct than either the short (**C1**, **C2**) or long (**C7**, **C8**) chain homologs.

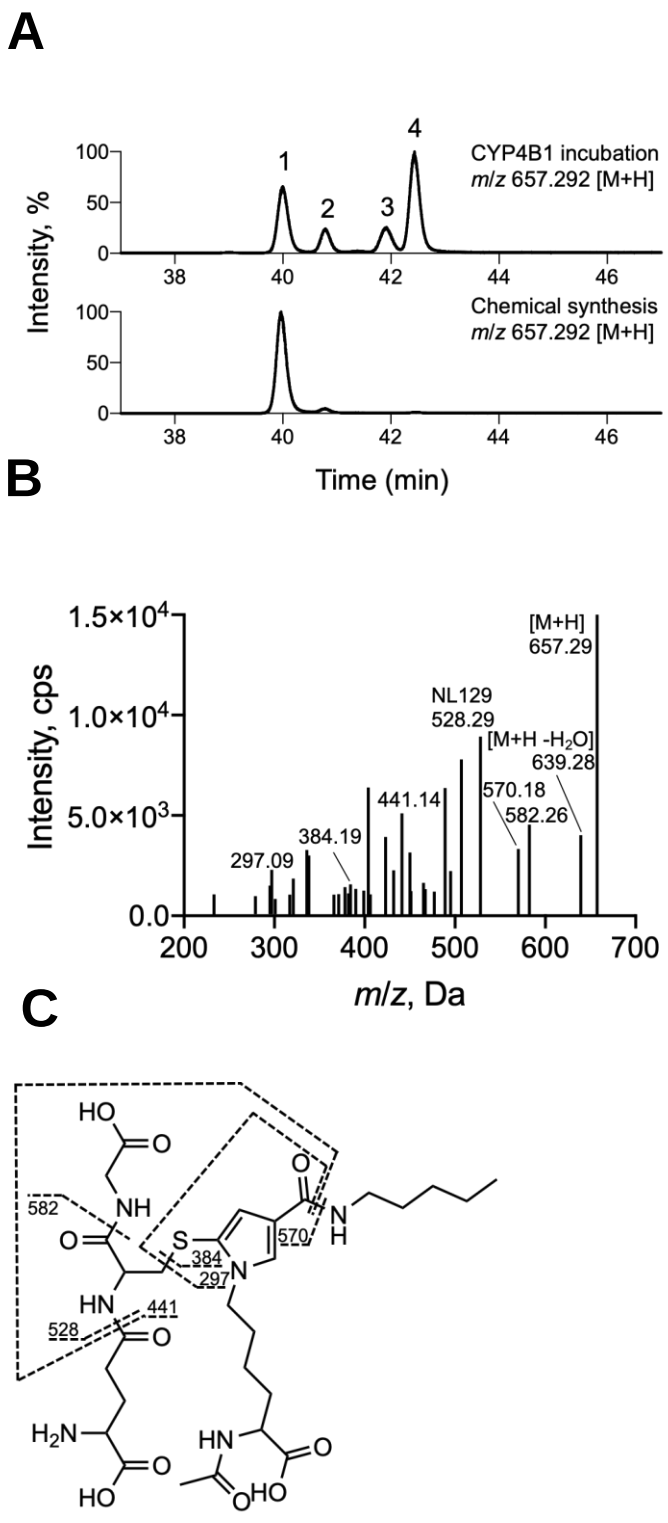

Figure 2.3. Characterization of GSH/NAL-containing **C5**-**Adducts**. (**A**) An extended chromatographic separation of the **C5-Adduct** from the CYP4B1 incubation revealed four isobaric species at *m/z* 657.292 (upper chromatogram). Chemical synthesis of a **C5**-**GSH/NAL** adduct produced one dominant species of the same mass, with the same chromatographic profile as isomer 1. A trace amount of isomer 2 at RT 40.8 min was also observed (lower chromatogram). (**B**) MS/MS analysis of isomer 1 was identical to that of the synthesized standard and produced ions typical of a GSH adduct. MS/MS spectra for isomers 2 – 4 is shown in the supplemental section. (**C**) The assigned structure for isomer 1, as elucidated from 2D-NMR techniques performed on the synthesized adduct (**Fig. S3 and S4**), with annotated fragmentation pattern corresponding to the MS/MS spectrum.

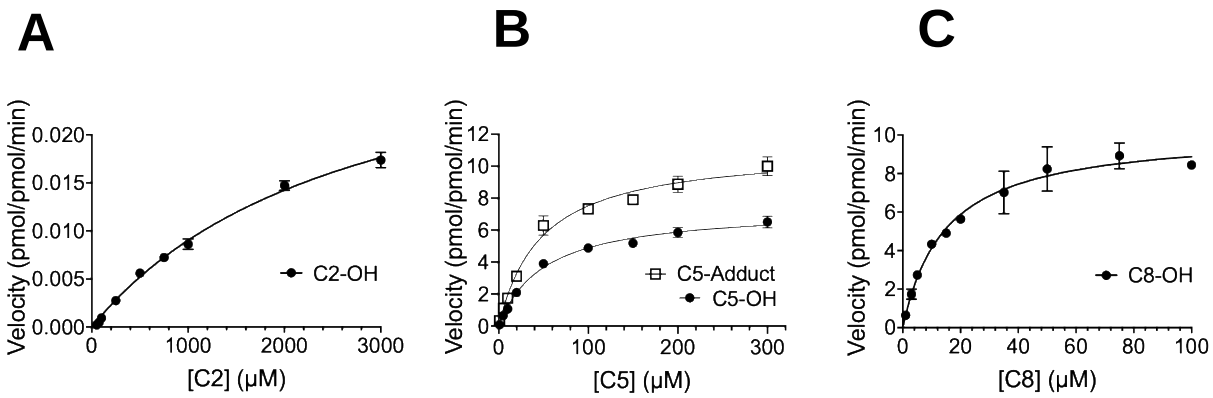

D

Biotransformation	K_m (μM)	V_{max} (min^{-1})	V_{max} / K_m (μM^{-1} min^{-1})
C2 → C2-OH	2740 ± 220	0.03 ± 0.003	1.2e-5
C5 → C5-OH	51.1 ± 4.8	7.4 ± 0.3	0.15
C5 → C5-Adduct	47.9 ± 3.4	11.1 ± 0.5	0.23
C8 → C8-OH	14.7 ± 0.3	10.2 ± 0.3	0.67

Figure 2.4. Kinetics for CYP4B1 metabolism of compounds **C2**, **C5**, and **C8**. (**A**) Rate assessment for ω-hydroxylation of **C2** (**C2-OH**), (**B**) **C5** (**C5-OH**), and (**C**) **C8** (**C8-OH**). The kinetics for **C5** bioactivation and adduct (**C5-Adduct**) formation were also evaluated (**B**). (**D**) The kinetic constants for ω-hydroxylation showed a decrease in K_m and an overall increase in catalytic efficiency as the aliphatic chain was extended. The V_{max} for **C5-Adduct** formation was ~1.5-times that of **C5-OH**. Shown is the mean ± SD from three replicates.

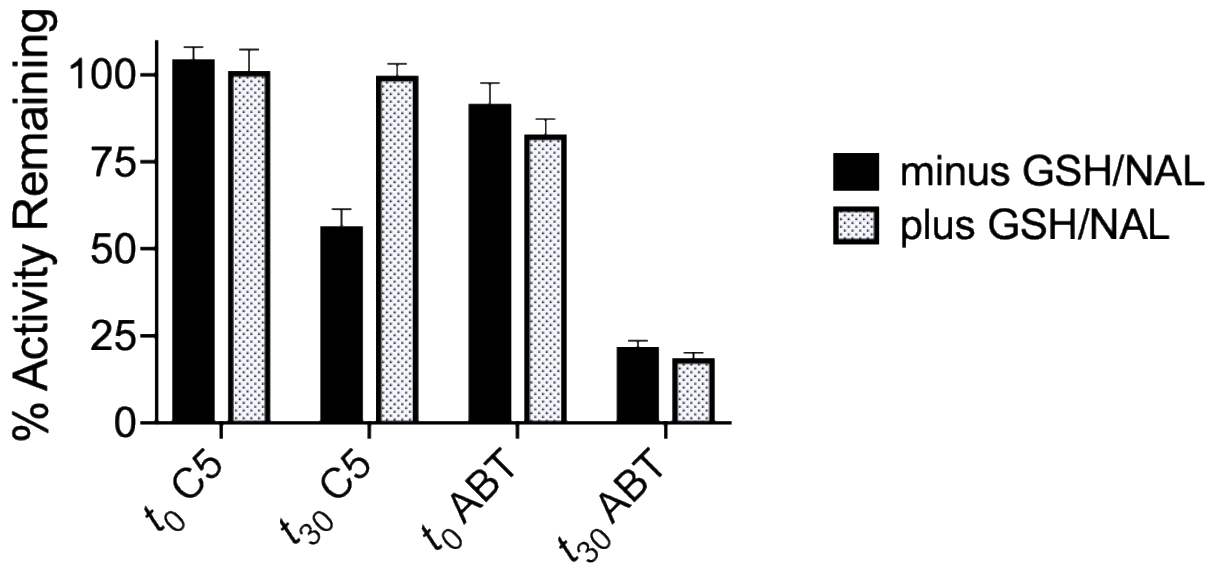

Figure 2.5. CYP4B1 time-dependent inhibition (TDI) investigation for compound **C5**. A 30-min (t_{30}) incubation of CYP4B1 with 100 μM **C5** and NADPH resulted in a ~44% reduction in enzyme activity, as normalized to vehicle control. Addition of GSH and NAL to the incubation abolished this observed TDI. The 0-min (t_0) incubation, prior to probe substrate turnover, shows **C5** is not engaging in reversible inhibition of CYP4B1. The pan-CYP inhibitor ABT was used as a positive control for MBI and was unaffected by the addition of the trapping agents GSH/NAL.

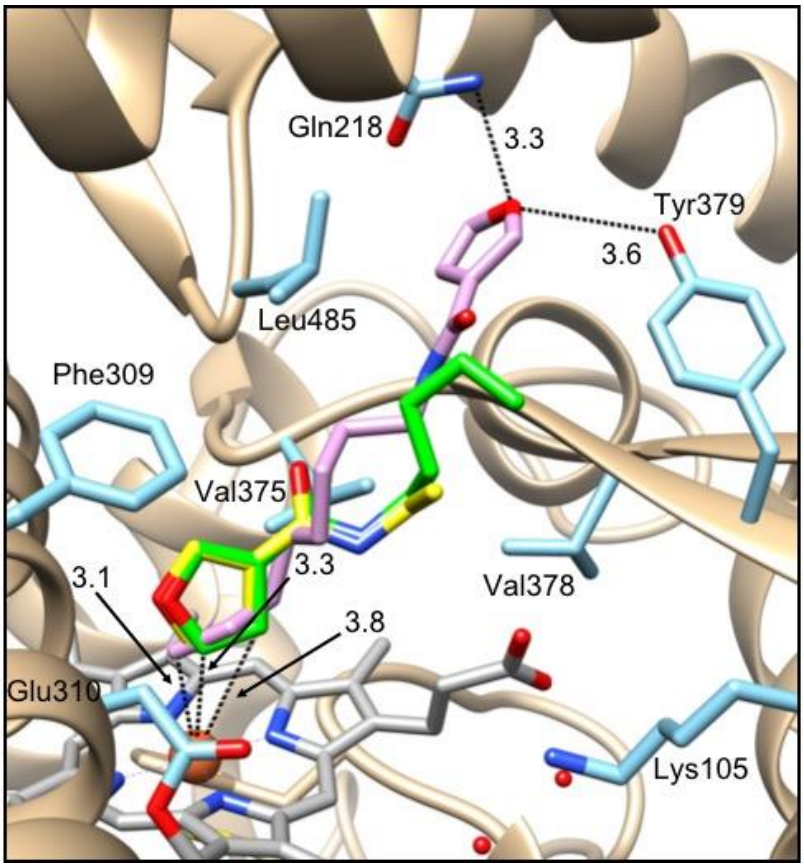

Figure 2.6. Docking of compounds **C2** (yellow), **C5** (green) and **C8** (plum) in the CYP4B1 crystal structure. The CYP4B1 active site contains hydrophobic residues Leu485, Val378, Val375, and Phe309 that aid in the enzyme's preference for aliphatic substrates. As the carbon tail chain length increases for **C2** through **C8**, improved affinity for these substrates is predicted. The preferred pose from multiple simulations showed both **C2** and **C5** positioned with their furan moiety located directly above the heme, with carbons at the 2' and 3' positions 3.3 and 3.8 Å away from the heme iron. The preferred pose for **C8** reversed this positioning, with the carbon tail now centered over the heme, 3.1 Å away from the iron. Gln218 and Tyr379 at the mouth of the active site may play a role in hydrogen-bond stabilization of the **C8** furan.

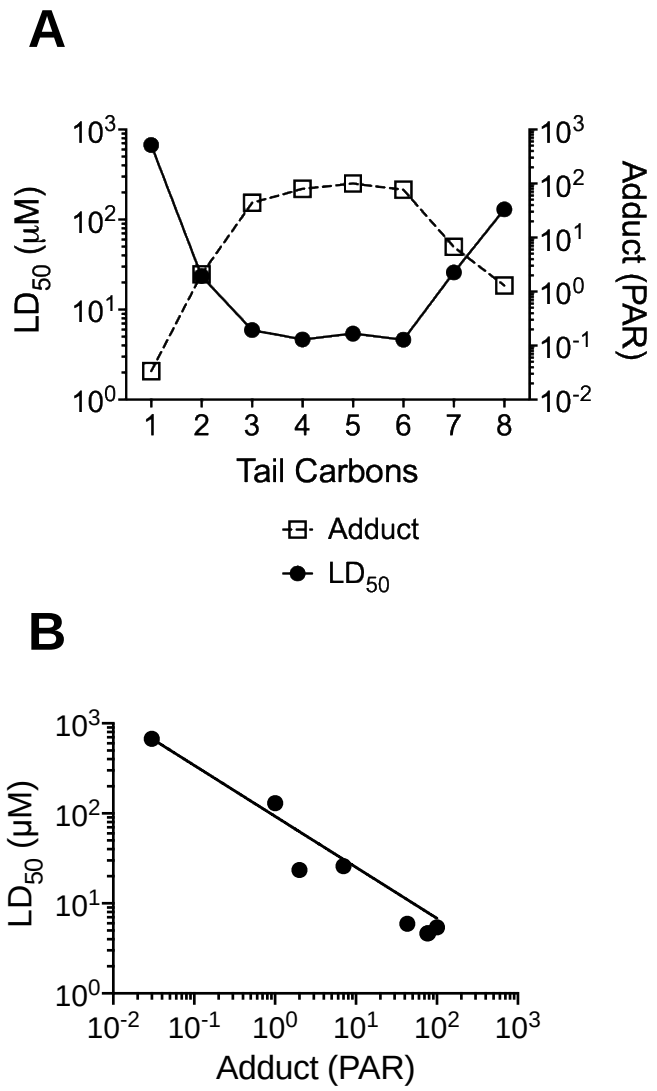

Figure 2.7. Correlation between CYP4B1-mediated reactive metabolite formation and cytotoxicity. (**A**) The parabolic relationship between the relative amount of **C1 – C8-Adduct** formed from trapped reactive intermediate and alkyl chain length directly reflects the association between cytotoxic potency (as measured by LD_{50}) and alkyl chain length for **C1 – C8.** Averages have been plotted, and standard deviations (reported earlier) have been omitted for clarity. (**B**) A linear dependency results from a log-log plot of normalized adduct amount versus LD_{50} and can be modeled by the equation $y = 2.6x^{-0.6} + 90.3x^{-0.6}$ which has been fit to the data, this is indicative of a power relationship between these two variables.

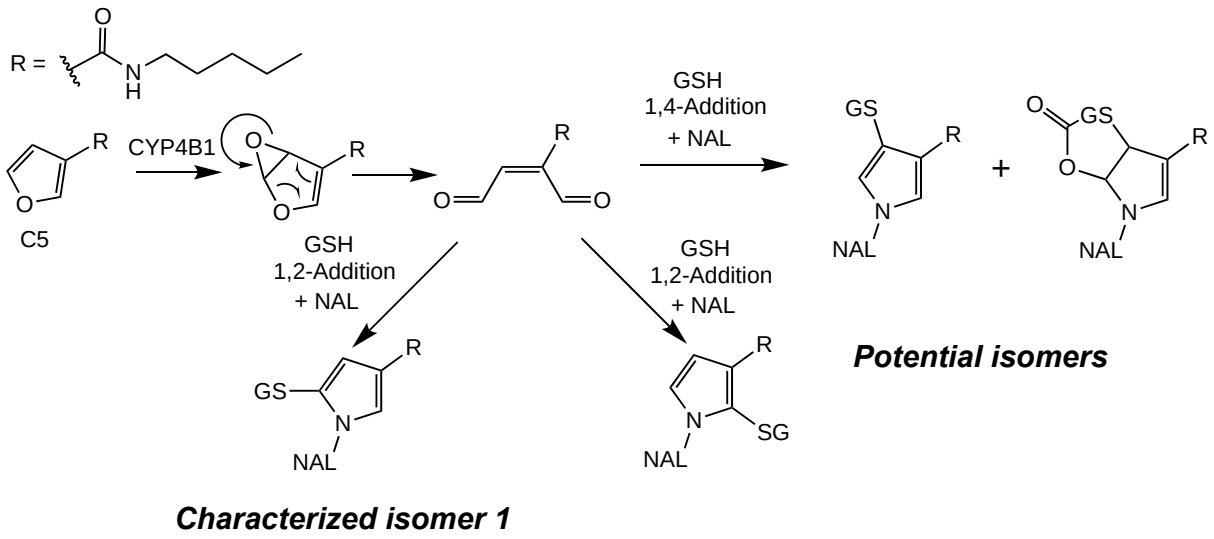

Figure 2.8. Proposed mechanism for the formation of GSH/NAL-trapped **C5-Adducts**. Characterized isomer 1 can be formed through 1,2-addition of GSH to the putative enedial species and reaction with NAL. Both 1,2- and 1,4-addition of GSH to the enedial and reaction with NAL may account for the additional **C5-Adducts** identified through LC-MS/MS; the structures for the potential isomers 2 – 4 are shown.

2.5 Supporting Information

Western blot assessment of CYP4B1 expression levels in HepG2 cells; MS/MS Fragmentation data for **C5**-**Adduct** isomers 2 – 4; HSQC Structural validation for **C5**-**GSH/NAL**; ROESY Characterization of **C5**-**GSH/NAL**; **C2-, C5-, C8-OH** Metabolite identification; *N*-Alkyl-3-furancarboxamide stability assessment in tissue culture media; Supplemental Methods: NMR Spectroscopy; ^{1}H NMR Spectra

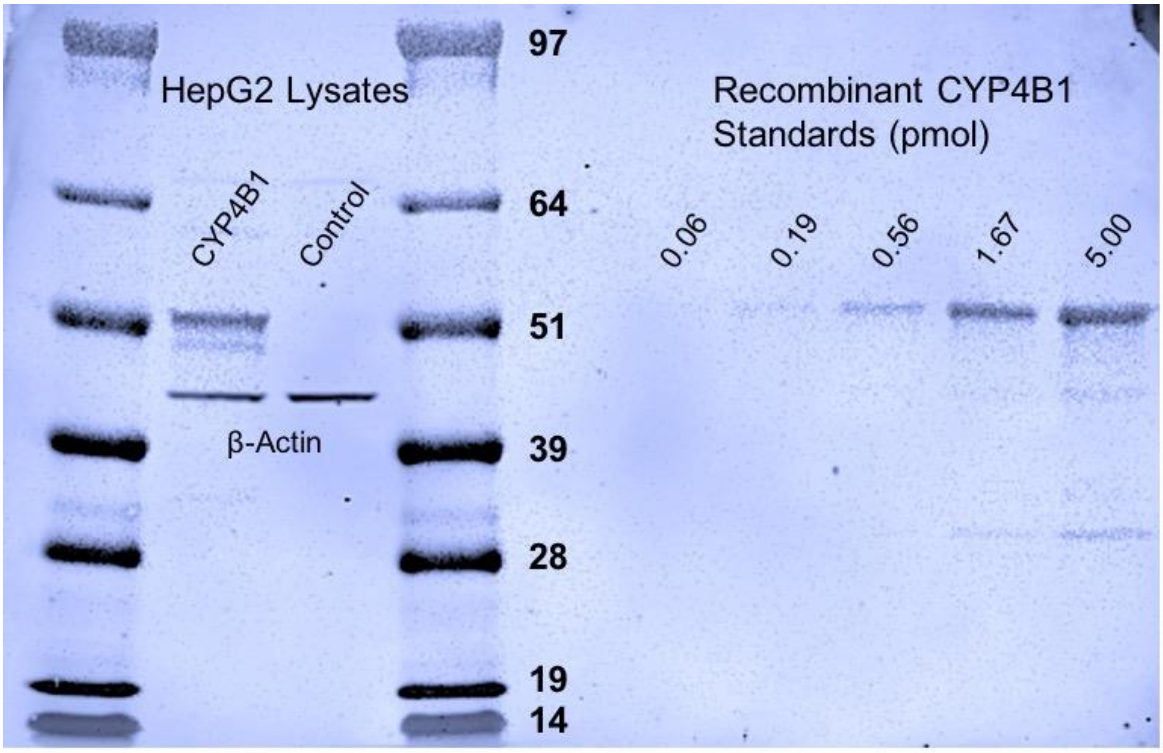

Fig. S2.1. Cell lines were modified with lentivirus to over-express CYP4B1 and control vector. HepG2-CYP4B1 cells showed ~130 pmol CYP4B1/mg total protein in lysates, migrating at ~55 kDa, as quantified using the recombinantly expressed and purified enzyme as standards. CYP4B1 was not detected in the control vector cell line. *B*-Actin was used as loading control to ensure equal protein was loaded for both cell lines onto the gel.

(A) C5-Adduct isomer 2 MS/MS

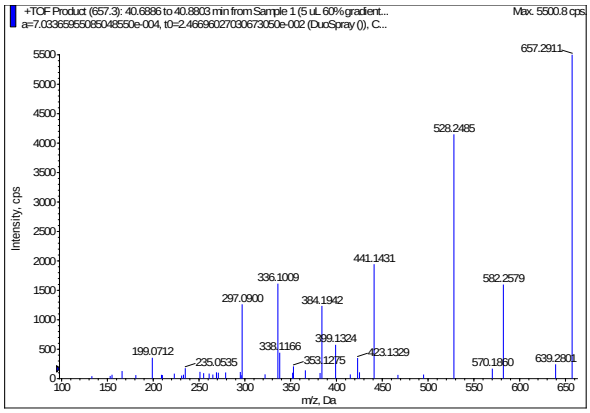

(B) C5-Adduct isomer 3 MS/MS

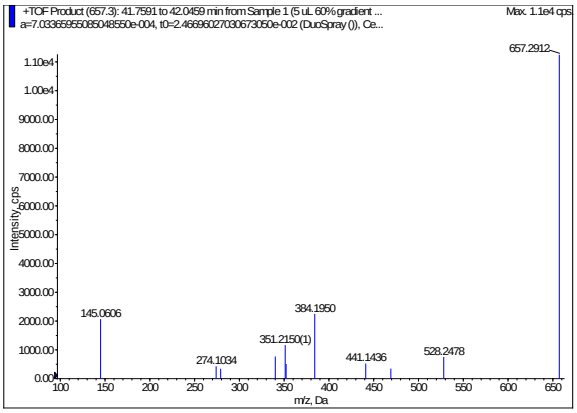

(C) C5-Adduct isomer 4 MS/MS

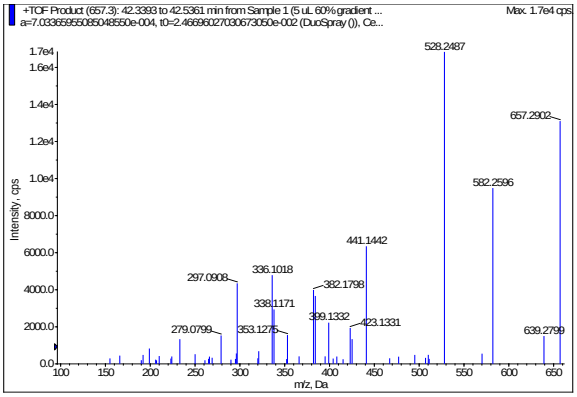

(D) Proposed mechanism, structure, and fragmentation for **C5-Adduct** isomer 3

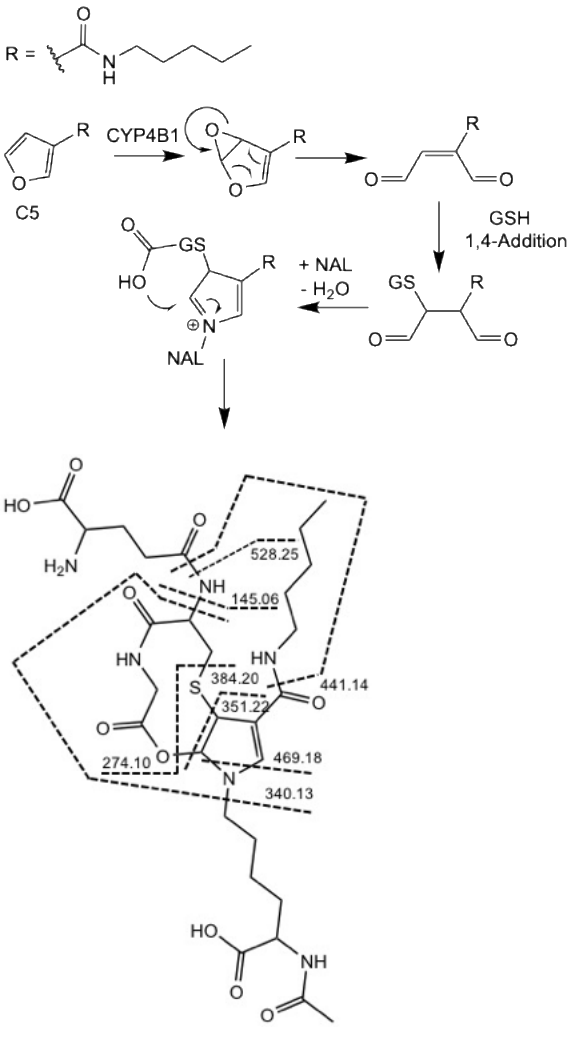

Fig. S2.2. MS/MS spectra were analyzed for the adducts generated by **C5** incubation with CYP4B1 in the presence of GSH and NAL; these suggested **C5-Adduct** isomers of each other were not definitively characterized by NMR techniques. Isomer 2 **(A)** eluted at 40.8 min and isomer 4 **(C)** eluted at 42.4 min, both showed the accurate parent m/z 657.29 for the trapped pyrrole species and the characteristic fragmentation of GSH adducts of [M+H – 129] (m/z 528) and [M+H – 75] (m/z 582). Isomer 3 **(B)**, eluted at 41.9 min, had the accurate parent m/z 657.29, and the GSH fragmentation corresponding to [M+H – 129] (m/z 528), but did not show the species for [M+H – 75] (m/z 582). Therefore, it was postulated that isomer 3 could be a cyclized variant that results from first GSH 1,4-addition to the reactive ene-dial of bioactivated **C5**, followed by NAL addition and then the free acid of the GSH-glycine moiety attacking an iminium intermediate resulting in a cyclic adduct. A possible structure and mechanism, along with assigned fragmentation data, is provided (**D**).

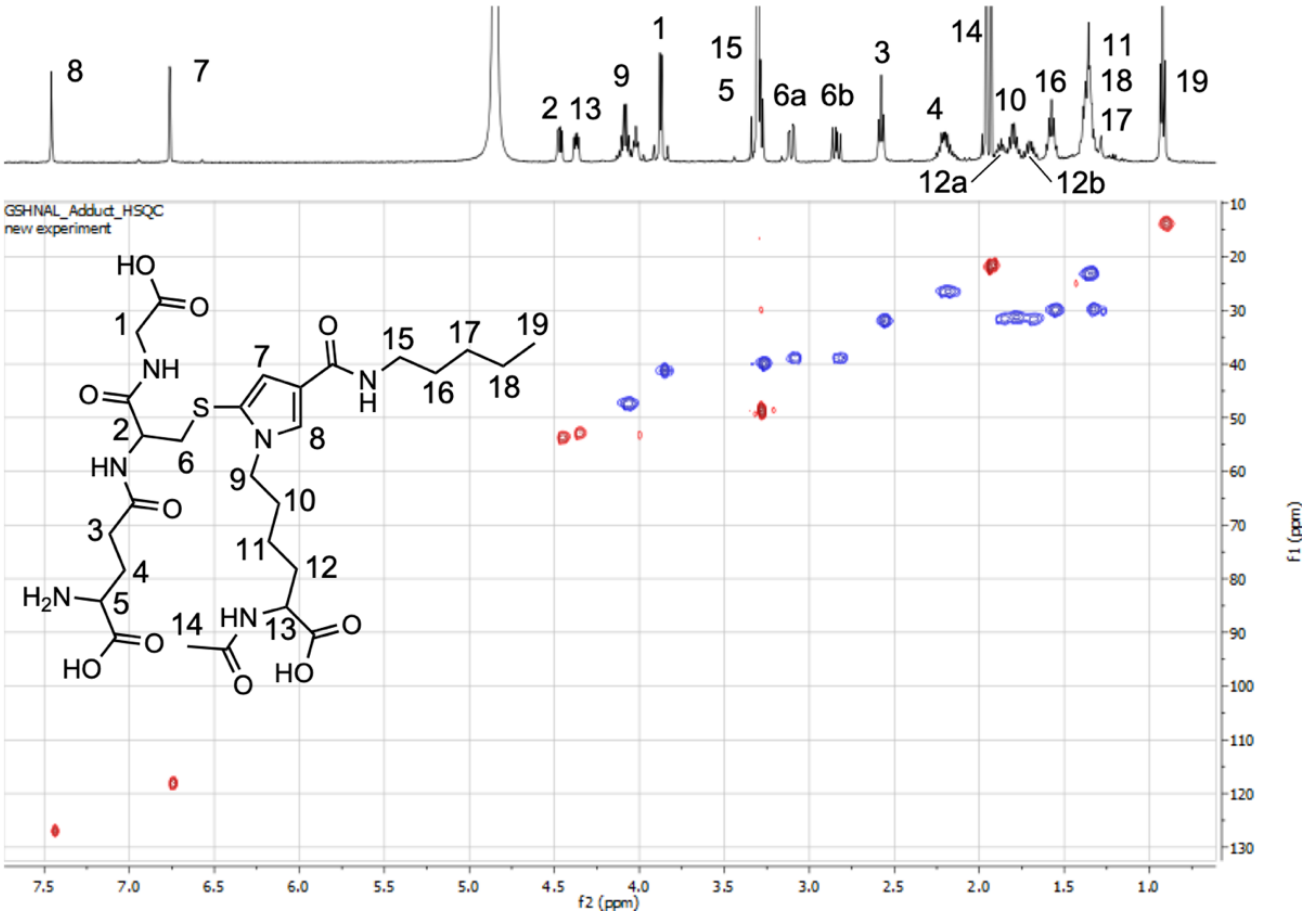

Position	1	2	3	4	5	6a	6b	7	8	9	10	11	12a	12b	13	14	15	16	17	18	19
^{1}H δ	3.8	4.4	2.6	2.2	3.3	3.1	2.8	6.8	7.4	4.1	1.8	1.4	1.9	1.7	4.3	1.9	3.3	1.6	1.3	1.4	0.9
^{13}C δ	41	54	32	26	49	39	39	118	126	47	31	23	32	32	53	22	40	30	30	23	14

Fig. S2.3. Structural validation for **C5-GSH/NAL** isomer 1 (synthesized) was performed *via* multiplicity-edited Heteronuclear Single Quantum Correlation (HSQC) NMR (methanol-d4 solvent). The annotated spectra show CH and CH_3 groups denoted by red and CH_2 groups denoted by blue. Chemical shifts have also been provided.

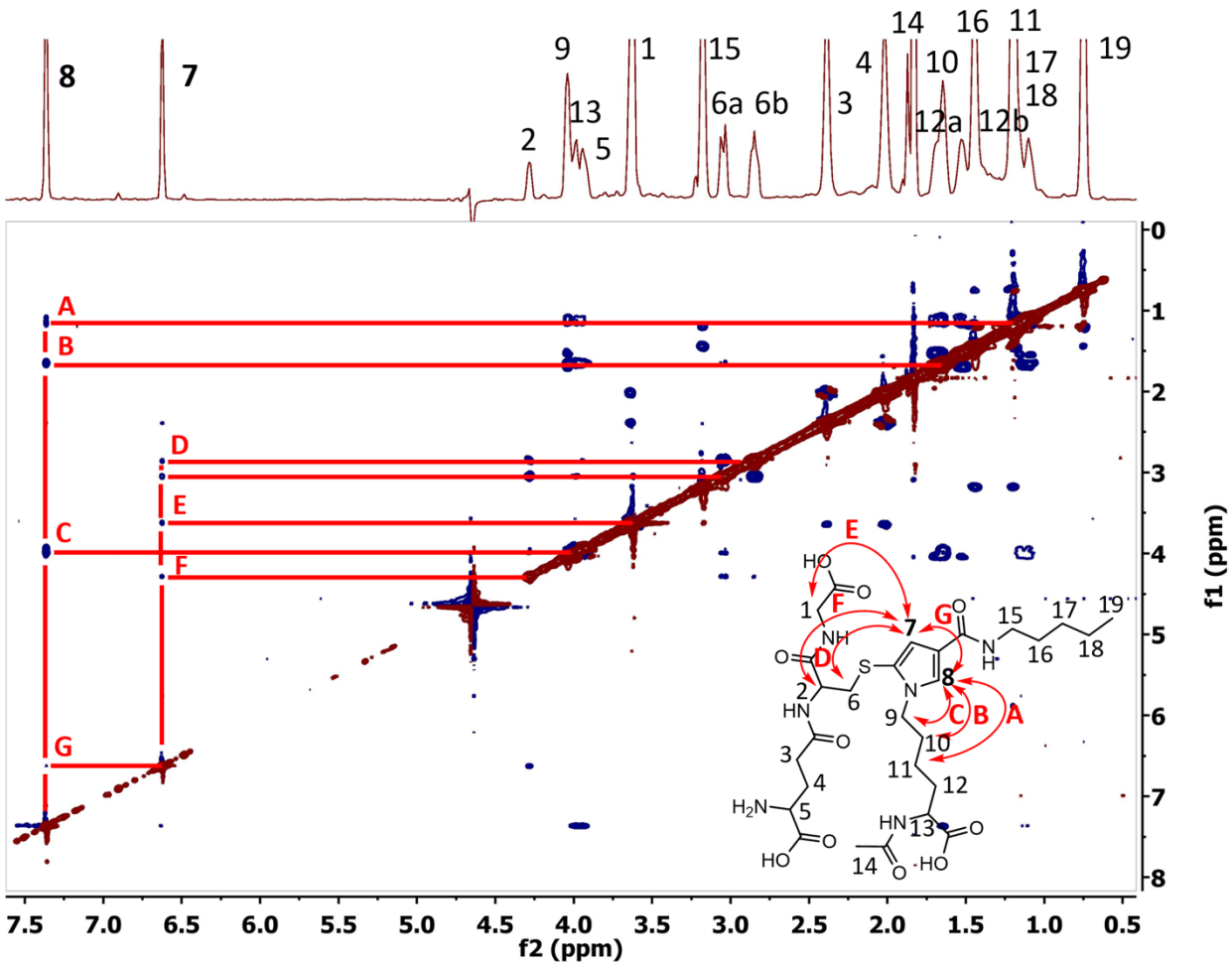

Interaction	A	B	C	D	E	F	G
^{1}H Position 1	8	8	8	7	7	7	7
^{1}H Position 2	11	10	9	6	1	2	8

Fig. S2.4. 2D Rotating-frame Overhauser Effect SpectroscopY (ROESY) (D_2O solvent) was used to characterize the thiol attachment site to the pyrrole adduct from through-space proton interactions for **C5-GSH/NAL** isomer 1 (synthesized). The pyrrole proton (8H) showed proximity to the NAL protons (9H, 10H, 11H) as well as the other pyrrole proton (7H), denoted by double-ended arrows C, B, A, and G, respectively. Conversely, pyrrole proton (7H) lacked interaction with NAL aliphatic chain protons but showed clear proximity with GSH protons (6_aH, 6_bH, 2H, 1H) denoted by double-ended arrows D, E, and F, respectively. Lastly, the GSH proton (6_aH) shows interaction with the NAL proton (9H); the lack of GSH proton (6_bH) interaction with NAL proton (9H) may be attributed to a shielding effect from the GSH Sulfur. These assignments specified the pyrrole protons (7H, 8H) as straddling the carboxamide with the GSH moiety attached adjacent to the NAL side chain.

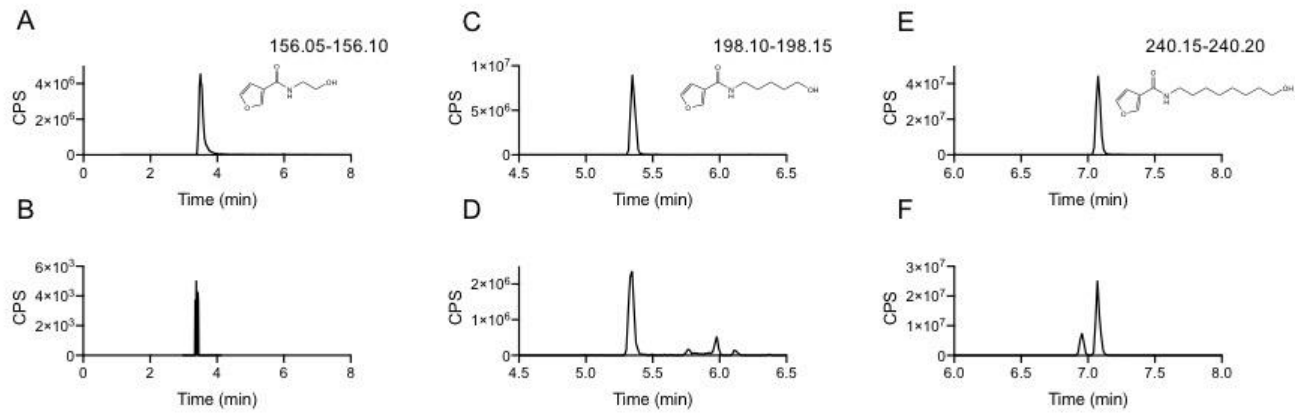

Fig. S2.5. C2-, **C5**-, **C8-OH** Metabolite identification. Upper panels **A**, **C**, and **E** are the synthetic standards for **C2-OH**, **C5-OH**, and **C8-OH**, respectively. The extracted ion chromatogram (XIC) windows (in daltons) are provided above the chemical structures. Lower panels **B**, **D**, and **F** show the metabolic products generated by CYP4B1 from **C2**, **C5**, and **C8** with matching retention times for **C2-OH**, **C5-OH**, and **C8-OH**, respectively, and used the same XIC window. Minor products which may correspond to internal hydroxylation metabolites of the same mass were observed for both **C5** and **C8**.

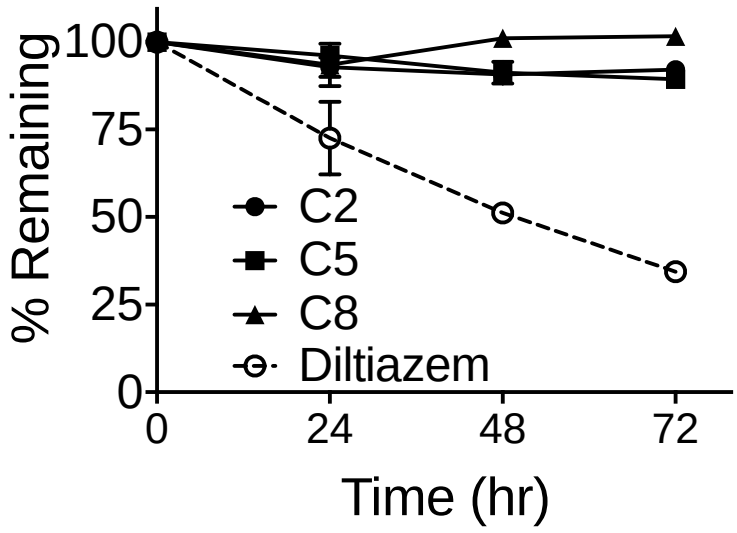

Fig. S2.6. *N*-Alkyl-3-furancarboxamide stability assessment in tissue culture media. Compounds **C2**, **C5**, **C8** and diltiazem (a compound with a labile acetate ester commonly used as a stability control in depletion experiments) were dosed to complete tissue culture media at 100 μM. Samples were taken at times 0, 24, 48, and 72 hours and the % remaining compound was determined *via* LC-UV at 254 nm. No significant depletion of **C2**, **C5**, or **C8** was observed after 72 hours, while diltiazem, with a labile ester, dropped to ~35%. Data shown represents the mean ± SD, from three replicates.

Supplemental Methods: NMR Spectroscopy

All NMR experiments were performed at 25 °C on a 499.73 MHz Agilent DD2 spectrometer equipped with either a 5 mm triple-resonance $^{1}H(^{13}C/^{15}N)$, z-axis pulsed-field gradient probe head. For characterization and spectral assignment purposes, the samples were ~20 mM solutions in either CD_3OD (99.8% D, Cambridge Isotopes) or D_2O (99.9% D, Cambridge Isotopes). The spectra were referenced to residual solvent peaks at 4.8 (CD_3OD or D_2O). GSH/NAL proton resonances were assigned through a combination of two-dimensional (2D) ROESY and HSQC experiments. Homonuclear 2D experiments were acquired with 1024 complex data points in the t2 time domain (sw = 5000 Hz, d = 1.5 s) and 32 scans were averaged for each of the 400 increments in the t1 domain. The 2-D ROESY experiment was recorded in phase sensitive Hypercomplex 2D mode with States-TPPI in F1, and a 350 ms spinlock mixing sequence. Carbon resonances were assigned through two dimensional $^{1}H–^{13}C$ HSQC, acquired at natural isotopic abundance with 1024 complex data points in the t2 time domain (sw = 5000 Hz, d1= 1 s) and 64 averaged accumulations for each of the 400 increments in the t1 domain. All two-dimensional spectra were acquired in phase-sensitive Hypercomplex 2D mode with States-TPPI for quadrature detection in F1. The NMR data were analyzed using MNova 14.0 processing software (Mestrelab Research, Santiago de Compostela, Spain).

^{1}H NMR (500 MHz, $CDCl_3$): *N*-Methyl-3-furancarboxamide (**C1**)

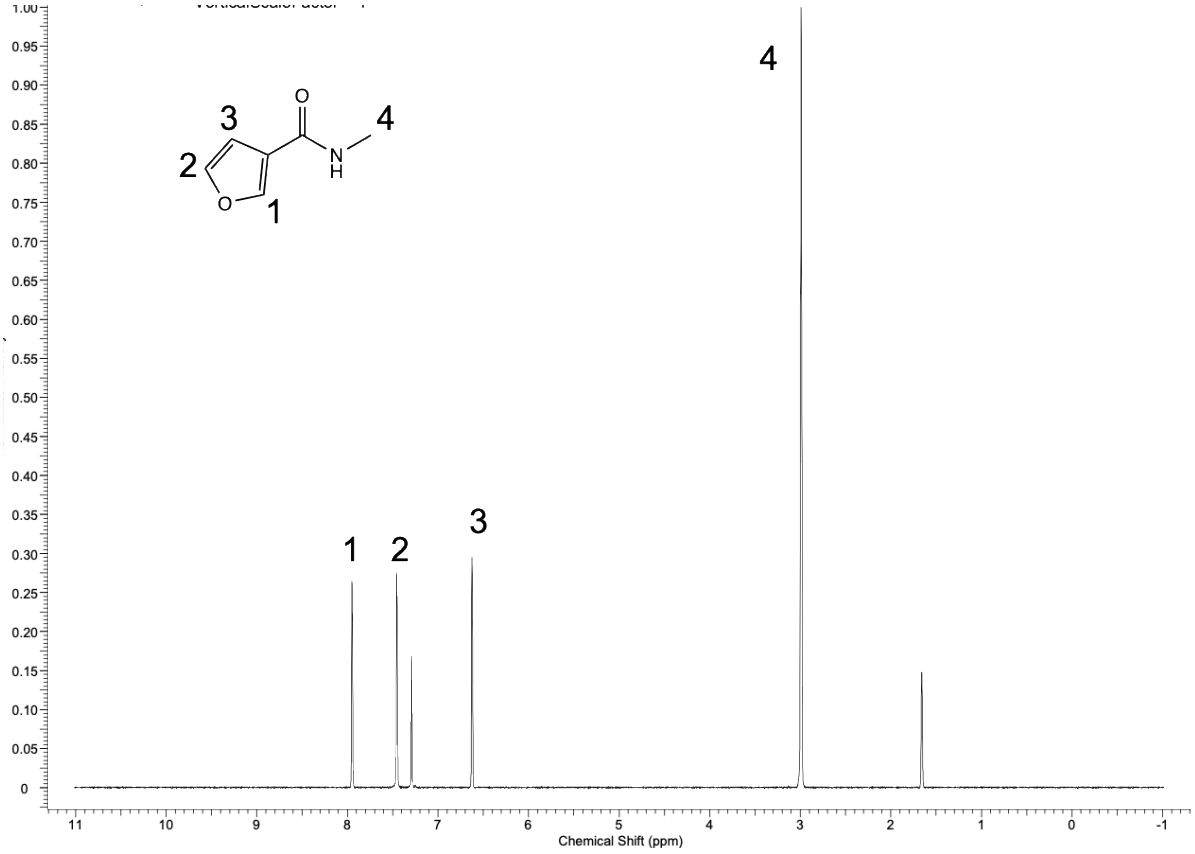

^{1}H NMR (500 MHz, $CDCl_3$): *N*-Ethyl-3-furancarboxamide (**C2**)

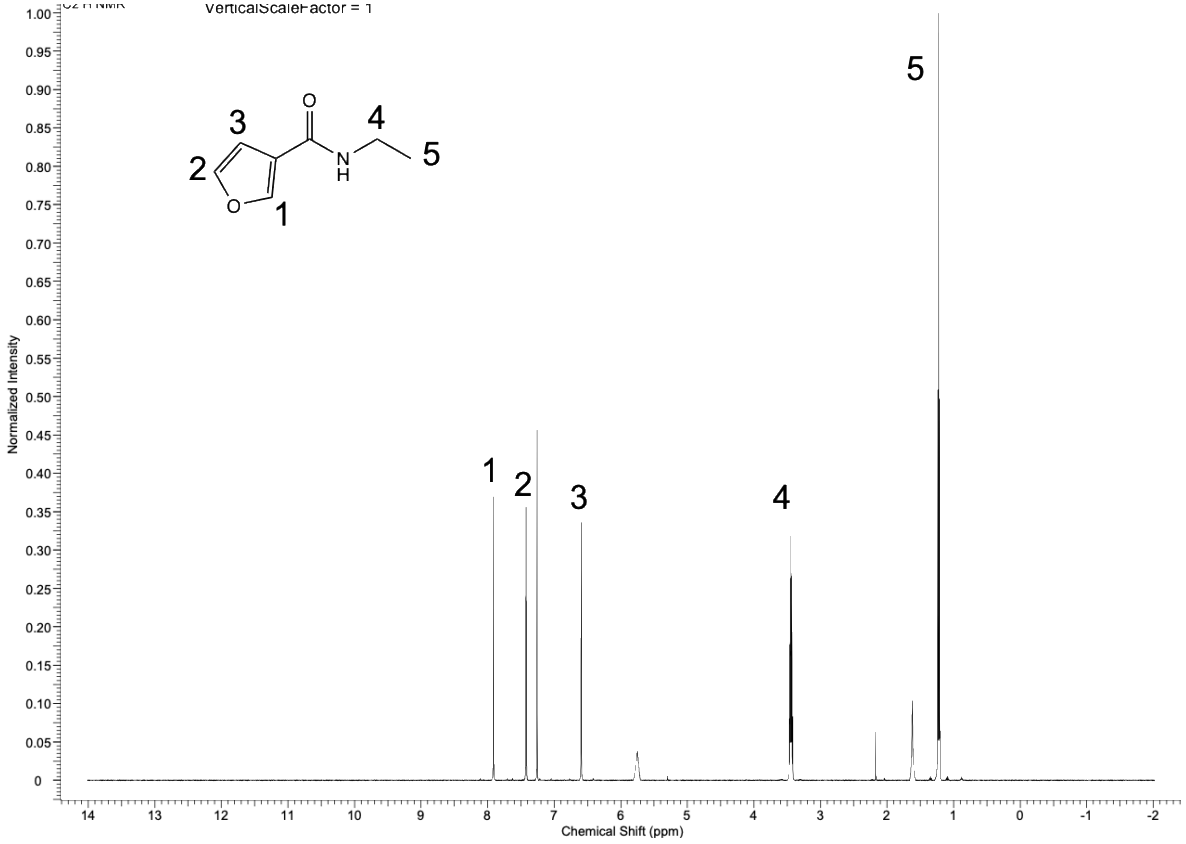

^{1}H NMR (500 MHz, $CDCl_3$): *N*-Propyl-3-furancarboxamide (**C3**)

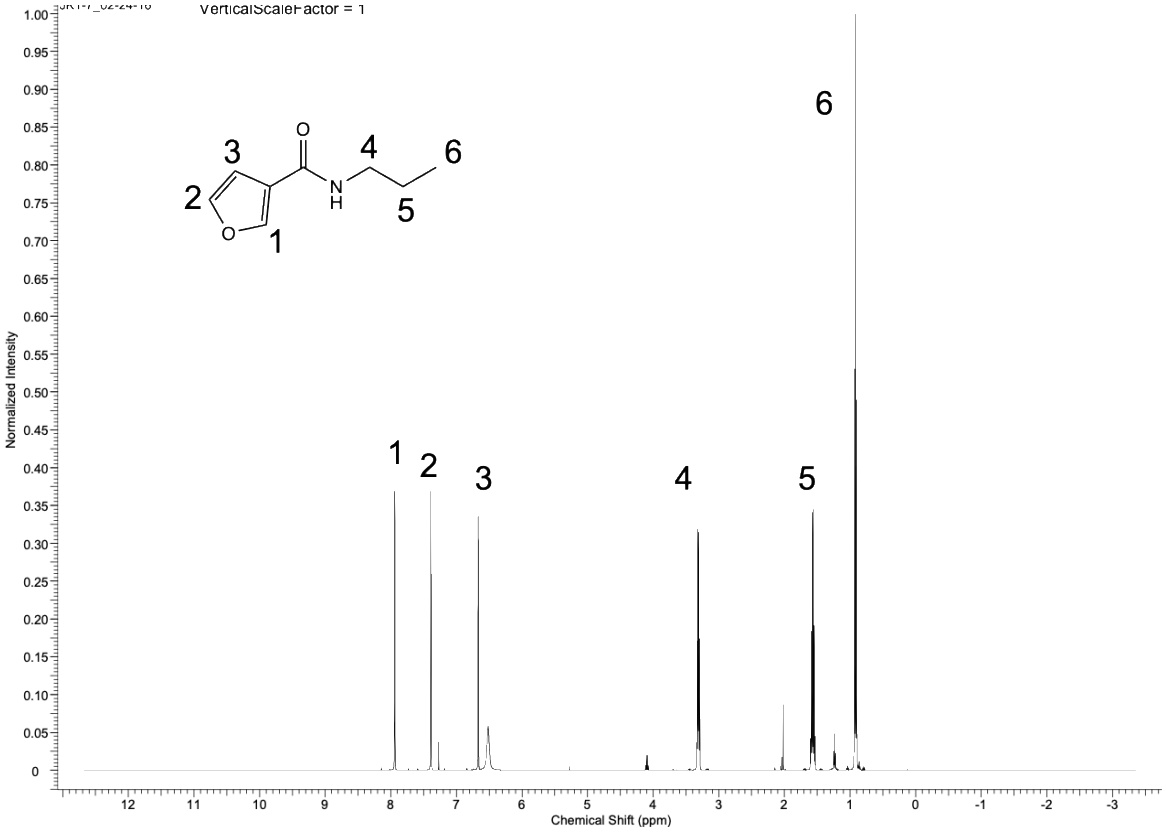

^{1}H NMR (500 MHz, $CDCl_3$): *N*-Butyl-3-furancarboxamide (**C4**)

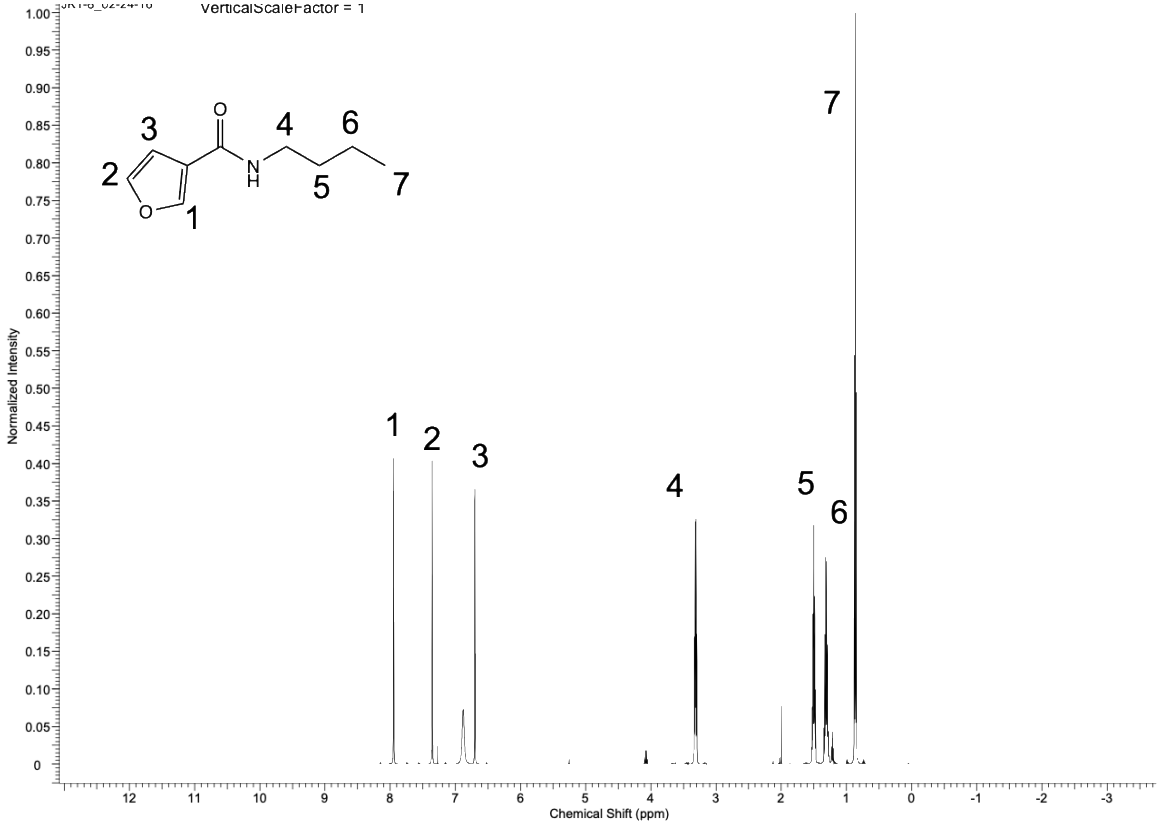

^{1}H NMR (500 MHz, $CDCl_3$): *N*-Pentyl-3-furancarboxamide (**C5**)

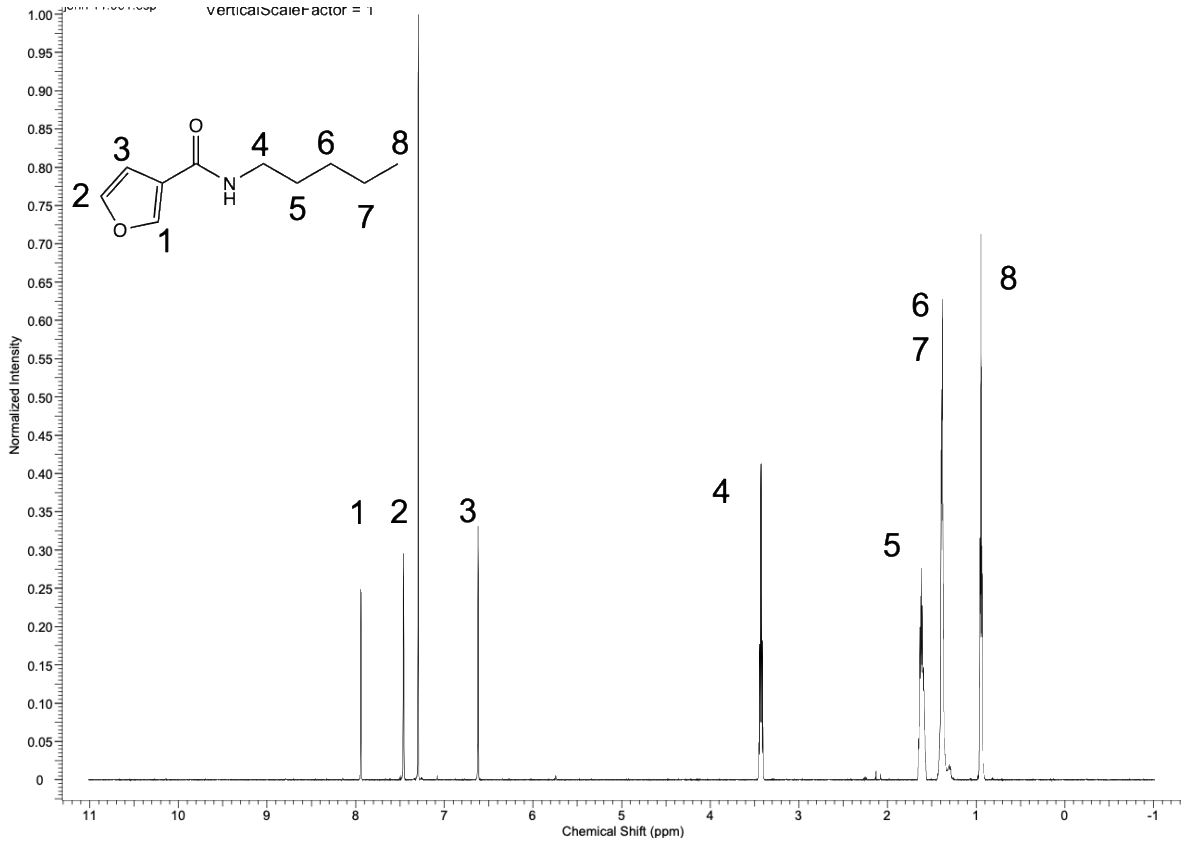

^{1}H NMR (500 MHz, $CDCl_3$): *N*-Hexyl-3-furancarboxamide (**C6**)

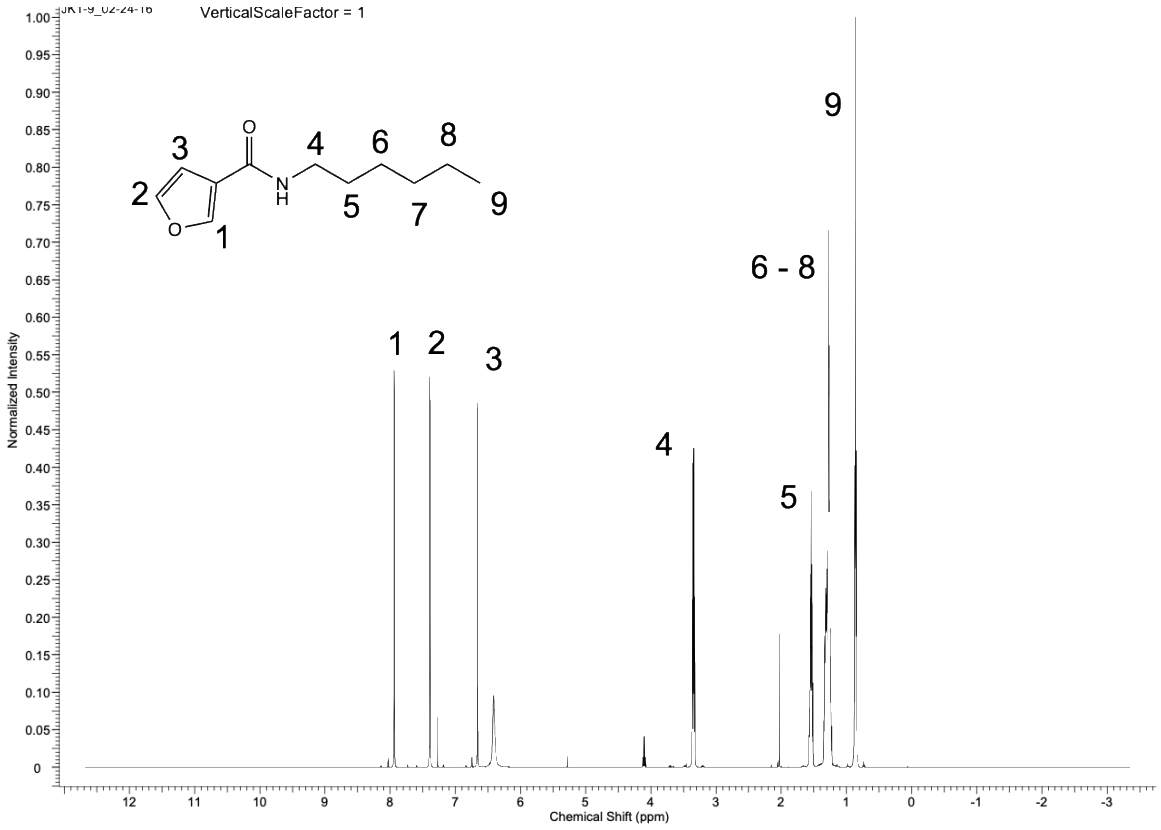

^{1}H NMR (500 MHz, $CDCl_3$): *N*-Heptyl-3-furancarboxamide (**C7**)

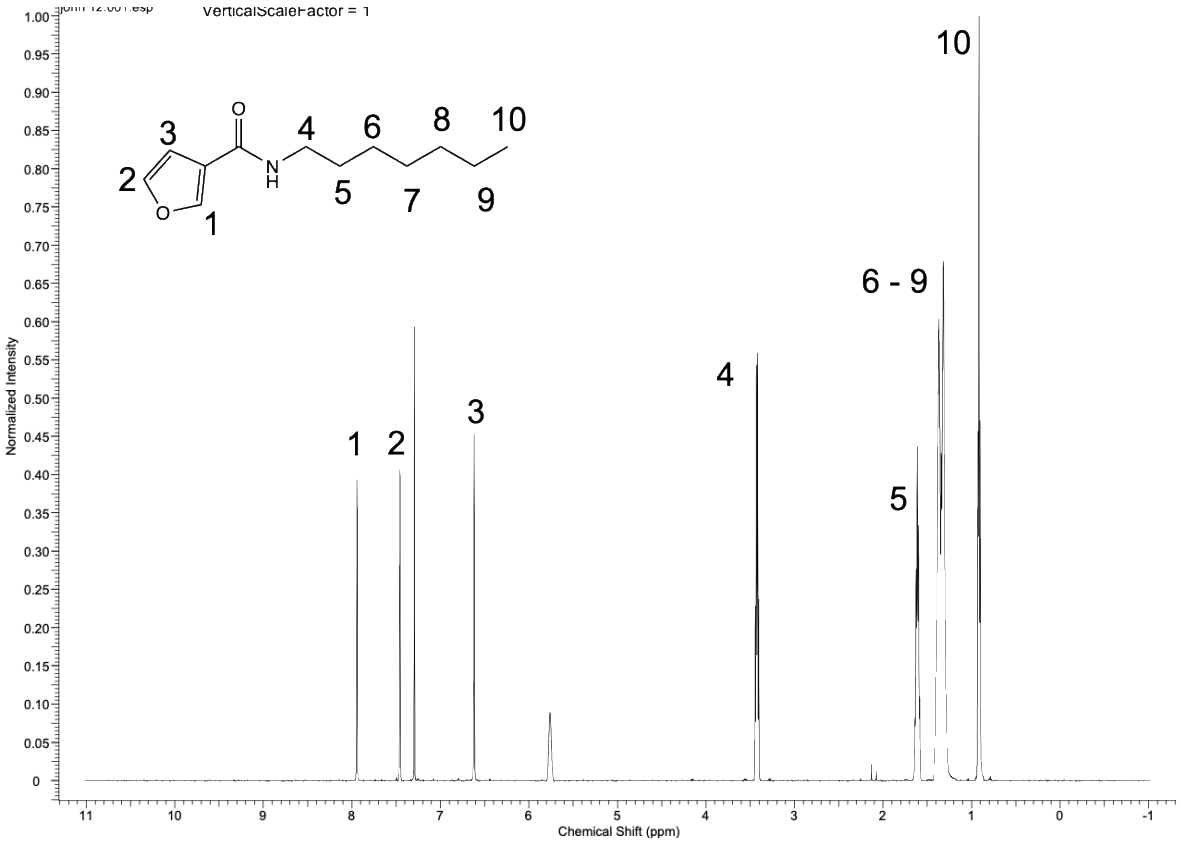

^{1}H NMR (500 MHz, $CDCl_3$): *N*-Octyl-3-furancarboxamide (**C8**)

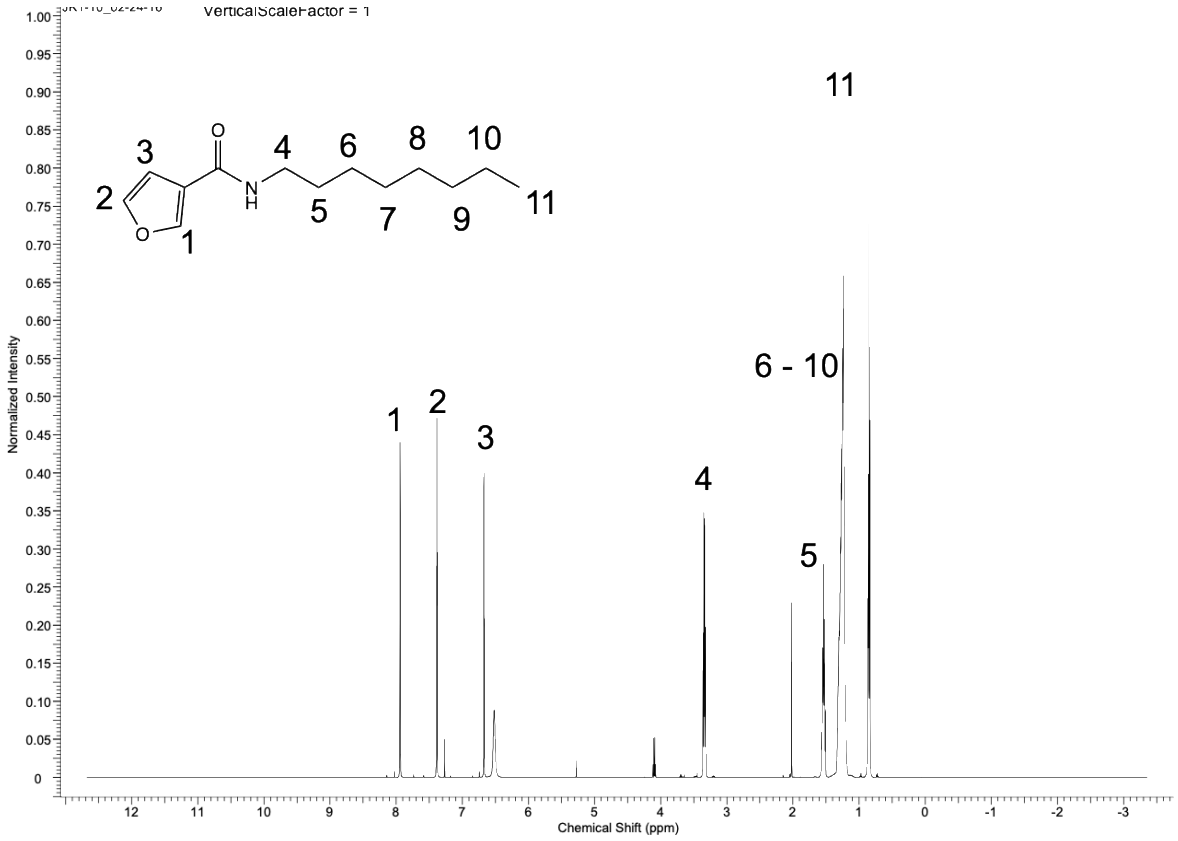

^{1}H NMR (500 MHz, $CDCl_3$): *N*-(2-hydroxyethyl)-3-furancarboxamide (**C2-OH**)

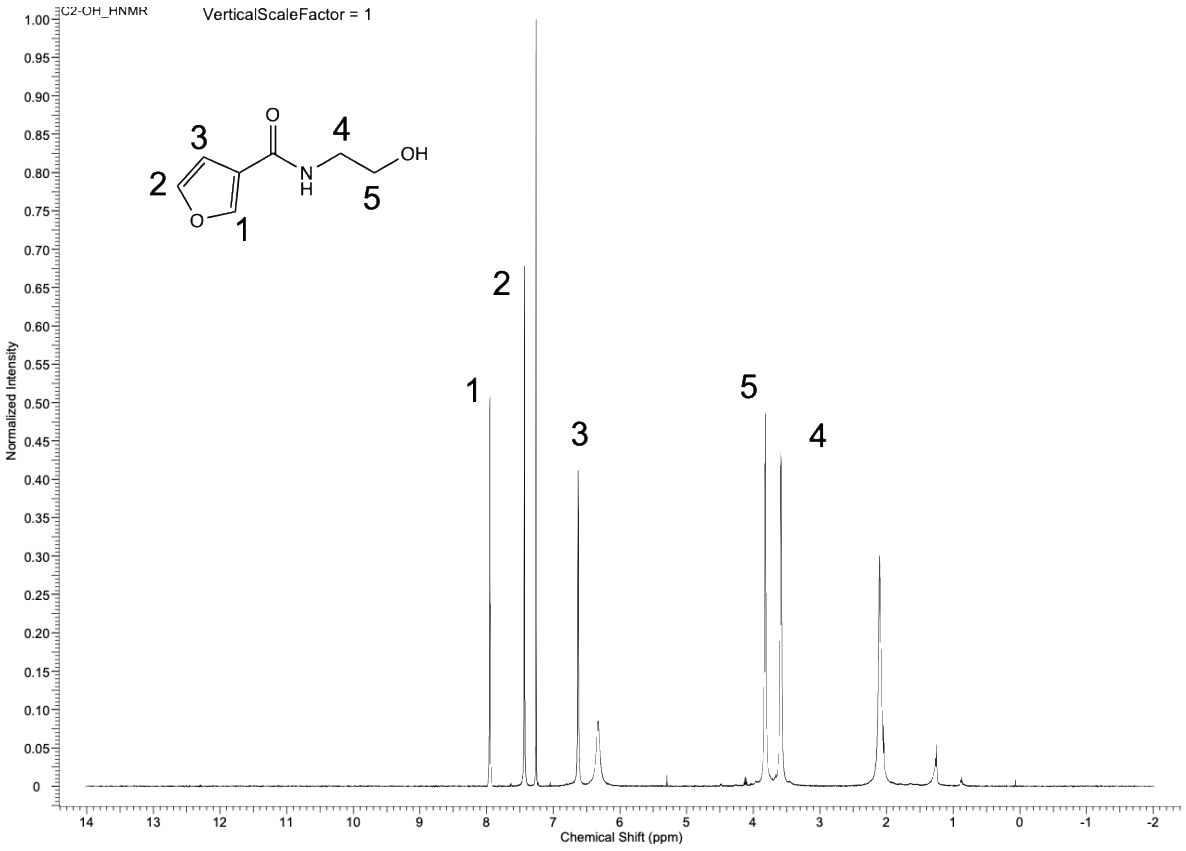

^{1}H NMR (500 MHz, $CDCl_3$): *N*-(2-hydroxypentyl)-3-furancarboxamide (**C5-OH**)

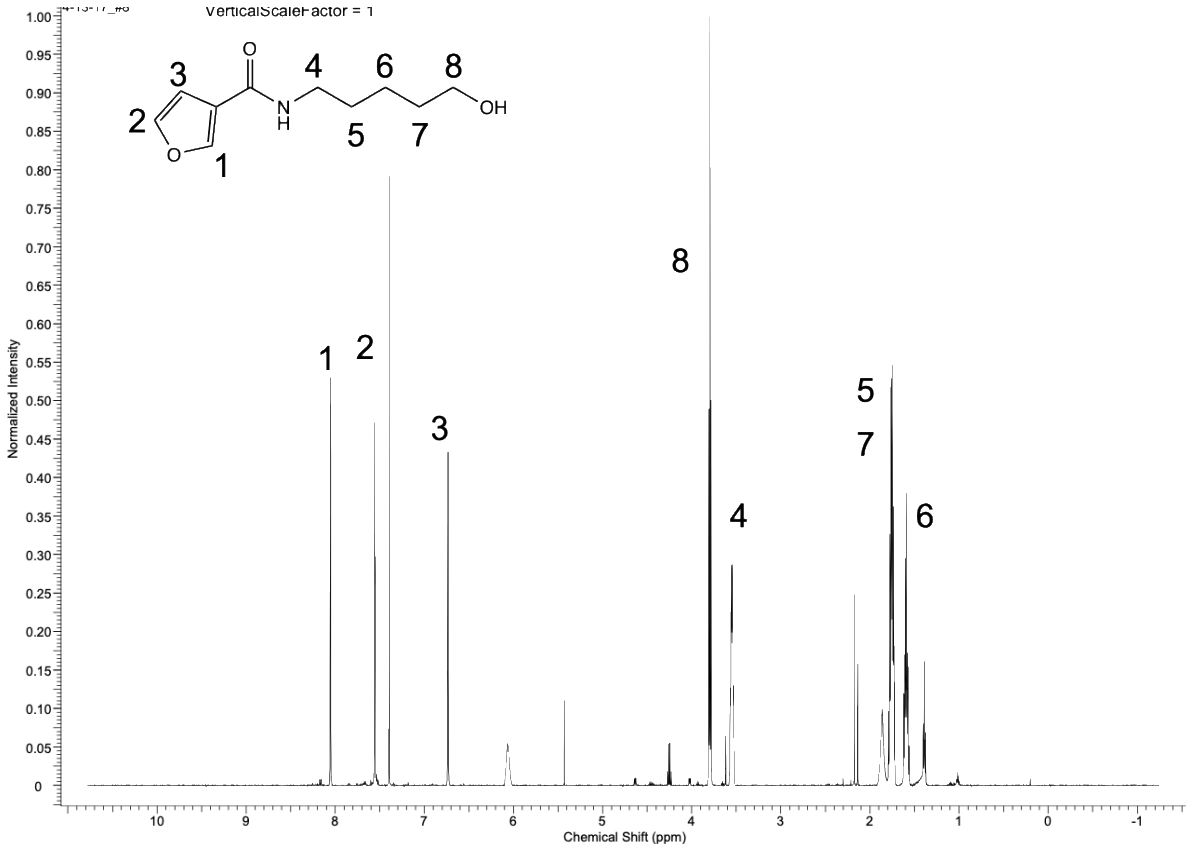

^{1}H NMR (500 MHz, $CDCl_3$): *N*-(2-hydroxyoctyl)-3-furancarboxamide (**C8-OH**)

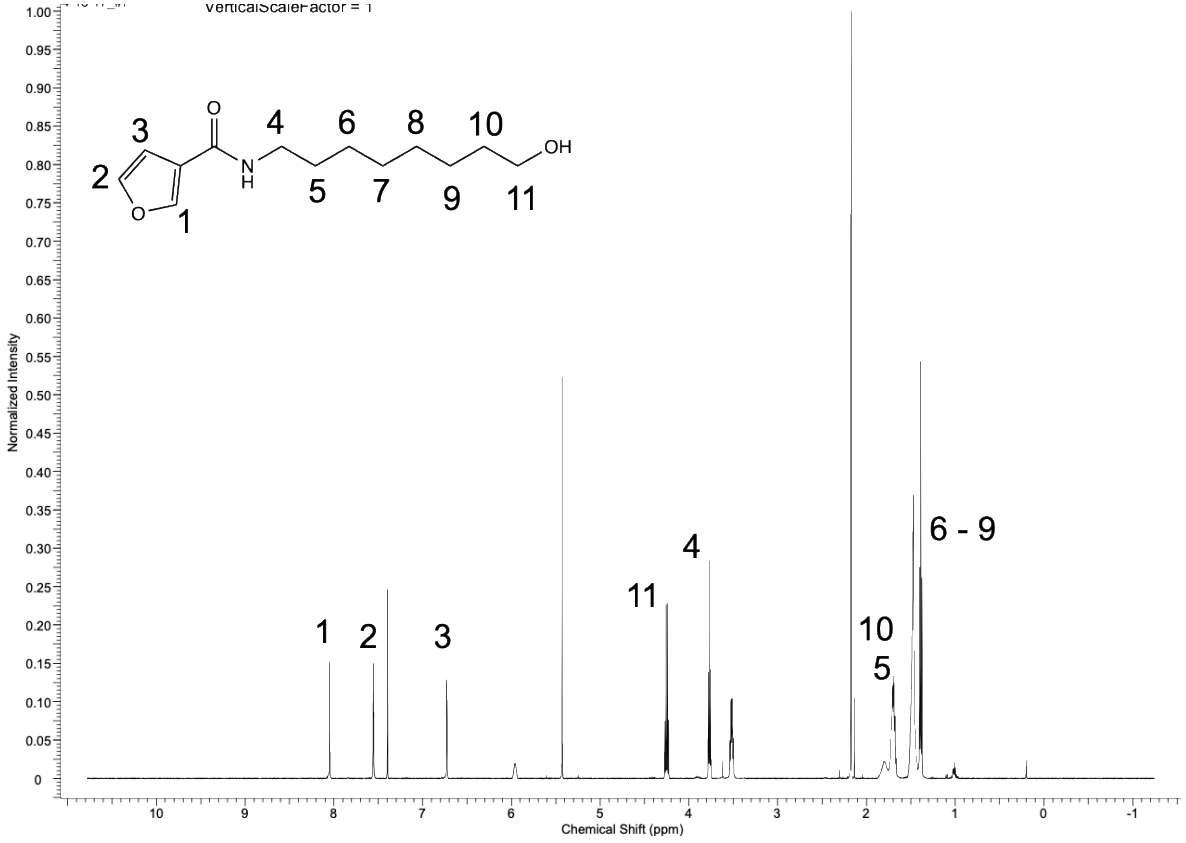

References

Baer BR, Rettie AE. (2006). CYP4B1: an enigmatic P450 at the interface between xenobiotic and endobiotic metabolism. Drug Metab Rev, 38, 451-76.

Baer BR, Rettie AE, Henne KR. (2005a). Bioactivation of 4-ipomeanol by CYP4B1: adduct characterization and evidence for an enedial intermediate. Chem Res Toxicol, 18, 855-64.

Baer BR, Schuman JT, Campbell AP, Cheesman MJ, Nakano M, Moguilevsky N, Kunze KL, Rettie AE. (2005b). Sites of covalent attachment of CYP4 enzymes to heme: evidence for microheterogeneity of P450 heme orientation. Biochemistry, 44, 13914-20.

Bonini C, Mondino A. (2015). Adoptive T-cell therapy for cancer: The era of engineered T cells. Eur J Immunol, 45, 2457-69.

Cheesman MJ, Baer BR, Zheng YM, Gillam EM, Rettie AE. (2003). Rabbit CYP4B1 engineered for high-level expression in Escherichia coli: ligand stabilization and processing of the N-terminus and heme prosthetic group. Arch Biochem Biophys, 416, 17-24.

Chen LJ, DeRose EF, Burka LT. (2006). Metabolism of furans in vitro: ipomeanine and 4-ipomeanol. Chem Res Toxicol, 19, 1320-9.

Chen W, Koenigs LL, Thompson SJ, Peter RM, Rettie AE, Trager WF, Nelson SD. (1998). Oxidation of acetaminophen to its toxic quinone imine and nontoxic catechol metabolites by baculovirus-expressed and purified human cytochromes P450 2E1 and 2A6. Chem Res Toxicol, 11, 295-301.

Ciceri F, Bonini C, Gallo-Stampino C, Bordignon C. (2005). Modulation of GvHD by suicide-gene transduced donor T lymphocytes: clinical applications in mismatched transplantation. Cytotherapy, 7, 144-9.

Ortiz de Montellano PR (2018). 1-Aminobenzotriazole: A Mechanism-Based Cytochrome P450 Inhibitor and Probe of Cytochrome P450 Biology. Med Chem (Los Angeles), 8.

Edson KZ, Rettie AE. (2013). CYP4 enzymes as potential drug targets: focus on enzyme multiplicity, inducers and inhibitors, and therapeutic modulation of 20-hydroxyeicosatetraenoic acid (20-HETE) synthase and fatty acid omega-hydroxylase activities. Curr Top Med Chem, 13, 1429-40.

Fisher MB, Zheng YM, Rettie AE. (1998). Positional specificity of rabbit CYP4B1 for omega-hydroxylation1 of short-medium chain fatty acids and hydrocarbons. Biochem Biophys Res Commun, 248, 352-5.

Gillette JR. (1974). Commentary. A perspective on the role of chemically reactive metabolites of foreign compounds in toxicity. I. Correlation of changes in covalent binding of reactivity metabolites with changes in the incidence and severity of toxicity. Biochem Pharmacol, 23, 2785-94.

Hsu MH, Baer BR, Rettie AE, Johnson EF. (2017). The Crystal Structure of Cytochrome P450 4B1 (CYP4B1) Monooxygenase Complexed with Octane Discloses Several Structural

Adaptations for omega-Hydroxylation. J Biol Chem, 292, 5610-21.

Hyster TK, Rovis T. (2010). Rhodium-catalyzed oxidative cycloaddition of benzamides and alkynes via C-H/N-H activation. J Am Chem Soc, 132, 10565-9.

Li C, Lin D, Gao H, Hua H, Peng Y, Zheng J. (2015). N-Acetyl Lysine/Glutathione-Derived Pyrroles as Potential Ex Vivo Biomarkers of Bioactivated Furan-Containing Compounds. Chemical Research in Toxicology, 28, 384-93.

McDonald MG, Ray S, Amorosi CJ, Sitko KA, Kowalski JP, Paco L, Nath A, Gallis B, Totah RA, Dunham MJ and others. (2017). Expression and Functional Characterization of Breast Cancer-Associated Cytochrome P450 4Z1 in Saccharomyces cerevisiae. Drug Metab Dispos, 45, 1364-71.

O'Boyle NM, Banck M, James CA, Morley C, Vandermeersch T, Hutchison GR. (2011). Open Babel: An open chemical toolbox. J Cheminform, 3, 33.

Obach RS, Kalgutkar AS, Soglia JR, Zhao SX. (2008). Can in vitro metabolism-dependent covalent binding data in liver microsomes distinguish hepatotoxic from nonhepatotoxic drugs? An analysis of 18 drugs with consideration of intrinsic clearance and daily dose. Chem Res Toxicol, 21, 1814-22.

Parkinson OT, Teitelbaum AM, Whittington D, Kelly EJ, Rettie AE. (2016). Species Differences in Microsomal Oxidation and Glucuronidation of 4-Ipomeanol: Relationship to Target Organ Toxicity. Drug Metab Dispos, 44, 1598-602.

Peterson LA. (2013). Reactive metabolites in the biotransformation of molecules containing a furan ring. Chem Res Toxicol, 26, 6-25.

Pettersen EF, Goddard TD, Huang CC, Couch GS, Greenblatt DM, Meng EC, Ferrin TE. (2004). UCSF Chimera--a visualization system for exploratory research and analysis. J Comput Chem, 25, 1605-12.

Rainov NG, Sena-Esteves M, Fraefel C, Dobberstein KU, Chiocca EA, Breakefield XO. (1998). A chimeric fusion protein of cytochrome CYP4B1 and green fluorescent protein for detection of pro-drug activating gene delivery and for gene therapy in malignant glioma. Advances in experimental medicine and biology, 451, 393.

Roellecke K, Jager VD, Gyurov VH, Kowalski JP, Mielke S, Rettie AE, Hanenberg H, Wiek C, Girhard M. (2017). Ligand characterization of CYP4B1 isoforms modified for high-level expression in Escherichia coli and HepG2 cells. Protein Eng Des Sel, 30, 205-16.

Roellecke K, Virts EL, Einholz R, Edson KZ, Altvater B, Rossig C, von Laer D, Scheckenbach K, Wagenmann M, Reinhardt D and others. (2016). Optimized human CYP4B1 in combination with the alkylator prodrug 4-ipomeanol serves as a novel suicide gene system for adoptive T-cell therapies.

Rowinsky EK, Noe DA, Ettinger DS, Christian MC, Lubejko BG, Fishman EK, Sartorius SE, Boyd MR, Donehower RC. (1993). Phase I and pharmacological study of the pulmonary cytotoxin 4-ipomeanol on a single dose schedule in lung cancer patients: hepatotoxicity is dose limiting in humans. Cancer Res, 53, 1794-801.

Schmidt EM, Wiek C, Parkinson OT, Roellecke K, Freund M, Gombert M, Lottmann N, Steward CA, Kramm CM, Yarov-Yarovoy V and others. (2015). Characterization of an Additional Splice Acceptor Site Introduced into CYP4B1 in Hominoidae during Evolution. PLoS One, 10, e0137110.

Silverman, R. B. (1988) Mechanism-based enzyme inactivation: chemistry and enzymology. CRC Press.

Statham CN, Dutcher JS, Kim SH, Boyd MR. (1982). Ipomeanol 4-glucuronide, a major urinary metabolite of 4-ipomeanol in the rat. Drug Metab Dispos, 10, 264-7.

Teitelbaum AM, McDonald MG, Kowalski JP, Parkinson OT, Scian M, Whittington D, Roellecke K, Hanenberg H, Wiek C, Rettie AE. (2019). Influence of Stereochemistry on the Bioactivation and Glucuronidation of 4-Ipomeanol. J Pharmacol Exp Ther, 368, 308-16.

Trott O, Olson AJ. (2010). AutoDock Vina: improving the speed and accuracy of docking with a new scoring function, efficient optimization and multithreading. J Comput Chem, 31, 455-61.

Turtle CJ, Hanafi LA, Berger C, Gooley TA, Cherian S, Hudecek M, Sommermeyer D, Melville K, Pender B, Budiarto TM and others. (2016). CD19 CAR-T cells of defined CD4+:CD8+ composition in adult B cell ALL patients. J Clin Invest.

Wiek C, Schmidt EM, Roellecke K, Freund M, Nakano M, Kelly EJ, Kaisers W, Yarov-Yarovoy V, Kramm CM, Rettie AE and others. (2015). Identification of amino acid determinants in CYP4B1 for optimal catalytic processing of 4-ipomeanol. Biochem J, 465, 103-14.

Zheng YM, Fisher MB, Yokotani N, Fujii-Kuriyama Y, Rettie AE. (1998). Identification of a meander region proline residue critical for heme binding to cytochrome P450: implications for the catalytic function of human CYP4B1. Biochemistry, 37, 12847-51.

Chapter 3

Design and characterization of the first selective and potent mechanism-based inhibitor of cytochrome P450 4Z1

This is adapted, with permission, from the following publication:

Kowalski JP, McDonald MG, Pelletier RD, Hanenberg H, Wiek C, Rettie AE. (2020). Design and Characterization of the First Selective and Potent Mechanism-Based Inhibitor of Cytochrome P450 4Z1. Journal of Medicinal Chemistry.

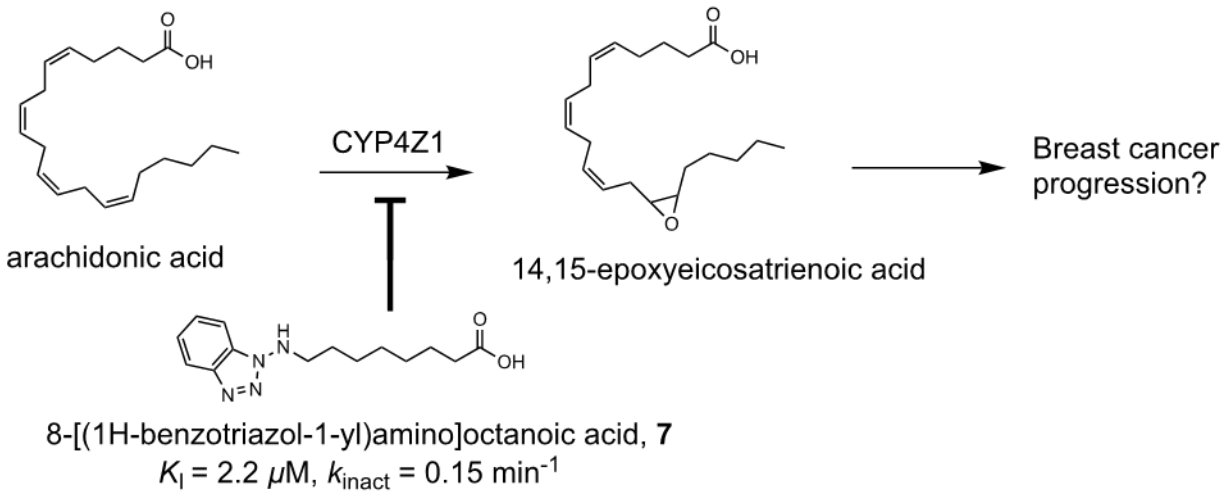

3.1 Introduction

Cytochrome P450 (CYP) enzymes are a critical family of hemoproteins that are involved in the metabolism of both xenobiotic and endogenous molecules (Ortiz de Montellano, 2005). In 2004, CYP4Z1 was cloned from a breast carcinoma line and subsequently shown by several groups to be up-regulated in breast carcinoma (Rieger et al., 2004; Radvanyi et al., 2005; Li et al., 2017). Other expression profiling studies also demonstrate consistently that CYP4Z1

transcript level is associated with an elevated tumor grade and increased tumor aggressiveness (Yang et al., 2017; Murray et al., 2010; Al-Esawi et al., 2020). Some mechanistic insight has been provided by the finding that overexpression of CYP4Z1 promotes angiogenesis and tumor growth both *in vitro* and *in vivo* (Yu et al., 2012).

Many CYP4 enzymes are capable of metabolizing polyunsaturated fatty acids (PUFAs) to biological compounds that participate in a complex web of signaling (Edson and Rettie, 2013). Key metabolites of arachidonic acid (AA, **Fig. 3.1**), namely 20-hydroxyeicosatetraenoic acid (20-HETE) and 14,15-epoxyeicosatrienoic acid (14,15-EET), are thought to play roles in human cancer progression, by influencing angiogenesis, tumor growth and metastasis (Johnson et al., 2015; Luo et al., 2016; Panigrahy et al., 2011). We recently established that 14,15-EET is a dominant metabolite of CYP4Z1-dependent AA metabolism and have speculated that a role for CYP4Z1 in breast cancer may involve this signaling ligand (McDonald et al., 2017).

Breast cancer is one of the leading causes of death in women, with more than 2 million new cases diagnosed worldwide in 2018 (World Cancer Research Fund). Novel therapeutic modalities are needed urgently, especially for recurrent and metastatic tumors (Capper et al., 2016). Endogenous mammary-specific expression of CYP4Z1 offers a new avenue to explore for breast cancer treatment, and there has already been success with CYP inhibitors developed for anti-cancer therapy. For example, aromatase (CYP19) inhibitors, such as exemestane, letrozole and anastrozole, are useful in breast cancer treatment because they effectively limit estrogen production (Bruno and Njar, 2007).

Therefore, the goal of this study was to develop a potent and selective mechanism-based inhibitor (MBI) of CYP4Z1 to enable biochemical characterization of this enzyme and help unravel the role that bioactive lipid metabolites play in breast cancer progression. Herein, we show that analogs of 1-aminobenzotriazole (**ABT**) are potent time-dependent inhibitors of CYP4Z1. Two analogs (**6, 7**) showed pronounced selectivity as reversible inhibitors of CYP4Z1,

compared to other CYP enzymes, and even higher selectivity when they were evaluated for their time-dependent effects on off-target CYPs. Further, we confirmed mechanism-based inhibition for our most potent and selective analog, 8-[(1H-benzotriazol-1-yl)amino]octanoic acid (**7**), determined the kinetics of inactivation, interrogated the mechanistic pathway leading to inactivation, and assessed the potency of **7** towards inhibition of CYP4Z1-mediated 14,15-EET production in a breast cancer cell line.

3.2 Experimental procedures

3.2.1 General information for synthesis

All solvents and reagents were purchased from commercial sources (Alfa Aesar, Acros Organics, AstaTech, Fisher, Oakwood Chemical, Sigma-Aldrich, and TCI) and used as received. All reactions were monitored by thin-layer chromatography, visualized by either UV (254 nm) or potassium permanganate stain. For isolation of purified compounds, normal phase chromatography was carried out on a Teledyne Isco Combiflash system (Lincoln, NE). ^{1}H and ^{13}C NMR spectra were recorded at 25 °C in deuterated chloroform ($CDCl_3$) on either a 499.73 MHz Agilent DD2 (Santa Clara, CA) or 499.96 MHz Bruker Avance series (Billerica, MA) spectrometer, respectively. Chemical shifts are reported below relative to the solvent peak in $CDCl_3$ at 7.26 ppm (^{1}H NMR), or tetramethylsilane at 0.00 ppm (^{13}C NMR). Coupling constants (*J*) are noted in hertz (Hz), and peak multiplicities as either a singlet (s), doublet (d), triplet (t), pentet (p), or multiplet (m). All ^{1}H and ^{13}C NMR spectra have been provided in the Supporting Information. Accurate mass and purity analyses of the synthesized compounds were determined via UPLC−MS on a Waters Acquity UPLC (Milford, MA) coupled in tandem with a Waters Acquity tunable UV detector and a Thermo LTQ-Orbitrap mass spectrometer (San Jose,

CA). Purity as assessed by UPLC−UV (254 and 280 nm) and ^{1}H NMR spectroscopy were ≥ 95% for all compounds.

3.2.2 Alcohol oxidation (General Procedure I)

A modified version of an existing method that has been published was utilized (Vogel et al., 1996) and was as follows: A dried and N_2-purged round-bottom flask containing 1-2 g celite was charged with pyridinium chlorochromate (PCC, 3-5 mmol, 1.5 eq), solvated in ~50 mL anhydrous dichloromethane. The appropriate primary alcohol (2-3 mmol), solvated in a minimal amount of anhydrous dichloromethane, was subsequently added to the reaction flask, and the mixture was stirred at room temperature under N_2 for 90 minutes. Next, anhydrous diethyl ether was added to the slurry and the mixture was filtered through a pad of celite, rinsed with several portions of diethyl ether, and solvent was removed from the combined organic fractions under vacuum. The residue was then washed thrice with portions of diethyl ether to harvest the soluble oxo-product and the combined diethyl ether fractions were once again filtered through celite and solvent was removed under vacuum to afford the corresponding aldehyde.

3.2.3 Imine formation (General Procedure II)

Modified versions of existing methods that have been published were utilized for both general procedures II and III (Mathews and Bend, 1993) and were as follows: A dried and N_2-purged round-bottom flask was charged with **ABT** (0.75 mmol), the appropriate aldehyde (4.5 mmol, 6.0 eq), and ~20 mL glacial acetic acid. For inhibitors **6** – **9**, the oxo-product derived from general procedure I (0.5-0.8 mmol) was reacted with 1.5 eq of **ABT**. The reaction mixture was stirred at room temperature overnight and the acetic acid was subsequently removed under vacuum. The crude product was purified via flash chromatography using a dichloromethane/ethyl acetate gradient to afford the corresponding imine intermediate (for

analogs containing terminal carboxylic acid groups, 2% acetic acid was added to the mobile phase for improved chromatographic separation).

3.2.4 Imine reduction (General Procedure III)

A dried round-bottom flask was charged with the appropriate imine intermediate (0.3-0.7 mmol), $NaBH_4$ (~20 eq), and ~40 mL of a 2:1 solution of methanol/dichloromethane. The reaction mixture was stirred at room temperature for 1 hour and then the solvents were removed under vacuum. The remaining mixture was solvated in a 20:1 solution of dichloromethane/methanol and then washed thrice with H_2O; for the carboxylic acid-containing analogs, the H_2O was adjusted with 1N HCl to a pH of ~2 prior to washing. The organic fraction was dried over Na_2SO_4, filtered, and the crude product was purified via flash chromatography using a hexane/ethyl acetate gradient to afford the corresponding inhibitors **1 – 9.**

3.2.5 Synthesized ABT-analogs

*N-butyl-1H-1,2,3-benzotriazol-1-amine (**1**).* Synthesized from butanal and **ABT** according to general procedures II and III, with respective yields of 89 and 80%. ^{1}H NMR (500 MHz, $CDCl_3$) δ 8.02 (d, *J* = 8.4 Hz, 1H), 7.61 (d, *J* = 8.3, 1H), 7.50 (t, *J* = 7.9 1H), 7.37 (t, *J* = 7.4, 1H), 3.42 (t, *J* = 7.1, 2H), 1.52 (p, *J* = 7.0, 2H), 1.46 (sx, *J* = 7.5, 2H), 0.93 (t, *J* = 7.2, 3H); ^{13}C NMR (125 MHz, $CDCl_3$) δ 144.4, 132.3, 127.7, 124.1, 119.9, 109.8, 52.91, 29.91, 19.96, 13.80; HRMS (ESI+) *m/z* [M+H] calculated ($C_{10}H_{15}N_4$) 191.1291, observed 191.1292, δ ppm 0.5.

*N-hexyl-1H-1,2,3-benzotriazol-1-amine (**2**).* Synthesized from hexanal and **ABT** according to general procedures II and III, with respective yields of 80 and 84%. ^{1}H NMR (500 MHz, $CDCl_3$) δ 8.02 (d, *J* = 8.4 Hz, 1H), 7.61 (d, *J* = 8.3, 1H), 7.50 (t, *J* = 7.5 1H), 7.37 (t, *J* = 7.2, 1H), 3.41 (t, *J* = 7.2, 2H), 1.53 (p, *J* = 7.3, 2H), 1.42 (p, *J* = 8.2, 2H), 1.29 (m, 4H), 0.88 (t, *J* = 6.9, 3H); ^{13}C NMR (125 MHz, $CDCl_3$) δ 144.4, 132.3, 127.6, 124.1, 119.9, 109.8, 53.22, 31.53,

27.84, 26.45, 22.52, 13.97; HRMS (ESI+) *m/z* [M+H] calculated ($C_{12}H_{19}N_4$) 219.1604, observed 219.1606, δ ppm 0.9.

*N-octyl-1H-1,2,3-benzotriazol-1-amine (**3**).* Synthesized from octanal and **ABT** according to general procedures II and III, with respective yields of 77 and 70%. ^{1}H NMR (500 MHz, $CDCl_3$) δ 8.00 (d, *J* = 8.4 Hz, 1H), 7.60 (d, *J* = 8.3, 1H), 7.48 (t, *J* = 7.3 1H), 7.35 (t, *J* = 7.2, 1H), 3.40 (t, *J* = 7.2, 2H), 1.52 (p, *J* = 7.3, 2H), 1.40 (p, *J* = 7.6, 2H), 1.26 (m, 8H), 0.87 (t, *J* = 7.1, 3H); ^{13}C NMR (125 MHz, $CDCl_3$) δ 144.4, 132.3, 127.7, 124.1, 119.9, 109.8, 53.27, 31.77, 29.31, 29.17, 27.88, 26.79, 22.62, 14.06; HRMS (ESI+) *m/z* [M+H] calculated ($C_{14}H_{23}N_4$) 247.1917, observed 247.1922, δ ppm 2.0.

*N-decyl-1H-1,2,3-benzotriazol-1-amine (**4**)*. Synthesized from decanal and **ABT** according to general procedures II and III, with respective yields of 67 and 70%. ^{1}H NMR (500 MHz, $CDCl_3$) δ 8.01 (d, *J* = 8.0 Hz, 1H), 7.60 (d, *J* = 8.3, 1H), 7.49 (t, *J* = 7.2 1H), 7.36 (t, *J* = 8.1, 1H), 3.40 (t, *J* = 6.8, 2H), 1.52 (p, *J* = 7.1, 2H), 1.41 (p, *J* = 6.9, 2H), 1.25 (m, 12H), 0.87 (t, *J* = 7.2, 3H); ^{13}C NMR (125 MHz, $CDCl_3$) δ 144.4, 132.3, 127.6, 124.1, 119.9, 109.8, 53.24, 31.88, 29.52, 29.35, 29.28, 27.89, 26.79, 22.67, 14.10; HRMS (ESI+) *m/z* [M+H] calculated ($C_{16}H_{27}N_4$) 275.2230, observed 275.2234, δ ppm 1.5.

*N-dodecyl-1H-1,2,3-benzotriazol-1-amine (**5**).* Synthesized from dodecanal and **ABT** according to general procedures II and III, with respective yields of 65 and 74%. ^{1}H NMR (500 MHz, $CDCl_3$) δ 8.02 (d, *J* = 8.4 Hz, 1H), 7.61 (d, *J* = 8.3, 1H), 7.50 (t, *J* = 7.7 1H), 7.37 (t, *J* = 7.3, 1H), 3.41 (t, *J* = 7.2, 2H), 1.53 (p, *J* = 7.4, 2H), 1.41 (p, *J* = 7.6, 2H), 1.25 (m, 16H), 0.88 (t, *J* = 6.9, 3H); ^{13}C NMR (125 MHz, $CDCl_3$) δ 144.4, 132.3, 127.7, 124.1, 119.9, 109.8, 53.28, 31.92, 29.63, 29.56, 29.52, 29.35, 27.89, 26.79, 22.69, 14.11; HRMS (ESI+) *m/z* [M+H] calculated ($C_{18}H_{31}N_4$) 303.2543, observed 303.2546, δ ppm 1.0.

*6-[(1H-1,2,3-benzotriazol-1-yl)amino]hexanoic acid (**6**).* Synthesized from 6-hydroxyhexanoic acid and **ABT** according to general procedures I, II and III, with respective yields of 23, 50 and 76%. ^{1}H NMR (500 MHz, $CDCl_3$) δ 8.01 (d, *J* = 8.4 Hz, 1H), 7.60 (d, *J* = 8.3, 1H), 7.49 (t, *J* = 7.8 1H), 7.36 (t, *J* = 7.9, 1H), 3.42 (t, *J* = 6.8, 2H), 2.36 (t, *J* = 7.3, 2H), 1.66 (p, *J* = 7.4, 2H), 1.52 (m, 4H); ^{13}C NMR (125 MHz, $CDCl_3$) δ 178.7, 144.3, 132.3, 127.9, 124.3, 119.9, 109.8, 52.87, 33.74, 27.56, 26.19, 24.34; HRMS (ESI+) *m/z* [M+H] calculated ($C_{12}H_{17}N_4O_2$) 249.1346, observed 249.1357, δ ppm 4.4.

*8-[(1H-1,2,3-benzotriazol-1-yl)amino]octanoic acid (**7**).* Synthesized from 8-hydroxyoctanoic acid and **ABT** according to general procedures I, II and III, with respective yields of 25, 60 and 80%. ^{1}H NMR (500 MHz, $CDCl_3$) δ 8.02 (d, *J* = 8.4 Hz, 1H), 7.60 (d, *J* = 8.3, 1H), 7.49 (t, *J* = 7.8 1H), 7.36 (t, *J* = 7.5, 1H), 3.40 (t, *J* = 7.1, 2H), 2.34 (t, *J* = 7.5, 2H), 1.63 (p, *J* = 7.3, 2H), 1.53 (p, *J* = 7.4, 2H), 1.43 (p, *J* = 6.7, 2H), 1.33 (m, 4H); ^{13}C NMR (125 MHz, $CDCl_3$) δ 179.3, 144.3, 132.3, 127.8, 124.3, 119.8, 109.8, 53.13, 33.99, 28.91, 28.88, 27.75, 26.53, 24.56; HRMS (ESI+) *m/z* [M+H] calculated ($C_{14}H_{21}N_4O_2$) 277.1659, observed 277.1670, δ ppm 4.0.

*10-[(1H-1,2,3-benzotriazol-1-yl)amino]decanoic acid (**8**).* Synthesized from 10-hydroxydecanoic acid and **ABT** according to general procedures I, II and III, with respective yields of 21, 43 and 56%. ^{1}H NMR (500 MHz, $CDCl_3$) δ 8.01 (d, *J* = 8.4 Hz, 1H), 7.60 (d, *J* = 8.3, 1H), 7.49 (t, *J* = 7.8 1H), 7.36 (t, *J* = 7.5, 1H), 3.40 (t, *J* = 7.1, 2H), 2.34 (t, *J* = 7.5, 2H), 1.62 (p, *J* = 7.4, 2H), 1.52 (p, *J* = 7.5, 2H), 1.40 (p, *J* = 6.7, 2H), 1.28 (m, 8H); ^{13}C NMR (125 MHz, $CDCl_3$) δ 179.2, 144.3, 132.2, 127.7, 124.2, 119.9, 109.8, 53.23, 33.96, 29.21, 29.08, 28.97, 27.82, 26.69, 24.65; HRMS (ESI+) *m/z* [M+H] calculated ($C_{16}H_{25}N_4O_2$) 305.1972, observed 305.1984, δ ppm 3.9.

*12-[(1H-1,2,3-benzotriazol-1-yl)amino]dodecanoic acid (**9**).* Synthesized from 12-hydroxydodecanoic acid and **ABT** according to general procedures I, II and III, with respective yields of 22, 55 and 71%. ^{1}H NMR (500 MHz, $CDCl_3$) δ 8.02 (d, *J* = 8.4 Hz, 1H), 7.61 (d, *J* = 8.3, 1H), 7.49 (t, *J* = 8.0 1H), 7.36 (t, *J* = 7.8, 1H), 3.40 (t, *J* = 7.2, 2H), 2.35 (t, *J* = 7.5, 2H), 1.63 (p, *J* = 7.4, 2H), 1.53 (p, *J* = 7.5, 2H), 1.41 (p, *J* = 7.6, 2H), 1.26 (m, 12h); ^{13}C NMR (125 MHz, $CDCl_3$) δ 179.5, 144.3, 132.2, 127.7, 124.2, 119.9, 109.8, 53.27, 34.06, 29.39, 29.32, 29.28, 29.16, 29.02, 27.83, 26.73, 24.70; HRMS (ESI+) *m/z* $[M+H]^+$ calculated ($C_{18}H_{29}N_4O_2$) 333.2285, observed 333.2297, δ ppm 3.6.

3.2.6 CYP4Z1-mediated luciferin-benzyl ether (Luc-BE) *O*-debenzylation

To compare Luc-BE (Promega, Madison, Wisconsin) *O*-debenzylation activity between the CYP4Z1-HepG2 (81 pmol CYP4Z1/mg membrane protein) and Vector-HepG2 membrane stocks (Supporting Information: **Method for Membrane Preparation**), metabolic reactions were set up in triplicate on ice and contained 0.6 mg/mL HepG2 membrane protein in 100 mM KPi, pH 7.4, in a final volume of 100 μL. Luc-BE was added to achieve a final concentration of 50 μM and samples were equilibrated at 37 °C for 5 min. NADPH was added for a final concentration of 1mM, or KPi was added for the minus NADPH controls. Metabolic reactions were allowed to proceed for 20 min at 37 °C. To assess the kinetics of CYP4Z1-mediated Luc-BE *O*-debenzylation, metabolic reactions were set up in triplicate on ice and contained 3 pmol of CYP4Z1, in 100 mM KPi, pH 7.4, in a final volume of 100 μL. Luc-BE was added for final concentrations of 1, 5, 10, 25, 50, 75, 100, and 150 μM and the reactions were equilibrated at 37 °C for 5 min. NADPH was added for a final concentration of 1 mM, and metabolism was allowed to proceed for 10 minutes at 37 °C.

3.2.7 Luminescence assay (General Procedure IV)

The CYP4Z1-mediated Luc-BE *O*-debenzylation reactions outlined above, those discussed below to assess inhibition of CYP4Z1 activity, and the other CYP-mediated pro-luciferin metabolism reactions, were quenched (with P450 glo) and assayed as follows: Reactions were transferred from their incubation tubes to white walled 96-well plates containing an equal volume of P450-glo luciferase detection reagent (Promega, Madison, Wisconsin). Beetle luciferin metabolite standards (Promega), prepared in identical matrices, were added at the same time as the metabolic reactions to the plates. After gently mixing and a 20-minute incubation at room temperature, the plates were read on a Biotek Synergy HTX Microplate Reader (Winooski, VT). The luminescence generated (relative light units, RLU) from the calibration luciferin standards was used to generate a standard curve to quantitate the metabolite concentrations in the reactions. These data were subsequently used to determine rates of CYP4Z1 activity and for comparisons between inhibitor and vehicle treated reactions.

3.2.8 CYP4 isozyme IC_{50}-shift experiments

IC_{50}-shift experiments to test inhibition of recombinantly expressed CYP4 isozymes were each performed separately, with duplicate technical replicates, and the experiments were repeated two to three times on separate days. Each metabolic reaction in the experiments contained one of the following: 4 pmol of CYP4Z1 (HepG2 membranes), 1.5 pmol CYP4F8 (HepG2 membranes), 4 pmol of CYP4A11, CYP4F2, CYP4F3a, CYP4F3b, CYP4F12 (Corning Supersomes™, New York, NY). Total protein concentration for all reactions was ~0.20 – 0.25 mg/mL, except for CYP4F8, which was 0.35 mg/mL due to the lower specific content of the enzyme in the HepG2 membrane preparation. Reactions were set up on ice containing the specific CYP4 isozyme in 100 mM KPi, pH 7.4, in a final volume of 200 μL. All inhibitors were solvated in DMSO to make 200× stocks and added to the reactions to achieve final concentrations spanning 0.001 – 100 μM (**1 – 9** for CYP4Z1), 0.03 – 1000 μM (**ABT** for

CYP4Z1), 1 – 3000 μM (**6** for off-target CYP4 isozymes), or 1 – 1000 μM (**7** for off-target CYP4 isozymes). An equal volume of DMSO was added to all vehicle control samples and DMSO concentrations did not exceed 0.5% v/v for all reactions. In order to assess time-dependent inhibition for the inhibitors, half of the metabolic reactions (for each isozyme) included a pre-incubation step plus the cofactor NADPH and the other half a pre-incubation step minus NADPH. The temporal and reagent addition scheme used was as follows: After a 5-min equilibration at 37 °C, NADPH was added from a 50× stock solution for a final concentration of 1 mM to the plus NADPH pre-incubation samples, and an equal volume of buffer to the minus NADPH pre-incubation samples. After a subsequent 30-minute pre-incubation at 37 °C, pro-luciferin probe substrates for each isozyme (detailed below) were added to both sets of pre-incubation reactions from 50× stocks (all at final concentrations ≤ K_m values). Next, NADPH was added to the minus NADPH pre-incubation reactions and an equal volume of buffer to the plus NADPH pre-incubation reactions. The probe substrate reactions were allowed to proceed for 10 minutes at 37 °C and reactions were assayed according to general procedure IV. The pro-luciferins (all from Promega) that were used as CYP4 isozyme probe substrates (concentrations) and the biotransformations that were monitored were as follows: CYP4Z1 Luc-BE (29 μM), CYP4F8 Luc-BE (12 μM), and CYP4F12 Luc-BE (23 μM) *O*-debenzylation; CYP4A11 Luc-4A (80 μM) *O*-demethylation; CYP4F2, CYP4F3a, and CYP4F3b, Luc-4F2/3 (2 μM, due to substrate inhibition kinetics that was observed for all three enzymes, **Figure S7**) *O*-(4-methylthio)-debenzylation. As no metabolite standard for Luc-4A or Luc-4F2/3 was available, enzymatic activity was assessed in a semi-quantitative fashion for isozymes metabolizing these probe substrates. The counter-screening TDI experiment that is presented in **Figure 4** used the same methods as detailed above except with only a single concentration of 30 μM for inhibitors **2 – 9** and HET0016, as a general CYP4 inhibitor positive control, at 0.5 μM.

3.2.9 Hepatic CYP isozyme IC_{50}-shift experiments

IC_{50}-shift experiments to test Inhibition of hepatic CYP isoforms by **6** and **7** were performed with duplicate technical replicates and experiments were repeated three times on separate days. The assays utilized pooled human liver microsomes (HLM) made up from eight random, individual donor livers, that had been prepared for a previous study (McDonald et al., 2015) and followed a cocktail approach similar to previously published methods (Kozakai et al., 2014; Li et al., 2015). The metabolic reactions contained HLM at 0.25 mg/mL total protein, inhibitor **6** or **7** at 1 – 3000 or 1 – 1000 μM, respectively, and used the same setup, timing, and reagent addition scheme as that followed for the CYP4 isozyme IC_{50}-shift experiments. However, after the pre-incubation period, a cocktail of seven selective probe substrates (see below) combined was added from a 50× stock. The CYP isoforms evaluated, substrates (concentrations), and biotransformations were as follows: CYP1A2 phenacetin (100 μM) *O*-deethylation; CYP2B6 bupropion (12 μM) 1'-hydroxylation; CYP2C8 amodiaquine (1 μM) *N*-deethylation; CYP2C9 tolbutamide (100 μM) methyl-hydroxylation; CYP2C19 (*S*)-mephenytoin (50 μM) 4'-hydroxylation; CYP2D6 dextromethorphan (2.5 μM) *O*-demethylation; and CYP3A4/5 midazolam (2.5 μM) 1'-hydroxylation. All probe substrates were used at concentrations $\leq K_m$. After probe substrate turnover had proceeded for 10 minutes at 37 °C, reactions were subsequently terminated with an equal volume of ice-cold acetonitrile containing 200 nM of each deuterated internal standard (listed below) and centrifuged at 15,000 × *g* for 10 min. A supernatant aliquot (5 μL) was analyzed by UPLC−MS/MS on a Waters Acquity UPLC connected to a Waters Xevo TQ-S instrument in ESI+ mode, with the following settings: capillary 3.1 kV, source offset 60.0 V, source temperature 150 °C, desolvation temperature 350 °C, cone gas flow 150 L/h, desolvation gas flow 800 L/hour, and collision gas flow 0.15 mL/min. Cone voltage and collision energies varied between analytes and are noted below. Analytes were separated chromatographically using a Waters HSS T3 column (2.1 × 100 mm, 1.8 μm),

starting with 95% mobile phase A (0.1% formic acid in H2O) and 5% mobile phase B (0.1% formic acid in acetonitrile) at a flow rate of 0.3 mL/min. After holding for 1 min, B was increased linearly from 5 to 60% between 1 and 7 min, immediately elevated to 95%, and then held at 95% between 7 and 8.5 min; total run time was 11 min following a 2.5 min equilibration period. The metabolites were detected by multiple reaction monitoring (MRM) with the following transitions, cone voltages (CV), and collision energies (CE): acetaminophen *m/z* 152.2 > 110, CV = 40 V, CE = 20 eV; hydroxybupropion *m/z* 256.1 > 238.1, CV = 32 V, CE = 10 eV; *N*-desethylamodiaquine *m/z* 328.1 > 283, CV = 40 V, CE = 20 eV; hydroxytolbutamide *m/z* 287.1 > 107, CV = 40 V, CE = 20 eV; 4-hydroxymephenytoin *m/z* 235.1 > 150.1, CV = 30 V, CE = 20 eV; dextrorphan *m/z* 258.1 > 157, CV = 40 V, CE = 30 eV; and 1'-hydroxymidazolam *m/z* 342.1 > 203, CV = 40 V, CE = 30 eV. The corresponding isotope-labeled internal standards and MRM transitions were as follows: acetaminophen-d3 *m/z* 155.2 > 111.06, hydroxybupropion-d6 *m/z* 262.2 > 244.2, *N*-desethylamodiaquine-d5 *m/z* 333.1 > 283.1, hydroxytolbutamide-d9 *m/z* 296.1 > 107, 4-hydroxymephenytoin-d3 *m/z* 238.1 > 150.1, dextrorphan-d3 *m/z* 261.2 > 157, and 1'-hydroxymidazolam-d4 *m/z* 346.1 > 203.05. Metabolite standards, using identical matrix and work-up conditions, were used to create standard curves that were utilized in quantitation of the metabolites and subsequent comparison of enzymatic activity between inhibitor and vehicle treated metabolic reactions.

3.2.10 Kinetics of CYP4Z1 inactivation from 7

Inhibition reactions were set up on ice in triplicate and contained 5 pmol CYP4Z1 in 100 mM KPi, pH 7.4, in a final volume of 100 µL. Inhibitor **7** was added to achieve final concentrations of 0.3, 1, 3, 6, 10, and 20 µM, and DMSO alone was utilized as a vehicle control. After a 5 min equilibration at 37 °C, the reactions were initiated by the addition of NADPH (1 mM final concentration). Aliquots of the inhibition reaction (10 µL) were taken at times 0, 3, 5, 10, 15,

and 20 min, diluted 10-fold into a 100 µL probe substrate reaction containing Luc-BE, at 10× the determined K_m for CYP4Z1 (290 µM), in 100 mM KPi buffer with 1 mM NADPH. The probe substrate reactions progressed for 10 min at 37 °C and were quenched with an equal volume of ice-cold acetonitrile containing 200 nM Luc-4A as an internal standard and centrifuged at 15,000 × *g* for 10 min. Note: due to the timing constraints of assaying for the kinetics of enzyme inactivation, LC-MS/MS was utilized to detect the luciferin metabolite from CYP4Z1 Luc-BE *O*-debenzylation. A supernatant aliquot (3 µL) was analyzed by UPLC−MS/MS on a Waters Acquity UPLC connected to a Waters Xevo TQ-S instrument in ESI+ mode, with the following settings: capillary 2.8 kV, cone 40.0 V, collision 20.0 V, source offset 60.0 V, source temperature 150 °C, desolvation temperature 350 °C, cone gas flow 150 L/h, desolvation gas flow 800 L/hour, and collision gas flow 0.15 mL/min. Analytes were separated chromatographically using a Waters BEH C18 column (2.1 × 50 mm, 1.7 µm), starting with 95% mobile phase A (0.1% formic acid in H2O) and 5% mobile phase B (0.1% formic acid in acetonitrile) at a flow rate of 0.3 mL/min. After holding for 1 min, B was increased linearly from 5 to 95% between 1 and 4 min and held at 95% between 4 and 6 min; total run time was 8.5 min following a 2.5 min equilibration period. The metabolite luciferin was detected by MRM at *m/z* 281.0 > 234.92 and the internal standard Luc-4A was detected by MRM at *m/z* 289.1 > 201.96. The metabolite luciferin, using identical matrix and work-up conditions, was used to create a standard curve that was utilized in quantitation of the metabolite concentration in the reactions and subsequent comparison of enzymatic activity between inhibitor and vehicle treated metabolic reactions. The natural logarithm of the remaining CYP4Z1 activity after treatment with varying concentrations of **7** was plotted versus pre-incubation time. The resultant differential slopes generated k_{obs} rates, which were then plotted against the concentrations of **7** to allow for the determination of the inactivation parameters K_I and k_{inact}.

3.2.11 Examination of the effects of dialysis on CYP4Z1 inactivation by 7

Inhibition reactions were set up on ice in triplicate and contained 3 pmol CYP4Z1 in 100 mM KPi, pH 7.4, in a final volume of 100 µL. Inhibitor **7** was added for a final concentration of 3 µM, and DMSO was added to vehicle reactions. After a 5 min equilibration at 37 °C, the reactions were initiated by the addition of NADPH (1 mM final concentration), or KPi buffer only for the minus NADPH samples. The reactions were allowed to proceed for 15 min and then, for the pre-dialysis samples, aliquots (10 µL) were removed and diluted 10-fold into a 100 µL probe substrate reaction containing Luc-BE, at 10× the determined K_m for CYP4Z1 (290 µM), in 100 mM KPi buffer with 1 mM NADPH. The probe substrate reactions progressed for 10 min at 37 °C and were assayed according to general procedure IV. For the post-dialysis samples (following the 15 min inhibition reaction), the entirety of the reaction was immediately transferred to 10,000 molecular weight cut-off mini dialysis cups (Thermo Scientific Slide-A-Lyzer) suspended in 1 L of 100 mM KPi, pH 7.4, and incubated at 4° C with gentle stirring overnight. The next morning, aliquots were removed, diluted into probe substrate reactions, and assayed as described for the pre-dialysis samples.

3.2.12 Examination of the effects of trapping agents and reactive oxygen-scavenging enzymes on CYP4Z1 inactivation by 7

Inhibition reactions were set up on ice in triplicate and contained 3 pmol CYP4Z1 in 100 mM KPi, pH 7.4, in a final volume of 100 µL. Inhibitor **7** was added for a final concentration of 3 µM, and DMSO was added to vehicle reactions. Reduced glutathione, *N*-acetyl-lysine, methoxyamine, *N*-acetyl-cysteine, and semicarbazide were added individually to reactions for final concentrations of 5 mM, and potassium cyanide was added to a reaction for a final concentration of 1 mM. Catalase (CAT) and super oxide dismutase (SOD), from Sigma (St. Louis, MO), were both added to an inhibition reaction together at 80 units each. Both inhibitor **7** and DMSO vehicle reactions were set up for each additive listed above. After a 5 min

equilibration at 37 °C, the reactions were initiated by the addition of NADPH (1 mM final concentration) or KPi for the minus NADPH samples. The reactions were allowed to proceed for 15 min at 37 °C, and then aliquots of the inhibition reaction (10 µL) were diluted 10-fold into a 100 µL probe substrate reaction containing Luc-BE, at 10× the determined K_m for CYP4Z1 (290 µM), in 100 mM KPi buffer with 1 mM NADPH. The probe substrate reactions progressed for 10 min at 37 °C and were assayed according to general procedure IV.

3.2.13 Determination of the partition ratio

The number of molecules of **7** metabolized per molecule of CYP4Z1 inactivated, the partition ratio, was estimated from a dilution method. Inhibition reactions were set up on ice in triplicate and contained 5 pmol CYP4Z1 in 100 mM KPi, pH 7.4, in a final volume of 100 µL. Inhibitor **7** was added at 11 different final concentrations spanning 0 to 50 µM. After a 5 min equilibration at 37 °C, the inactivation reactions were initiated by the addition of NADPH (1 mM final concentration). The reactions were allowed to proceed for 45 minutes at 37 °C to allow for maximal inactivation, and then aliquots of the inhibition reaction (10 µL) were diluted 10-fold into a 100 µL probe substrate reaction containing Luc-BE, at 10× the determined K_m for CYP4Z1 (290 µM), in 100 mM KPi buffer with 1 mM NADPH. The probe substrate reactions progressed for 10 min at 37 °C and were assayed according to general procedure IV. The percentage of remaining CYP4Z1 activity was plotted versus the molar ratio of [**7**]/[CYP4Z1]. Extrapolation of the initial linear portion to the *x*-intercept generated the turnover number; the partition number was then calculated as the turnover number minus 1.

3.2.14 Interrogation of heme adducts from CYP4Z1 Inactivation by 7

Inactivation reactions were set up on ice and contained 10 pmol of CYP4Z1, or an equal amount of control membranes (~1 mg/mL total protein), in 100 mM KPi, pH 7.4, in a final

volume of 100 µL. Inhibitor **7** or **ABT** was added to achieve a final concentration of 100 µM from 200x DMSO stocks, or an equal amount of DMSO was added. After a 5 min equilibration at 37 °C, the inactivation reactions were initiated by the addition of NADPH (1 mM final concentration). The reactions were allowed to proceed for 30 minutes at 37 °C to allow for maximal inactivation, and then quenched with an equal volume of acetonitrile/methanol (1:1) containing 1% formic acid and centrifuged at 15,000 × *g* for 2 min. Note, the full matrix of conditions for both control and CYP4Z1-HepG2 membranes with either inhibitor **7**, **ABT**, or DMSO vehicle was tested with and without the addition of NADPH.

A supernatant aliquot (20 µL) was analyzed by UPLC−MS/MS on a Waters Acquity UPLC connected to an AB SCIEX 5600 TripleTOF instrument in ESI+ mode similar to as reported by Pelletier (unpublished, 2020) for the elucidation of heme adducts. The following parameters were used; general settings: curtain gas 35, temperature 600℃, gas 1/2 60, ISVF 4500 V. Survey scan settings: range 100 – 2000 *m/z*, accumulation time 0.1 sec, declustering potential 100, collision energy 5, collision energy spread 0. Information-dependent acquisition settings: 4 scans/cycle, range 100 – 2000 *m/z*, accumulation time 0.1 sec, declustering potential 100, collision energy 35, collision energy spread 20, IDA trigger type of mass defect filter and largest peak. Mass defect filter settings: 70 mDa error window, 400 Da window of $C_{34}H_{34}N_4O_4$ (protoporphyrin IX) + $C_{14}H_{20}N_4O_2$ (inhibitor **7**) and also $C_{34}H_{34}N_4O_4Fe$ (heme-B) + $C_{14}H_{20}N_4O_2$ (inhibitor **7**), exclude previous ions for 1 sec, and minimum CPS for trigger of 200. Analytes were separated chromatographically using a Waters XBridge C8 2.1 x 50 mm, 5 µ column, starting with 100% mobile phase A (0.1% ammonium hydroxide in H_2O) and 0% mobile phase B (0.1% ammonium hydroxide in isopropyl alcohol) at a flow rate of 0.5 mL/min. After holding for 1 min, B was increased linearly from 0 to 100% between 1 and 14 min and held at 100% between 14 and 15 min; total run time was 20 min following a 5 min equilibration period.

3.2.15 Inhibition of CYP4Z1-Mediated AA metabolism in T47D cells by 7

T47D cells were modified to express CYP4Z1 (CYP4Z1-T47D), or a control vector (Vector-T47D), in a similar fashion to the HepG2 cell lines. A schematic outline of the lentiviral vector system has been provided in the Supporting Information (**Figure S1A**). Western blot analysis was performed as previously described (McDonald et al., 2017). The stably transduced cell lines were grown in tissue culture media consisting of RPMI-1640, 1% Glutamine, 10% FBS, and 0.01 mg/ml Insulin and selected with puromycin treatment (2 µg/mL) over a 4-day period to ensure homogenous transduction profiles. Both CYP4Z1- and Vector-T47D cell lines were seeded into 6-well tissue culture-treated plates at 2.5×10^5 cells/mL in a volume of 2 mL/well. The CYP4Z1-T47D cells were then dosed with inhibitor **7** to achieve final concentrations of 1 and 3 µM from 1000× DMSO stocks, or DMSO vehicle was added (plus 24-hour pre-incubation samples); Vector-T47D cells were dosed with DMSO. The cells were then placed in a tissue culture incubator at 37° C. After 24 hours, AA was added to all wells for a final concentration of 50 µM from a 400× concentrated stock solvated in degassed ethanol. Inhibitor **7** was then added to the CYP4Z1-T47D cells, which had not been dosed the day prior (minus 24-hour pre-incubation samples), at 1 and 3 µM, or DMSO vehicle was added; Vector-T47D cells were dosed with DMSO. Cells were placed back into the tissue culture incubator for 2 hours to allow for CYP4Z1-mediated AA oxidation. Following this incubation period, media was collected from each well and 0.5 mL H_2O was added to the wells which were then incubated at room temperature for 1 minute. Subsequently, 1 mL of a 1:1 mixture of acetonitrile and methanol was added to each well and cells were scraped to remove them from the tissue culture dish. The aqueous and organic mixture was pooled with the respective media collections and a further 1 mL of the acetonitrile/methanol mixture was added to rinse the wells of any remaining cells and/or extracted analytes. The combined aqueous and organic fractions were then subjected to a previously described workup (McDonald et al., 2017) and a supernatant

aliquot (10 μL) was analyzed by UPLC−MS/MS on a Waters Acquity UPLC connected to a Waters Xevo TQ-S instrument in ESI- mode using settings, chromatography gradient, and column as previously described by McDonald et al. The oxidative AA metabolites 14,15-DiHET, 19-HETE, 20-HETE, and 14,15-EET were detected by MRM at *m/z* 337.10 > 207.00, 319.1 > 231, 319 > 245, and 319.1 > 219, respectively. The deuterated internal standards 14,15-DiHET-d11, 20-HETE-d6, and 14,15-EET-d11 were detected by MRM at *m/z* 348.30 > 207.20, 325.10 > 281.10, and 330.20 > 218.80, respectively. Relative inhibition of AA metabolite formation was determined by comparing the peak area ratios of the analytes divided by their respective deuterated internal standards from cells treated with **7** compared to vehicle, at the various timepoints and conditions noted above. As no deuterated internal standard for 19-HETE is available, 20-HETE-d6 was utilized as the internal standard for this AA metabolite. The entire experiment was repeated under similar conditions and yielded comparable results (data not shown).

3.2.16 Data analysis

GraphPad Prism 7.00 (San Diego, CA) was used for graphing all results, to estimate all kinetic parameters (K_m, V_{max}, K_I, and k_{inact}), and to determine the half maximal inhibitory concentration (IC_{50}) values. IC_{50} values from each individual experiment were averaged and standard deviations calculated. Mass spectral analysis was performed with Waters MassLynx V4.1, Thermo Xcalibur V2.0, and Applied Biosystems Metabolite Pilot V2.0.2. ^{1}H and ^{13}C NMR spectral analysis was performed with Bruker TopSpin V4.0.7.

3.3 Results and Discussion

3.3.1 CYP4Z1 assay for rapid inhibitor screening

A mammalian enzyme source was preferred and, historically, HepG2 cells have been suitable for heterologous expression of CYPs due to their very low basal CYP levels (although some CYP2J2 is present) and catalytically sufficient amounts of the co-enzymes cytochrome P450 reductase and cytochrome b5 (Westerink and Schoonen, 2007; Schulz et al., 2019). Therefore, a CYP4Z1-expressing HepG2 cell line was generated via lentiviral transduction (**Figure S3.1A**) and membranes prepared from these cells to use as the primary enzyme source for screening. This expression system provided an adequate amount of CYP4Z1, with no detectable enzyme in a control vector cell line, as analyzed by western blot (**Figure S3.1B**). Quantification *via* carbon monoxide-binding spectra (Guengerich et al., 2009) showed that HepG2 membrane preparations contained 1 μM of active CYP4Z1 enzyme (**Figure S3.1D**). To test for CYP4Z1 inhibition, we established a simple, sensitive functional assay using the recently identified CYP4Z1 substrate luciferin-benzyl ether (Yan et al., 2017) (Luc-BE, **Figure 3.1**). Utilization of this probe substrate enabled higher throughput evaluation of inhibitor potency versus the use of more technically cumbersome fatty acid(s) such as laurate and arachidonate (McDonald et al., 2017). Luc-BE turnover to its luminescent metabolite, luciferin, is easily analyzed with Promega's P450 Glo kit. The reaction is NADPH-dependent, turnover is >500-fold higher than background (**Figure 3.2A)** and displays apparent Michaelis-Menten kinetics (**Figure 3.2B**). For determination of half maximal inhibitory concentration (IC_{50}) values for CYP4Z1 inhibition, the probe substrate Luc-BE was used at a concentration equal to the determined K_m (29 μM). To evaluate both the reversible, and time-dependent nature of potential inhibitors, we used a non-dilution (also termed addition) method IC_{50} shift assay (Parkinson et al., 2011; Henne et al., 2012; Kozakai et al., 2014). Typically, if a compound elicits an IC_{50} shift of ≥1.5 it is considered to be a time-dependent inhibitor of the enzyme being evaluated (Grimm et al., 2009).

3.3.2 Design and synthesis of ABT-analogs for CYP4Z1 inhibition

We undertook a targeted design strategy for a CYP4Z1 mechanism-based inhibitor in order to capitalize on potential selectivity benefits. The rationale for increased specificity is based on the following features: i) reversible binding of the inhibitor to the enzyme must be of appropriate affinity, ii) the inhibitor must also serve as a substrate for bioactivation by the target, and iii) the reactive metabolite that is generated requires an active site target to inactivate the enzyme (Ortiz de Montellano, 2005; Hollenberg et al., 2008).

The known inhibitors of CYP4Z1 are promiscuous towards the CYP4 family and other hepatic CYP enzymes (McDonald et al., 2017; Yan et al., 2017). Our preliminary work demonstrated that **ABT**, a mechanism-based pan-CYP inhibitor (Hollenberg et al., 2008; Emoto et al., 2003), displayed significant time-dependent inhibition of CYP4Z1. Thus, **ABT** appeared to offer a promising bioactivatable pharmacophore, and our data agreed with prior research, which indicated that **ABT** effectively inactivates AA-oxidizing CYPs (Ortiz de Montellano, 2018). Additionally, there was already considerable precedent for exploration of ABT-analogs, as prior studies have characterized *N*-benzyl-aminobenzotriazole, *N*-α-methylbenzyl-aminobenzotriazole, and *N*-α-ethylbenzyl-aminobenzotriazole as isozyme-selective MBIs of rabbit, guinea pig, and rat CYPs (Mathews and Bend, 1986; 1993; Woodcraft et al., 1990; Kent et al., 1997).

CYP4B1 is the only CYP4 member that has been crystallized (Hsu et al., 2017), therefore, structural inferences that can be made about CYP4Z1 are limited. However, catalytic work with CYP4Z1 provided a useful basis for simple inhibitor design. Unlike most other CYP4 enzymes, CYP4Z1 catalyzes oxidations internally rather than at the ω-terminus (McDonald et al., 2017; Yan et al., 2017; Zollner et al., 2009). In addition to AA metabolism, the internal preference for oxidation is evident for the substrates lauric acid (LA) and Luc-BE (**Figure 3.1**). Therefore, we made simple chemical modifications to the **ABT** scaffold to generate CYP4Z1

inhibitors by adding carbon tails to **ABT** to incorporate structural elements of the known CYP4Z1 substrate, LA. Ideally, we wanted to take advantage of the relatively high mid-chain oxidation rate of LA to 8-hydroxy-LA (V_{max} = ~40 min^{-1}) in the hope that this would translate to CYP4Z1-mediated bioactivation of ABT-analogs. The position of the exocyclic nitrogen that was expected to undergo P450-mediated activation in these new *N*-alkylated **ABT** congeners approximates the internal site of CYP4Z1-dependent metabolism of LA. Moreover, as illustrated by the docking of LA to the recently published CYP4Z1 homology model (McDonald et al., 2017), hydrophilic residues Asn381 and Ser383 are positioned to potentially engage with the free acid moiety of fatty acid substrates. This hypothesis was tested by evaluating ABT-analog inhibitors which contained a terminal carboxylic acid group alongside inhibitors where that moiety had been removed.

Neutral chain analogs were prepared from readily available aliphatic aldehyde building blocks using methodology based on that previously used in the synthesis of *N*-benzyl-aminobenzotriazole (Mathews and Bend, 1986). Acid-containing analogs were synthesized using terminal acid, primary alcohol starting materials and employing PCC-mediated oxidation to generate the aldehyde moiety. Condensation of the aldehyde with **ABT** formed an imine which was then reduced to the target compounds (**Scheme 3.1**).

3.3.3 Evaluation of time-dependent inhibition (TDI) of CYP4Z1 by ABT-analogs

Representative dose-response curves are provided in **Figure 3.3**, which shows the potency comparison between **ABT** and inhibitor **7** (all dose-response curves have been provided in the Supporting Information, **Figure S3.2**). IC_{50} values for all ABT-analogs are shown in **Table 3.1**. **ABT** itself only weakly inhibited CYP4Z1 without a prior pre-incubation with NADPH. However, the addition of aliphatic tails (compounds **1** – **5**) dramatically increased affinity for CYP4Z1 over that of **ABT**, exemplified by a 50-fold decrease in the reversible IC_{50}

value from 154 to 2.9 μM for inhibitor **2**. While **ABT** itself showed a potent time-dependent effect for inhibition of CYP4Z1 (i.e. a 30-minute pre-incubation of NADPH with CYP4Z1 produced a shifted-IC_{50} of 12 μM), inhibitors **2-9** exhibited much lower shifted-IC_{50} values that indicated up to 120-fold higher potency compared to **ABT**.

Analysis of the terminal acid-containing analogs showed similar gains in affinity over **ABT** itself for CYP4Z1 inhibition. The most potent congeners, **7** and **8 (**with eight and ten carbon tails respectively), exhibited shifted-IC_{50} values of 200 nM, *i.e.* a 60-fold increase in potency over **ABT**. Interestingly, the addition of the acid moiety did not have a dramatic effect on CYP4Z1 inhibition potency (neither affinity nor inactivation) compared to the neutral-chain aliphatic variants. However, the benefits of adding a terminal acid group became apparent as counter-screening proceeded as described below. Finally, despite changes in apparent potencies for reversible and time-dependent inhibition across the entire analog series, the shift ratios (IC_{50} / Shifted-IC_{50}) varied only from 13 – 30 (omission of **3** narrowed this range to 23 – 30), which seems consistent with all inhibitors inactivating CYP4Z1 via a common mechanism.

3.3.4 Counter-screening against CYP4 family enzymes

Due to the complex nature of the role that fatty acid metabolites play in signaling in both healthy and disease states (Edson and Rettie, 2013; Johnson et al., 2015), non-specific CYP4Z1 inhibitors such as **ABT** (Yan et al., 2017; Ortiz de Montellano, 2018) and HET0016 (Yu et al., 2012; McDonald et al., 2017; Miyata et al., 2001; Nakamura et al., 2003) do not provide adequately discriminatory molecular tools with which to assess the physiological role of CYP4Z1. Consequently, we next evaluated the selectivity of the new ABT-analogs against recombinantly-expressed, and commercially available, CYP4 enzymes; CYP4A11, -4F2, -4F3a, -4F3b, and -4F12. As it is not commercially available, but was still of interest to us, CYP4F8 was expressed in HepG2 cells and membranes were prepared identically to that for CYP4Z1. Pro-

luciferin probe substrates at concentrations ≤ K_m (see Experimental Section) were used for all CYP4 isozymes to determine inhibition, including CYP4F8 (as elucidated from in-house testing, **Figure S3.8**), an isozyme in which limited substrate information has been published. A TDI assay at a single, moderate, concentration of 30 μM was utilized in order to assess whether any analogs significantly inhibited the off-target enzymes. A 30-minute enzyme/NADPH pre-incubation step was used to assess time-dependent effects (akin to a full IC_{50}-shift assay), which were modest for all enzymes and analogs tested (**Figure 3.4**). Initial screening against off-target CYP4 isozymes was performed with inhibitors **2 – 9** (inhibitor **1** was excluded due to its low potency). The alkyl-modified analogs **2** – **5** inhibited CYP4F2, CYP4F3a and b and CYP4F12 substantially, whereas the acid modified analogs containing 10 and 12 carbon tails, **8** and **9**, respectively, substantially inhibited CYP4A11, CYP4F8 and 4F12. Importantly, however, two acid analogs **6** and **7** exhibited negligible or very low activity towards the CYP4 enzymes tested and were therefore selected for further study.

3.3.5 Evaluation of TDI for inhibitors 6 and 7 against off-target CYP isozymes

Full IC_{50}-shift assays (**Figures S3.3, S3.4**) were performed with **6** and **7** to thoroughly assess off-target inhibition towards the other recombinantly-expressed CYP4 enzymes (**Table 3.2**). As determined from the specificity ratios (off-target CYP IC_{50} / CYP4Z1 IC_{50}), both **6** and **7** were comparatively poor reversible inhibitors of these isozymes compared to CYP4Z1. Relatively small shift ratios (~1-3) were obtained for both inhibitors against the six CYP4 isozymes tested, indicating low propensity of **6** and **7** for enzyme-mediated bioactivation. Of note, any shift values <1 (indicative of inhibitors with lowered potency after a plus NADPH pre-incubation) likely result from significant metabolism of the inhibitor by the CYP to non-bioreactive species. The contrasting reactivity of **6** and **7** between these off-target isozymes and CYP4Z1 is readily apparent from the resultant TDI specificity ratios (off-target CYP shifted-IC_{50} /

CYP4Z1 shifted-IC_{50}) that ranged from 137 to 2235. Therefore, CYP4Z1 selectivity becomes greatly enhanced as the result of TDI for these two inhibitors.

Overall, inhibitor **7** possessed a higher degree of selectivity for CYP4Z1 than **6.** Additionally, although **7** showed relatively similar affinity across the off-target CYP4 isozymes, only CYP4F8 and CYP4F12 were well above the significance threshold for TDI (i.e. shift ratio $\geq$ 1.5). This indicates that these two enzymes are more likely to bind **7** in a position which leads directly to bioactivation. We suggest that this is the result of structural similarities with CYP4Z1 that are not present in the other CYP4 enzymes tested, namely, a lack of the active site glutamate residue necessary to form a covalent attachment with the heme (McDonald et al., 2017). The recent publication on the crystal structure of octane-bound CYP4B1, an ω-hydroxylase with a covalently attached heme, showed that this structural element is an important determinant of the enzyme's (and most likely other similar CYP4 isozymes) regio-specificity for oxidation at the terminal position of alkyl-chain containing substrates (Hsu et al., 2017). Indeed, both CYP4F8 and CYP4F12 enzymes, neither of which possess a covalently attached heme, primarily produce an internal ω-3-hydroxylated AA metabolite, 18-HETE (Bylund et al., 2000; 2001), and thus seem to more closely mimic CYP4Z1 than the 20-HETE producing CYP4 family members. However, although the shift ratios pass the threshold of significance for these two isozymes, they are ~10-fold lower than the shift ratio observed for **7** and CYP4Z1. This results in CYP4F8 and CYP4F12 being inhibited 285-fold and 230-fold less, respectively, than CYP4Z1 after a pre-incubation with cofactor. We speculate that this observation reflects the fact that 18-HETE is still three to four C-C bond lengths away from the major site of CYP4Z1-mediated AA metabolism, and thus bioactivation of **7** is limited for CYP4F8 and CYP4F12 because the exocyclic nitrogen for this analog is not positioned optimally for these two isozymes.

Full IC_{50}-shift assays were also performed with **6** and **7** to evaluate off-target inhibition towards hepatic CYP isozymes (**Figures S3.5, S3.6**), chosen based on the seven FDA recommended CYPs for drug-drug interaction (DDI) testing (U.S. Food & Drug Administration). Human liver microsomes (HLM) served as the enzyme source and a cocktail method was employed to evaluate inhibition of CYP1A2, -2B6, -2C8, -2C9, -2C19, -2D6, and -3A4/5 concurrently (**Table 3.3**). Of note, in-house testing for inhibition, using isozyme-specific inhibitor probes, of metabolism by the seven hepatic CYPs in the cocktail assays yielded data in agreement with that reported in the literature (Li et al., 2015) (**Figure S3.9**). Similar to the results obtained with the CYP4 isozymes, inhibitors **6** and **7** did not potently inhibit off-target hepatic CYPs, either reversibly or irreversibly, with specificity and TDI specificity ratios spanning 23 – 140 and 134 – 1650, respectively. For both inhibitors, the largest shift ratios were observed for CYP1A2, at 12.2 and 11.2 for **6** and **7**, respectively. The large degree of bioactivation observed may be explained by CYP1A2, like CYP4Z1, having a propensity, itself, for internal oxidation of PUFAs. The 14,15-EET synthase activity for CYP1A2 has been reported to be ~0.54 pmol/pmol/min (at 50 μM AA) (Fer et al., 2008; Kaspera and Totah, 2009), and is in a similar range to that observed for CYP4Z1 of 1.9 pmol/pmol/min (at 75 μM AA) (McDonald et al., 2017). Furthermore, all seven of the hepatic CYP isozymes that we analyzed have been shown previously to metabolize AA to 14,15-EET, albeit with a large range of efficiencies and regio-specificities (Kaspera and Totah, 2009). Although for most AA-metabolizing CYPs their role in breast cancer progression is largely unknown, CYP3A4 expression has been specifically linked to decreased survival and is required for growth in several breast cancer cell lines (Mitra et al., 2011). Therefore, the low off-target inhibition of the generally liver-localized CYPs studied herein was a desired trait for both broad selectivity purposes and will also allow for discriminatory probing of the role of CYP4Z1-dependent epoxygenase activity in a breast cancer setting. Overall, both inhibitors **6** and **7** demonstrated their lack of activity towards off-target enzymes

primarily through low rates of bioactivation that resulted in modest time-dependent inhibition and high TDI specificity ratios. Due to its combined properties of high potency and excellent selectivity for CYP4Z1, inhibitor **7** was chosen for in-depth characterization as an MBI.

3.3.6 Characterization of mechanism-based inactivation of CYP4Z1 by 7

Mechanism-based inactivation is typically viewed as a characteristic to be designed away from in drug development, as the enzymes affected by this process are frequently off-target CYPs. When this occurs, DDIs are common liabilities as these off-target enzymes are rendered catalytically incompetent and must then be newly biosynthesized. However, numerous irreversible inhibitors (including MBIs) have emerged recently as therapeutics and have the benefits of increased biochemical efficiency, a longer duration of action, efficient inactivation of the target, and the potential to avoid some resistance mechanisms (Johnson et al., 2010). Examples of CYP MBI drugs include some aromatase (CYP19A) inhibitors that have shown efficacy in the clinic and are currently used for breast cancer treatment; an example being the steroidal mimetic exemestane (Brueggemeier et al., 2005). Evaluating the characteristics of an MBI (not simply establishing TDI) enables insight into inhibitor structure-activity relationships, mechanisms of action, guides future analog work, and provides a better understanding of the biochemistry of the target CYP. Therefore, the action of inhibitor **7** towards CYP4Z1 was considered in light of the Silverman criteria for an MBI (Silverman, 1988).

As seen in **Figure 3.5A**, **7** displayed concentration- and time-dependent loss of enzyme activity, as first indicated by the single time point assays described above. When the values for k_{obs} were plotted against concentrations of **7**, a K_I = 2.2 μM and a k_{inact} = 0.15 min^{-1} (**Figure 3.5B**) were determined; the observed maximal rate of inactivation indicating saturation kinetics. Comparison with exemestane, where a k_{inact} for aromatase inhibition of 0.05 min^{-1} has been determined, emphasizes how rapidly **7** inactivates CYP4Z1, although it must be noted that

exemestane inactivation of aromatase is highly efficient due to its tight-binding affinity (K_I = 26 nM) for the enzyme (Giudici et al., 1988). In order to show irreversibility of mechanism-based inactivation, we assessed the fraction of activity remaining, from CYP4Z1 treated with **7**, before and after overnight dialysis to remove excess inhibitor (**Figure 3.5C**). No increased activity was observed after dialysis, indicating irreversible enzyme destruction. Multiple experiments confirmed the necessity of a catalytic step for the time-dependent inhibition of CYP4Z1 by **7**. This is directly shown in the dialysis experiment where lack of a pre-incubation step with the NADPH cofactor prior to the substrate turnover reaction resulted in no inactivation of the enzyme. The addition of hard or soft nucleophiles, at commonly used concentrations for reactive intermediate trapping experiments (Sodhi et al., 2017) – glutathione (GSH), *N*-acetyl lysine (NAL), methoxyamine ($MeONH_2$), *N*-acetyl cysteine (NAC), semicarbazide (Semicarb.), potassium cyanide (KCN) – did not abrogate inactivation of CYP4Z1 by **7** (**Figure 3.5D**). Additionally, the presence of the reactive oxygen species scavenging enzymes, catalase (CAT) and superoxide dismutase (SOD), did not rescue CYP4Z1 activity, eliminating the possibility of non-specific, and non-enzymatic, oxidation reactions causing inactivation of CYP4Z1. These data indicate that inactivation of CYP4Z1 occurs prior to release of bioactivated **7** from the active site.

Next, the partition ratio for inactivation of CYP4Z1 by **7** was determined (**Figure 3.5E**). As a measure of efficiency, the partition ratio is the number of latent inactivator molecules converted and released as a product relative to each catalytic cycle resulting in enzyme inactivation (Silverman, 1988; Wang and Walsh, 1978). Partition ratios for MBIs of CYPs can span a large range, with values reported from 1 to >5000 (Lim et al., 2005). Therefore, the partition ratio of 14 for **7** lies towards the efficient end of this spectrum.

3.3.7 Interrogation of heme adducts from CYP4Z1 inactivation by 7

The mechanism for the inactivation of CYP enzymes by **ABT** has been studied extensively by multiple groups. The canonical pathway that has been proposed consists of sequential H-abstraction from the exocyclic nitrogen, followed by loss of molecular nitrogen, resulting in the formation of benzyne. This reactive species then adds across the heme cofactor of CYPs to form a detectable *N,N*-bridged dialkylated protoporphyrin IX derivative (Ortiz de Montellano, 2018). One of the ABT-analogs previously mentioned, benzylaminobenzotriazole (BBT), has been shown to inactivate rabbit lung CYP enzymes with identical formation of the porphyrin adduct as that seen with **ABT** (Mathews and Bend, 1986). Interestingly, in a study by Kent and coworkers, BBT also exhibited MBI of CYP2B1, but mainly by covalently binding to an unidentified amino acid residue, with only minor heme alkylation (Kent et al., 1997).

Using methodology optimized by Pelletier (unpublished, 2020), we observed that CYP4Z1-dependent metabolism of **ABT** produces the aforementioned *N,N*-dialkylated protoporphyrin IX. The adduct was CYP4Z1/NADPH-dependent and was confirmed through both accurate mass analysis (δ ppm < 1.0) and MS/MS spectra. However, we were unable to detect this adduct in a CYP4Z1 incubation with inhibitor **7** (**Figure 3.6**). Therefore, the increased potency observed for **7** in comparison to **ABT** is due to both improved affinity and a different mechanism for CYP4Z1 inactivation. Analysis of the IC_{50}-shift ratios between **ABT** and **7**, which are 13 and 30, respectively, suggests that the rate of CYP4Z1 inactivation becomes elevated through modification of the exocyclic nitrogen. Prior to this heme analysis experiment it was unknown if the relative inactivation rate increase was due to augmented benzyne formation or if a different reactive species was generated, clearly that question has been answered. However, the issue of whether the mechanism differs due to an undetected heme adduct, heme destruction, or covalent modification of the apoprotein remains to be answered. *In silico* studies to probe the mechanism of CYP inactivation by BBT suggested a sequential pathway that involves an imine intermediate, followed by either cleavage to an aldehyde and a nitrene

species or the formation of a reactive oxaziridine moiety (Chuanprasit et al., 2015). It is tempting to suggest that an oxaziridine metabolite is responsible for the observed covalent binding of BBT to the apoprotein of CYP2B1.

In our own *in vitro* studies, we did observe the CYP4Z1-dependent formation of an analogous imine, as confirmed through LC-MS/MS comparisons to the intermediate generated in the synthesis of **7** (data not shown). Unfortunately, incubations with numerous exogenously added nucleophiles (outlined above for other experiments) yielded no detectable trapped adducts that would have helped to infer the identity of reactive metabolites generated by CYP4Z1. Whether the formation of an imine followed by further bioactivation characterizes the inactivation mechanism for this MBI – enzyme tandem is unknown at this time. This, and other proposed pathways for the inactivation of CYP4Z1 by **7** are presented in **Figure 3.7**.

3.3.8 Inhibition of CYP4Z1 AA metabolism in T47D cells by 7

We next evaluated the inhibition of CYP4Z1-dependent metabolism of AA in breast cancer derived T47D cells (Holliday and Speirs, 2011). Although a low level of CYP4Z1 mRNA is detectable in breast cancer cell lines, which may be induced ~15-fold from dexamethasone treatment (Savas et al., 2005), immortalization appears to eliminate expression of endogenous CYP4Z1 (Yu et al., 2012). Therefore, T47D cells were modified to constitutively express CYP4Z1 (T47D-CYP4Z1) using a recombinant lentivirus. Western blot analysis showed ample CYP4Z1 expression in the CYP4Z1-T47D cells and no observable endogenous CYP4Z1 expression in the Vector-T47D cells (**Figure S3.1C**). Concentrations of free AA in human plasma span a wide range, from 2.7 to 50 μM (Nishikiori et al., 2015; Wang et al., 2015). Therefore, a 50 μM dose of AA was used to reflect this upper boundary. The previously characterized CYP4Z1 metabolites of AA, 19-HETE and 14,15-EET, along with the metabolite commonly generated by other CYP4 isozymes, 20-HETE, were monitored (McDonald et al.,

2017). Also included in the AA metabolite profile was the degradation product 14,15-dihydroxy eicosatrienoic acid (14,15-DiHET), as this could be generated by 14,15-EET hydrolysis both non-enzymatically, in the tissue culture environment, and enzymatically through the action of epoxide hydrolases potentially present in T47D cells (Kaspera and Totah, 2009; Decker et al., 2012).

The T47D-CYP4Z1 cells were exposed to **7**, incorporating a 24-hour inhibitor pre-incubation step prior to introduction of substrate, to assess TDI. At 3 μM, potent inhibition of AA metabolism was observed (**Figure 3.8**). Comparing peak area ratios (PAR), of metabolites divided by their respective deuterated internal standards, showed that production of 14,15-EET, 19-HETE, and 14,15-DiHET was inhibited 83, 86, and 80%, respectively. When inhibitor and substrate were administered together to T47D-CYP4Z1 cells, without a pre-incubation step, 3 μM of **7** produced lower levels of inhibition against production of 14,15-EET, 19-HETE, and 14,15-DiHET, (**Table 3.6**), as expected. When dosed at 1 μM, a comparable time-dependent effect was observed with a ~2-fold decrease in potency. Similar results were also attained when investigating AA metabolism in CYP4Z1-HepG2 membranes, where a time-dependent, ~90% loss in CYP4Z1 activity (**Figure S3.10)** was observed with inhibitor **7** utilized at 3 μM**.**

Finally, we confirmed the preference for CYP4Z1-mediated 14,15-EET production over that of 20-HETE (only a trace amount was detected, slightly above lower limit of detection) in a mammalian whole cell setting. Although other internal oxidation products from CYP4Z1 AA metabolism were observed in both the HepG2 membranes and T47D cells (decreasing proportionally with inhibitor and tentatively identified as 15-, 16-, 17-, and 18-HETE), these apparently minor metabolites were not characterized further here.

These data demonstrate the efficacy of inhibitor **7** in a whole cell environment, and are comparable to results we obtained for the inhibition of CYP4Z1-mediated Luc-BE *O*-

debenzylation in HepG2 cells (**Figure S3.11A**). Therefore, although not tested directly, potentially lower inhibitor permeability and stability in whole cells appear not to be major issues. Additionally, these results are not confounded by possible cytotoxicity of inhibitor **7**, as a 3 μM treatment did not cause noticeable changes in viability 24 hours later for any of the cell lines assayed (**Figure S3.11B**). Although we hypothesize **7** to have anti-proliferative effects against breast cancer cells expressing CYP4Z1, the specific conditions required to capture this effect (e.g. temporal, growth factor, and PUFA substrate variables) were not assessed here as it was beyond the scope of this study. To our knowledge, no studies utilizing primary cells have been performed to interrogate CYP4Z1. However, due to its effectiveness in a breast-cancer derived cell line for inhibiting the generation of the pro-angiogenic and pro-proliferative metabolite 14,15-EET, we posit that inhibitor **7** will be an effective molecular tool to probe the druggability of CYP4Z1 as a target for breast cancer therapy in varied *in vitro* settings.

3.4 Conclusion

In summary, we leveraged our knowledge of the product selectivity of CYP4Z1 to generate ABT-analogs that are efficient time-dependent inhibitors of the enzyme with substantially increased potency over **ABT**. The design strategy of incorporating a terminal acid to produce fatty acid mimetics resulted in high selectivity for CYP4Z1 for two analogs, **6** and **7**. Further characterization, monitoring isozyme-specific inhibition in a large panel of off-target CYPs, identified **7** as the inhibitor with the best combination of isozyme selectivity and potency. **7** was further characterized as a relatively efficient mechanism-based inhibitor (k_{inact}/K_i = 0.07 $min^{-1}\mu M^{-1}$), possessing an inactivating mechanism distinct from **ABT,** and with demonstrated time-dependent inhibition of CYP4Z1 in transfected breast cancer-derived whole cells.

Future studies will continue to investigate the mechanism of CYP4Z1 inactivation by **7** through further heme/apoprotein-adduct analysis. These first-generation inhibitors are potentially useful lead compounds for the development of more potent CYP4Z1 inhibitors with appropriate pharmacokinetic features to support *in vivo* studies and potential clinical applicability.

Abbreviations

CYP4Z1, cytochrome P450 4Z1; KPi, potassium phosphate buffer; **ABT**, 1-aminobenzotriazole; Luc-BE, luciferin-benzyl ether; NADPH, Reduced β-nicotinamide-adenine dinucleotide phosphate; MBI, mechanism-based inhibitor; TDI, time-dependent inhibition; IC_{50}, half maximal inhibitory concentration; AA, arachidonic acid; LA, lauric acid; 14,15-EET, 14,15-epoxyeicosatrienoic acid; 20-HETE, 20-hydroxyeicosatetraenoic acid; PUFA, polyunsaturated fatty acid; CAT, catalase; SOD, super oxide dismutase; GSH, glutathione; NAL, *N*-acetyl lysine; $MeONH_2$, methoxyamine; NAC, *N*-acetyl cysteine; KCN, potassium cyanide

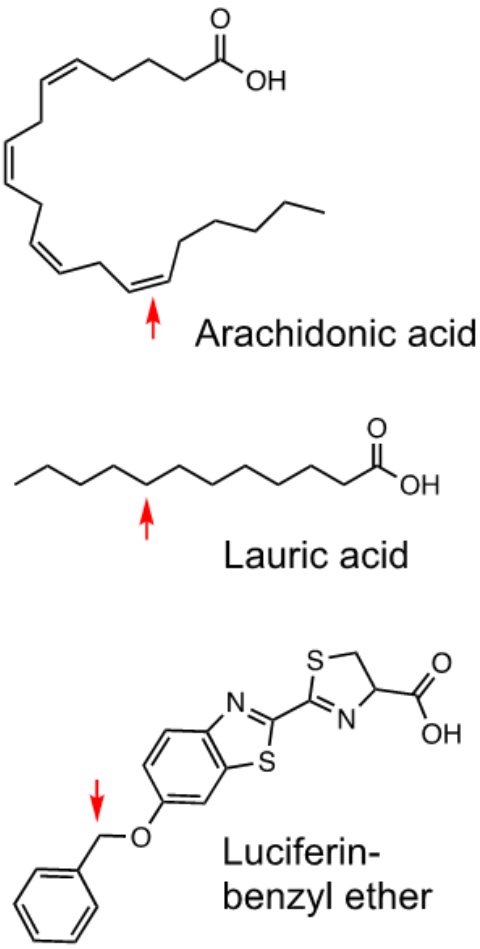

Figure 3.1. CYP4Z1 metabolizes substrates internally. The primary oxidation positions for substrates arachidonic acid (AA), lauric acid (LA), and luciferin-benzyl ether (Luc-BE) are denoted by the red arrows, generating products 14,15-epoxyeicosatrienoic acid (14,15-EET), 8-hydroxy LA, and luciferin (*via* *O*-dealkylation), respectively (McDonald et al., 2017; Yan et al., 2017; Zollner et al., 2009).

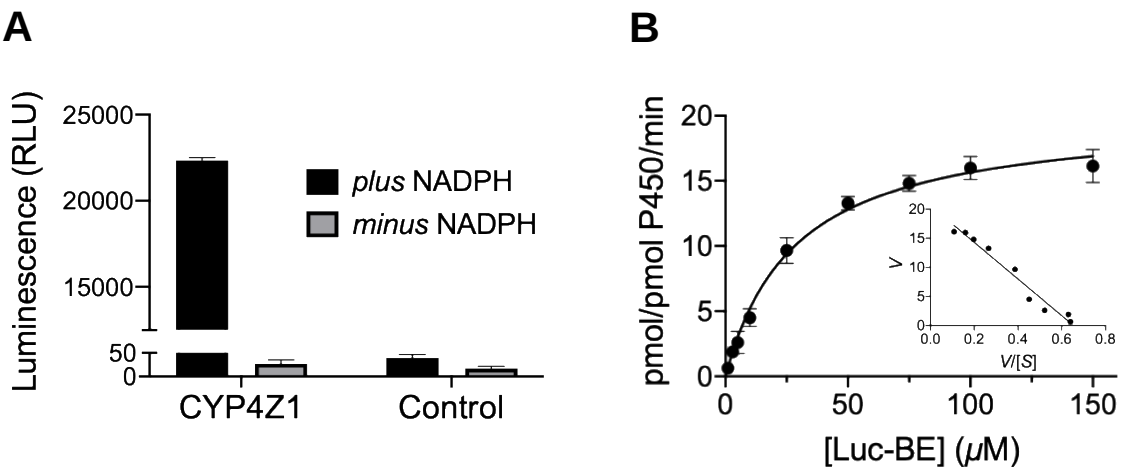

Figure 3.2. Probe substrate Luc-BE metabolism in the HepG2 membranes is both CYP4Z1- and NADPH-dependent (**A**)**.** CYP4Z1-HepG2 membrane metabolism of Luc-BE displays Michaelis-Menten kinetics at the substrate concentrations tested, with a K_m = 29 μM and a V_{max} = 20 pmol/pmol CYP4Z1/min; the Eadie-Hofstee plot (inset) shows apparent linearity (**B**)**.** Shown is the average ± SD from at least three replicates.

Scheme 3.1. Synthesis of ABT-Analogs[a]

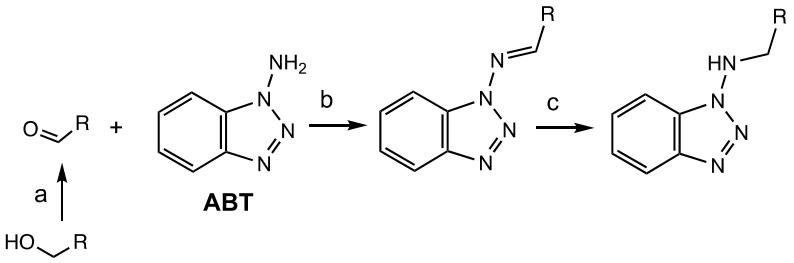

ID	R =
1	propyl
2	pentyl
3	heptyl
4	nonyl
5	undecyl
6	pentanoic acid
7	heptanoic acid
8	nonanoic acid
9	undecanoic acid

[a]Reagents and conditions: (a) celite, PCC, CH_2Cl_2, RT, 1 h, 21-25%, (analogs **6-9**); (b) acetic acid, RT, 18 h, 43-89%; (c) $NaBH_4$, CH_2Cl_2, MeOH, RT, 2 h, 56-84%

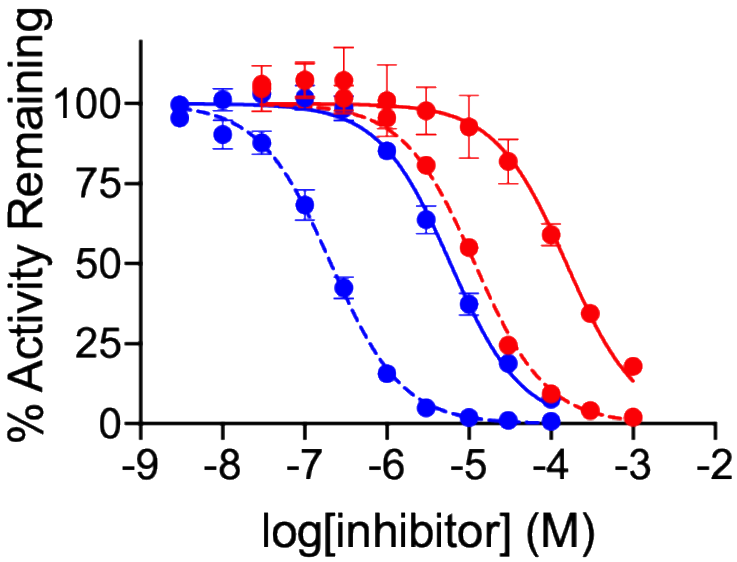

Figure 3.3. Time-dependent inhibition of CYP4Z1-mediated Luc-BE *O*-debenzylation by **ABT** (red) and inhibitor **7** (blue). Shown is percent activity remaining versus inhibitor concentration, with (dashed lines) and without (solid lines) the presence of NADPH in a pre-incubation step. The ABT-analog **7** exhibited gains in affinity and rate of enzyme inactivation for CYP4Z1 compared to the parent compound. IC_{50} values are reported in **Table 1**. Shown is the average ± SD from three independent experiments.

Table 3.1. IC_{50} and shifted-IC_{50} values for the inhibition of CYP4Z1-mediated Luc-BE *O*-debenzylation by ABT and analogs

Inhibitor	IC_{50} ± SD (μM)	Shifted-IC_{50} ± SD (μM)	Shift Ratio[a]
ABT	154 ± 23	12 ± 0.8	13
1	19 ± 2.6	0.7 ± 0.06	27
2	2.9 ± 0.1	0.1 ± 0.01	30
3	4.9 ± 0.3	0.4 ± 0.05	13
4	12 ± 1.6	0.5 ± 0.05	24
5	46 ± 10	1.4 ± 0.4	32
6	41 ± 2.4	1.7 ± 0.06	24
7	5.9 ± 0.9	0.2 ± 0.04	30
8	4.5 ± 0.4	0.2 ± 0.02	23
9	7.2 ± 0.5	0.3 ± 0.02	24

[a] IC_{50} / Shifted-IC_{50}

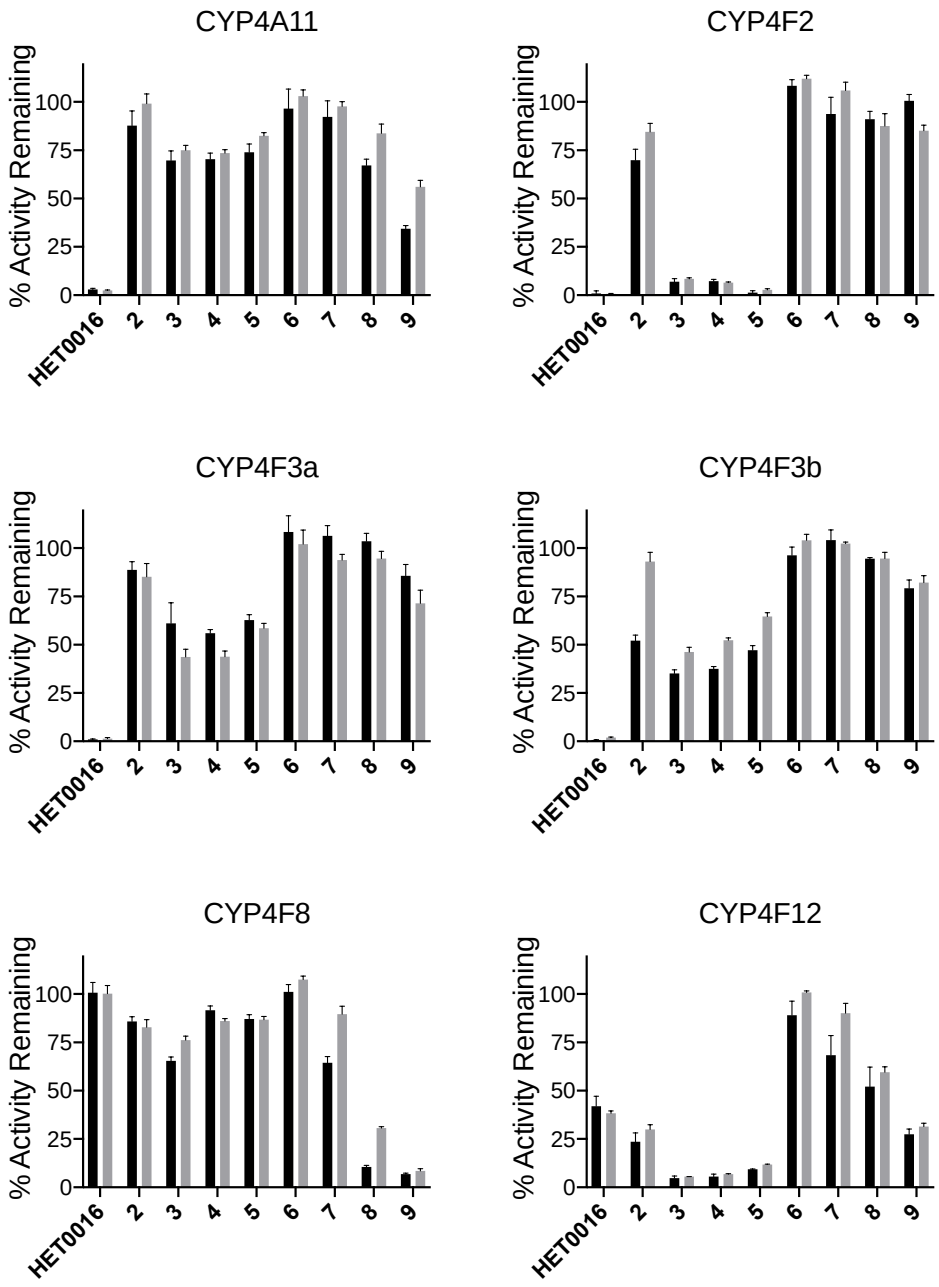

Figure 3.4. Time-dependent inhibition of CYP4A11-mediated Luc-4A *O*-demethylation, CYP4F2-, CYP4F3a-, CYP4F3b-mediated Luc-4F2/3 *O*-(4-methylthio)-debenzylation, and CYP4F8-, CYP4F12-mediated Luc-BE *O*-debenzylation by ABT-analogs screened at 30 µM. The pan-CYP4 inhibitor HET0016 was dosed at 0.5 µM as an inhibition control. All probe substrates were used at concentrations ≤ K_m. All enzymes were recombinantly expressed in insect cells (Supersomes™), except for CYP4F8 which was recombinantly expressed in HepG2 cells. The black and grey bars show the percent activity remaining when the inhibitor was pre-incubated for 30 minutes with enzyme plus and minus NADPH, respectively. Shown is the average ± SD from three replicates.

Table 3.2. IC_{50} and shifted-IC_{50} values for inhibition of CYP4-mediated pro-luciferin metabolism by inhibitors 6 and 7

CYP	Inhibitor	IC_{50} ± SD (μM)	Shifted-IC_{50} ± SD (μM)	Shift Ratio[a]	Specificity Ratio[b]	TDI Specificity Ratio[c]
4A11	**6**	1330 ± 134	455 ± 20	2.9	32	268
	7	282 ± 15	179 ± 51	1.6	48	895
4F2	**6**	1130 ± 114	647 ± 83	1.7	28	381
	7	212 ± 15	221 ± 36	1.0	36	1105
4F3a	**6**	1240 ± 40	1370 ± 198	0.9	30	808
	7	264 ± 31	447 ± 75	0.6	45	2235
4F3b	**6**	1520 ± 191	1690 ± 185	0.9	37	991
	7	187 ± 6	213 ± 46	0.9	32	1065
4F8	**6**	1180 ± 137	778 ± 53	1.5	29	458
	7	167 ± 23	57 ± 13	2.9	28	285
4F12	**6**	380 ± 39	233 ± 11	1.6	9	137
	7	91 ± 17	46 ± 8	2.0	15	230

[a] IC_{50} / Shifted-IC_{50}

[b] Off-target CYP IC_{50} / CYP4Z1 IC_{50}

[c] Off-target CYP Shifted-IC_{50} / CYP4Z1 Shifted-IC_{50}

Table 3.3. IC_{50} and shifted-IC_{50} values for inhibition of hepatic CYP-mediated substrate cocktail metabolism by inhibitors 6 and 7

CYP	Inhibitor	IC_{50} ± SD (μM)	Shifted-IC_{50} ± SD (μM)	Shift Ratio[a]	Specificity Ratio[b]	TDI Specificity Ratio[c]
1A2	**6**	2790 ± 272	228 ± 18	12.2	68	134
	7	614 ± 117	55 ± 8	11.2	104	275
2B6	**6**	923 ± 152	258 ± 28	3.6	23	152
	7	257 ± 68	62 ± 21	4.1	44	310
2C8	**6**	2310 ± 71	954 ± 31	2.4	56	561
	7	306 ± 44	84 ± 16	3.6	52	420
2C9	**6**	>3000	1940 ± 56	>1.5	>73	1141
	7	343 ± 88	330 ± 41	1.0	58	1650
2C19	**6**	>3000	1640 ± 189	>1.8	>73	965
	7	759 ± 138	246 ± 62	3.1	129	1230
2D6	**6**	2850 ± 404	1710 ± 107	1.7	70	1006
	7	826 ± 177	299 ± 86	2.8	140	1495
3A4/5	**6**	1310 ± 172	766 ± 29	1.7	32	451
	7	244 ± 8	128 ± 10	1.9	41	640

[a] IC_{50} / Shifted-IC_{50}

[b] Off-target CYP IC_{50} / CYP4Z1 IC_{50}

[c] Off-target CYP Shifted-IC_{50} / CYP4Z1 Shifted-IC_{50}

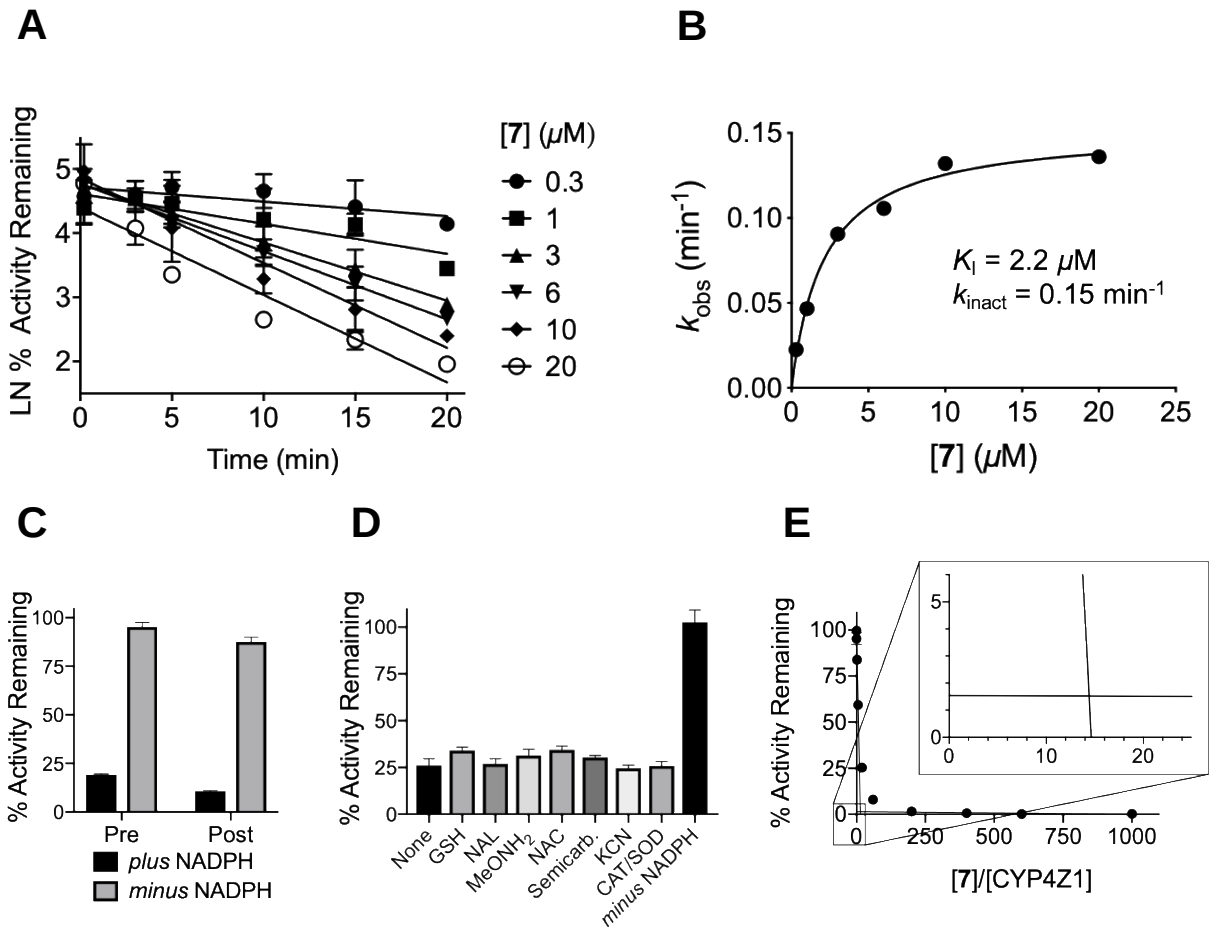

Figure 3.5. Characterization of mechanism-based inactivation of CYP4Z1 by **7**. Time- and concentration-dependent loss of CYP4Z1-mediated Luc-BE *O*-debenzylation activity from treatment with **7**, K_I = 2.2 μM, k_{inact} = 0.15 min^{-1} (**A, B**). The percent of CYP4Z1 activity remaining when inhibitor **7** was pre-incubated with enzyme plus (black bars) and minus (grey bars) NADPH was assessed both prior to (Pre) and after (Post) overnight dialysis. The TDI of CYP4Z1 was not affected by this dialysis step (**C**). The percent of CYP4Z1 activity remaining when inhibitor **7** was pre-incubated with enzyme plus NADPH was assessed with the following nucleophilic additives: glutathione (GSH), *N*-acetyl-lysine (NAL), methoxyamine ($MeONH_2$), *N*-acetyl-cysteine (NAC), and semicarbazide (semicarb.) at 5 mM and potassium cyanide (KCN) at 1 mM. Inclusion of these trapping agents did not significantly abrogate TDI of CYP4Z1 by **7**. Similarly, addition of the reactive oxygen-scavenging enzymes catalase (CAT) and superoxide dismutase (SOD) did not affect TDI of CYP4Z1 by **7** (**D**). In both (**C**) and (**D**) the minus NADPH sample controls exhibit cofactor dependency for the bioactivation reaction. A plot of the percent of CYP4Z1 activity, when inhibitor **7** was pre-incubated with enzyme plus NADPH, versus the concentration ratio of **7**/CYP4Z1 was used to determine the number of inactivator molecules converted and released as a product relative to each inactivation event. Extrapolation of the initial linear portion of the plot to the x-intercept (inset) shows a turnover number of 15, resulting in a partition ratio of ~14 (**E**)**.** For all assays, data shown is the average ± SD from three replicates.

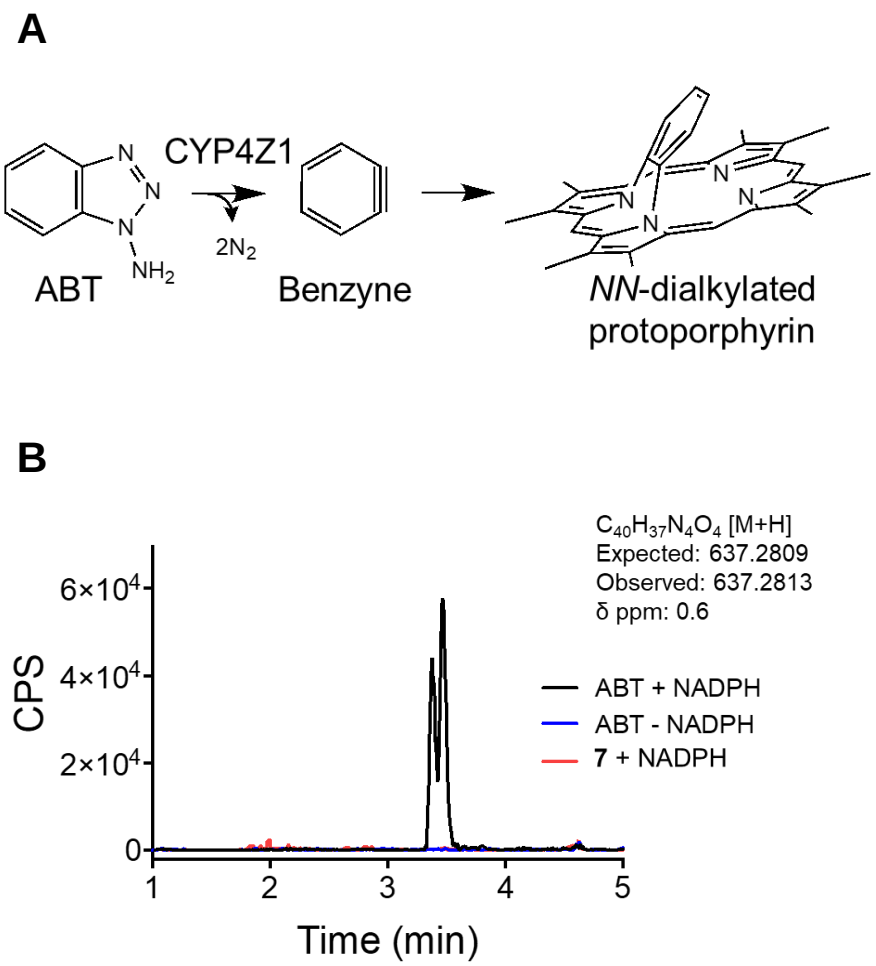

Figure 3.6. CYP4Z1-mediated bioactivation of **ABT** and **7**. The formation of benzyne and structure of the expected, and detectable adduct (**A**). Mass spectrometry confirmation of the *N,N*-dialkylated porphyrin adduct resulting from CYP4Z1-mediated bioactivation of **ABT**; note the NADPH cofactor dependence**.** The split peak suggests the formation of multiple adduct regioisomers. CYP4Z1-mediated bioactivation of **7** did not result in the formation of this adduct (**B**).

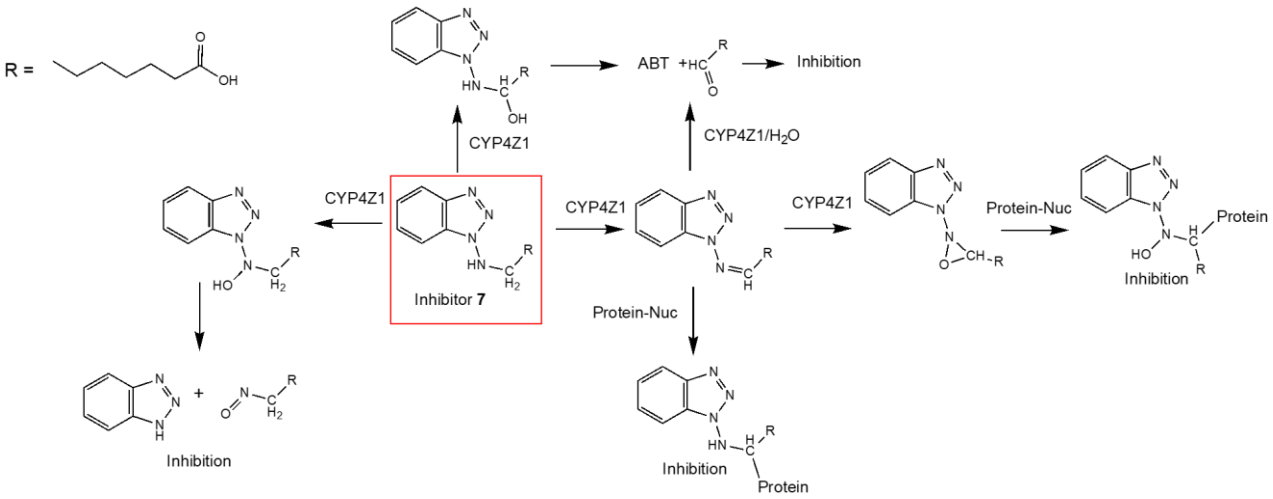

Figure 3.7. Potential pathways for CYP4Z1 inactivation from **7.**

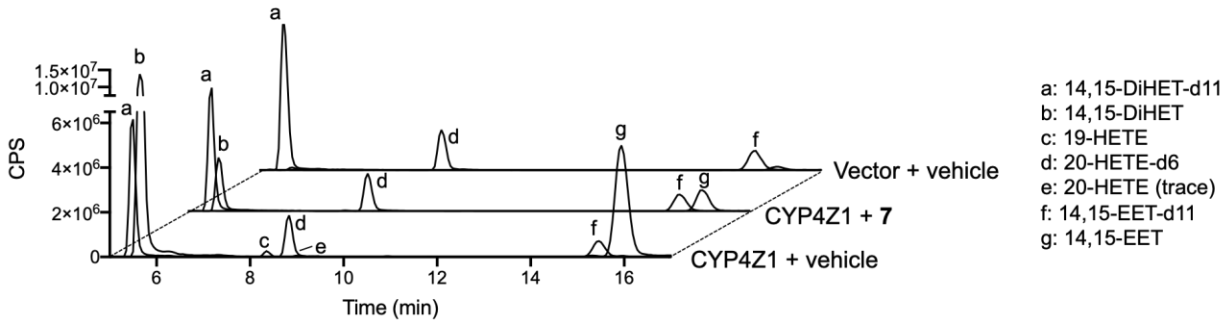

Figure 3.8. Inhibition of CYP4Z1-mediated AA metabolism in T47D whole cells by **7**. LC-MS/MS chromatograms showing the AA metabolite profile from CYP4Z1-T47D cells treated with DMSO vehicle (bottom trace) or inhibitor **7** (middle trace), and Vector-T47D cells treated with vehicle (top trace). Cells were treated with 3 μM of **7**, or vehicle, and underwent a 24-hour pre-incubation prior to addition of 50 μM AA, which was followed by a 2-hour incubation for substrate metabolism. This resulted in 14,15-EET, 19-HETE, and 14,15-DiHET metabolite formation being inhibited 83, 86, and 80%, respectively, as compared to vehicle treated CYP4Z1-T47D cells. Vector-T47D cells dosed with vehicle and 50 μM AA showed a minimal amount of background AA metabolism.

Table 3.4. Inhibition of AA metabolite formation in CYP4Z1-T47D cells by 7

[**7**] (μM)	14,15-EET		19-HETE		14,15-DiHET	
	minus[a]	*plus*[b]	*minus*	*plus*	*minus*	*plus*
1	47%	70%	41%	73%	25%	59%
3	56%	83%	55%	86%	42%	80%

[a] *Minus* pre-incubation with **7**
[b] *Plus* 24-hour pre-incubation with **7**

3.5 Supporting information

CYP4Z1 expression systems; Method for Membrane Preparation; IC_{50} and shifted-IC_{50} determination for inhibition of CYP4Z1 by **1** – **9**; IC_{50} and shifted-IC_{50} determination for inhibition of CYP4 isoforms by **6**; IC_{50} and shifted-IC_{50} determination for inhibition of CYP4 isoforms by **7**; IC_{50} and shifted-IC_{50} determination for inhibition of hepatic CYP isoforms by **6**; IC_{50} and shifted-IC_{50} determination for inhibition of hepatic CYP isoforms by **7**; Luc-4F2/3 metabolism kinetics for CYP4F2, CYP4F3a, and CYP4F3b; Analysis of CYP4F8 metabolism of pro-luciferins; Internal validation of HLM cocktail inhibition assay; Inhibition of CYP4Z1-mediated AA Metabolism by **7** in HepG2 Membranes; Inhibition of CYP4Z1 in HepG2 Cells and HepG2, T47D Cell Viability; ^{1}H and ^{13}C NMR Spectra

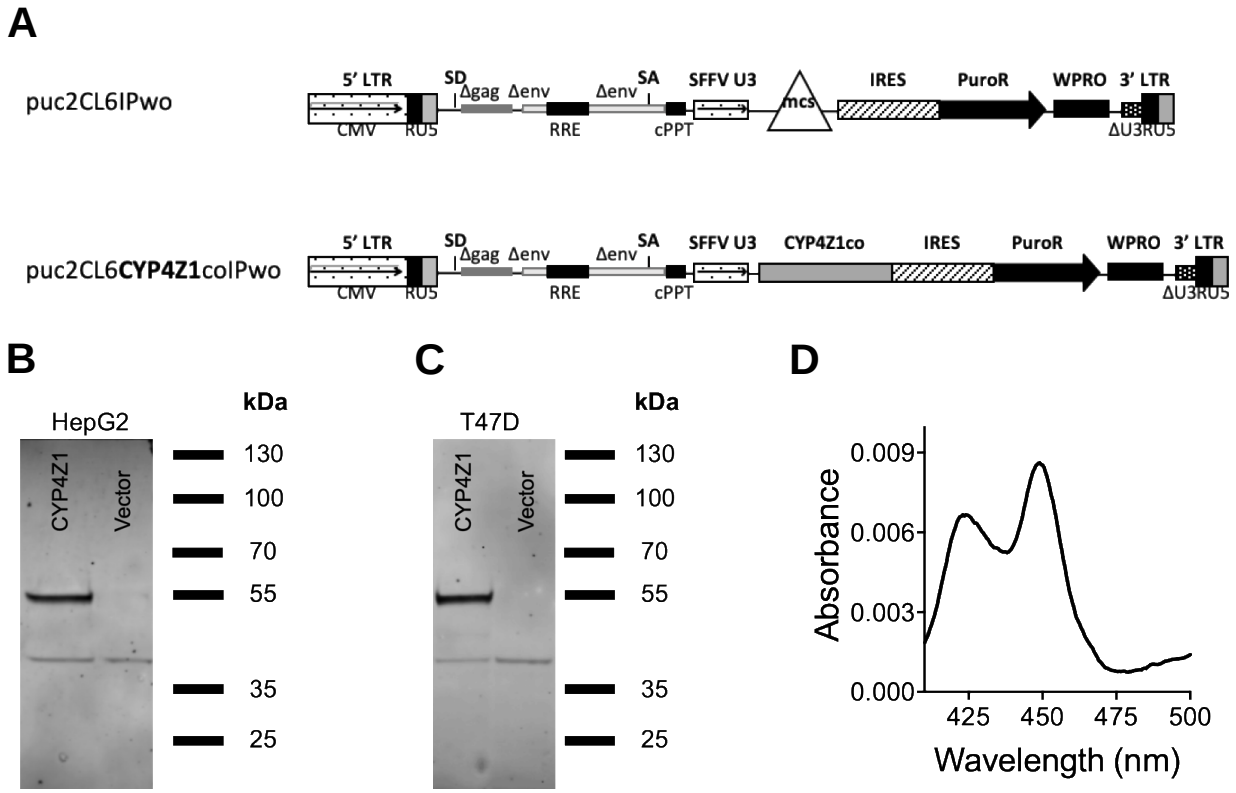

Figure S3.1. CYP4Z1 expression systems. Schematic outline of the lentiviral vector puc2CL6IPwo used for expression of codon-optimized (co) CYP4Z1 in both HepG2 cells (used for membrane preparations), and T47D cells (used for whole cell assays). CMV: CMV promoter; SD: splice donor; LTR: long terminal repeat; SA: splice acceptor; RRE: Rev responsive element; cPPT, central polypurine binding tract; SFFV U3: U3 promoter of the spleen focus-forming virus; mcs: multicloning site; IRES: internal ribosomal entry site; PuroR: puromycin resistance cDNA; WPRO, woodchuck hepatitis virus post-transcriptional regulatory element (optimized) (**A**). Western blot characterization of HepG2 (**B**) and T47D (**C**) cells modified with the above described lentivirus to express CYP4Z1 (~55 kDa, source: Atlas Antibodies). No expression was detected in the vector control cell lines; the loading control GAPDH is also shown (~37 kDa, source: Invitrogen). Carbon monoxide (CO) binding spectra, indicates ~1 µM CYP4Z1 in the HepG2 membranes *via* analysis of the absorbance at 450 nm, the large absorbance signal at 420 nm is common to expression systems that contain other hemeproteins (Guengerich et al., 2009) (**D**)**.**

Method for membrane preparation

CYP4Z1-HepG2, CYP4F8-HepG2, and Vector-HepG2 membranes were prepared as follows: HepG2 cells were modified by lentiviral transduction to express CYP4Z1, CYP4F8, or with a control vector, as previously described (Wiek et al., 2015; Roellecke et al., 2016). A schematic outline of the lentiviral vector system has been provided in the Supporting Information (**Figure S1A**). Western blot analysis was performed as previously described (McDonald et al., 2017). The stably transduced HepG2 cells were grown in tissue culture media consisting of DMEM, 10% FBS, 1% pen/strep, and 10 mM HEPES, and were selected with puromycin treatment (2 μg/mL) over a 7-day period as previously described (Kowalski et al., 2019). HepG2 cell lines were scaled up by expanding over a duration of 2.5-3 weeks (split 1:10 twice), with periodic refeeding at 2 μg/mL puromycin to maintain selection, ultimately generating 100 × 15 cm 90+% confluent plates. Approximately 1×10^9 cells were harvested, washed thrice with PBS, homogenized on ice by sonication and membranes prepared at 100,000 × *g* for 60 min after first subjecting the homogenate to a very low speed spin of 1,000 × *g* for 5 min to remove large cellular debris. The pellets were homogenized in a storage buffer containing 100 mM potassium phosphate buffer (KPi) pH 7.4, 20% glycerol, and 1 mM EDTA. CYP450 concentration was measured from the conventional carbon monoxide difference spectrum (Guengerich et al., 2009). These procedures yielded a specific content of 81 pmol CYP4Z1/mg protein (~15 nanomoles total) in the CYP4Z1-HepG2 membranes for our metabolic studies; no CYP4Z1 was detectable in the Vector-HepG2 membranes. The CYP4F8-HepG2 membranes had a specific content of 20 pmol CYP4F8/mg protein (~3 nanomoles total).

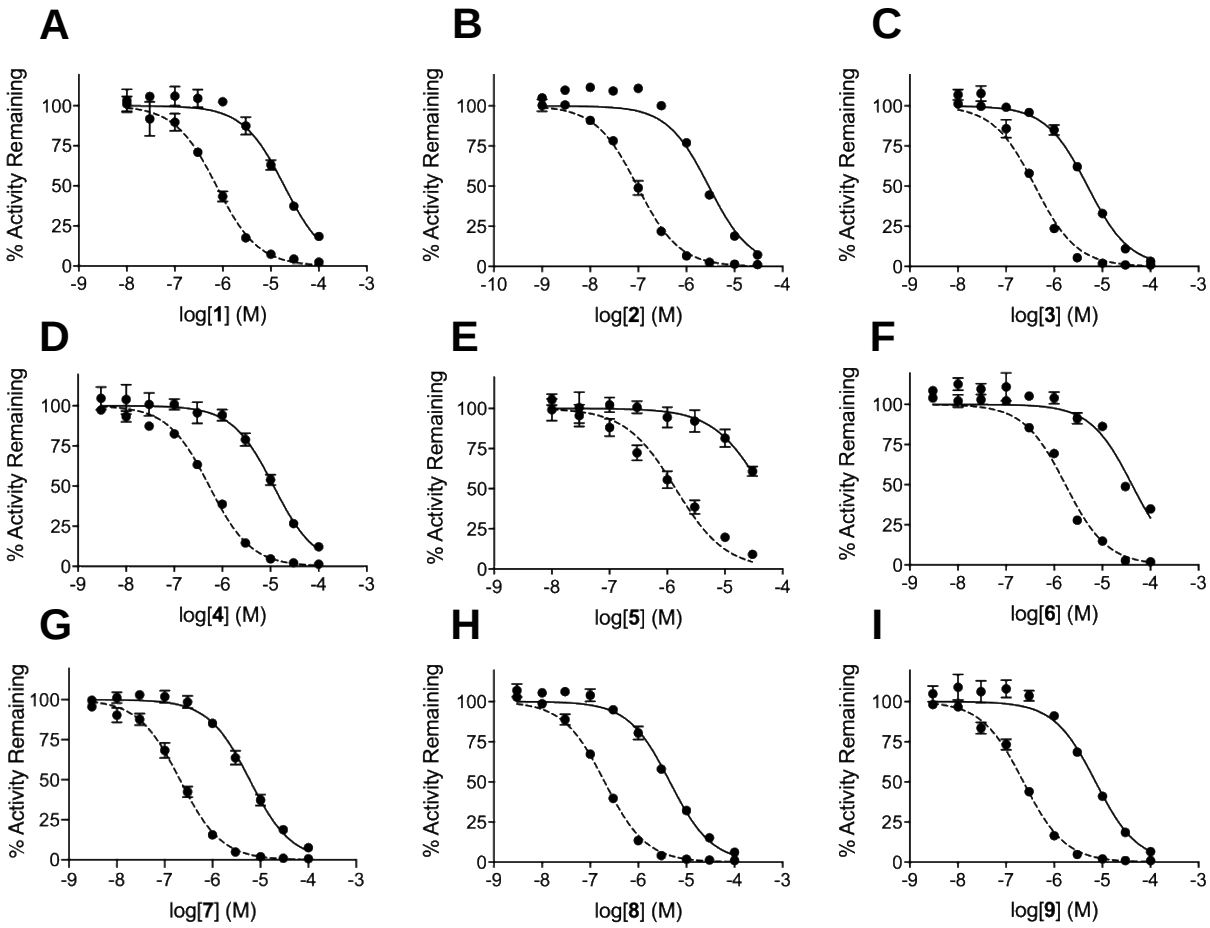

Figure S3.2. IC_{50} and shifted-IC_{50} determination for inhibition of CYP4Z1 by **1** – **9.** CYP4Z1 inhibition from treatment with compounds **1** (**A**), **2** (**B**), **3** (**C**), **4** (**D**), **5** (**E**), **6** (**F**), **7** (**G**), **8** (**H**), and **9** (**I**) was determined from the dose-response curves of percent remaining activity of CYP4Z1-mediated Luc-BE *O*-debenzylation, compared to treatment with vehicle (DMSO). The minus NADPH pre-incubation reactions (solid lines) correspond to the reported IC_{50} values and the plus NADPH pre-incubation reactions (dashed lines) correspond to the reported shifted-IC_{50} values. Data shown represents the mean and standard deviation from multiple independent experiments.

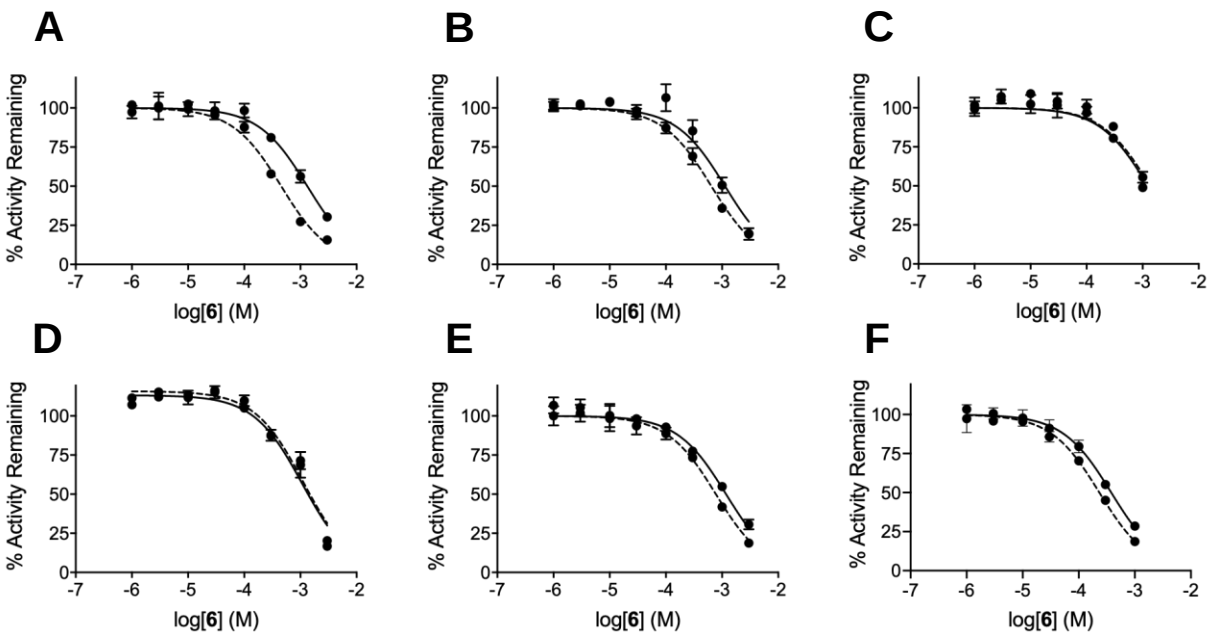

Figure S3.3. IC_{50} and shifted-IC_{50} determination for inhibition of CYP4 isozymes by **6.** Inhibition of CYP4A11 Luc-4A *O*-demethylation (**A**), CYP4F2 (**B**), CYP4F3a (**C**), and CYP4F3b Luc-4F2/3 *O*-(4-methylthio)-debenzylation (**D**), CYP4F8 (**E**), and CYP4F12 Luc-BE *O*-debenzylation (**F**) was determined from the dose-response curves of percent remaining activity from treatment with inhibitor **6** compared to treatment with vehicle (DMSO). The minus NADPH pre-incubation reactions (solid lines) correspond to the reported IC_{50} values and the plus NADPH pre-incubation reactions (dashed lines) correspond to the reported shifted-IC_{50} values. Data shown represents the mean and standard deviation from multiple independent experiments. Of note, IC_{50} determinations for inhibition of CYP4F3a by **6** are an approximation as concentrations >1 mM to fully define 50% inhibition were not tested due to lack of enzyme.

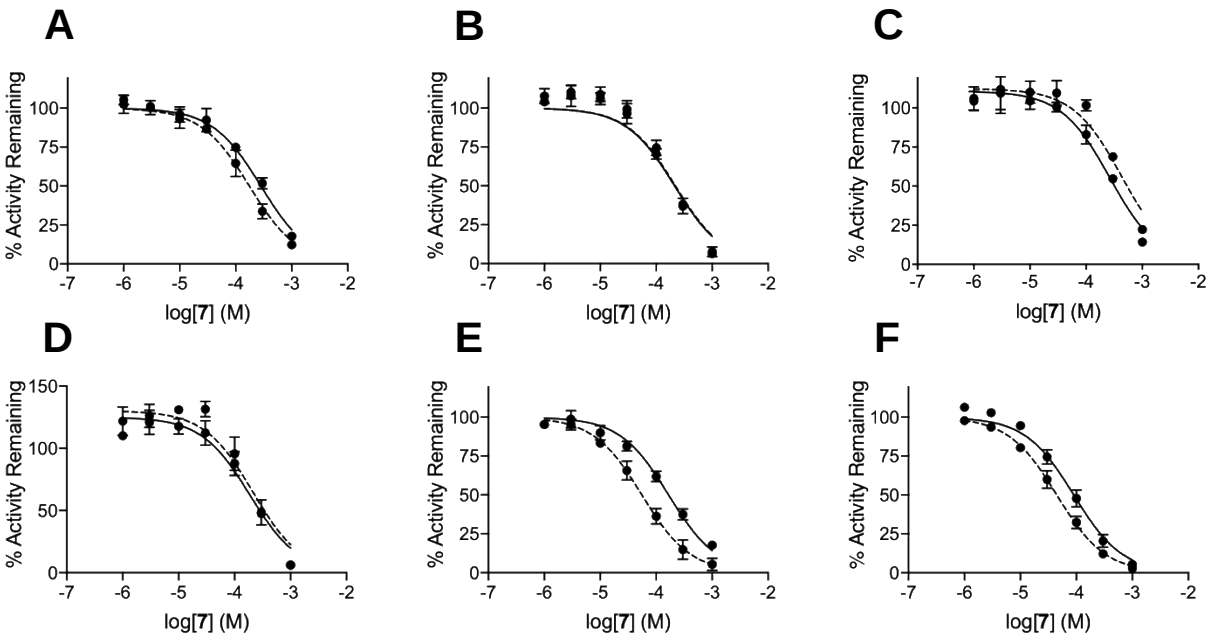

Figure S3.4. IC_{50} and shifted-IC_{50} determination for inhibition of CYP4 isozymes by **7.** Inhibition of CYP4A11 Luc-4A *O*-demethylation (**A**), CYP4F2 (**B**), CYP4F3a (**C**), and CYP4F3b Luc-4F2/3 *O*-(4-methylthio)-debenzylation (**D**), CYP4F8 (**E**), and CYP4F12 Luc-BE *O*-debenzylation (**F**) was determined from the dose-response curves of percent remaining activity from treatment with inhibitor **7** compared to treatment with vehicle (DMSO). The minus NADPH pre-incubation reactions (solid lines) correspond to the reported IC_{50} values and the plus NADPH pre-incubation reactions (dashed lines) correspond to the reported shifted-IC_{50} values. Data shown represents the mean and standard deviation from multiple independent experiments. Of note, CYP4F3b exhibited what may be modelled as a bell-shaped dose-response curve (**D**), where low concentrations of **7** stimulated CYP4F3b Luc-4F2/3 metabolism and higher concentrations inhibited the enzyme, however, this was not used for IC_{50} determinations, nor investigated further.

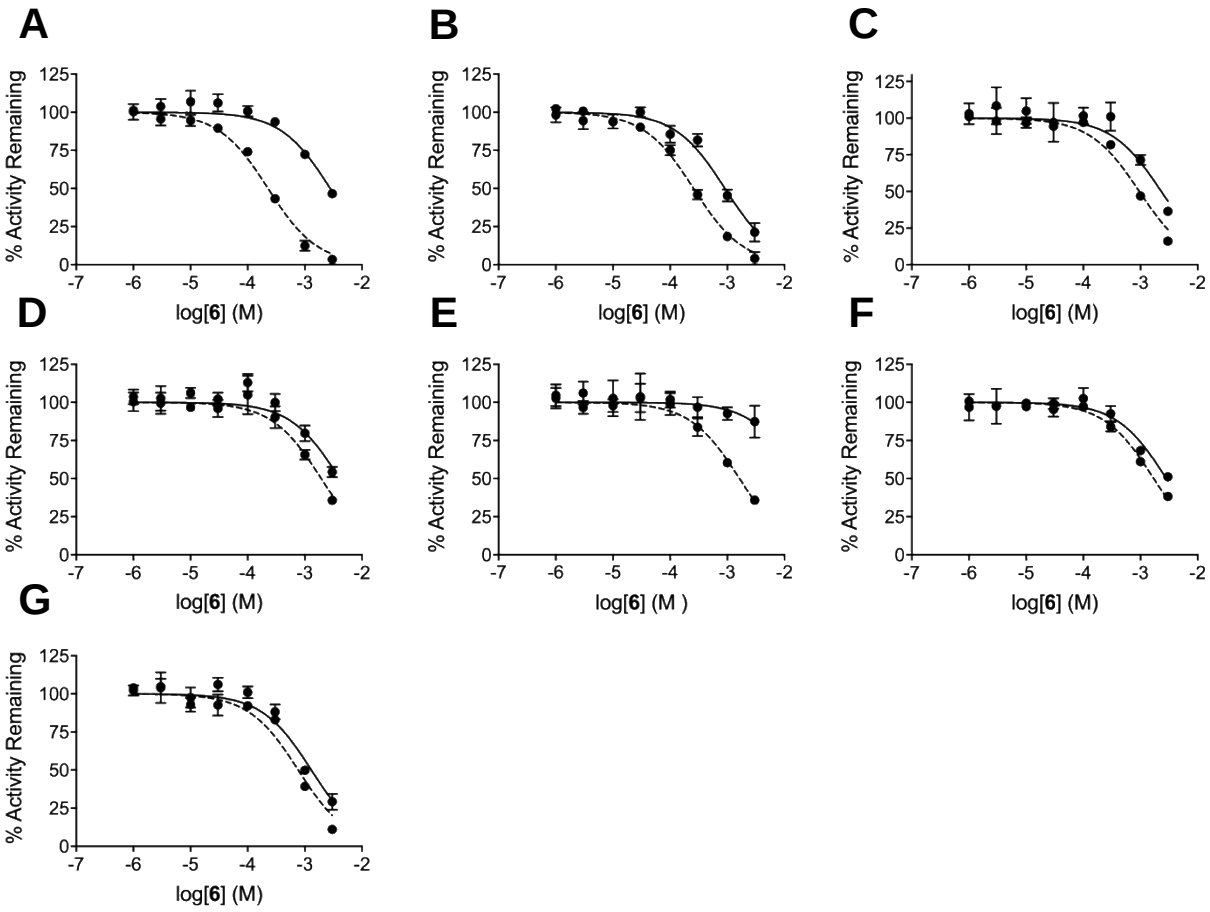

Figure S3.5. IC_{50} and shifted-IC_{50} determination for inhibition of hepatic CYP isozymes by **6**. Inhibition of CYP1A2 phenacetin *O*-deethylation (**A**), CYP2B6 bupropion hydroxylation (**B**), CYP2C8 amodiaquine *N*-deethylation (**C**), CYP2C9 tolbutamide methyl-hydroxylation (**D**), CYP2C19 (*S*)-mephenytoin 4'-hydroxylation (**E**), CYP2D6 dextromethorphan *O*-demethylation (**F**), and CYP3A4/5 midazolam 1'-hydroxylation (**G**) was determined from the dose-response curves of percent remaining activity from treatment with inhibitor **6** compared to treatment with vehicle (DMSO). The minus NADPH pre-incubation reactions (solid lines) correspond to the reported IC_{50} values and the plus NADPH pre-incubation reactions (dashed lines) correspond to the reported shifted-IC_{50} values. Data shown represents the mean and standard deviation from multiple independent experiments.

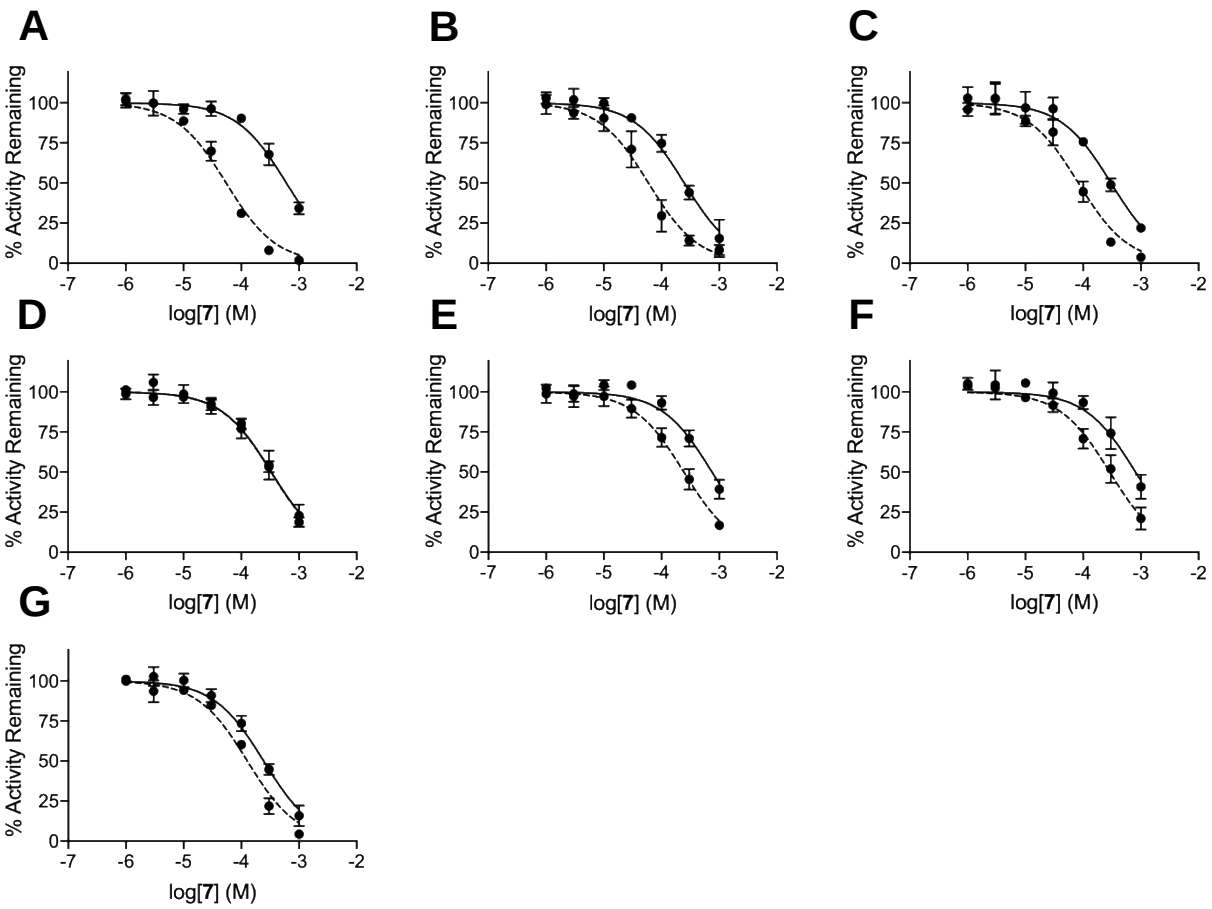

Figure S3.6. IC_{50} and shifted-IC_{50} determination for inhibition of hepatic CYP isozymes by **7**. Inhibition of CYP1A2 phenacetin *O*-deethylation (**A**), CYP2B6 bupropion hydroxylation (**B**), CYP2C8 amodiaquine *N*-deethylation (**C**), CYP2C9 tolbutamide methyl-hydroxylation (**D**), CYP2C19 (*S*)-mephenytoin 4'-hydroxylation (**E**), CYP2D6 dextromethorphan *O*-demethylation (**F**), and CYP3A4/5 midazolam 1'-hydroxylation (**G**) was determined from the dose-response curves of percent remaining activity from treatment with inhibitor **7** compared to treatment with vehicle (DMSO). The minus NADPH pre-incubation reactions (solid lines) correspond to the reported IC_{50} values and the plus NADPH pre-incubation reactions (dashed lines) correspond to the reported shifted-IC_{50} values. Data shown represents the mean and standard deviation from multiple independent experiments.

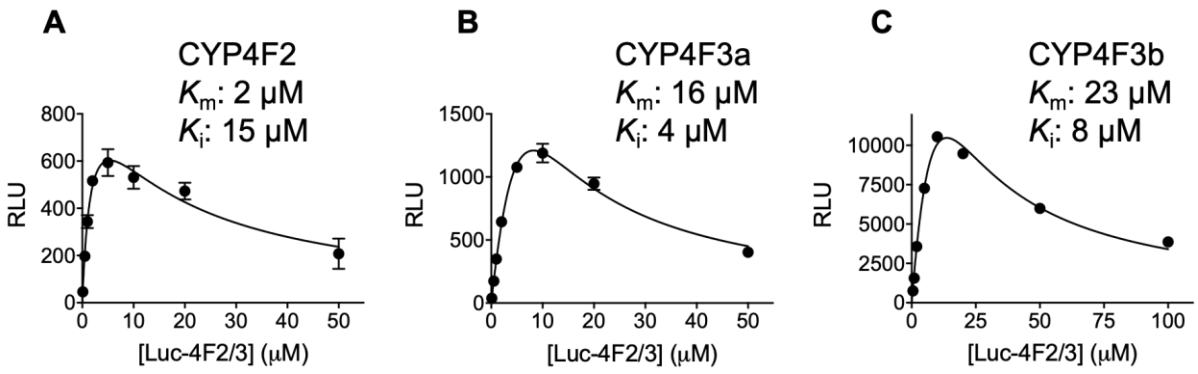

Figure S3.7. Luc-4F2/3 metabolism kinetics for CYP4F2, CYP4F3a, and CYP4F3b. 4F2 (**A**), 4F3a (**B**), and 4F3b (**C**) all displayed substrate inhibition kinetics; therefore, the ABT-analog inhibition studies were performed at the probe substrate concentration of 2 µM for all three enzymes. This probe substrate concentration utilized was approximately within the linear phases of turnover and ≤ K_m and < K_i values. Data shown represents the mean and standard deviation from three replicates.

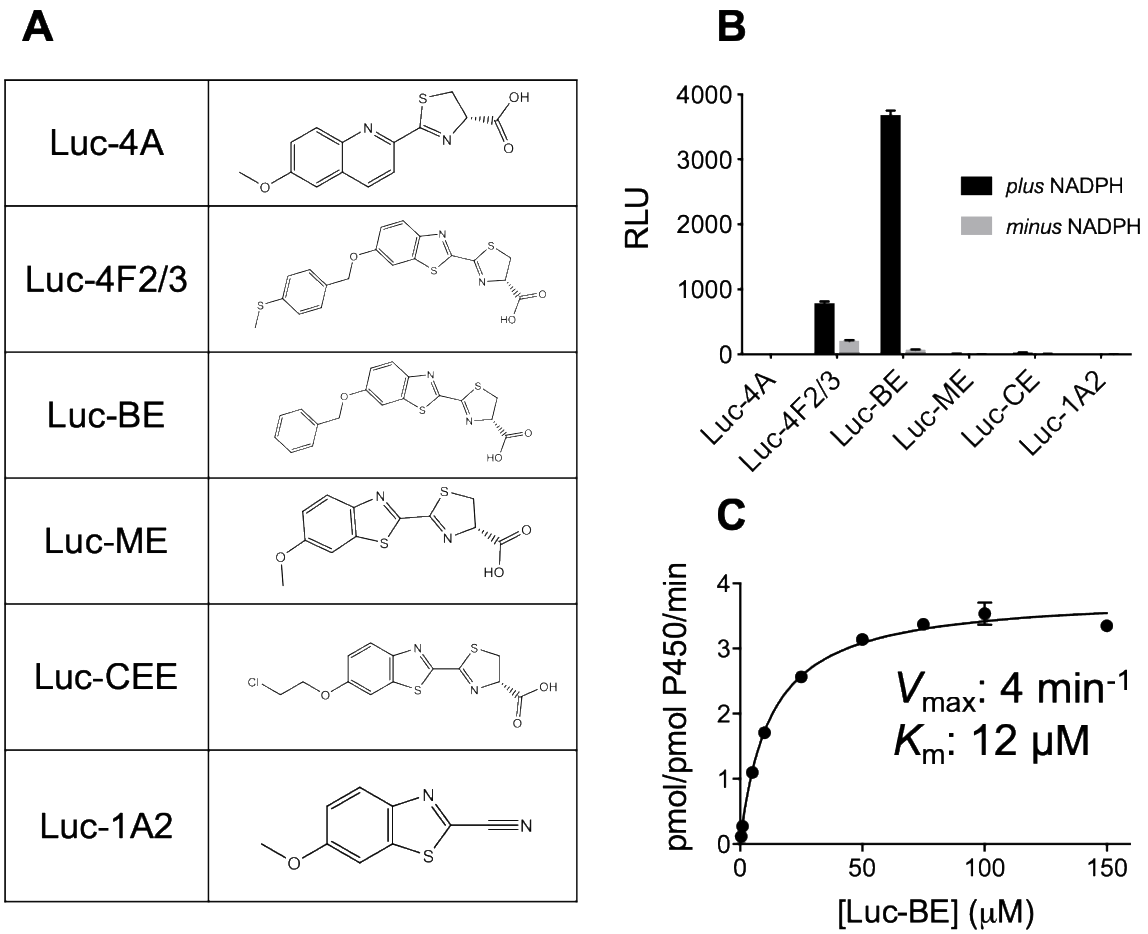

Figure S3.8. Analysis of CYP4F8 metabolism of pro-luciferins. Chemical structures of Promega's pro-luciferins used for screening (**A**). Screening of six different pro-luciferins for metabolism by CYP4F8 showed Luc-BE as a potential probe substrate (**B**). Kinetic analysis of CYP4F8-mediated Luc-BE turnover shows a V_{max} = 4 pmol/pmol CYP4F8/min and a K_m = 12 µM (**C**)**.** Data shown represents the mean and standard deviation from three replicates.

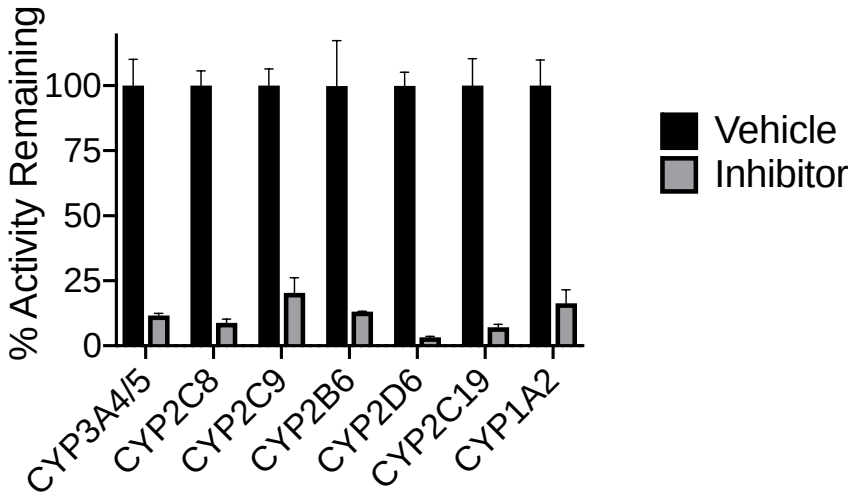

Figure S3.9. Internal validation of HLM cocktail inhibition assay. Inhibition of CYP-3A4/5, -2C8, -2C9, -2B6, -2D6, -2C19, -1A2 was assessed using ketoconazole (0.5 µM), quercetin (20 µM), sulfaphenazole (2.5 µM), ticlopidine (5 µM), quinidine (2.5 µM), ticlopidine (17.5 µM), and furafylline (20 µM), respectively. The concentrations used were ~5X literature reported IC_{50} values. The percent remaining activity after inhibition (as compared to vehicle control) is within error to full IC_{50} data when both cocktail and single substrate inhibition experiments are performed using HLM and these conditions (Li et al., 2015). Data shown represents the mean and standard deviation from three replicates.

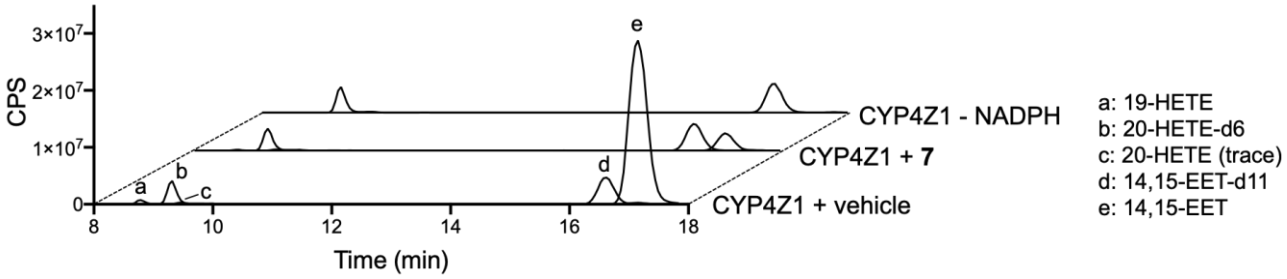

Figure S3.10. Inhibition of CYP4Z1-mediated AA Metabolism by **7** in HepG2 Membranes. After a 30-minute preincubation, treatment with 3 µM of **7** results in ~90% loss of CYP4Z1 activity, relative to vehicle, as assessed by comparing PARs for 14,15-EET production. The substrate AA was incubated with CYP4Z1 at 75 µM. No significant AA metabolism was observed when NADPH cofactor was not included in the incubation. Equal amounts of each internal standard (100 ng) were added prior to sample work-up.

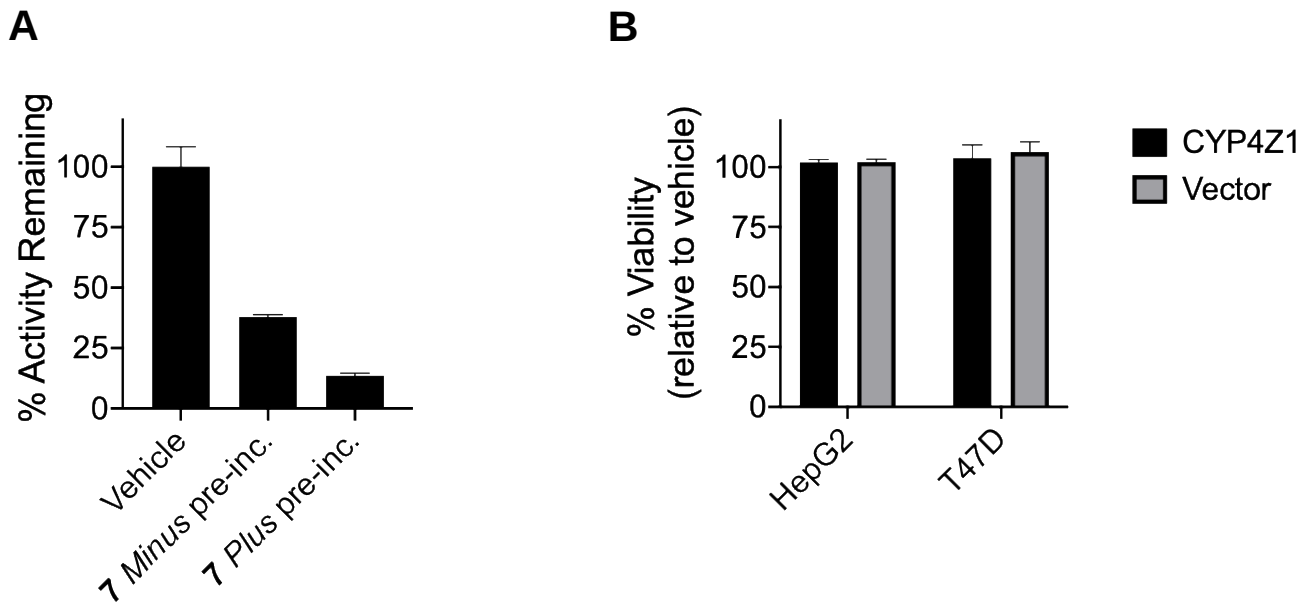

Figure S3.11. Inhibition of CYP4Z1 in HepG2 Cells and HepG2, T47D Cell Viability. CYP4Z1- and vector-HepG2 cells were seeded into 96-well white-walled plates at 15,000 cells/well in 100 µL of cell culture media. A 1000× stock of inhibitor **7**, or DMSO vehicle, was diluted into a 100× stock solution in tissue culture medium and added to achieve a final concentration of 3 µM (*Plus* pre-inc.) and 24 hours later, a different subset of wells received inhibitor **7** at a final concentration of 3 µM (*Minus* pre-inc.). Immediately following, Luc-BE was added to all wells to achieve a final concentration of 30 µM and the cells were incubated for a further 1 hour, and then assayed as described in the Experimental Section. In whole HepG2 cells, CYP4Z1-mediated Luc-BE *O*-debenzylation was inhibited ~63% without a pre-incubation, and ~86% with a pre-incubation, by inhibitor **7** at 3 µM (**A**). Minimal Luc-BE *O*-debenzylation was observed in the vector-HepG2 cells (data not shown). Using the same seeding and stock solutions outlined above, both CYP4Z1 and vector -HepG2, -T47D cells received inhibitor **7** to achieve a final concentration of 3 µM. The cells were assessed 24 hours later using Promega's CellTiter-Glo Luminescent Cell Viability Assay and the percent viability, relative to vehicle treated cells, was compared. No cytotoxicity from treatment with **7** at 3 µM was observed for any of the cell lines under the conditions tested (**B**). For both **A** and **B**, shown is the average and SD from three replicates.

^{1}H NMR (500 MHz, $CDCl_3$)

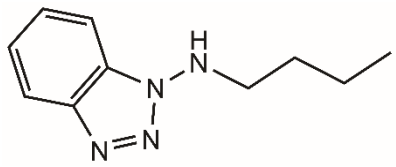

1

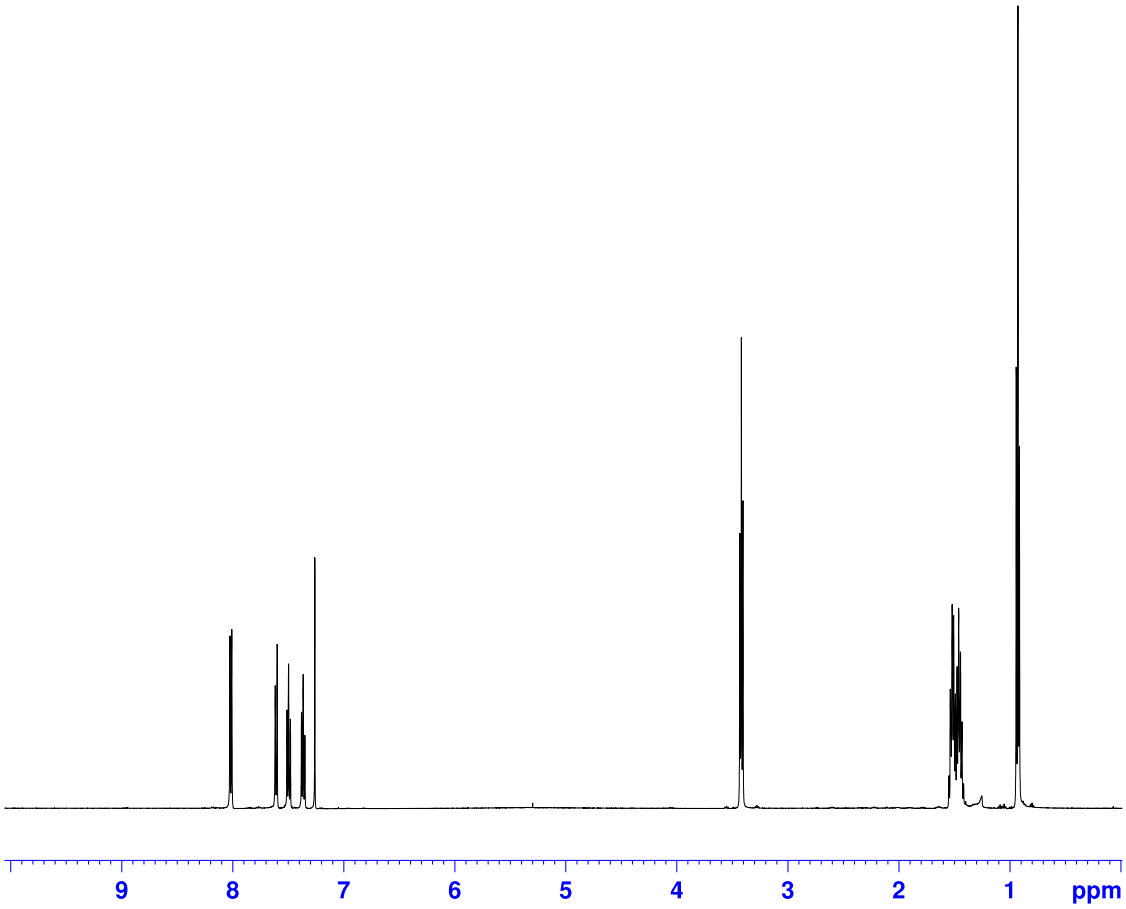

^{13}C NMR (125 MHz, $CDCl_3$)

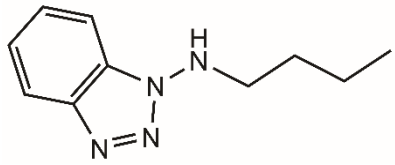

1

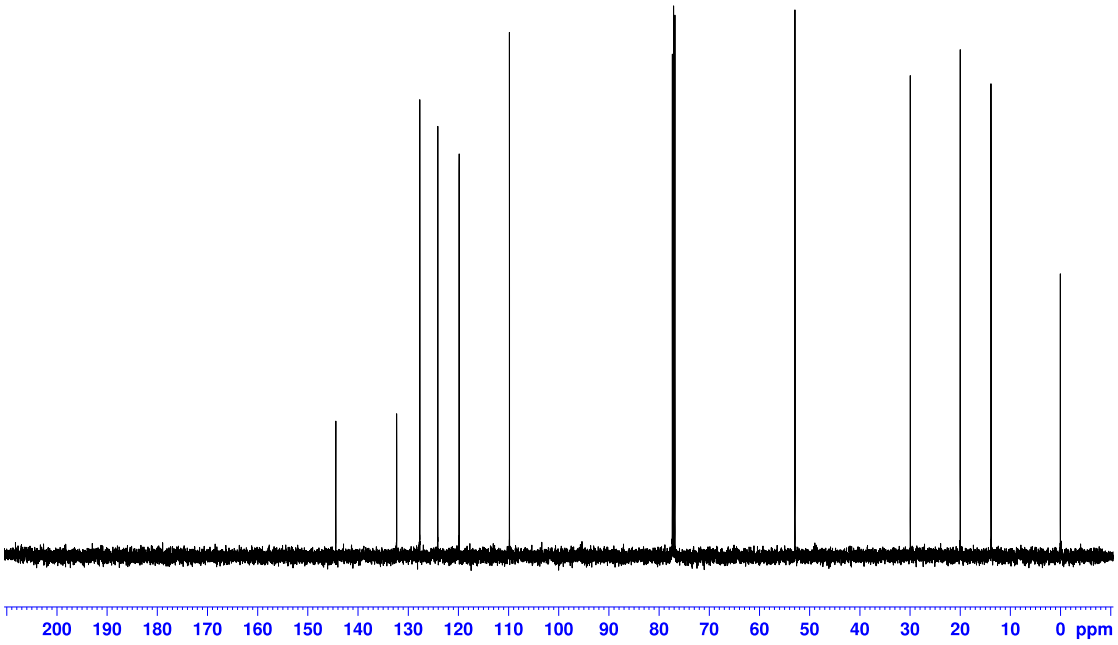

^{1}H NMR (500 MHz, $CDCl_3$)

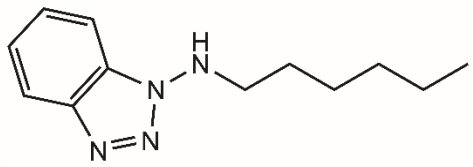

2

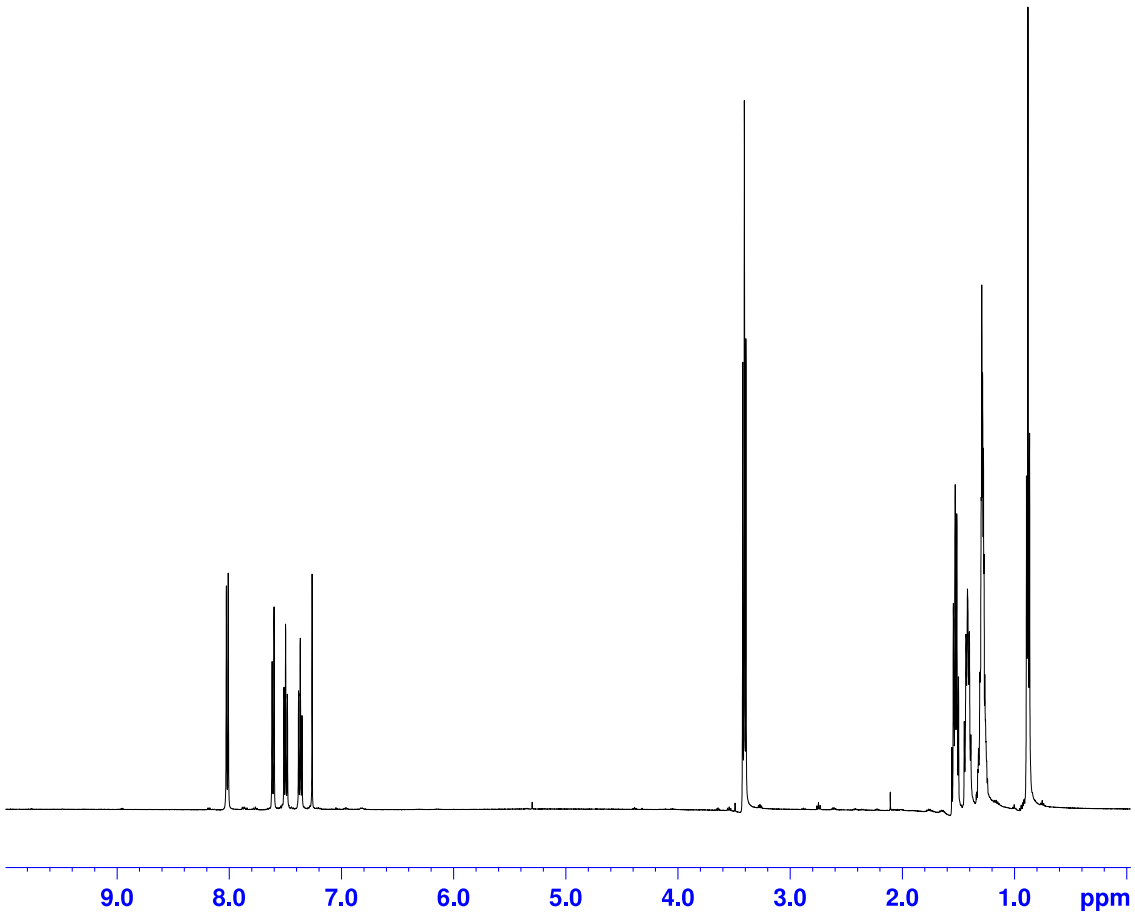

^{13}C NMR (125 MHz, $CDCl_3$)

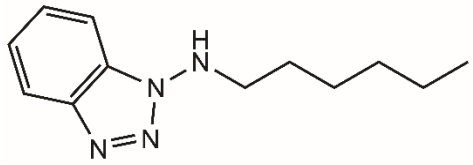

2

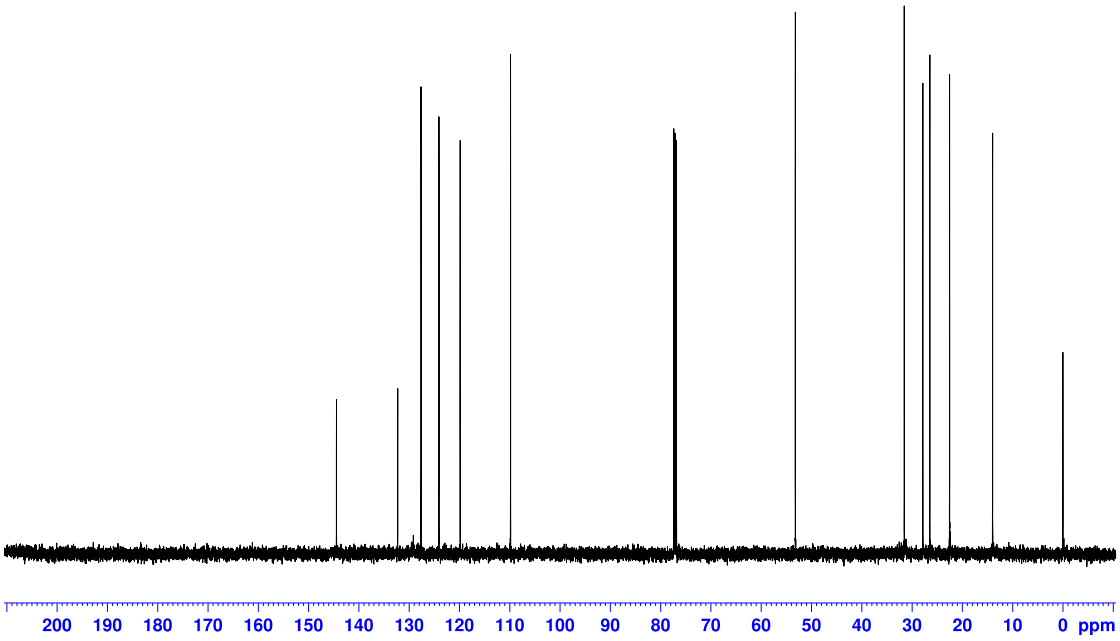

^{1}H NMR (500 MHz, $CDCl_3$)

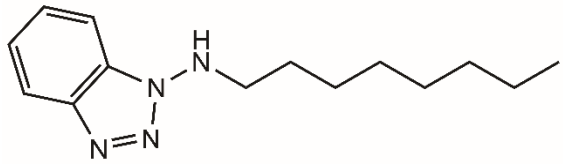

3

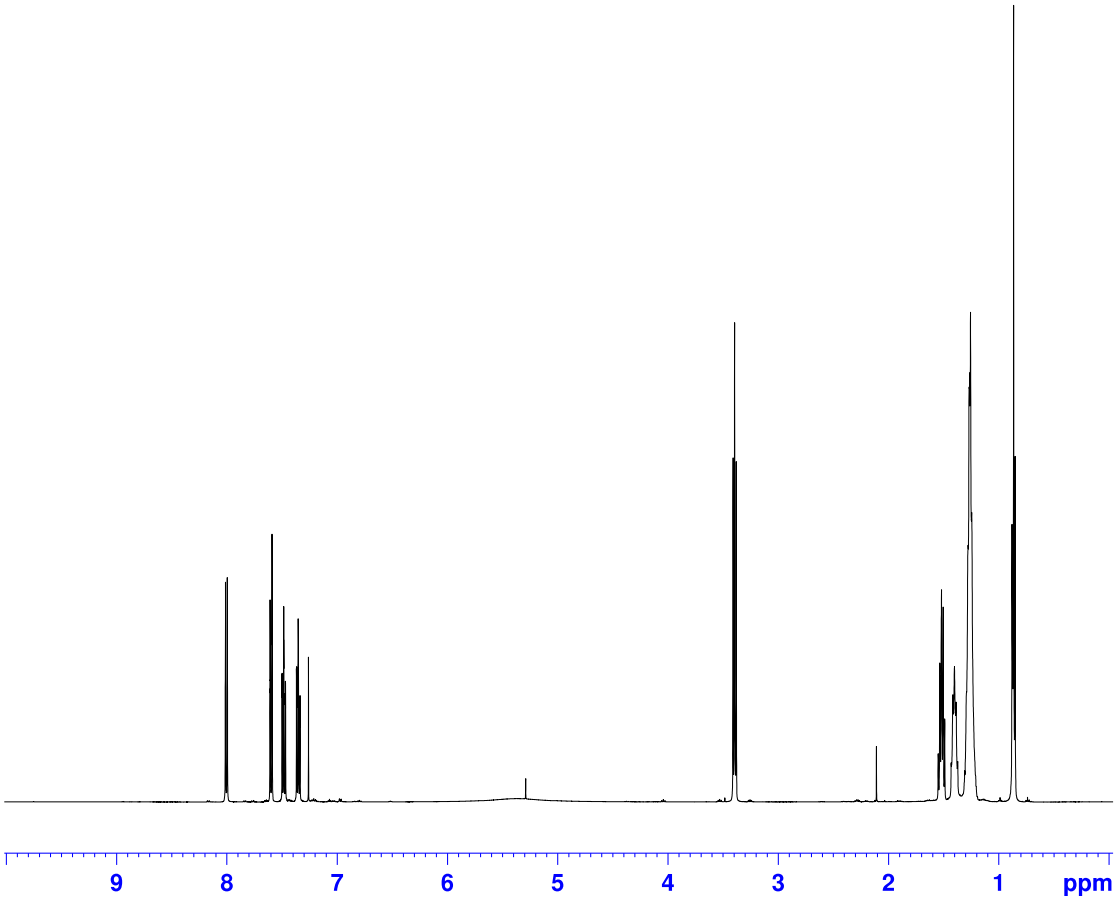

^{13}C NMR (125 MHz, $CDCl_3$)

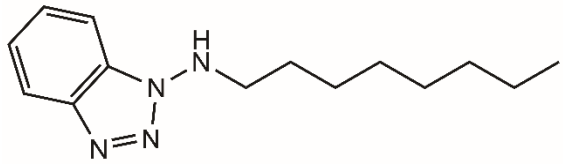

3

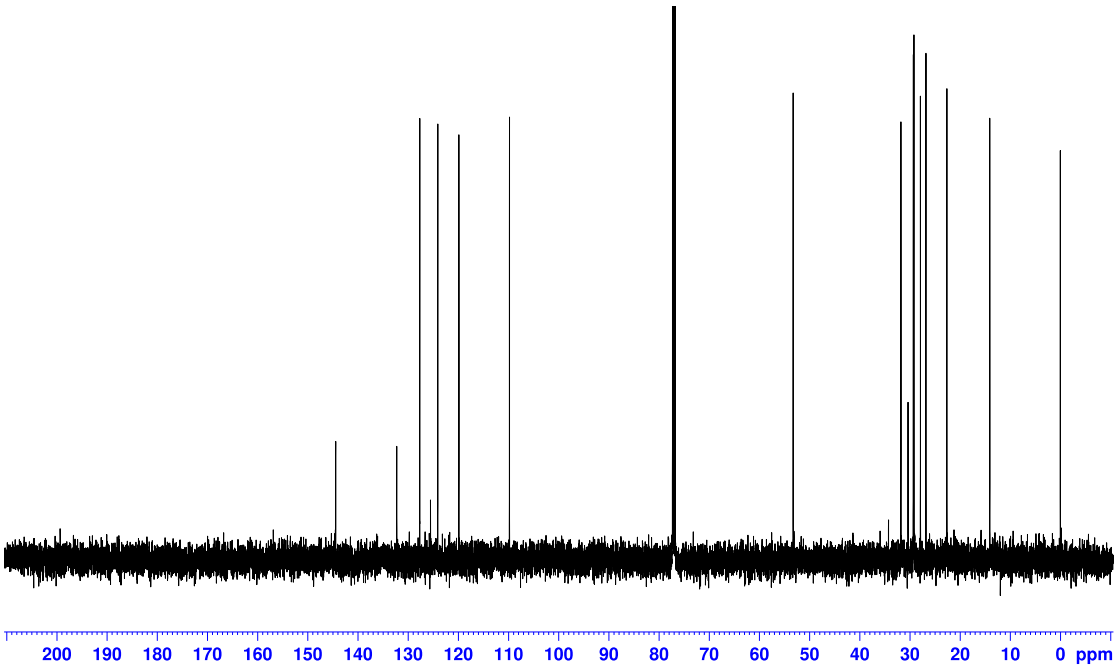

^{1}H NMR (500 MHz, $CDCl_3$)

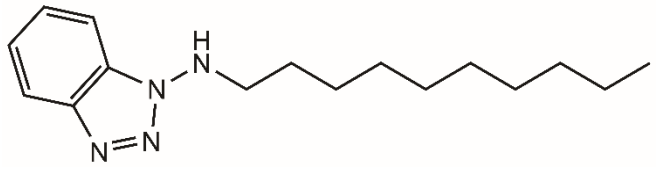

4

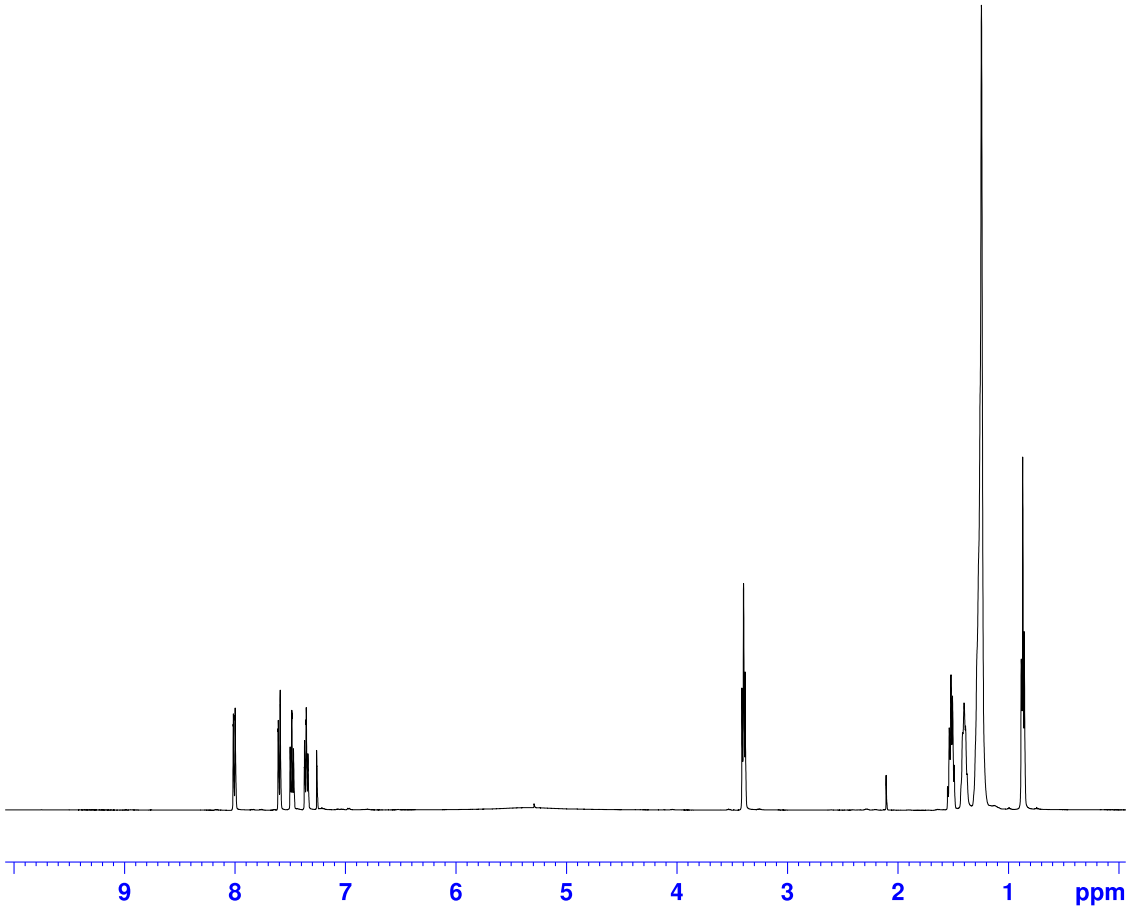

^{13}C NMR (125 MHz, $CDCl_3$)

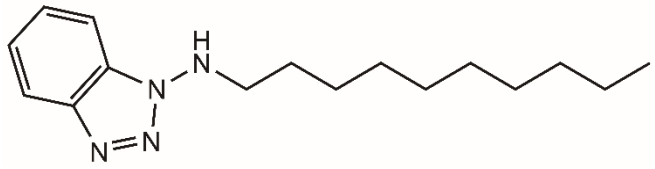

4

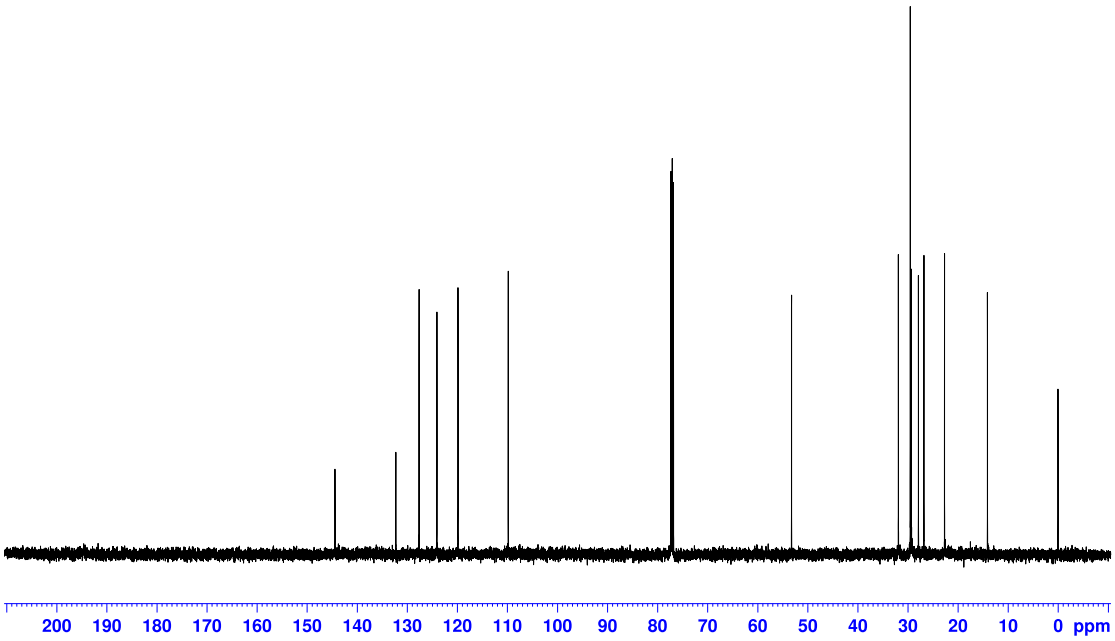

^{1}H NMR (500 MHz, $CDCl_3$)

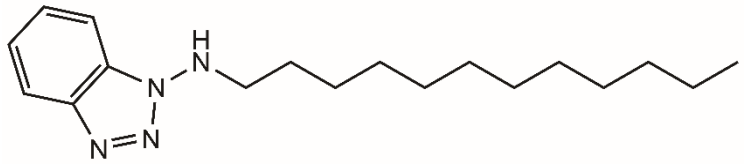

5

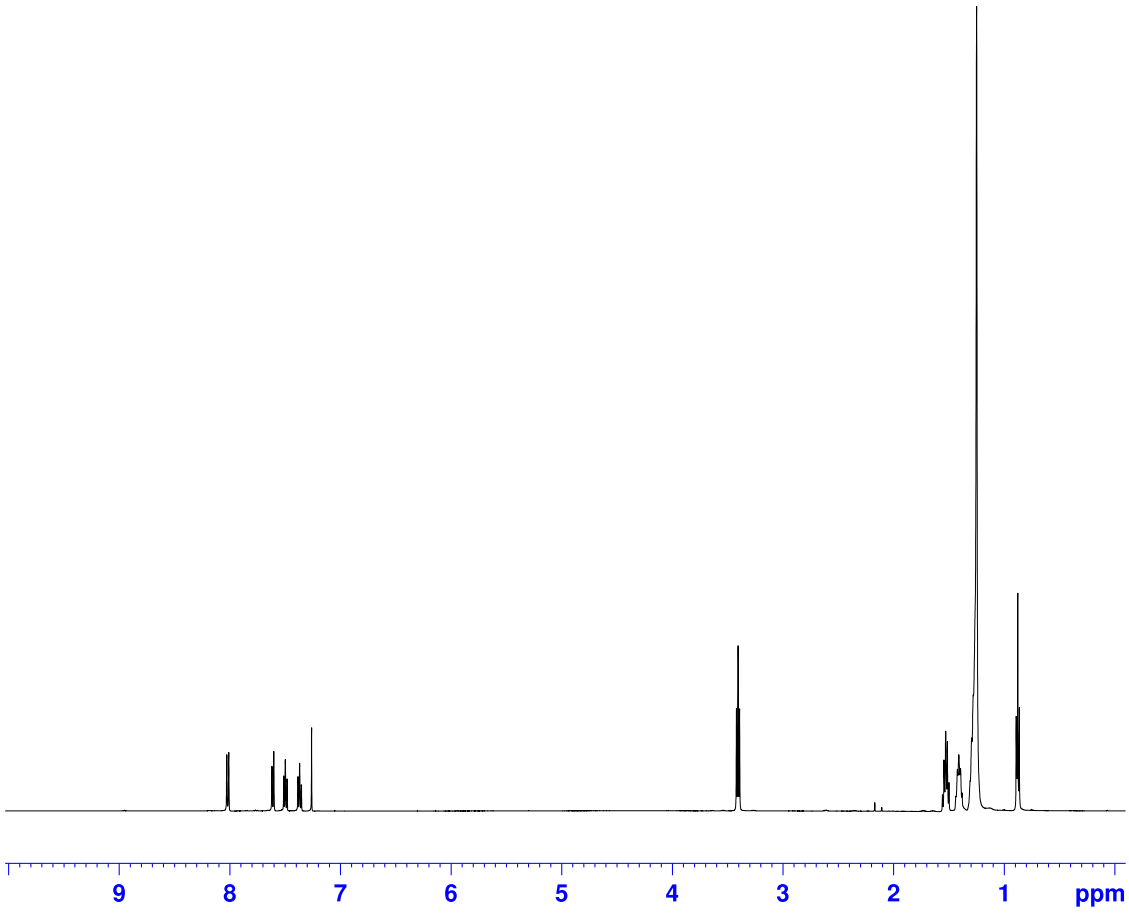

^{13}C NMR (125 MHz, $CDCl_3$)

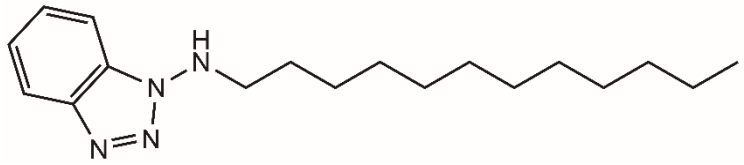

5

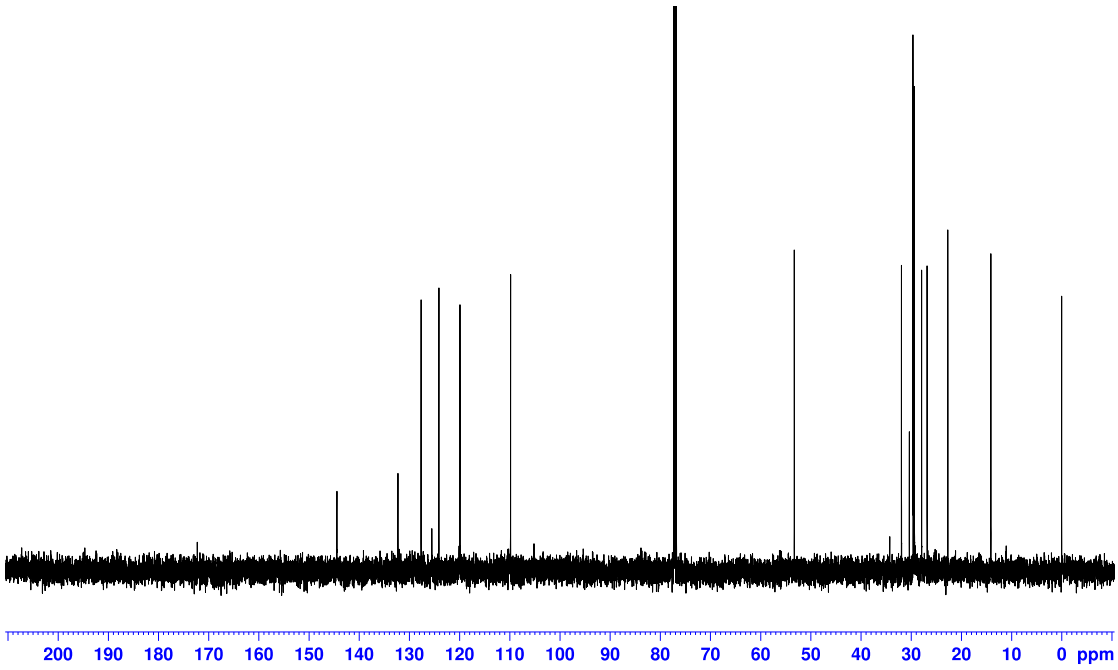

^{1}H NMR (500 MHz, $CDCl_3$)

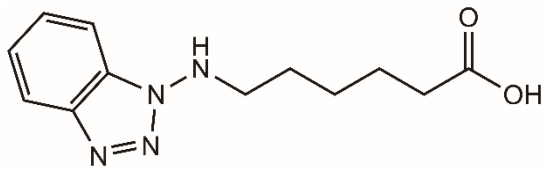

6

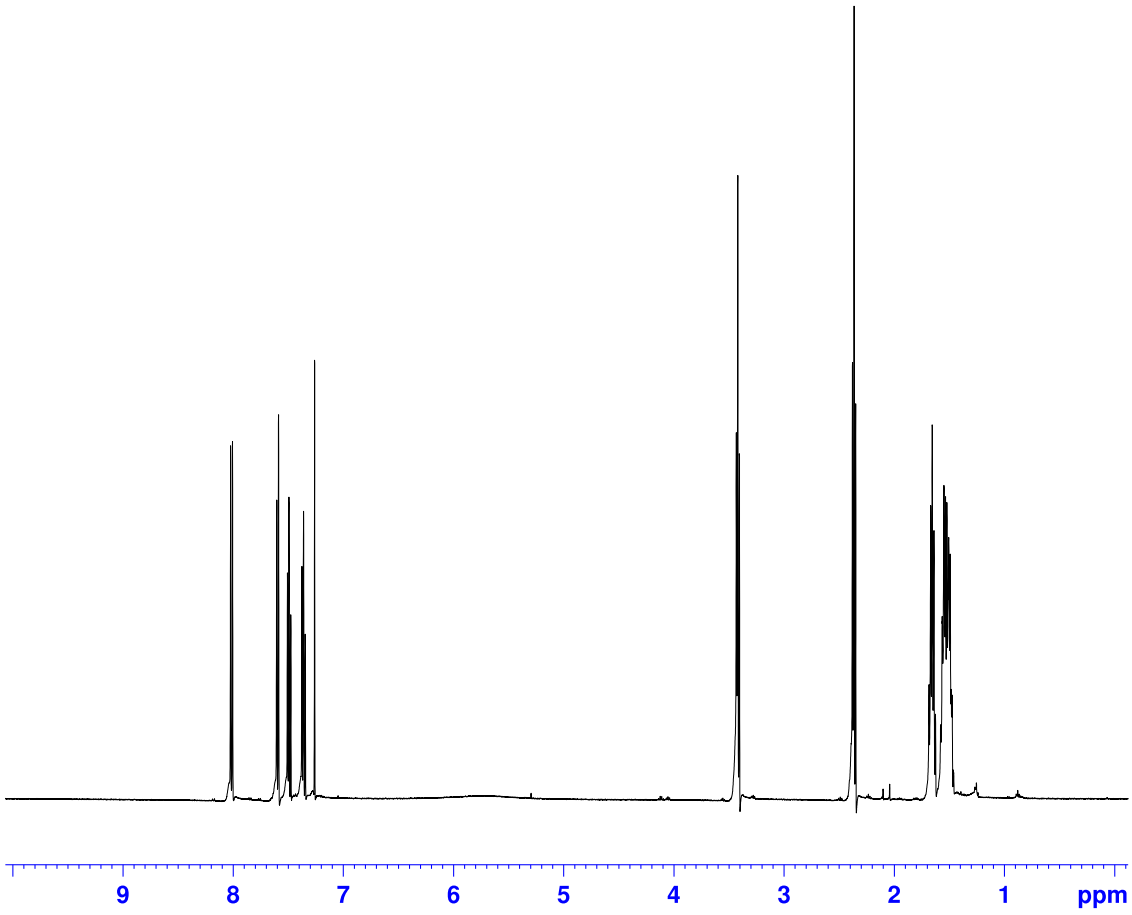

^{13}C NMR (125 MHz, $CDCl_3$)

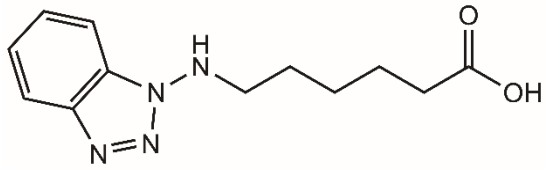

6

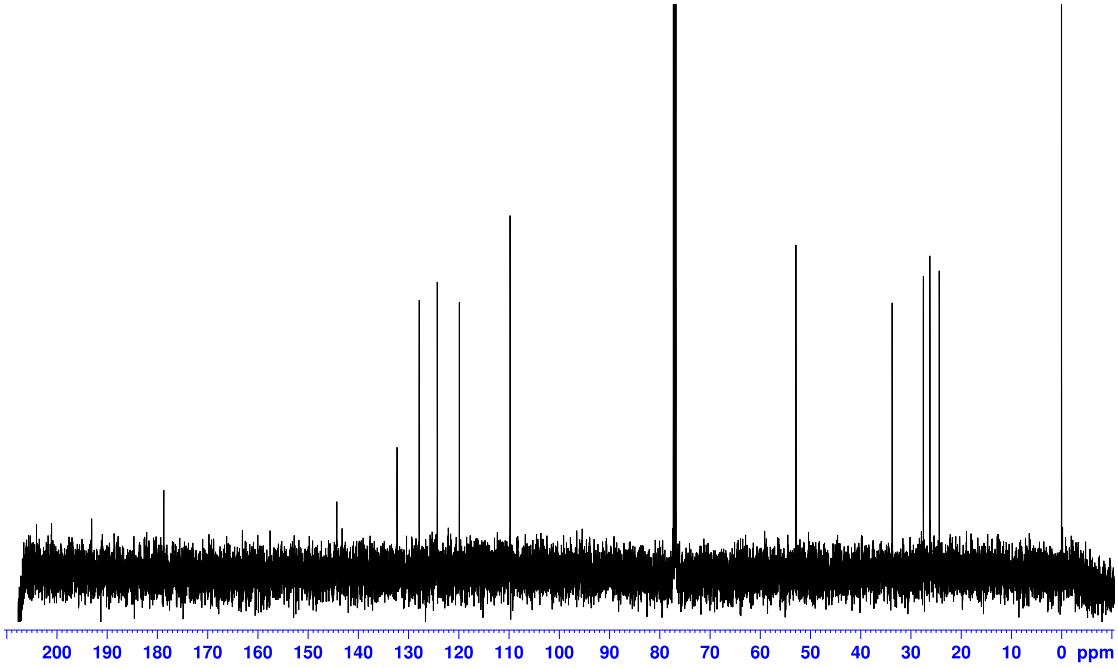

^{1}H NMR (500 MHz, $CDCl_3$)

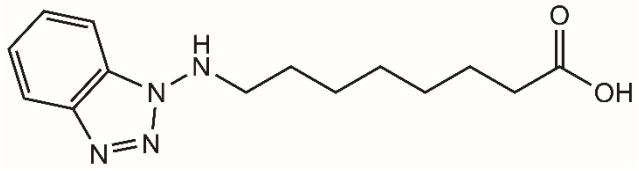

7

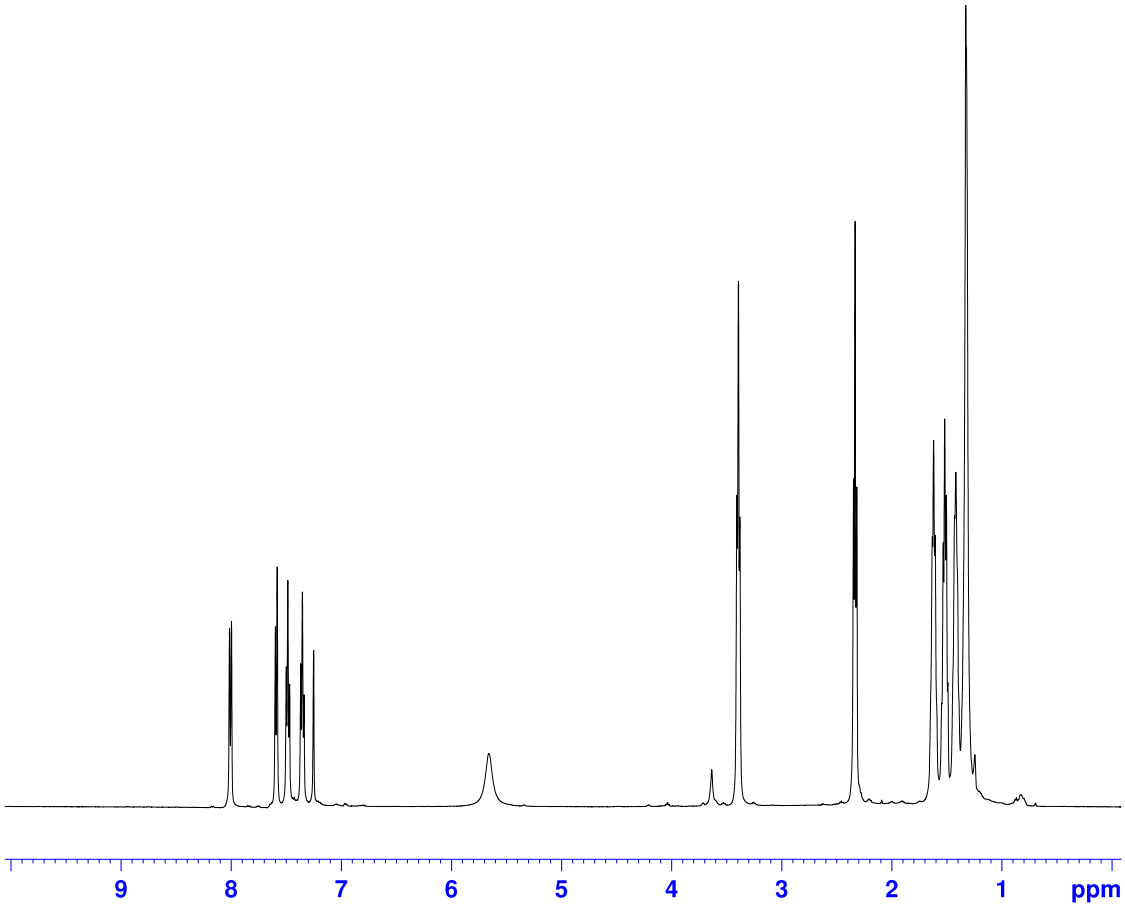

^{13}C NMR (125 MHz, $CDCl_3$)

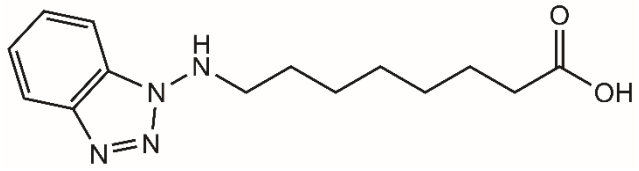

7

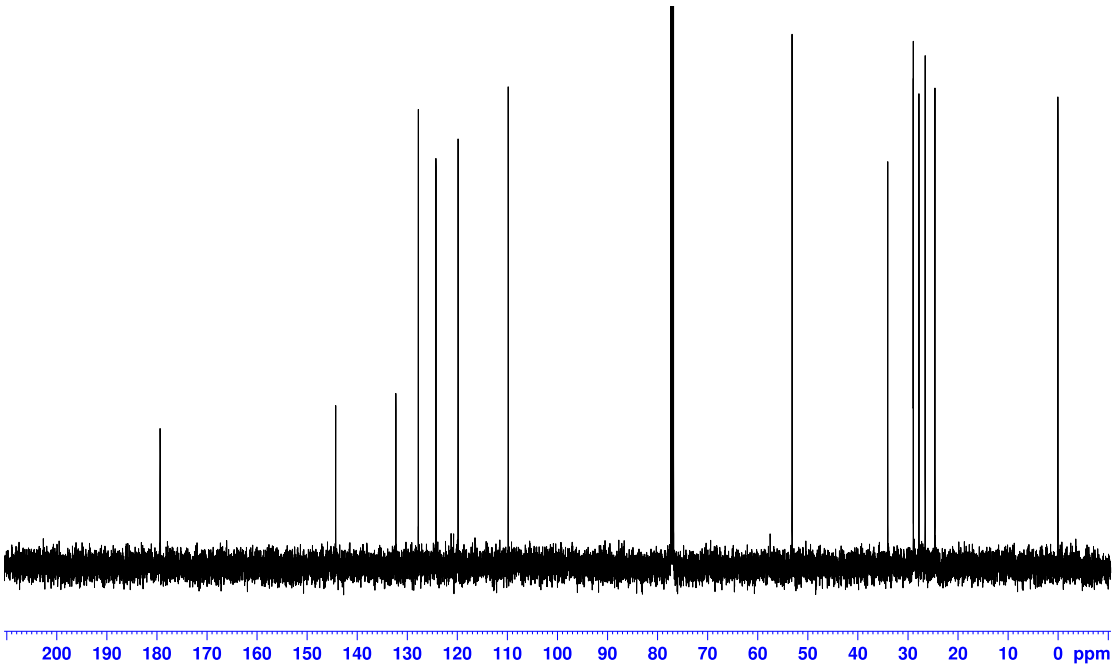

^{1}H NMR (500 MHz, $CDCl_3$)

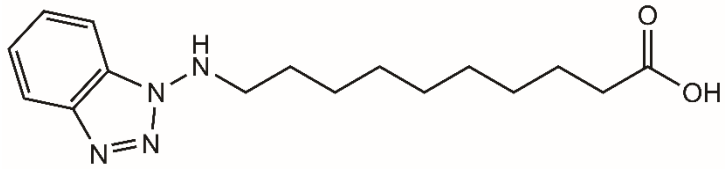

8

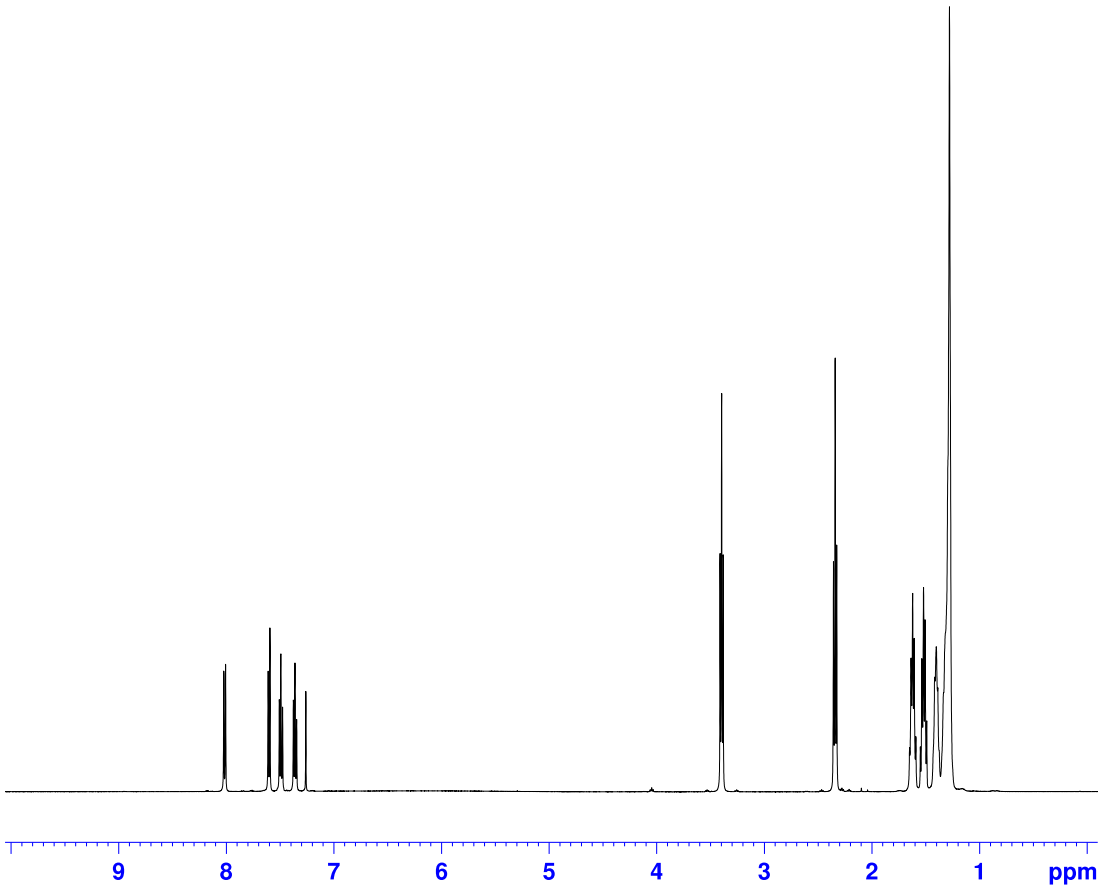

^{13}C NMR (125 MHz, $CDCl_3$)

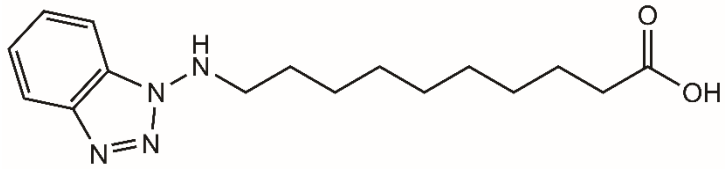

8

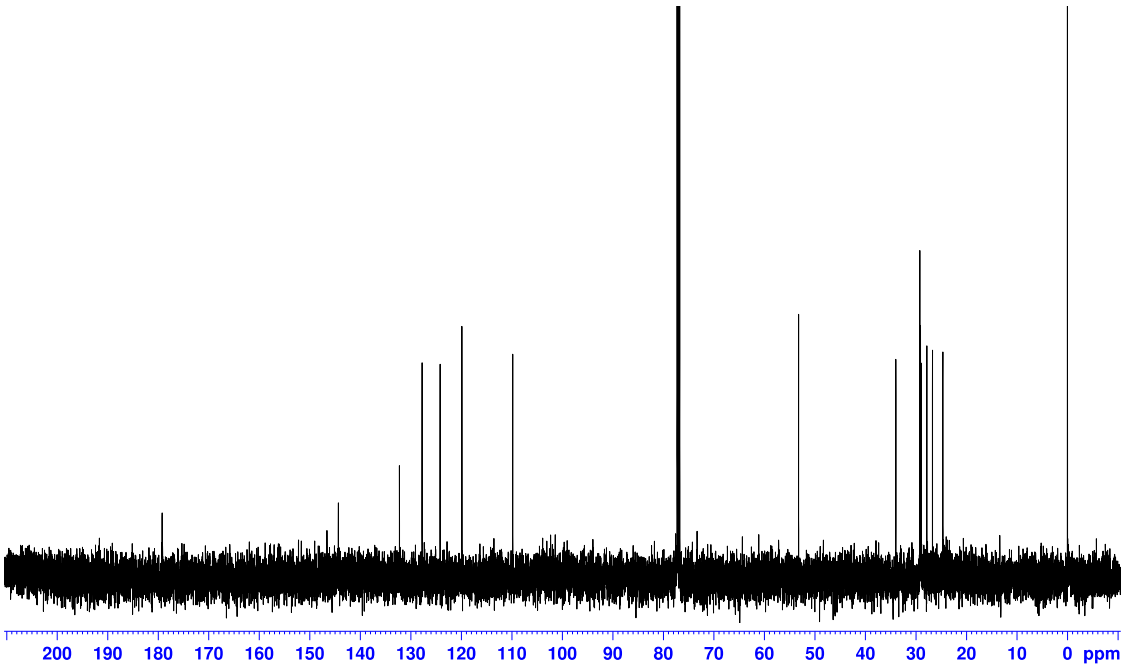

^{1}H NMR (500 MHz, $CDCl_3$)

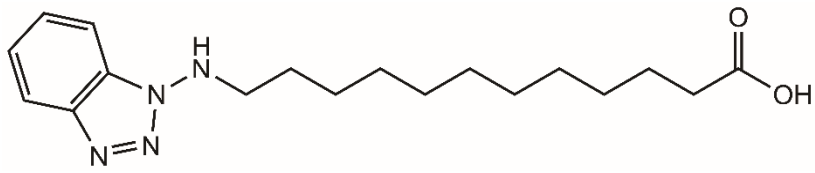

9

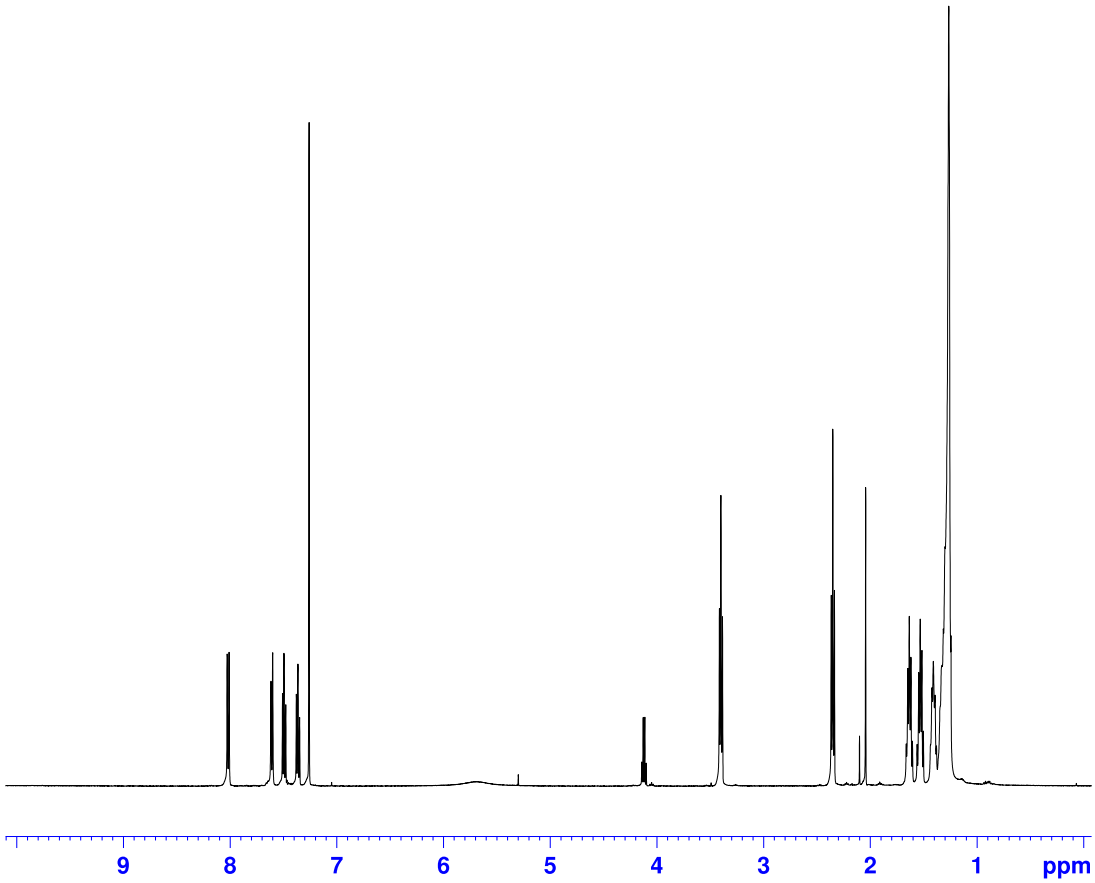

^{13}C NMR (125 MHz, $CDCl_3$)

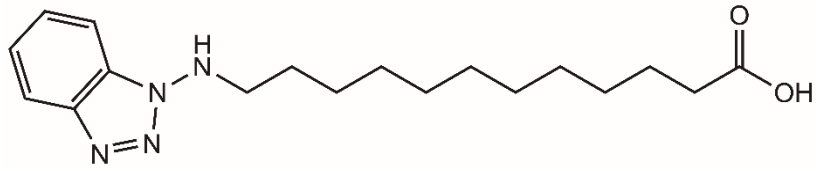

9

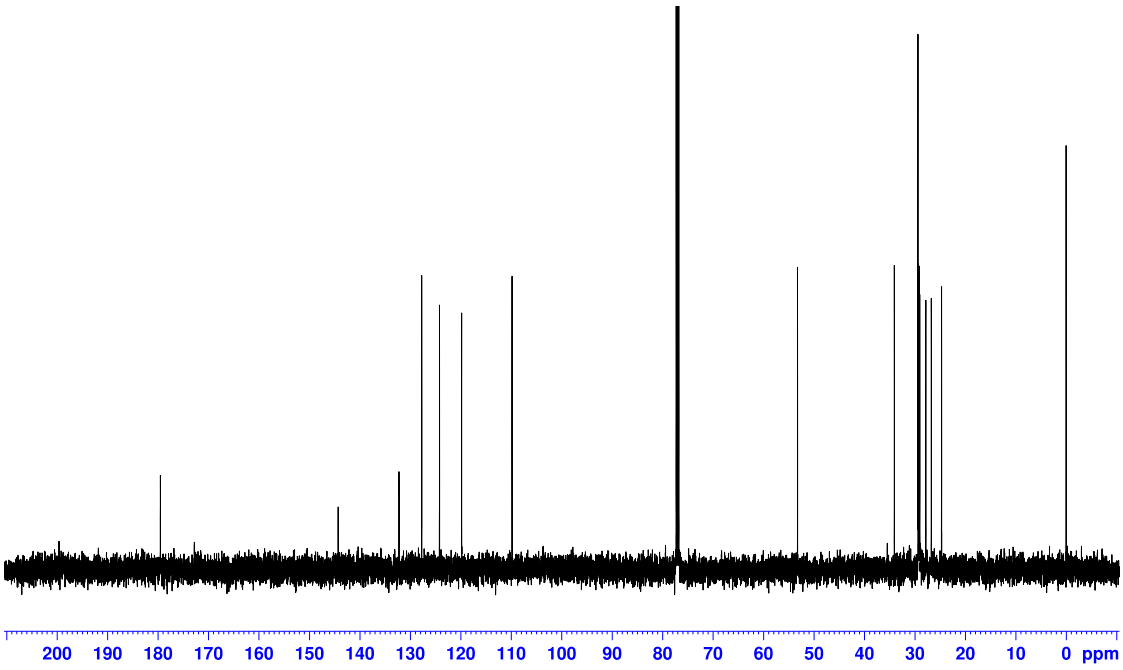

References

Al-Esawi NSE, Geeran ARM, Alajeely MHJ, Al-Isawi AOJ. (2020). Expression of CYT4Z1 in breast carcinoma; Correlating with clinicopathological parameters. Biomed Pharmacol J, 13(1).

Brueggemeier RW, Hackett JC, Diaz-Cruz ES. (2005). Aromatase inhibitors in the treatment of breast cancer. Endocr Rev, 26, 331-45.

Bruno RD, Njar VC. (2007). Targeting cytochrome P450 enzymes: a new approach in anti-cancer drug development. Bioorg Med Chem, 15, 5047-60.

Bylund J, Bylund M, Oliw EH. (2001). cDna cloning and expression of CYP4F12, a novel human cytochrome P450. Biochem Biophys Res Commun, 280, 892-7.

Bylund J, Hidestrand M, Ingelman-Sundberg M, Oliw EH. (2000). Identification of CYP4F8 in human seminal vesicles as a prominent 19-hydroxylase of prostaglandin endoperoxides. J Biol Chem, 275, 21844-9.

Capper CP, Rae JM, Auchus RJ. (2016). The metabolism, analysis, and targeting of steroid hormones in breast and prostate cancer. Horm Cancer, 7, 149-164.

Chuanprasit P, Goh SH, Hirao H. (2015). Benzyne Formation in the Mechanism-Based Inactivation of Cytochrome P450 by 1-Aminobenzotriazole and N-Benzyl-1-Aminobenzotriazole: Computational Insights. ACS Catalysis, 5 (5), 2952-2960.

Decker M, Adamska M, Cronin A, Di Giallonardo F, Burgener J, Marowsky A, Falck JR, Morisseau C, Hammock BD, Gruzdev A and others. (2012). EH3 (ABHD9): the first member of a new epoxide hydrolase family with high activity for fatty acid epoxides. J Lipid Res, 53, 2038-45.

Edson KZ, Rettie AE. (2013). CYP4 enzymes as potential drug targets: focus on enzyme multiplicity, inducers and inhibitors, and therapeutic modulation of 20-hydroxyeicosatetraenoic acid (20-HETE) synthase and fatty acid omega-hydroxylase activities. Curr Top Med Chem, 13, 1429-40.

Emoto C, Murase S, Sawada Y, Jones BC, Iwasaki K. (2003). In vitro inhibitory effect of 1-aminobenzotriazole on drug oxidations catalyzed by human cytochrome P450 enzymes: a comparison with SKF-525A and ketoconazole. Drug Metab Pharmacokinet, 18, 287-95.

Fer M, Dreano Y, Lucas D, Corcos L, Salaun JP, Berthou F, Amet Y. (2008). Metabolism of eicosapentaenoic and docosahexaenoic acids by recombinant human cytochromes P450. Arch Biochem Biophys, 471, 116-25.

Giudici D, Ornati G, Briatico G, Buzzetti F, Lombardi P, di Salle E. (1988). 6-Methylenandrosta-1,4-diene-3,17-dione (FCE 24304): a new irreversible aromatase inhibitor. J Steroid Biochem, 30, 391-4.

Grimm SW, Einolf HJ, Hall SD, He K, Lim HK, Ling KH, Lu C, Nomeir AA, Seibert E, Skordos

KW and others. (2009). The conduct of in vitro studies to address time-dependent inhibition of drug-metabolizing enzymes: a perspective of the pharmaceutical research and manufacturers of America. Drug Metab Dispos, 37, 1355-70.

Guengerich FP, Martin MV, Sohl CD, Cheng Q. (2009). Measurement of cytochrome P450 and NADPH-cytochrome P450 reductase. Nat Protoc, 4, 1245-51.

Henne KR, Tran TB, VandenBrink BM, Rock DA, Aidasani DK, Subramanian R, Mason AK, Stresser DM, Teffera Y, Wong SG and others. (2012). Sequential metabolism of AMG 487, a novel CXCR3 antagonist, results in formation of quinone reactive metabolites that covalently modify CYP3A4 Cys239 and cause time-dependent inhibition of the enzyme. Drug Metab Dispos, 40, 1429-40.

Hollenberg PF, Kent UM, Bumpus NN. (2008). Mechanism-based inactivation of human cytochromes p450s: experimental characterization, reactive intermediates, and clinical implications. Chem Res Toxicol, 21, 189-205.

Holliday DL, Speirs V. (2011). Choosing the right cell line for breast cancer research. Breast Cancer Res, 13, 215.

Hsu MH, Baer BR, Rettie AE, Johnson EF. (2017). The Crystal Structure of Cytochrome P450 4B1 (CYP4B1) Monooxygenase Complexed with Octane Discloses Several Structural Adaptations for omega-Hydroxylation. J Biol Chem, 292, 5610-21.

Johnson AL, Edson KZ, Totah RA, Rettie AE. (2015). Cytochrome P450 omega-Hydroxylases in Inflammation and Cancer. Adv Pharmacol, 74, 223-62.

Johnson DS, Weerapana E, Cravatt BF. (2010). Strategies for discovering and derisking covalent, irreversible enzyme inhibitors. Future Med Chem, 2, 949-64.

Kaspera R, Totah RA. (2009). Epoxyeicosatrienoic acids: formation, metabolism and potential role in tissue physiology and pathophysiology. Expert Opin Drug Metab Toxicol, 5, 757-71.

Kent UM, Bend JR, Chamberlin BA, Gage DA, Hollenberg PF. (1997). Mechanism-based inactivation of cytochrome P450 2B1 by N-benzyl-1-aminobenzotriazole. Chem Res Toxicol, 10, 600-8.

Kowalski JP, McDonald MG, Whittington D, Guttman M, Scian M, Girhard M, Hanenberg H, Wiek C, Rettie AE. (2019). Structure-Activity Relationships for CYP4B1 Bioactivation of 4-Ipomeanol Congeners: Direct Correlation between Cytotoxicity and Trapped Reactive Intermediates. Chem Res Toxicol, 32, 2488-98.

Kozakai K, Yamada Y, Oshikata M, Kawase T, Suzuki E, Haramaki Y, Taniguchi H. (2014). Cocktail-substrate approach-based high-throughput assay for evaluation of direct and time-dependent inhibition of multiple cytochrome P450 isoforms. Drug Metab Pharmacokinet, 29, 198-207.

Li G, Huang K, Nikolic D, van Breemen RB. (2015). High-Throughput Cytochrome P450 Cocktail Inhibition Assay for Assessing Drug-Drug and Drug-Botanical Interactions. Drug Metab Dispos, 43, 1670-8.

Li Y, Steppi A, Zhou Y, Mao F, Miller PC, He MM, Zhao T, Sun Q, Zhang J. (2017). Tumoral expression of drug and xenobiotic metabolizing enzymes in breast cancer patients of different ethnicities with implications to personalized medicine. Sci Rep, 7, 4747.

Lim HK, Duczak N, Jr., Brougham L, Elliot M, Patel K, Chan K. (2005). Automated screening with confirmation of mechanism-based inactivation of CYP3A4, CYP2C9, CYP2C19, CYP2D6, and CYP1A2 in pooled human liver microsomes. Drug Metab Dispos, 33, 1211-9.

Luo J, Feng XX, Luo C, Wang Y, Li D, Shu Y, Wang SS, Qin J, Li YC, Zou JM and others. (2016). 14,15-EET induces the infiltration and tumor-promoting function of neutrophils to trigger the growth of minimal dormant metastases. Oncotarget, 7, 43324-36.

Mathews JM, Bend JR. (1986). N-alkylaminobenzotriazoles as isozyme-selective suicide inhibitors of rabbit pulmonary microsomal cytochrome P-450. Mol Pharmacol, 30, 25-32.

Mathews JM, Bend JR. (1993). N-aralkyl derivatives of 1-aminobenzotriazole as potent isozyme-selective mechanism-based inhibitors of rabbit pulmonary cytochrome P450 in vivo. J Pharmacol Exp Ther, 265, 281-5.

McDonald MG, Au NT, Rettie AE. (2015). P450-Based Drug-Drug Interactions of Amiodarone and its Metabolites: Diversity of Inhibitory Mechanisms. Drug Metab Dispos, 43, 1661-9.

McDonald MG, Ray S, Amorosi CJ, Sitko KA, Kowalski JP, Paco L, Nath A, Gallis B, Totah RA, Dunham MJ and others. (2017). Expression and Functional Characterization of Breast Cancer-Associated Cytochrome P450 4Z1 in Saccharomyces cerevisiae. Drug Metab Dispos, 45, 1364-71.

Mitra R, Guo Z, Milani M, Mesaros C, Rodriguez M, Nguyen J, Luo X, Clarke D, Lamba J, Schuetz E and others. (2011). CYP3A4 mediates growth of estrogen receptor-positive breast cancer cells in part by inducing nuclear translocation of phospho-Stat3 through biosynthesis of (+/-)-14,15-epoxyeicosatrienoic acid (EET). J Biol Chem, 286, 17543-59.

Miyata N, Taniguchi K, Seki T, Ishimoto T, Sato-Watanabe M, Yasuda Y, Doi M, Kametani S, Tomishima Y, Ueki T and others. (2001). HET0016, a potent and selective inhibitor of 20-HETE synthesizing enzyme. Br J Pharmacol, 133, 325-9.

Murray GI, Patimalla S, Stewart KN, Miller ID, Heys SD. (2010). Profiling the expression of cytochrome P450 in breast cancer. Histopathology, 57, 202-11.

Nakamura T, Sato M, Kakinuma H, Miyata N, Taniguchi K, Bando K, Koda A, Kameo K. (2003). Pyrazole and isoxazole derivatives as new, potent, and selective 20-hydroxy-5,8,11,14-eicosatetraenoic acid synthase inhibitors. J Med Chem, 46, 5416-27.

Nishikiori M, Iizuka H, Ichiba H, Sadamoto K, Fukushima T. (2015). Determination of free fatty acids in human serum by HPLC with fluorescence detection. J Chromatogr Sci, 53, 537-41.

Ortiz de Montellano PR. (2005). Cytochrome P450: Structure, Mechanism, and Biochemistry. New York, NY: Kluwer Academic/Plenum Publishers.

Ortiz de Montellano PR. (2018). 1-Aminobenzotriazole: A Mechanism-Based Cytochrome P450 Inhibitor and Probe of Cytochrome P450 Biology. Med Chem (Los Angeles), 8.

Promega P450-Glo. https://www.promega.com/resources/protocols/technical-bulletins/101/p450-glo-assays-protocol/ (accessed October 2019)

Panigrahy D, Greene ER, Pozzi A, Wang DW, Zeldin DC. (2011). EET signaling in cancer. Cancer Metastasis Rev, 30, 525-40.

Parkinson A, Kazmi F, Buckley DB, Yerino P, Paris BL, Holsapple J, Toren P, Otradovec SM, Ogilvie BW. (2011). An evaluation of the dilution method for identifying metabolism-dependent inhibitors of cytochrome P450 enzymes. Drug Metab Dispos, 39, 1370-87.

Radvanyi L, Singh-Sandhu D, Gallichan S, Lovitt C, Pedyczak A, Mallo G, Gish K, Kwok K, Hanna W, Zubovits J and others. (2005). The gene associated with trichorhinophalangeal syndrome in humans is overexpressed in breast cancer. Proc Natl Acad Sci U S A, 102, 11005-10.

Rieger MA, Ebner R, Bell DR, Kiessling A, Rohayem J, Schmitz M, Temme A, Rieber EP, Weigle B. (2004). Identification of a novel mammary-restricted cytochrome P450, CYP4Z1, with overexpression in breast carcinoma. Cancer Res, 64, 2357-64.

Roellecke K, Virts EL, Einholz R, Edson KZ, Altvater B, Rossig C, von Laer D, Scheckenbach K, Wagenmann M, Reinhardt D and others. (2016). Optimized human CYP4B1 in combination with the alkylator prodrug 4-ipomeanol serves as a novel suicide gene system for adoptive T-cell therapies.

Savas U, Hsu M-H, Griffin KJ, Bell DR, Johnson EF. (2005). Conditional regulation of the human CYP4X1 and CYP4Z1 genes. Archives of biochemistry and biophysics, 436, 377-85

Schulz C, Kammerer S, Küpper JH. (2019). NADPH-cytochrome P450 reductase expression and enzymatic activity in primary-like human hepatocytes and HepG2 cells for in vitro biotransformation studies. Clin Hemorheol Microcirc, 73, 249-60.

Silverman RB. (1988). Mechanism-Based Enzyme Inactivation: Chemistry and Enzymology. Boca Raton, FL: CRC Press.

Sodhi JK, Delarosa EM, Halladay JS, Driscoll JP, Mulder T, Dansette PM, Khojasteh SC. (2017). Inhibitory Effects of Trapping Agents of Sulfur Drug Reactive Intermediates against Major Human Cytochrome P450 Isoforms. Int J Mol Sci, 18.

U.S. Food & Drug Administration. https://www.fda.gov/drugs/drug-interactions-labeling/drug-development-and-drug-interactions-table-substrates-inhibitors-and-inducers (accessed October 2019)

Vogel AI, Tatchell A, Furnis BS, Hannaford AJ, Smith PWG. (1996). Vogel's Textbook of Practical Organic Chemistry, 5th Edition. New York, NY: John Wiley & Sons.

Wang E, Walsh C. (1978). Suicide substrates for the alanine racemase of Escherichia coli B. Biochemistry, 17, 1313-21.

Wang W, Qin S, Li L, Chen X, Wang Q, Wei J. (2015). An Optimized High Throughput Clean-Up Method Using Mixed-Mode SPE Plate for the Analysis of Free Arachidonic Acid in Plasma by LC-MS/MS. Int J Anal Chem, 2015, 374819.

Westerink WM, Schoonen WG. (2007). Cytochrome P450 enzyme levels in HepG2 cells and cryopreserved primary human hepatocytes and their induction in HepG2 cells. Toxicol In Vitro, 21, 1581-91.

Wiek C, Schmidt EM, Roellecke K, Freund M, Nakano M, Kelly EJ, Kaisers W, Yarov-Yarovoy V, Kramm CM, Rettie AE and others. (2015). Identification of amino acid determinants in CYP4B1 for optimal catalytic processing of 4-ipomeanol. Biochem J, 465, 103-14.

Woodcroft KJ, Szczepan EW, Knickle LC, Bend JR. (1990). Three N-aralkylated derivatives of 1-aminobenzotriazole as potent and isozyme-selective, mechanism-based inhibitors of guinea pig pulmonary cytochrome P-450 in vitro. Drug Metab Dispos, 18, 1031-7.

World Cancer Research Fund. https://www.wcrf.org/dietandcancer/cancer-trends/breast-cancer-statistics (accessed October 2019)

Yan Q, Machalz D, Zollner A, Sorensen EJ, Wolber G, Bureik M. (2017). Efficient substrate screening and inhibitor testing of human CYP4Z1 using permeabilized recombinant fission yeast. Biochem Pharmacol, 146, 174-87.

Yang X, Hutter M, Goh WWB, Bureik M. (2017). CYP4Z1 - A Human Cytochrome P450 Enzyme that Might Hold the Key to Curing Breast Cancer. Curr Pharm Des, 23, 2060-4.

Yu W, Chai H, Li Y, Zhao H, Xie X, Zheng H, Wang C, Wang X, Yang G, Cai X and others. (2012). Increased expression of CYP4Z1 promotes tumor angiogenesis and growth in human breast cancer. Toxicol Appl Pharmacol, 264, 73-83.

Zollner A, Dragan CA, Pistorius D, Muller R, Bode HB, Peters FT, Maurer HH, Bureik M. (2009). Human CYP4Z1 catalyzes the in-chain hydroxylation of lauric acid and myristic acid. Biol Chem, 390, 313-7.

Chapter 4

Pharmacokinetics, metabolism and off-target effects of 8-[(1H- benzotriazol-1-yl)amino]octanoic acid, a selective inhibitor of human cytochrome P450 4Z1, in the rat: *β*-oxidation as a potential augmenting pathway for inhibition

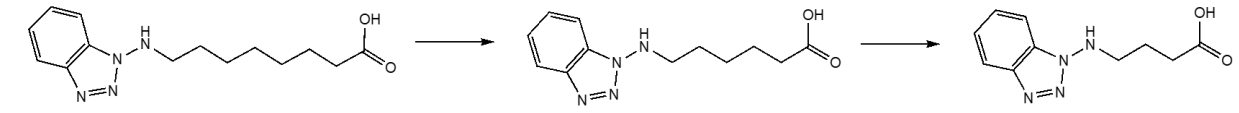

8-[(1H- benzotriazol-1-yl)amino]octanoic acid (**Parent**)

M9

M3

4.1 Introduction

During their lifetime, nearly 13% of US women will be diagnosed with invasive breast cancer, which is the most prevalent form and the second leading cause of mortality for this group (DeSantis et al., 2019). The elucidation of new molecular drivers of this complex disease and new drugs to treat metastases are urgently needed (Capper et al., 2016). Cytochrome P450 4Z1 (CYP4Z1) has been identified as a mammary tissue-restricted enzyme that is upregulated in breast cancer, with transcript levels that are associated with increased tumor grade and aggressiveness (Rieger et al., 2004; Radvanyi et al., 2005; Murray et al., 2010; Li et al., 2017; Al-Esawi et al., 2020). Furthermore, human CYP4Z1 is the only currently known functional enzyme in this subfamily (Yang et al., 2017).

As described in Chapter 3, 8-[(1H-1,2,3-benzotriazol-1-yl)amino]octanoic acid (8-BOA) is a selective and potent mechanism-based inactivator (MBI) of CYP4Z1 that can effectively inhibit

this enzyme's production of 14,15-epoxyeicosatrienoic acid (14,15-EET) (Kowalski et al., 2020), a pro-angiogenic and pro-metastatic metabolite of arachidonic acid (McDonald et al., 2017). While cell culture studies can be utilized to interrogate the role of CYP4Z1 in breast cancer the lack of interaction with a tumor microenvironment limits the predictive power of these experiments (Murayama and Gotoh, 2019). Therefore, to further the validation of CYP4Z1 as a drug target in breast cancer, a more complex cellular milieu, with its attendant heterogeneity of signaling ligands, is desirable for inhibitor testing.

The rat is preferred for pre-clinical rodent models of human disease due to the many physiological similarities between the species that are absent when using mice. The benefits are especially pronounced for breast cancer studies, as xenografted tumors in rats better parallel those in humans in regard to estrogen dependency, hormone therapy sensitivity, development, ductal origin, and simulation of phenotypic heterogeneity (Smits et al., 2007; Iannaccone and Jacob, 2009; Mollard et al., 2011). Additionally, recent advances in the generation of immunodeficient rats has furthered the use of this species in varied transplant settings, such as cell- or patient-derived xenograft (CDX/PDX) models of tumor growth (Noto et al., 2018; He et al., 2019).

Therefore, the aim of this pilot-scale study was to assess the *in vivo* characteristics of 8-BOA in the rat in order to design future CDX/PDX model breast cancer studies with this inhibitor. Herein, we show biphasic pharmacokinetics for 8-BOA, characterized by a rapid initial phase and a prolonged terminal phase. The derived pharmacokinetic parameters from a whole body two-compartment model fit indicate relatively low clearance and a high volume of distribution. Plasma concentrations were achieved that indicated CYP4Z1 inactivation could occur in a xenograft model. *β*-oxidation was identified as a major route of metabolism, generating a metabolite previously characterized as a CYP4Z1 MBI that may prolong the

desired inhibition effect. Finally, off-target CYP inactivation was found to be minimal and no indication of acute toxicity was observed.

4.2 Experimental procedures

4.2.1 Reagents

Stocks of 8-BOA and 6-[(1H-1,2,3-benzotriazol-1-yl)amino]hexanoic acid (6-BHA) used for all experiments were synthesized as described in Chapter 3. Benzotriazole-d_4 was purchased from CDN Isotopes (Pointe-Claire, Canada) and was used for inhouse synthesis of the deuterated internal standard (see below). Pooled rat (male Sprague Dawley) plasma and urine used as the matrix for protein binding and standards for 8-BOA quantification was purchased from BioIVT (Westbury, NY). Pooled rat (male Sprague Dawley) liver and kidney microsomes (RLM, RKM), derived from control and treated group rats for *ex vivo* experiments, were generated according to standard procedures for subcellular fractionation (Sadeque et al., 1992), and quantified *via* BCA assay (Thermo Fisher Scientific, Waltham, MA) according to the manufacturer's protocol. RLM and RKM used for *in vitro* experiments were purchased from Sekisui Xenotech (Kansas City, KS). Chloroform-d was purchased from Cambridge Isotope Laboratories, Inc (Andover, MA), reduced *β*-nicotinamide adenine dinucleotide phosphate (NADPH) was purchased from OYC Americas (Vista, CA), and formulation reagents (DMSO, PBS, and Solutol) were provided by Alliance Pharma. All solvents (Optima grade) were purchased from Thermo Fisher Scientific, and all other chemicals were purchased Sigma-Aldrich (St. Louis, MO).

4.2.2 Internal standard synthesis

8-{[(4,5,6,7-$^{2}H_4$)-1H-1,2,3-benzotriazol-1-yl]amino}octanoic acid (8-BOA-d_4) was synthesized using a modified protocol from our previous study and has been summarized in **Figure S4.1**. The additional step, amination of benzotriazole-d_4, was performed analogous to a previously reported method (Campbell and Rees, 1969). Accurate mass was determined *via* UPLC-MS on a Waters Acquity UPLC (Milford, MA) coupled to an AB Sciex TripleTOF 5600 mass spectrometer (Framingham, MA). ^{1}H NMR spectra was recorded at 25℃ in deuterated chloroform on a 499.73 MHz Agilent DD2 (Santa Clara, CA) spectrometer. Purity as determined by ^{1}H NMR spectroscopy was ≥95%. ^{1}H NMR (500 MHz, Chloroform-d) δ ppm 3.42 (t, J = 7.09 Hz, 2 H), 2.35 (t, J = 7.34 Hz, 2 H), 1.59 - 1.69 (m, 2 H), 1.54 (quin, J = 7.21 Hz, 2 H), 1.40 - 1.49 (m, 2 H), 1.31 - 1.38 (m, 4 H). HRMS (ESI^{+}) *m/z* $[M+H]^{+}$ calculated ($C_{14}H_{17}D_4N_4O_2$) 281.1910, observed 281.1909, δ ppm 0.4.The ^{1}H NMR spectrum for 8-BOA-d_4 has been provided in **Figure S4.2A** and the ^{1}H NMR spectrum for 8-BOA has been provided in **Figure S4.2B** for a comparison.

4.2.3 Depletion assays

To assess microsomal stability, the depletion of 8-BOA (and assay controls) was assessed after extended incubation in fortified microsomes. Reactions were set up on ice in triplicate and contained 0.5 mg/mL of either RLM or RKM, in 100 mM potassium phosphate (KPi), pH 7.4, and 3.2 mM $MgCl_2$, in a final volume of 0.5 mL. 8-BOA was added to both RLM and RKM reactions, while 7-hydroxy coumarin and midazolam were added only to RLM reactions, from 400 x DMSO stocks, to achieve final concentrations of 1 µM. After a 5 min equilibration at 37℃, the reactions were initiated by the addition of a mixture of NADPH, uridine 5′-diphosphoglucuronic acid (UDPGA), and alamethicin to achieve final concentrations of 1.5 mM, 5 mM, and 10 µg/mL, respectively. Aliquots (50 µL) were removed at times 0, 5, 15, 30, 60,

and 90 min and added to tubes containing identical volumes of ice-cold acetonitrile containing 0.5 μM of the internal standard 8-BOA-d_4 (for 8-BOA stability studies) or 7-hydroxy coumarin-d_3 (for 7-hydroxy coumarin and midazolam stability studies) to quench the reactions. All quenched reactions were stored at -20℃ until the end of the experiment. The samples were centrifuged for 10 min at 10,000 x g and 4℃, and then the supernatants were transferred to new tubes. For quantitation, calibration curves were prepared by separately spiking unlabeled standards for each test compound into an identical microsomal matrix spanning concentrations of 30 nM – 3 μM, in half-log dilutions, and underwent sample workup identical to that described above. Aliquots for all samples (5 μL) were then analyzed according to the *General LC-MS/MS method for the quantitation of 8-BOA, 6BHA, and assay controls* described below.

4.2.4 General LC-MS/MS method for the quantitation of 8-BOA, 6-BHA and assay controls

Aliquots were analyzed by UPLC-MS/MS on a Waters Acquity UPLC connected to a Waters Xevo TQ-S instrument in ESI^- mode, with the following settings: capillary 2.0 kV, source offset 60.0 V, source temperature 150℃, desolvation temperature 350℃, cone gas flow 150 L/hr, desolvation gas flow 800 L/hr, collision gas flow 0.15 mL/min, cone voltage 30 V, and collision energy 15 eV. Chromatographic separation of analytes was achieved using a Waters BEH C_{18} column (2.1 x 50 mm, 1.7 μm), starting with 90% mobile phase A (0.1% formic acid in water) and 10% mobile phase B (0.1% formic acid in acetonitrile) at a flow rate of 0.3 mL/min. After a 1 min hold, B was increased linearly from 10 to 95% between 1 and 3 min and held at 95% between 3.5 and 5.5 min; the total run time was 7 min following a 1.5 min period for equilibration. The analytes and isotope-labeled internal standards were detected by multiple reaction monitoring (MRM) in electrospray negative mode (ESI^-) with the following transitions and retention times: 8-BOA *m/z* 275.15 > 154, 8-BOA-d_4 279.16 > 154 (2.9 min), warfarin 307 > 161, warfarin-d_5 312 > 161 (3.2 min), and 6-BHA 247 > 118 (2.7 min). The following were detected by MRM in ESI^+ mode: 7-hydroxy coumarin *m/z* 163 > 119, 7-hydroxy coumarin-d_3 166

> 122 (2.4 min), and midazolam 327 > 292 (2.5 min). Analysis of the mass spectra was performed with Waters MassLynx V4.1**.**

4.2.5 Plasma protein binding

In vitro analysis of plasma protein binding was performed for 8-BOA, 6-BHA, and Warfarin as an assay control. Compounds were spiked separately into pooled male Sprague Dawley rat plasma to achieve final concentrations of 3 µM. A dialysis method was followed using rapid equilibrium dialysis devices according to the manufacturer's protocol (ThermoFisher Scientific). After the incubation period, ice-cold acetonitrile, containing the internal standard 8-BOA-d_4 (for both 8-BOA and 6-BHA samples), or Warfarin-d_5, at 0.5 µM and 0.1% formic acid was added at a 3:1 ratio. The samples were centrifuged for 10 min at 10,000 x g and 4℃, and then the supernatants were transferred to new tubes. Aliquots for all samples (5 µL) were then analyzed according to the *General LC-MS/MS method for the quantitation of 8-BOA, 6BHA, and assay controls.*

4.2.6 Determination of CYP content

In vitro inactivation

Inactivation reactions were set up on ice and contained RLM (Sekisui Xenotech) at 1 mg/mL in 100 mM KPi, pH 7.4 and 3.2 mM $MgCl_2$, in a final volume of 1.2 mL. 8-BOA was added from 400 x DSMO stocks to achieve concentrations of 100 or 500 µM, or an equal volume of DMSO was added. After a 5 min period for equilibration at 37℃, NADPH was added (1 mM final concentration) to all conditions to initiate the reactions. Following a 30 min incubation, 0.55 mL aliquots were removed from each condition and immediately placed into either a sample or reference cuvette. CYP content was then measured with an Olis Aminco DW-2 spectrophotometer (Bogart, GA) following the standard procedure for carbon monoxide (CO)

binding difference spectra (Guengerich et al., 2009). Note: reactions were performed at separate times to ensure incubation time consistency between conditions.

Ex vivo CYP content

Mixtures were set up on ice in duplicate and contained either pooled RLM or RKM, that were derived from treated or control group rats, at concentrations of 2 mg/mL in 100 mM KPi, pH 7.4, with 0.5% sodium cholate w/v, in a final volume of 1.2 mL. 0.55 mL aliquots for each condition were split between sample and reference cuvettes and CYP content was measured as described above.

4.2.7 Animal studies

Animal procedures were performed in full compliance with all applicable regulations by Alliance Pharma (Malvern, PA). Following a two day facility acclimation period, three male Sprague Dawley rats, weighing between 0.307 – 0.316 kg, received intravenous (IV) bolus administration of 8-BOA (4 mg/mL in PBS, 67%; Solutol, 30%; DMSO, 3%) at 10 mg/kg and a dose volume of 2.5 mL/kg. A control group of three rats, weighing between 0.303 – 0.320 kg, received the same formulation as above, minus 8-BOA. The study proceeded for 24 hours and serial blood collections (tail bleeds) were taken at pre-dose, 5, 15, 30 min, 1, 2, 4, 8, and 24 hr, and plasma was separated. After euthanasia, necropsies were performed and liver and kidney were collected from each animal, and urine was collected from the bladders. Samples were then shipped on dry ice overnight for inhouse bioanalysis. Standard clinical chemistries were performed by Phoenix Lab (Mukilteo, WA) on plasma from both control and treated groups for pre-dose and 24-hour timepoints.

4.2.8 Determination of 8-BOA plasma concentrations

Plasma samples were thawed on ice and 20 µL aliquots were transferred to new tubes. To these, 60 µL of ice-cold acetonitrile, containing 5 µM 8-BOA-d_4 and 0.1% formic acid, was added. The samples were centrifuged for 10 min at 10,000 x g and 4℃, and then the supernatants were transferred to new tubes. A calibration curve was prepared for quantification; 8-BOA was spiked into pooled male Sprague Dawley rat plasma from 200 x DMSO stocks to achieve concentrations ranging from 1 nM – 1 mM, in half-log dilutions (a DMSO control was also prepared). The standards were subjected to the same sample workup as described above and aliquots for all samples (5 µL) were then analyzed according to the *General LC-MS/MS method for the quantitation of 8-BOA, 6BHA, and assay controls.*

After plotting the time – concentration profile, the data was then fit to the standard 2-compartment model using Graphpad Prism 7.00 (San Diego, CA) according to the equation: $C = Ae^{-\alpha t} + Be^{-\beta t}$. Pharmacokinetic parameters were subsequently calculated using the resultant hybrid constants.

4.2.9 Metabolite identification

Sample preparation

Equal volumes of remaining plasma were separately pooled from the time points spanning 5-min to 24-hr for treated and control group rats. A 6-fold volume of ice-cold acetonitrile was added, the samples vortexed briefly, centrifuged for 10 min at 10,000 x g and 4℃, and then the supernatants were transferred to new tubes. The samples were dried under a constant stream of N_2 at room temperature, resuspended in 150 µL of a 70/30 mixture of water/acetonitrile, and then stored at 4℃ until use.

Equal volumes of urine from the bladder collections at the 24-hr time point for the control group as well as for the 8-BOA treated rats were combined and the internal standard 8-BOA-d_4 was spiked in to achieve a final concentration of 100 nM (to enable quantification of any remaining 8-BOA parent). To create a callibration curve, pooled male Sprague Dawley rat urine was spiked with 8-BOA from 200 x DMSO stocks to achieve final concentrations from 1 – 1000 nM, in half-dilutions, and 8-BOA-d_4 was added to achieve a final concentration of 100 nM. The pH was adjusted to ~2 with acetic acid for all urine samples and they were subsequently extracted three times with a 50/50 mixture of diethyl ether/ethyl acetate. The combined organic fractions were dried under a constant stream of N_2 at room temperature, resuspended in 150 µL of a 70/30 mixture of water/acetonitrile, and then stored at 4 ℃ until use. A portion was assayed for 8-BOA concentration according to the *General LC-MS/MS method for the quantitation of 8-BOA, 6BHA, and assay controls.*

Qualitative LC-MS/MS profiling for 8-BOA rat metabolites

Aliquots (30 µL) were analyzed by UPLC-MS/MS on a Waters Acquity UPLC connected to an AB Sciex TripleTOF 5600 mass spectrometer in both $ESI^{+/-}$ modes (separately) with parent and product ions acquired concurrently in the same period using settings for experiment 1 and 2, respectively. For experiment 1, TOF MS scanning was restricted to a 50 – 1000 Da range with a cycle time of 0.55 sec and an accumulation time of 0.1 sec. Information dependent acquisition (IDA) used switch criteria settings that required ions to be >100 *m/z*, exceed 150 cps, and to exclude former target ions for 1 second. The nominal mass of 8-BOA was set to 276 Da, a 700 Da formula width was used, and a mass defect of 158.6261 mDa was applied; mass tolerance was 50 mDa. Settings for DP, CE, and XA1 were 100, 5, and 136.62, respectively. For experiment 2, TOF MS/MS scanning was again restricted to a 50 – 1000 Da range with an accumulation time of 0.1 sec. For this product ion acquisition, settings for DP, CE, CES, IRD,

IRW, and XA1 were 100, 35, 20, 67, 25, and 70.16, respectively. For both experiment 1 and 2, settings for GS1, GS2, CUR, TEM, and ISVF were 60, 60, 35, 600, and 4500, respectively.

Chromatographic separation of analytes was achieved using a Waters SunFire C_{18} column (2.1 x 150 mm, 3.5 µm), starting with 100% mobile phase A (0.1% formic acid in water) and 0% mobile phase B (0.1% formic acid in acetonitrile) at a flow rate of 0.3 mL/min. After a 1 min hold, B was increased linearly from 0 to 100% between 1 and 14 min and held at 100% between 14 and 15.1 min; the total run time was 20 min following a 4.9 min period for equilibration. Analysis of the mass spectra was performed with SCIEX Metabolite Pilot V2.0 with the settings as described below**.**

Metabolite pilot settings

8-BOA and 6-BHA were each run as parent compounds (as 6-BHA was identified later as a major metabolite that downstream biotransformation processes could conceivably occur to), therefore reference MS/MS spectra for both was provided. Control group samples for both urine and plasma matrices were run in conjunction with the treated group and acted as the background filtering control for metabolite peaks. The processing parameters for Metabolite Pilot in both $ESI^{+/-}$ modes consisted of the following TOF MS settings: predicted metabolites, generic peak finding, application of mass defect filter, and isotope pattern. The TOF MS/MS settings consisted of the following: find at least 2 characteristic product ions, find at least 1 characteristic neutral loss, and consider internal neutral losses. The biotransformation set contained 100 phase I/II and amino acid conjugation pathways. MS *m/z* tolerance was set to 20 ppm and the minimum MS peak intensity was set to 200 CPS; MS/MS *m/z* tolerance was set to 10 mDa and the minimum MS/MS peak intensity was set to 100 cps. In addition to identifying protonated/de-protonated metabolites, other common adducts were also searched for. Results were manually filtered and metabolites were excluded that either a) completely lacked MS/MS

spectra (and weren't identified in the other ESI mode), b) showed a <10-fold difference in signal intensity between control and sample, c) were readily interpreted as in-source fragmentation (unless they were notable and hence were included), or d) displayed peak chromatography consistent with a slight offset to a control peak and therefore was artifactually identified as a metabolite by the program.

4.2.10 CYP activity assays

Reaction set-up

For CYP activity comparisons between the pooled RLM derived from treated and control group rats, the probe substrates and the biotransformations that were monitored (all done separately) were as follows: CYP1A/-2C phenacetin *O*-deethylation, CYP2C/-2D dextromethorphan *O*-demethylation, and CYP3A/-CYPC midazolam 1'-hydroxylation. Reactions were set up on ice in triplicate and contained microsomes at 0.25 mg/mL protein in 100 mM KPi pH 7.4, with 3.2 mM $MgCl_2$, in a final volume of 200 µL. 400 x DMSO stocks of the above listed probe substrates were each added independently to the reactions to achieve final concentrations of 10 µM. After a 5 min period at 37℃ for equilibration, the reactions were started by the addition of NADPH at a final concentration 1 mM. The reactions were quenched after 20 min with an equal volume of ice-cold acetonitrile containing a mix of all deuterated internal standards at a concentration of 200 nM each. The samples were centrifuged for 10 min at 10,000 x g and 4℃, and then the supernatants were transferred to new tubes. For quantitation, metabolite standards were spiked all together into an identical matrix to attain concentrations spanning 0.001 – 1 µM, in half-log dilutions, and underwent sample workup identical to what is described above.

LC-MS/MS method for quantification of probe substrate metabolites

Aliquots (5 µL) were analyzed by UPLC-MS/MS on a Waters Acquity UPLC connected to a Waters Xevo TQ-S instrument in ESI^+ mode, with the following settings: capillary 2.9 kV, source offset 60.0 V, source temperature 150℃, desolvation temperature 350℃, cone gas flow 150 L/hr, desolvation gas flow 800 L/hr, collision gas flow 0.15 mL/min, cone voltage 40 V, and collision energies of 20 eV for acetaminophen and 30 eV for the other analytes. Chromatographic separation utilized a Waters HSS T3 column (2.1 x 100 mm, 1.8 µm), starting with 95% mobile phase A (0.1% formic acid in water) and 5% mobile phase B (0.1% formic acid in acetonitrile) at a flow rate of 0.3 mL/min. After a 1 min hold, B was increased linearly from 5 to 60% between 1 and 7 min, immediately increased to 95%, and then held at 95% between 7 and 8.5 min; the total run time was 11 min following a 2.5 min period for equilibration. The metabolites and isotope-labeled internal standards were detected by MRM with the following transitions and retention times: acetaminophen *m/z* 152 > 110, acetaminophen-d_3 155 > 111 (3.3 min), dextrorphan 258 > 157, dextrorphan-d_3 261 > 157 (4.5 min), 1-hydroxymidazolam 342 > 203, and 1-hydroxymidazolam-d_4 346 > 203 (5.4 min). Analysis of the mass spectra was performed with Waters MassLynx V4.1 software.

4.2.11 CYP inactivation simulations

The extrapolation of 8-BOA plasma concentrations to inactivation of the target CYP4Z1, in a theoretical rat xenograft, was performed using the 2-compartment model parameters outlined above to calculate drug concentrations and then using the following equations:

$$drug_{free} = f_u \times drug$$

$$\lambda = (drug_{free} \times k_{inact})/(drug_{free} + K_I)$$

$$\frac{E_I}{E_{SS}} = e^{-(\lambda + k_{deg}) \times \Delta t} + (k_{deg} \times \Delta t)$$

The simulation was performed in Excel with the following parameters:

$f_u = 0.02$

$k_{inact} = 0.15\ min^{-1}$

$K_I = 2.2\ \mu M\ \left(0.607\ \frac{\mu g}{mL}\right)$

$k_{deg} = 0.00048\ min^{-1}\ (t_{1/2} = 1\ day)$

$k_{deg} = 0.00024\ min^{-1} (t_{1/2} = 2\ days)$

$k_{deg} = 0.00012\ min^{-1} (t_{1/2} = 4\ days)$

$\Delta t = 15\ min.$

Values for $drug_{free}$ and then λ (rate of inactivation at the specific $drug_{free}$ concentrations), were determined for each timepoint in 15 min time-step intervals over the course of the 96-hr simulation. Subsequently, starting from values at time zero, the equation to calculate $\frac{E_I}{E_{SS}}$ (relative enzyme amount under inactivation conditions, E_I, compared to enzyme at steady state, E_{SS}) was employed. This equation combined the first-order processes of enzyme degradation and inactivation (exponential decay) with the zero-order process of enzyme re-synthesis. All subsequent values calculated for $\frac{E_I}{E_{SS}}$ were performed on the previously calculated $\frac{E_I}{E_{SS}}$ fraction such that inactivation was iterative with time. Values for $\frac{E_I}{E_{SS}}$ were computed using the three different k_{deg} values above that spanned 1 – 4 days, to assess a range of inactivation conditions. In this simulation, plasma $drug_{free}$ concentrations were assumed to equal intratumoral concentrations, the tumor was assumed to be in the central compartment, and the

protein binding of 8-BOA for the *in vitro* conditions used to calculate k_{inact} and K_I in CYP4Z1 membranes was assumed to be minimal. Although not determined experimentally, if protein binding of 8-BOA to membranes were substantial, this would result in a lowered effective K_I and increased potency of inactivation in this model.

4.3 Results

4.3.1 Metabolic stability

In order to evaluate microsomal stability and the contributions of CYP- and uridine 5'-diphospho-glucuronosyltransferase (UGT)- mediated metabolism to clearance, 8-BOA at an initial concentration of 1 µM was incubated for an extended period with RLM or RKM that had been fortified with NADPH and UDPGA. After 90 min, 8-BOA concentrations were reduced by ~6 and ~4% for RLM and RKM, respectively (**Figure 4.1A**). Minimal depletion was also evident when 3 µM of 8-BOA was used (data not shown). Although calculation of an *in vitro* microsomal $t_{1/2}$ for 8-BOA was not practical due to the negligible decline and margin of error for measurements, we estimate these values to be >12 hr. In control RLM studies, midazolam and 7-hydroxy coumarin depletion both displayed *in vitro* $t_{1/2}$ values of <5 min (data not shown).

4.3.2 Off-target CYP inactivation

To assess degree of off-target microsomal CYP inactivation caused by 8-BOA, carbon-monoxide (CO)-binding spectra were recorded for NADPH-fortified RLM after incubation with 8-BOA or DMSO vehicle (**Figure 4.1B)**. After 30-minute incubations the CYP contents were 0.62, 0.57, and 0.34 nmol/mg protein for the DMSO control, 100, and 500 µM of 8-BOA, respectively. This equates to dose-dependent losses of 7-45% in liver microsomal CYP content.

4.3.3 Plasma protein binding

As determined by rapid equilibrium dialysis with LC-MS/MS quantitation, 8-BOA and 6-BHA (3 µM) were bound 98 ± 0.2 and 75 ± 4%, respectively, to rat plasma proteins. Warfarin, used as an assay control, was bound 99 ± 0.01%, as expected.

4.3.4 Pharmacokinetics of 8-BOA

The time-concentration profile of 8-BOA in plasma after IV bolus administration at 10 mg/kg is shown in **Figure 4.2**. Inter-animal variability was relatively low, and the profile exhibited a multi-exponential pattern, indicative of both distribution and elimination phases being present. Therefore, the standard whole body 2-compartmental model was fit to the data, which yielded the following hybrid values: A = 43.45, α = 3.32, B = 0.068, β = 0.12. The pharmacokinetic constants resulting from this analysis are summarized in **Table 4.1**. Prolonged, albeit low, exposure to 8-BOA was observed and both the $t_{1/2}$ and V_d increased substantially from the *α* to *β* phases.

4.3.5 Metabolite identification

Plasma Profiling

LC-MS/MS analysis was performed in both ESI^+ and ESI^- mode to ensure the best coverage of analytes, since ESI^- would likely be required to detect some acid-containing metabolites. Given the complexity of the matrices involved, this ensured that mass-defect filtering with information-dependent acquisition (IDA) would have the most opportunities to trigger MS/MS fragmentation required for metabolite identification.

A complex profile of 25 total metabolites were detected by LC-MS/MS in the plasma of rats following IV administration of 8-BOA. The extracted ion chromatograms (XICs) for both ESI^+ and ESI^- modes used for metabolite identification are shown in **Figure 4.3.** While **M3 – M10, M13, M15,** and **M16** were detected in both modes, **M1, M2, M11, M12** and **M14** were detected only in ESI^+, and **M17 – M25** were detected only in ESI^-. Given that the plasma was pooled from timepoints spanning 5 min - 24 hr, in order to increase metabolite MS counts, the **Parent** 8-BOA constituted a dominant signal. Therefore, the chromatograms showing metabolites in both modes have the **Parent** peak plotted at 5% of the detected intensity for ease of viewing. In ESI^+ mode, **M9, M3, M6,** and **M8** were the major metabolites by peak area, and accounted for 67% of the total profile, with **M9** and **M3** themselves accounting for 28 and 20%, respectively. These same four metabolites accounted for 48% of the total profile in ESI^- mode.

ESI^+ plasma metabolite assignments

All metabolites were observed as the protonated ion $[M+H]^+$, except **M1** as $[M]^+$, and these were absent from pooled plasma derived from the control group. LC-MS/MS analysis of the reference standard for the **Parent** 8-BOA (**Figure 4.4B)** was identical to that observed in plasma and provided diagnostic fragments, e.g. *m/z* 135, 119, and 90, which aided in metabolite assignments. Characteristic dehydration of the carboxylic acid (minus 18 Da) and dehydration plus loss of N_2 (minus 46 Da) were also commonly observed. For ease of viewing, the annotated structure fragment ions are listed without defect values. These are shown in the MS/MS spectra where differential defects from equivalent nominal masses can be discerned between structures.

The largest metabolite by peak area, **M9** (*m/z* 249.13 $[M+H]^+$), was assigned as having the formula $C_{12}H_{16}N_4O_2$ that corresponded to the **Parent** 8-BOA undergoing one round of b-oxidation (loss of two methylene units). **M9** displayed ions *m/z* 231, corresponding to

dehydration, and *m/z* 203, corresponding to dehydration plus loss of N_2 (**Figure 4.5A**). The MS/MS and retention time of **M9** was identical to that of the reference standard for the chain-shortened analog 6-[(1H-1,2,3-benzotriazol-1-yl)amino]hexanoic acid (6-BHA, **Figure 4.4A, C**), thus confirming the structure for this major metabolite.

The metabolite with the next greatest peak area, **M3** (*m/z* 221.10 $[M+H]^+$), was assigned the formula $C_{10}H_{12}N_4O_2$, which is consistent with the **Parent** 8-BOA undergoing two rounds of b-oxidation (loss of four methylene units). MS/MS of **M3** identified an ion at *m/z* 175 corresponding to dehydration plus loss of N_2 (**Figure 4.5B**). Additionally, the retention time of **M3** matched the relative elution progression observed for the **Parent** 8-BOA and the metabolite 6-BHA (**M9**). Therefore, although lacking a reference standard, there is strong evidence for assigning **M3** as 4-[(1H-1,2,3-benzotriazol-1-yl)amino]butanoic acid (4-BBA).

The presence of four mono-hydroxylated metabolites in the profile was indicated by their shorter elution times and gain of 16 Da, relative to the **Parent**, resulting in molecular ions of *m/z* 293.16 $[M+H]^+$, with **M6** and **M8** dominating. The MS/MS spectra for **M6** is shown in **Figure 5C,** where sequential dehydration generated fragments of *m/z* 275 and 257, followed by removal of CO to generate *m/z* 231. This fragment ion of *m/z* 231 was unique to **M6** and definitively allows for assignment as the *β*-hydroxy metabolite since cleavage of this bond is diagnostic for such regiospecificity. The concomitant aldehyde that is formed from this fragmentation (oxidation of the former *β*-hydroxyl group) also resulted in the expected ion of *m/z* 233. Similarly, **M8** was assigned as the α-hydroxy metabolite due to the strong signal for the diagnostic ion of *m/z* 247, representing cleavage between the α-hydroxy and carboxylic acid moiety. For **M4** and **M5,** the fragment ions *m/z* 160 and 132 were consistent with oxidation occurring at the *γ*- through ε-positions of the aliphatic tail, and furthermore, no strong evidence of hydroxylation on the ABT

moiety was observed. However, due to the limited MS/MS spectra and lack of reference standards, absolute regiospecificity could not be defined.

The metabolite **M7** (*m/*z 291.14 $[M+H]^+$) exhibited fragmentation consistent with ketone formation at the *β*-carbon, while fragmentation of the desaturation metabolites **M11** and **M12** (*m/z* 275.15 $[M+H]^+$) placed the olefins on the alkyl-acid chain but could not define exact positions. **M15**, another apparent desaturation product, eluted later than the **Parent** and had a matching retention time to an intermediate from the synthesis of 8-BOA. Therefore, it was assigned as the imine positioned adjacent to ABT (data not shown). Various other metabolites were consistent with parent methylations of varying regiospecificity (**M13, M16**)**,** loss of the side chain $-C_8H_{14}O_2$ to generate **M2** (i.e. ABT, also confirmed through a reference standard) and **M1**, the carnitine conjugate of **M3**. All 16 metabolites identified in ESI^+ mode are summarized in **Table 4.2**, and the MS/MS spectra that aided in the structural assignments for all metabolites have been provided in the Supporting Information.

ESI^- plasma metabolite assignments

All metabolites were observed as the de-protonated ion $[M-H]^-$ (although other minor adducts were also present) and were absent from pooled plasma derived from the control group (Table 3). In ESI^- mode, the major metabolites **M9, M6,** and **M8** all possessed fragmentation consistent with the previously assigned structures derived from their ESI^+ fragmentation profile, although the ESI^- MS/MS spectra proved less diagnostic in general. While the molecular ion for **M3** (*m/z* 219.09 $[M-H]^-$) still generated a strong signal, no MS/MS spectral fragments were triggered for this metabolite.

Notably, ESI^- analysis revealed **M20 – M23** as glucuronide conjugates, which in total accounted for ~13% of the total peak area for metabolites observed in this mode (**Figure**

S4.3A). M20 and **M22** had identical mass fragmentation profiles (*m/z* 451.18 $[M-H]^-$) **(Figure S4.3B),** and were assigned the formula $C_{20}H_{28}N_4O_8$, which is consistent with glucuronidation of the **Parent**. Fragmentation produced the aglycone ion at *m/z* 275, with the corresponding dehydrated glucuronate at *m/z* 175, and the further dehydrated glucuronate minus CO_2 at *m/z* 113. Direct fragmentation evidence for the acyl-glucuronide is provided by the *m/z* 193 ion, which represents the full glucuronate that would be absent for the *N*-glucuronide. Furthermore, the ion at *m/z* 133 confirmed the presence of the ABT moiety. Although only the 1-*β* anomer is depicted in the annotated scheme, **M20** may in fact be the 1-*β* anomer while the **M22** cluster likely represents a mix of the 2-, 3- and 4-*α/β* acyl-glucuronide anomers.

Metabolites **M21** and **M23** also showed similar fragmentation profiles (*m/z* 319.14 $[M-H]^-$) and were assigned the formula $C_{14}H_{24}O_8$, which corresponded to acyl-glucuronide structures of the **Parent** minus the ABT moiety. Fragmentation of **M21** (**Figure S3C**) produced the aglycone ion at *m/z* 143, the expected dehydrated glucuronate at *m/z* 175, and the further dehydrated glucuronate minus CO_2 at *m/z* 113. **M21** and **M23** had nearly overlapping retention times with the aforementioned acyl-glucuronide cluster and therefore may be artifactually generated *via* in-source fragmentation of **M22** or sample work-up.

M17, M18, and **M25**, all exhibiting gains in mass over the **Parent**, could not be assigned as MS/MS fragmentation was limited. All 20 metabolites identified in ESI^- mode and their assigned structures have been summarized in **Table 3,** with the corresponding MS/MS spectra provided in the Supporting Information.

Major urinary metabolites

Analysis of urine was performed on a limited bladder collection volume from the 24-hr necropsies, therefore, only the major metabolites are reported. A small amount of the **Parent** 8-

BOA was excreted unchanged, with an average concentration of ~9 nM in the 24-hr urine. **M3**, the tetra-demethylenation product, was the major metabolite in ESI^+ mode, with matching retention time and fragmentation to that seen in plasma (**Figure S4.4A, C**). Semi-quantitation using 8-BOA calibration standards resulted in an average **M3** concentration of ~390 nM. **M21**, the acyl-glucuronide minus ABT, appeared to be the major metabolite in ESI^- mode, with matching retention time and fragmentation to that seen in plasma (**Figure S4.4B, D**). Again, **M21** may not be a unique metabolite in itself, but rather an artifact of in-source fragmentation.

4.3.6 Ex vivo analysis

Off-target CYP inactivation

To assess the degree of off-target CYP inactivation *in vivo* from 8-BOA treatment, liver and kidney microsomes prepared from both control and treated groups were used for *ex vivo* CO-binding experiments to quantify the total pool of CYP content. Pooled liver microsomes yielded values of 0.71 and 0.60 nmol/mg for the control and treated rats, respectively, equating to a ~15% decrease due to treatment with 8-BOA. No appreciable difference in kidney microsomal CYP content was evident, with concentrations equaling 0.13 and 0.14 nmol/mg for control and treated samples, respectively (**Figure 4.6A**).

Off-target CYP activity

As another measure of off-target inhibition*, ex vivo* analysis of midazolam 1'-hydroxylation (M1OH), dextromethorphan *O*-demethylation (DOD), and phenacetin *O*-deethylation (POD) activities was performed to assess CYP3A, -2C, and -1A activity, respectively, in liver microsomes derived from both control and treated groups. Rates of M1OH, DOD, and POD for control microsomes were 42.5 ± 1.0, 113 ± 0.7, and 31.0 ± 1.0 pmol/mg protein/min, respectively (average ± SD). Rates of M1OH, DOD, and POD for treated

microsomes were 43.7 ± 2.0, 118 ± 6.0, and 26.8 ± 2.0 pmol/mg protein/min, respectively (**Figure 6B**). While no decreases in M1OH or DOD activity were evident, a minimal 8.6% decrease in POD activity (CYP1A) was observed.

Clinical chemistries

Standard markers of liver and kidney function were assessed in plasma for the vehicle control group and the 8-BOA treated group for both pre-infusion and 24 hr post-infusion timepoints. Most analytes changed very little between conditions, with the exceptions of glucose (GLU) and aspartate aminotransferase (AST). Control and treated groups both saw ~2.7-fold decreases in GLU, and 2.0- and 1.7-fold increases, respectively, in AST levels from pre-infusion to 24-hr. Overall, no indication of acute toxicity arising from treatment with the test article was observed. The results for all analytes, groups, and timepoints are summarized in **Table S4.1**.

4.3.7 Simulated in vivo CYP4Z1 inhibition

The 8-BOA time – plasma concentration profile from the current study was used to simulate the effect this inhibitor would have on CYP4Z1, if it were expressed in a highly perfused xenografted tumor in the rat. Using constants obtained *in vitro* to characterize the inactivation kinetics of 8-BOA towards CYP4Z1 (*ie* K_I and k_{inact}), the fraction of CYP4Z1 enzyme inhibited (E_I) over enzyme at steady state (E_{SS}) was modeled from time 0 (pre-dose) to 96-hr post dose. From a starting point of 1.0 at time 0, the lowest values of E_I/E_{SS} were modeled to occur at 1.25, 1.5, and 2.25 hr and were 0.18, 0.16, and 0.15 for the scenarios corresponding to a $t_{1/2}$ of 1, 2, and 4 days, respectively. Values for E_I/E_{SS} at 24 hours post-treatment were 0.55, 0.37, and 0.23 for $t_{1/2}$ of 1, 2, and 4 days, respectively. After 96 hr, values of E_I/E_{SS} were 0.95, 0.78, 0.49 for $t_{1/2}$ of 1, 2, and 4 days, respectively (data not shown).

4.4 Discussion

We recently designed and characterized 8-BOA as a selective, and mechanism-based, inhibitor of mammary-restricted human CYP4Z1. Through inhibition of this target enzyme, we could expect to lower production of its PUFA-derived pro-angiogenic metabolites (such as 14,15-EET), thereby potentially reducing the growth of metastatic breast cancer. However, detailed assessment of the inhibitor's *in vivo* pharmacokinetic characteristics are necessary to guide the design of CDX/PDX-rodent model experiments and to evaluate whether a prodrug approach or bioisosteric modifications would further lead compound optimization. The complexities surrounding pre-clinical models of breast cancer are well modelled in rats, and this species better mimics human physiology in comparison to mice (Smits et al., 2007; Iannaccone and Jacob, 2009; Mollard et al., 2011). Therefore, the rat was used to capitalize on these aspects and, additionally, the practical considerations for this pilot study of enabling serial blood draws with a minimal number of animals.

Preliminary *in vitro* experiments assaying for metabolic stability of 8-BOA in liver and kidney microsomes (supplemented with co-factors to predict both CYP- and UGT-mediated clearance) indicated the test article is a highly stable compound, as minimal depletion of 8-BOA was observed. We reasoned that this lack of depletion might be due to potent inactivation of rat CYP isoforms by this ABT analog. However, as evidenced by minimal inactivation of the general pool of rat liver microsomal CYPs following treatment with 100 µM of 8-BOA, this was clearly not the case *in vitro*. Therefore, we hypothesized that 8-BOA may either experience a prolonged half-life *in vivo or* be excreted substantially unchanged.

A single low dose of 10 mg/kg was chosen to avoid potential organ toxicities that might arise, as this was the first *in vivo* study for this new chemical entity. IV bolus administration was utilized to enable the highest potential plasma concentration as we were not concerned with oral

bioavailability at this stage of interrogation. This produced a plasma C_{max} of 158 µM and a bi-phasic profile displaying a short $t_{1/2,\alpha}$ of 0.21 hr into a substantially longer $t_{1/2,\beta}$ of 5.6 hr. Analysis of the volumes of distribution showed that V_α and V_β were ~ 0.43- and 11-fold the total body water of the rat (~167 mL; Davies and Morris, 1993), respectively, suggesting that the test article becomes widely distributed. These half-lives and volumes are consistent with a rapid distribution phase followed by a slow elimination phase. Although we cannot say at this time that 8-BOA would infiltrate into a tumor microenvironment directly, these data provide evidence that 8-BOA penetrates tissues to a substantial extent. If future studies demonstrate that an increase in lipophilicity is required to raise tissue concentrations, esterification of the carboxylic acid may be an effective strategy. Typically, extraction ratios (*CL* / liver blood flow) of >0.7 are regarded as indicative of high, 0.3 – 0.7 as intermediate, and <0.3 as a low clearance compound (Rowland and Tozer, 2011). Assuming that hepatic clearance dominates, the extraction ratio for 8-BOA (relative to a rat blood flow of ~830 mL/hr; Davies and Morris, 1993) is 0.28, predicting low body clearance.

Scaling *in vitro* data for the prediction of drug-drug interactions due to mechanism-based inactivation of CYPs for drug candidates has become common practice (Obach et al., 2007). We previously characterized the MBI parameters *in vitro* for the inactivation of CYP4Z1 by 8-BOA, resulting in a K_I = 2.2 µM and a k_{inact} = 0.15 min^{-1} (Kowalski et al., 2020). These values, taken together with the pharmacokinetic profile, allowed for an estimation of the potential CYP4Z1 inactivation that would occur in a xenograft model where the tumor expresses this enzyme. Contrary to an *in vitro* setting where the target enzyme can become virtually all depleted, *de novo* synthesis occurring *in vivo* will regenerate the enzyme pool concurrently. The turnover half-lives that have been determined for CYPs vary widely due to both isoform differences as well as the technically challenging, and indirect methods of measurement that are employed. As this information is clearly lacking for CYP4Z1, we used a $t_{1/2}$ range of 1 – 4 days

to encompass the spectrum that has been reported for this constant (Zhang and Wong, 2005; Yang et al., 2008). Furthermore, for this simple exercise, intratumoral exposure to the unbound fraction of 8-BOA (2%) was modeled as occurring in the central compartment, ignoring both the lag-time to reach a peripheral tumor, and the potential for the concentration to build inside the tumor.

The simulation in **Figure 4.7** shows a rapid decline of enzyme after exposure to inhibitor (E_I), as a fraction of starting enzyme at steady state (E_{SS}). This resulted in a nadir of 0.15 – 0.18, suggesting CYP4Z1 activity would be decreased by 82 – 85%. After 24 hr, values for E_I/E_{SS} remained < 0.6, indicating that all three $t_{1/2}$ scenarios result in prolonged CYP4Z1 inactivation from a single administration of 8-BOA. Therefore, given the relatively rapid and potent inactivation from 8-BOA and the time required for enzyme re-synthesis, maintaining constant high concentrations for reversible inhibition *in vivo* is not expected to be required for efficacy against the hypothesized pro-metastatic activity of CYP4Z1 (*i.e.* as a 14,15-EET synthase).

Use of both ESI^+ and ESI^- modes in LC-MS/MS proved to be an effective strategy for metabolite identification as several metabolites were unique in their mode of ionization and fragmentation profile. While clearly there are ionization differences between metabolites, peak areas were used as a metric for qualitative comparisons of relative amounts as we lacked both a radiolabeled **Parent** and a majority of metabolite standards. We were particularly interested in assessing the circulating metabolites present in plasma for this pilot study to elucidate if any could contribute to either off- or on-target activity (Loi et al., 2013). Therefore, metabolite identification was performed with plasma pooled from the 5-min through 24-hr timepoints (low available sample volumes necessitated the use of all available timepoints).

Analysis of pooled plasma in ESI^+ mode revealed 16 metabolites. The principal metabolite by peak area was **M9**, which showed a loss of $-C_2H_4-$ from the **Parent**. This metabolite, 6-BHA, was confirmed through matching retention times and MS/MS fragmentation to a chemical standard. By inspection of diagnostic fragmentation ions, the next largest metabolite **M3,** was assigned as the further chain-shortened 4-BBA, a total loss of $-C_4H_8-$ from the **Parent**. The presence of **M3** and **M9** provide strong evidence that *β*-oxidation of 8-BOA is a major pathway of metabolism in the current study and may largely explain the discrepancy between microsomal *in vitro* and *in vivo* half-lives. It also seems likely that the desaturation, mono-oxidation, and ketone formation metabolites that were also identified may be intermediate products from *β*-oxidation according to the "leaky hosepipe" theory for this pathway (Stanley and Tubbs, 1973, 1975). The presence of **M19** as a hydroxylated variant of **M9**, and **M1** as the carnitine-conjugate of **M3**, are additional markers for *β*-oxidation (**Figure 4.8**); both mitochondria and peroxisomes could conceivably be the sites of this biotransformation (Suga, 2003). It should be noted that the multiplicity of isomers for desaturation, mono-oxidation, and ketone formation metabolites certainly suggests contributions from other sources of metabolism as well.

A notable drug example of *β*-oxidation metabolism occurs with the class of 3-Hydroxy-3-methylglutaryl-CoA reductase inhibitors, referred to as the "statins" (Li et al., 2005). At least in the case of lovastatin, the chain-shortened pentanoic acid derivative does not maintain any inhibitory activity towards its target enzyme (Vyas et al., 1989). Serendipitously, 6-BHA, the confirmed identity of the metabolite **M9**, had already undergone in-depth characterization as it was part of our congeneric series of analogs and showed promise as a CYP4Z1 MBI itself (Kowalski et al., 2020). Although less potent than 8-BOA, *in vitro* IC_{50} and shifted-IC_{50} values for 6-BHA were 41 and 1.7 µM, respectively, while maintaining a similar degree of low off-target inhibition of human CYPs. Additionally, the lowered plasma protein binding exhibited by 6-BHA, 75% versus 98% for 8-BOA, suggests that free concentrations of this metabolite are likely to be

more elevated *in vivo*. Although quantification of 6-BHA in plasma was not performed, it is tempting to speculate that the *β*-oxidation of 8-BOA may serve to augment the desired pharmacodynamic effect of CYP4Z1 inactivation through the generation of an active metabolite *in vivo*.

Analysis of pooled plasma in ESI^- mode revealed many of the same metabolites as seen in ESI^+ and again, **M3** and **M9** were majorly represented. As expected, the metabolite profile was increased and totaled 25 between the two modes of ionization, with glucuronide conjugates being newly revealed. **M20** at 7.8 min, and **M22**, denoting the cluster of peaks from 8.3 to 8.6 min, showed fragmentation indicative of acyl-glucuronides. These likely represent a mixture of the 1-*β* anomer as well as the 2-, 3- and 4-*α/β* acyl-glucuronide anomers akin to that seen in mouse metabolism of diclofenac (Sarda et al., 2012). Furthermore, **M21** and **M23** were identified as ions with fragmentation indicating that they were acyl-glucuronide structures that had lost their ABT moiety. These metabolites had overlapping retention times with the presumed acyl-glucuronide cluster and therefore may be artifactually generated *via* in-source fragmentation of **M22** or sample work-up. Regardless, acyl-glucuronidation was identified as an additional biotransformation pathway for 8-BOA.

For ABT itself, the *N*-acetylated and *N*-glucuronidated products are the major metabolites that have been identified in rats (Ortiz de Montellano, 2018). We were unable to find these particular metabolites, although **M24**, corresponding to the product of bis-methylation plus oxidation, could conceivably be due to acetylation on the exocyclic nitrogen followed by reduction, but MS/MS fragmentation was inconclusive. Seemingly, the flux towards biotransformation pathways targeted to the alkyl-carboxylic acid dominate over pathways targeted to the ABT moiety. Along with the products from CYP-mediated oxidation, metabolites that were identified in both modes of ionization included numerous methylated species and

unassigned adducts that possessed both more or less hydrophobicity than the **Parent** (as discerned through retention times)**.**

Analysis of urine was performed only on samples obtained during the terminal 24-hour necropsy, and therefore, conclusions drawn from its analysis are limited. Nevertheless, the major urinary metabolites by peak area in ESI^+/ESI^- provided further evidence for two of the main pathways of metabolism observed from plasma analysis. **M3**, assigned as 4-BBA, was the most dominant metabolite identified in ESI^+ mode and semi-quantitation (using standards for 8-BOA) showed a concentration of ~390 nM. As a comparison, the concentration of unchanged 8-BOA in the urine at the 24-hr collection was <10 nM. No metabolite pertaining to a full 8-BOA structure conjugated to a glucuronide (such as **M20** or **M22**) was detected in urine in ESI^- mode. However, the major metabolite identified was **M21** (exhibiting the same retention time and MS/MS fragmentation as that found in plasma), but again this metabolite may be artifactual.

The control arm group of the study (receiving the same formulation but without 8-BOA and undergoing the same blood draw schedule) enabled *ex vivo* assessment of liver and kidney CYP content/activity as well as clinical chemistries to evaluate acute toxicity. Given that 8-BOA showed heightened CYP4Z1-selectivity for time-dependent inhibition, we decided to limit our assessment to the proclivity for off-target CYP inactivation (presumably mechanism-based) to occur in the rat. The observed ~15% decrease in the CYP content in liver microsomes derived from the treated animals, where a C_{max} of 158 µM was determined, is in good agreement with our *in vitro* analysis that showed 7% off-target CYP inactivation from treatment with 100 µM of 8-BOA. Taken together, these data demonstrate a relatively low propensity for 8-BOA to target hepatic CYP isozymes in the rat.

Although no truly isozyme-specific probe substrates have been described for rat liver CYPs, multiple studies have used semi-selective metabolism of probe substrates (the minor

metabolizing isozymes are noted in parenthesis): midazolam 1'-hydroxylation (M1OH) to assess CYP3A1 and -3A2 (-C11, -C13), dextromethorphan *O*-demethylation (DOD) to assess CYP2C6 and -2C11 (-2D2), and phenacetin *O*-deethylation (POD) to assess CYP1A2 (-2C6) (Kobayashi et al., 2001, Chovan et al., 2007). Therefore, M1OH was used to probe residual CYP3A activity, DOD to probe CYP2C activity, and POD to probe CYP1A activity *ex vivo* in rat liver microsomes. A ~9% decrease in POD activity was observed in the microsomes derived from treated compared to control animals, while no decreases in M1OH or DOD activity was evident. Our previous characterization of 8-BOA inactivation of off-target human CYP isoforms showed that CYP1A2 experienced the largest degree of time-dependent inhibition, characterized by IC_{50} and shifted-IC_{50} values of 614 and 55 µM, respectively, equating to a shift ratio of 11. Since rat liver POD activity is driven mainly by CYP1A2, the minor ~9% decrease in treated versus control microsomes is in agreement with human CYP isozyme data. This indicates that while overall a minor process, CYP1A family enzymes may experience the largest off-target CYP inactivation liability from 8-BOA in both the human and rat.

Lastly, the results of clinical chemistries indicated that 8-BOA treatment causes no acute liver or kidney toxicity. Given that ABT, the bioactivatable pharmacophore of 8-BOA, has been itself dosed to numerous species and causes little toxicity (Ortiz de Montellano, 2018), this is not a surprising result. While the potential for acyl-glucuronides to covalently modify proteins is well known (Faed, 1984; Regan et al., 2010), xenobiotic fatty acids also have the ability to interfere with lipid metabolism. This can lead to their incorporation into triglycerides, the reduction of carnitine levels, and inhibition of *β*-oxidation, which can all trigger toxicological effects (Darnell and Weidolf, 2013). At least in the short time scale of this study, no indication of interference with these systems was apparent based on the results of the liver and kidney function tests. However, off-target CYP inactivation, transacylation with proteins, and lipid metabolism interference may all be metabolic liabilities at higher doses. Of note, both control and treated

groups showed a significant increase in aspartate aminotransferase (AST) levels from pre-infusion to the 24-hr timepoint; this was likely due to the infusion formulation that was utilized.

In summary, the pharmacokinetics of 8-BOA in rats were defined by a rapid initial phase ($t_{1/2,\alpha}$ = 0.21 hr), a slow terminal phase ($t_{1/2,\beta}$ = 5.6 hr), with a distribution (V_α = 72, V_β = 1,840 mL) and C_{max} (158 µM) suggestive of pharmacodynamic efficacy in an appropriate pre-clinical model. Metabolite identification revealed *β*-oxidation as a major biotransformation pathway, which produced a circulating metabolite (6-BHA) of known time-dependent inhibitory activity towards CYP4Z1. *Ex vivo* analysis showed only minor inactivation of off-target rat CYPs, matching that seen previously with human CYP isozymes. No indication of acute toxicity was observed. Therefore, this *in vivo* characterization of the inhibitor 8-BOA in rats suggests that we could appropriately interrogate the role of CYP4Z1 in breast cancer in a xenograft tumor model.

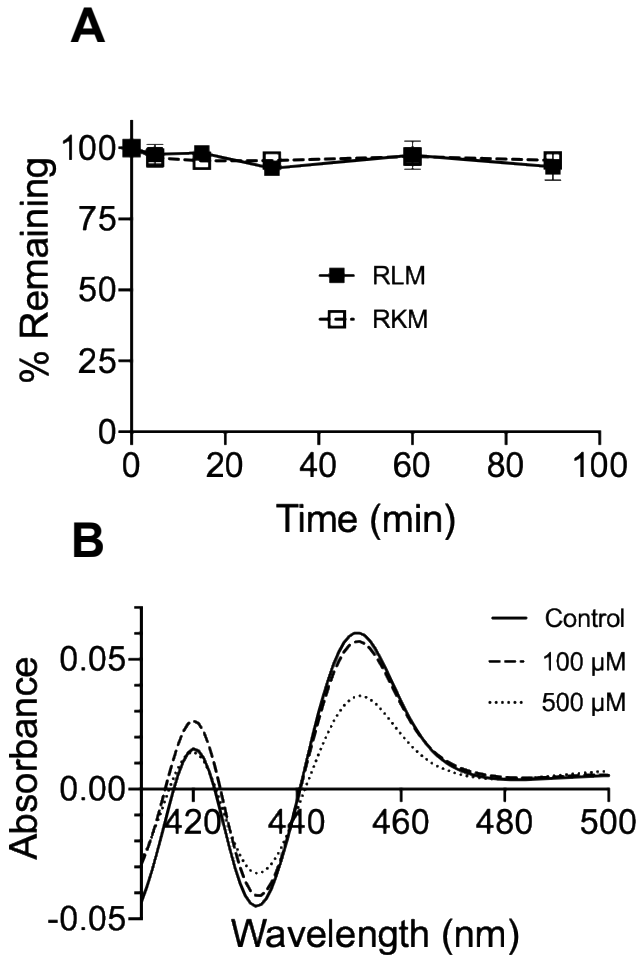

Figure 4.1. *In vitro* assessment of metabolic stability and off-target CYP inactivation. 8-BOA (1 µM) was incubated with pooled RLM or RKM (Xenotech) in the presence of NADPH (1.5 mM), UDPGA (5 mM), and alamethicin (10 µg/mL). Minimal depletion of 8-BOA was observed in either microsomal system over the course of 90 minutes. Shown is the average and standard deviation from three replicates (**A**). Pooled RLM was incubated in the presence of NADPH for 30 minutes with either DMSO (control) or 8-BOA**,** and standard CO-difference spectra was recorded for each sample. Absorbance at 450 nm decreased with increasing concentrations of 8-BOA, resulting in a ~7 and ~45% reduction of total CYP content at 100 and 500 µM, respectively.

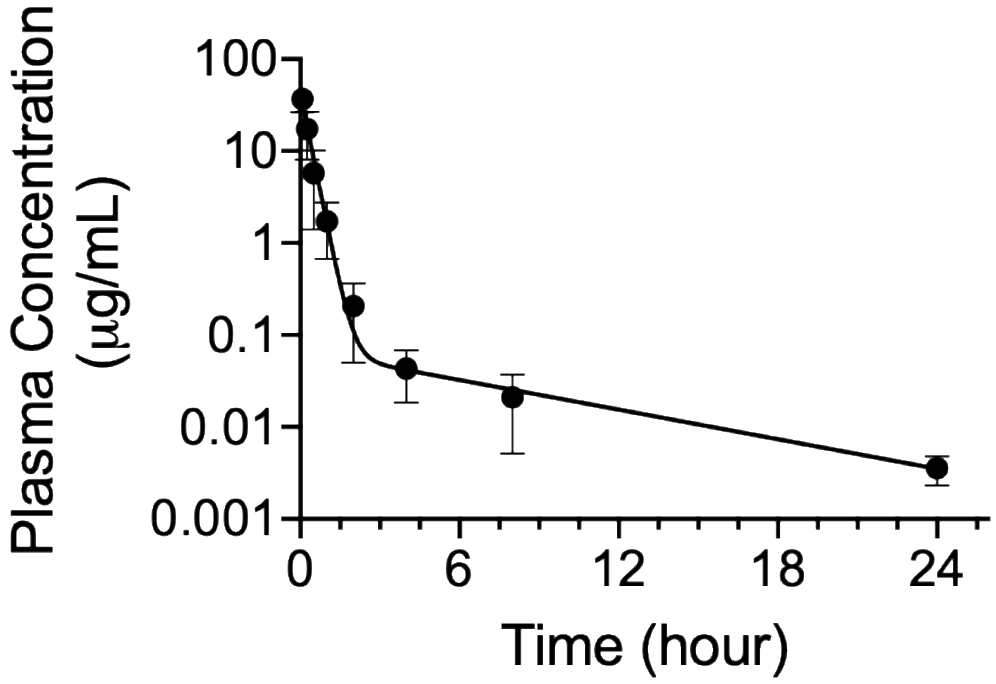

Figure 4.2. Plasma time-concentration profile for 8-BOA, administered *via* IV bolus at 10 mg/kg, in male Sprague Dawley rats. The standard 2-compartmental model was fit to the data, yielding the following parameters: A = 43.45, α = 3.32, B = 0.068, β = 0.12. Shown is the average and standard deviation from three animals.

Table 4.1. Pharmacokinetic parameters of 8-BOA in the rat

Parameter	
$t_{1/2,\alpha}$ (hr)	0.21
$t_{1/2,\beta}$ (hr)	5.6
V_{α} (mL)	72
V_{β} (mL)	1,840
$AUC_{0\rightarrow\infty}$ (μg hr mL^{-1})	13.7
CL (mL $hr^{-1)}$	228
C_{max} (μg mL^{-1} // μM)	43.5 // 158

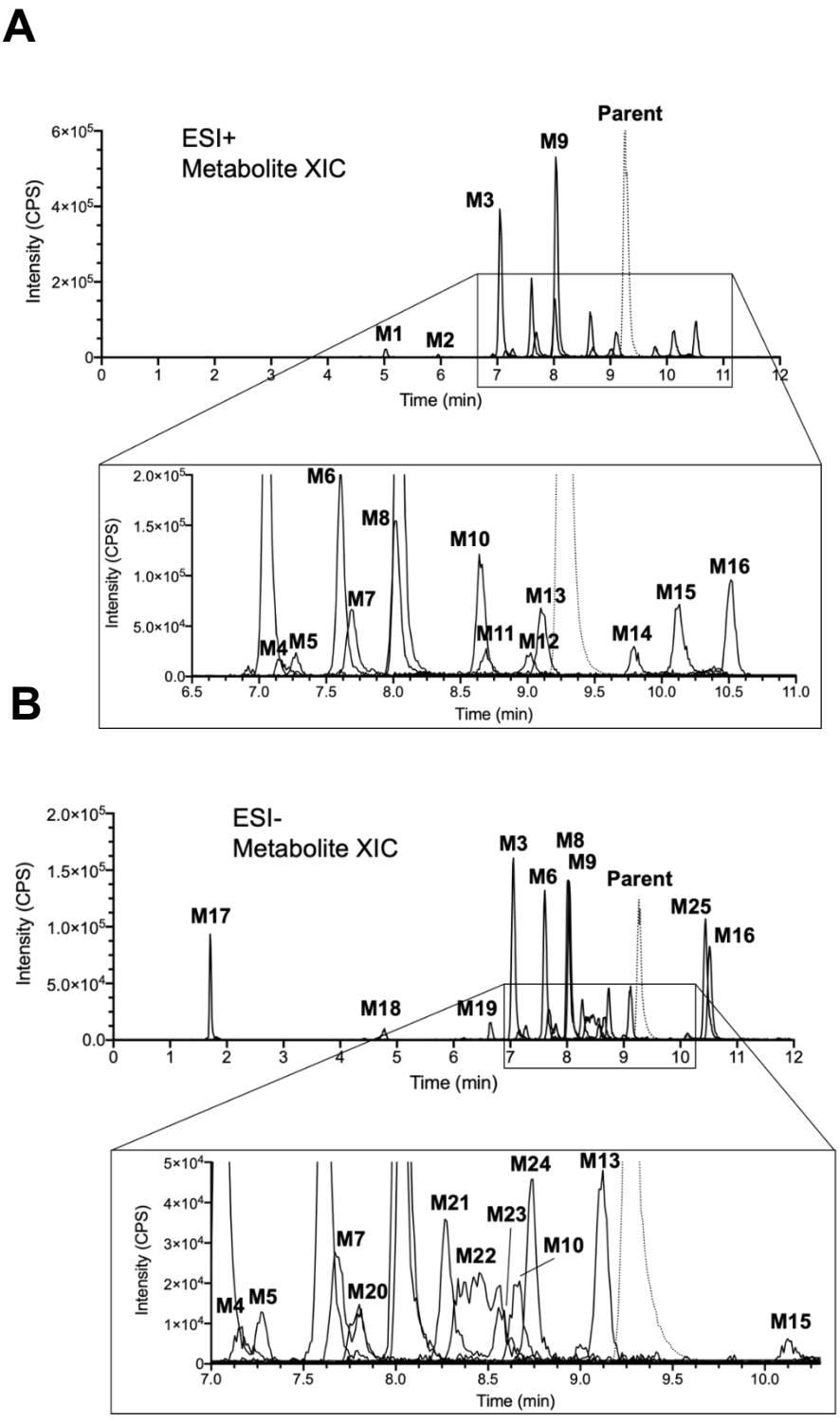

Figure 4.3. Metabolite identification in pooled rat plasma (5-min to 24-hr) *via* LC-MS/MS analysis. Overlaid extracted ion chromatograms (XIC) for detected metabolites in ESI^+ mode. The metabolites **M3** (tetra-demethylenated), **M9** (bis-demethylenated)**, M6** (hydroxylated), and **M8** (hydroxylated), displayed the largest peak areas (**A**). Overlaid XIC for detected metabolites in ESI^- mode; metabolites with the largest peak areas matched that which were observed in ESI^+ mode (**B**). **M1, M2, M11, M12** and **M14** were detected only in ESI^+, **M17 – M25** were detected only in ESI^-, and **M3 – M10, M13, M15, M16** were detected in both modes. The **Parent** (8-BOA, dotted peak) eluted at 9.3 min and has been plotted at 5% of intensity in both ESI^+ and ESI^- modes for visual comparison.

Table 4.2. Plasma metabolites detected in ESI$^+$ mode

Peak ID	Name	Formula	*m/z*	ppm	R.T. (min)	Peak Area
Parent	8-BAOA [M+H]+	$C_{14}H_{20}N_4O_2$	277.1662	1.2	9.26	7.83E+07
M1	Tetra-Demethylenation+Carnitine [M]+	$C_{17}H_{26}N_5O_4$	364.198	0.2	5.04	9.59E+04
M2	Loss of $C_8H_{14}O_2$ [M+H]+	$C_6H_6N_4$	135.0667	1.4	5.96	1.80E+04
M3	Tetra-Demethylenation [M+H]+	$C_{10}H_{12}N_4O_2$	221.1034	0.3	7.04	1.73E+06
M4	Oxidation [M+H]+	$C_{14}H_{20}N_4O_3$	293.1607	-0.3	7.14	5.79E+04
M5	Oxidation [M+H]+	$C_{14}H_{20}N_4O_3$	293.1609	0.4	7.27	9.44E+04
M6	Oxidation [M+H]+	$C_{14}H_{20}N_4O_3$	293.1609	0.4	7.61	8.74E+05
M7	Ketone Formation [M+H]+	$C_{14}H_{18}N_4O_3$	291.1453	0.5	7.69	3.68E+05
M8	Oxidation [M+H]+	$C_{14}H_{20}N_4O_3$	293.1607	-0.3	8.01	7.53E+05
M9	Bis-Demethylenation [M+H]+	$C_{12}H_{16}N_4O_2$	249.1347	0.4	8.03	2.44E+06
M10	Bis-Demethylenation+Methylation [M+H]+	$C_{13}H_{18}N_4O_2$	263.1502	-0.2	8.64	5.69E+05
M11	Desaturation [M+H]+	$C_{14}H_{18}N_4O_2$	275.1505	0.8	8.69	1.36E+05
M12	Desaturation [M+H]+	$C_{14}H_{18}N_4O_2$	275.1506	1.4	9.02	1.40E+05
M13	Ketone Formation+Methylation [M+H]+	$C_{15}H_{20}N_4O_3$	305.1608	-0.1	9.10	3.51E+05
M14	Methylation [M+H]+	$C_{15}H_{22}N_4O_2$	291.1813	0.3	9.79	1.49E+05
M15	Desaturation [M+H]+	$C_{14}H_{18}N_4O_2$	275.1503	0.1	10.13	4.12E+05
M16	Bis-Methylation [M+H]+	$C_{16}H_{24}N_4O_2$	305.1976	1.3	10.51	4.59E+05

Table 4.3. Plasma metabolites detected in ESI$^-$ mode

Peak ID	Name	Formula	*m/z*	ppm	R.T. (min)	Peak Area
Parent	8-BAOA [M-H]-	$C_{14}H_{20}N_4O_2$	275.1524	3.7	9.27	2.02E+07
M17	Unassigned Gain of 16.9885	Unassigned	292.1399	N/A	1.71	2.28E+05
M18	Unassigned Gain of 272.9481	Unassigned	548.1005	N/A	4.78	4.02E+04
M19	Bis-Demethylenation+Oxidation [M-H]-	$C_{12}H_{16}N_4O_3$	263.1156	2.5	6.66	6.94E+04
M3	Tetra-Demethylenation [M-H]-	$C_{10}H_{12}N_4O_2$	219.0896	4.1	7.05	7.51E+05
M4	Oxidation [M-H]-	$C_{14}H_{20}N_4O_3$	291.1463	0.1	7.17	3.61E+04
M5	Oxidation [M-H]-	$C_{14}H_{20}N_4O_3$	291.1457	-1.9	7.27	5.45E+04
M6	Oxidation [M-H]-	$C_{14}H_{20}N_4O_3$	291.1468	1.8	7.61	5.85E+05
M7	Ketone Formation [M-H]-	$C_{14}H_{18}N_4O_3$	289.1310	1.3	7.67	1.41E+05
M20	Glucuronidation [M-H]-	$C_{20}H_{28}N_4O_8$	451.1824	-2.3	7.80	8.33E+04
M8	Oxidation [M-H]-	$C_{14}H_{20}N_4O_3$	291.1465	0.9	8.02	7.20E+05
M9	Bis-Demethylenation [M-H]-	$C_{12}H_{16}N_4O_2$	247.1207	2.7	8.04	6.07E+05
M21	Loss of $C_6H_4N_4$+Glucuronidation [M-H]-	$C_{14}H_{24}O_8$	319.1389	-2.8	8.27	1.80E+05
M22	Glucuronidation [M-H]-	$C_{20}H_{28}N_4O_8$	451.1822	-2.7	8.31-8.64	3.43E+05
M23	Loss of $C_6H_4N_4$+Glucuronidation [M-H]-	$C_{14}H_{24}O_8$	319.1390	-2.8	8.56	8.28E+04
M10	Bis-Demethylenation+Methylation [M-H]-	$C_{13}H_{18}N_4O_2$	261.1358	0.3	8.67	1.12E+05
M24	Bis-Methylation+Oxidation [M-H]-	$C_{16}H_{24}N_4O_3$	319.1777	0.3	8.74	1.92E+05
M13	Ketone Formation+Methylation [M-H]-	$C_{15}H_{20}N_4O_3$	303.1466	1.1	9.12	2.23E+05
M15	Desaturation [M-H]-	$C_{14}H_{18}N_4O_2$	273.1368	4.0	10.12	3.53E+04
M25	Unassigned Gain of 102.0212	Unassigned	377.1726	N/A	10.44	5.70E+05
M16	Bis-Methylation [M-H]-	$C_{16}H_{24}N_4O_2$	303.1823	-1.0	10.52	4.49E+05

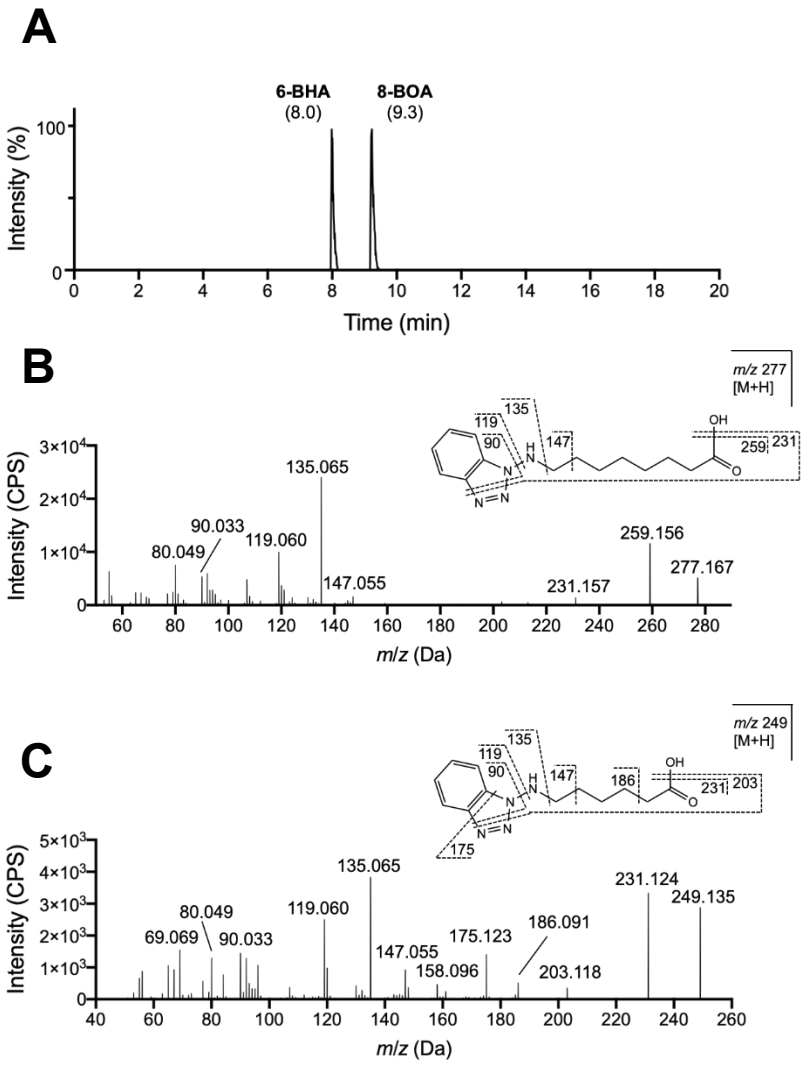

Figure 4.4. LC-MS/MS analysis, in ESI$^+$ mode, of reference standards. The extracted ion chromatograms (XIC) of the chain-shortened analog 6-BHA at *m/z* 249 and the **Parent** 8-BOA at *m/z* 277 show retention times (RT) of 8.0 and 9.3 minutes, respectively. Intensity was normalized to 100% for each compound to enable ease of viewing for comparison to the metabolite XICs (**A**). MS/MS spectra and annotated structures for 8-BOA (**B**) and 6-BHA (**C**) showing diagnostic fragmentation patterns.

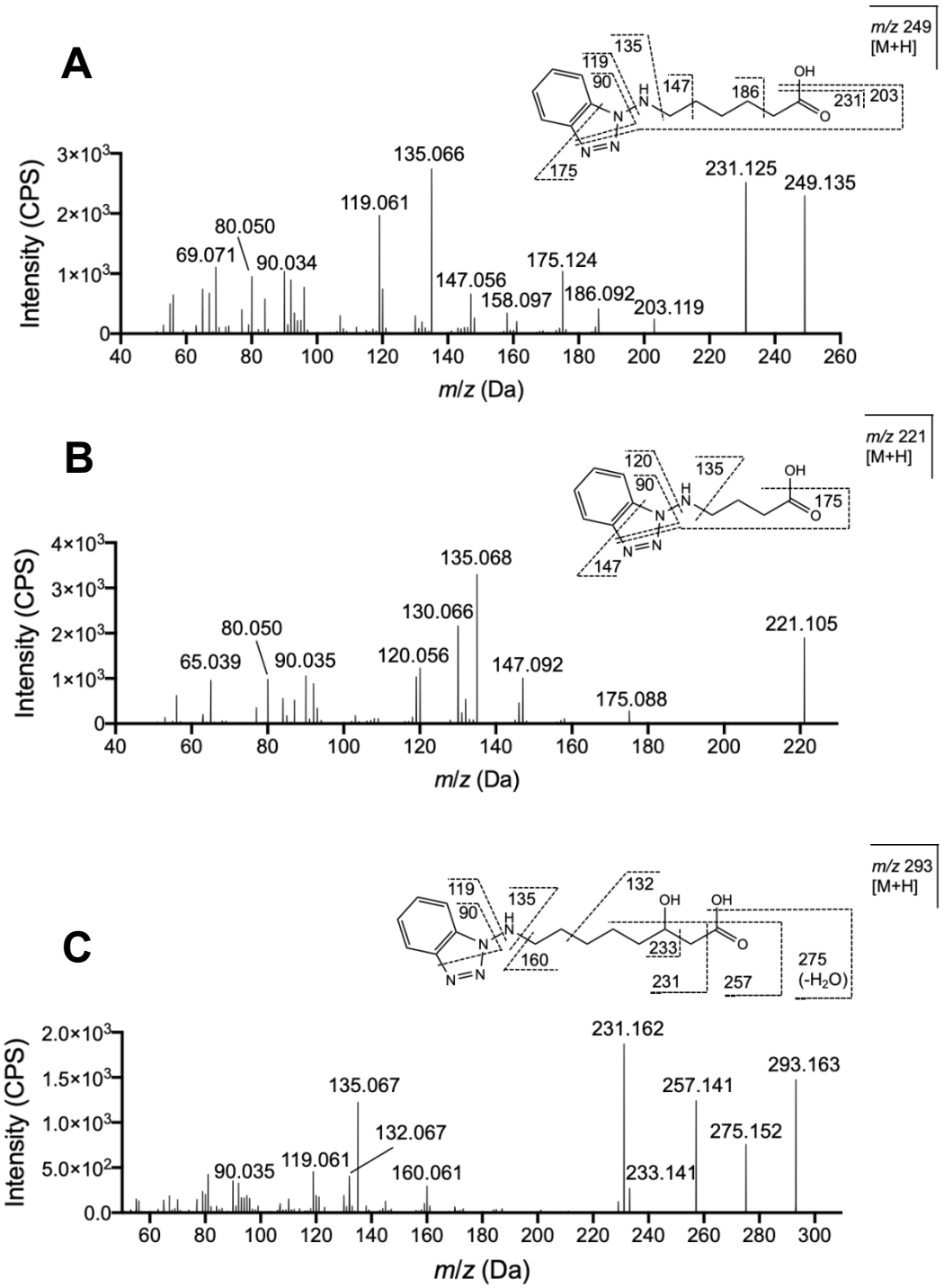

Figure 4.5. LC-MS/MS analysis, in ESI^+ mode, of the top three metabolites of 8-BOA (by peak area) in pooled rat plasma. **M9**, the metabolite with matching RT and MS/MS as the chain-shortened analog 6-BHA (see **Figure 4** for a comparison) is therefore confirmed as the result of a loss of $-C_2H_4-$ from the **Parent** (**A**). **M3** shows MS/MS spectra corresponding to a further chain-shortening of 6-BHA, resulting in a total loss of $-C_4H_8-$ from the **Parent**, and has been tentatively identified as 4-[(1H-1,2,3-benzotriazol-1-yl)amino]butanoic acid (4-BBA) (**B**). **M6** (Parent plus 16 Da), shows fragmentation consistent with hydroxylation at the *β*-carbon of the 8-BOA aliphatic tail (**C**).

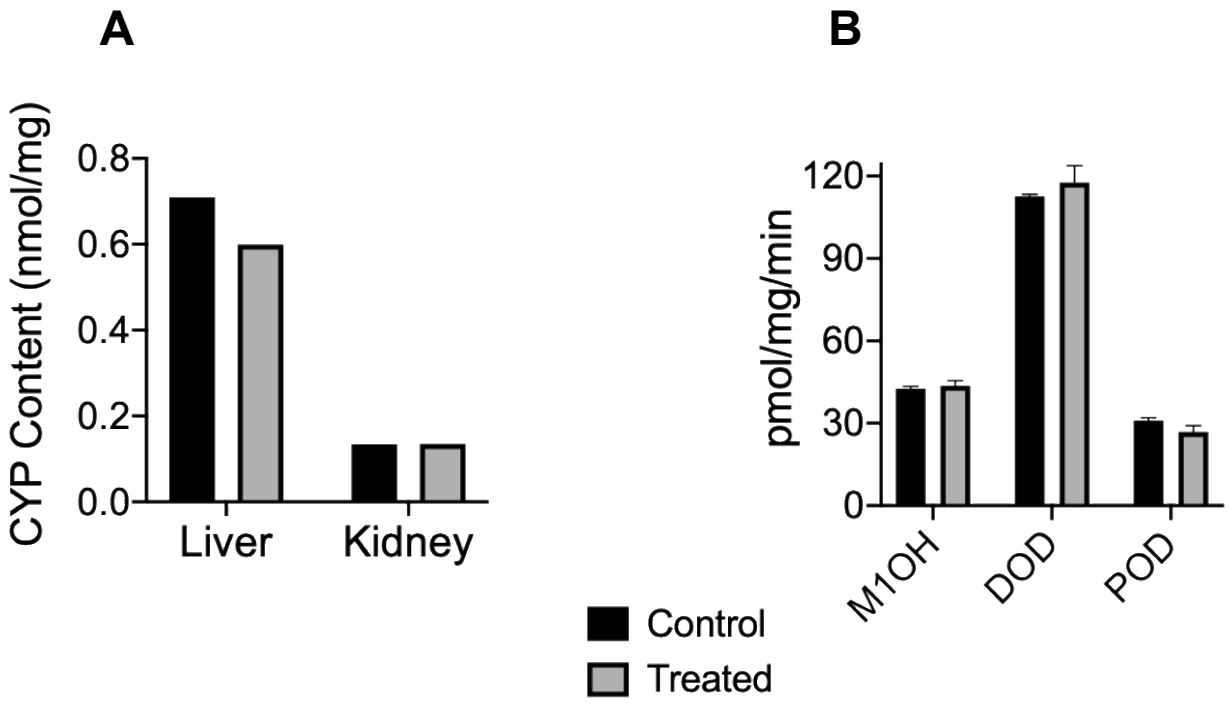

Figure 4.6. *Ex vivo* assessment of off-target CYP inactivation in rats treated with 8-BOA. Liver and kidney were harvested after 24 hours and microsomes were prepared from rats receiving either 8-BOA (treated, grey bars) or a vehicle infusion (control, black bars). CYP content from pooled microsomes was analyzed *via* CO-binding difference spectra, where a ~15% decrease in liver microsomal CYP content was observed; no appreciable decrease in kidney microsomal CYP content was evident. Shown is the average from two replicates (**A**)**.** Pooled liver microsomes derived from either control or treated animals were incubated with separate probe substrates in the presence of NADPH and rates of midazolam 1'-hydroxylation (M1OH), dextromethorphan *O*-demethylation (DOD), and phenacetin *O*-deethylation (POD) were determined. A ~9% decrease in POD activity was observed in the microsomes derived from treated compared to control animals, while no decreases in M1OH or DOD activity was evident. Shown is the average and standard deviation from three replicates (**B**).

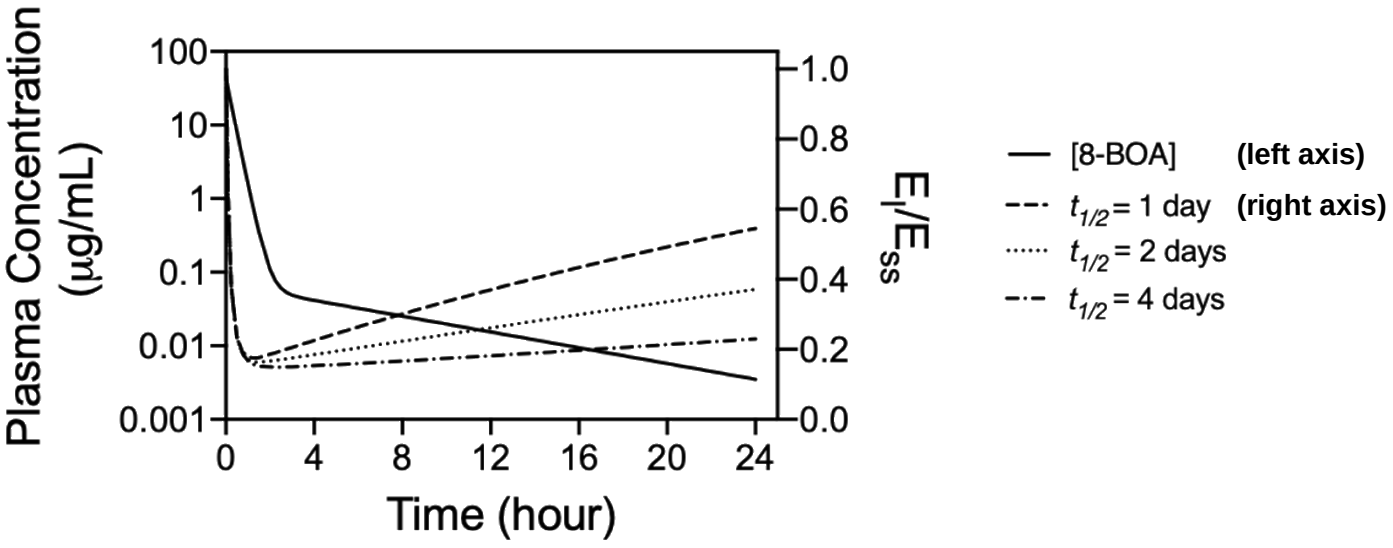

Figure 4.7. Simulation of the ratio of enzyme (CYP4Z1) remaining after treatment with the inhibitor 8-BOA (E_I) compared to enzyme at steady state (E_{SS}) in a theoretical breast cancer xenograft model. Plasma concentrations of 8-BOA were calculated using the equation generated from the time-concentration profile of this study and the enzyme amounts after inactivation calculated from the unbound fraction of 8-BOA (2%) at these time points and the parameters K_I = 2.2 μM and k_{inact} = 0.15 min^{-1}.The results from using different CYP turnover half-lives, ranging from 1 – 4 days, show that CYP4Z1 would remain 45 – 77% inactivated 24-hours post dose. [8-BOA] corresponds to the left axis, and $t_{1/2}$ = 1, 2, and 4 days correspond to the right axis.

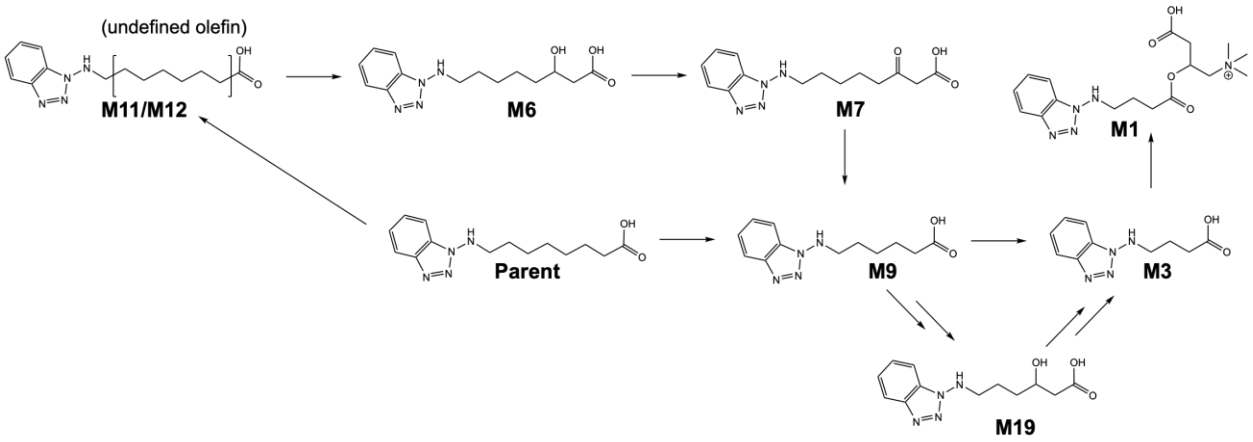

Figure 4.8. Structures of proposed metabolites in pooled plasma that provide evidence for the *β*-oxidation pathway. Successive removal of -C_2H_4- generates **M9** (6-BHA, confirmed through comparison to the chemical standard) and then **M3** (tentatively assigned as 4-BBA) from the **Parent** 8-BOA, typical metabolites expected from *β*-oxidation. The desaturations, hydroxylation, and ketone formation compounds, **M11/M12**, **M6,** and **M7**, respectively, may be products due to "intermediate leakage" from the *β*-oxidation pathway. The presence of **M19** as a *β*-hydroxylated variant of **M9**, and **M1** as the carnitine-conjugate of **M3**, are additional markers for this route of metabolism. The presence of multiple isomers of several of the metabolites is evidence that they are also derived from other (most likely CYP) biotransformation pathways.

4.5 Supporting information

Synthesis of 8-BOA-d4; ^{1}H NMR spectra for 8-BOA-d4 and 8-BOA; LC-MS/MS analysis of glucuronides in pooled plasma; LC-MS/MS analysis of the major metabolites identified in urine; Pre-infusion and 24-hour clinical chemistries; ESI+ MS/MS Spectra and proposed structures for plasma metabolites; ESI- MS/MS Spectra and proposed structures for plasma metabolites.

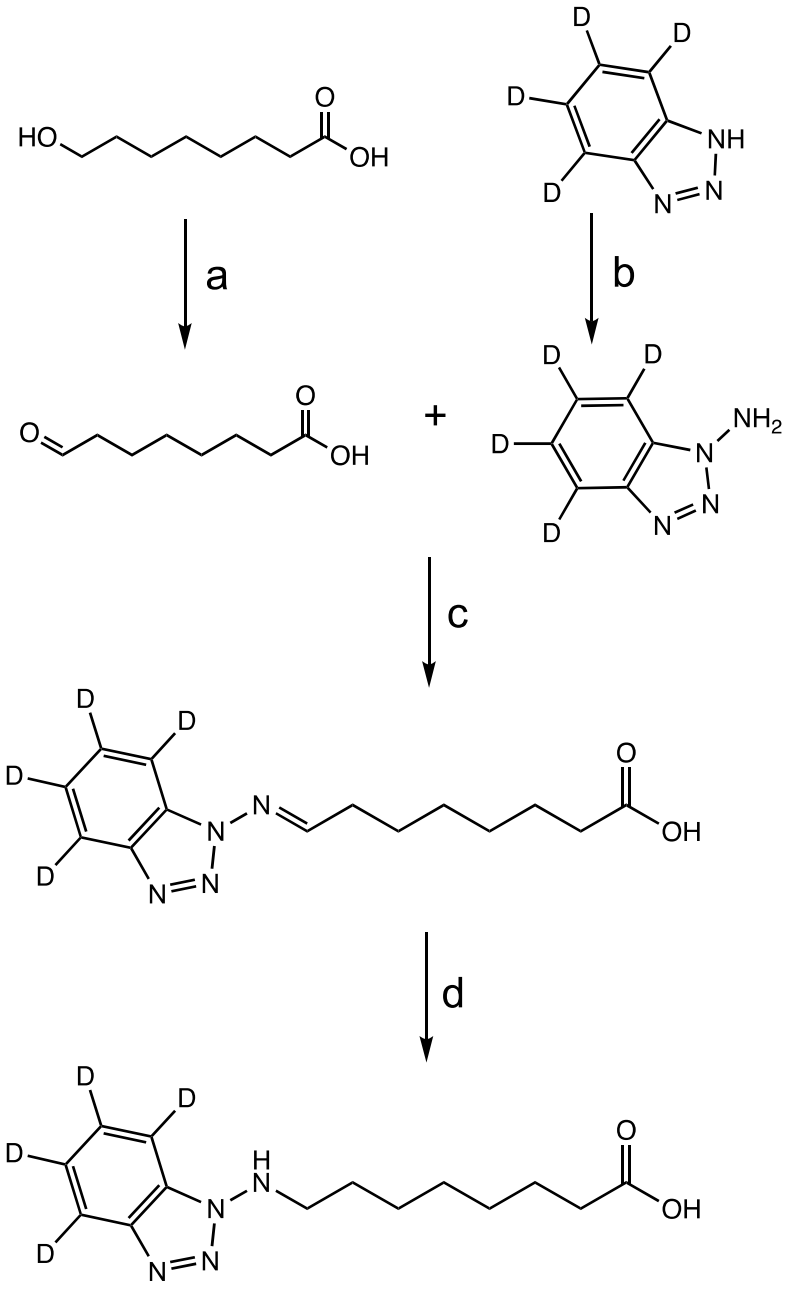

Figure S4.1. Synthesis of 8-{[(4,5,6,7-2H4)-1H-1,2,3-benzotriazol-1-yl]amino}octanoic acid (8-BOA-d4), the internal standard used for *in vitro* and *in vivo* quantification of 8-BOA**.** Reagents and conditions: (a) celite, PCC, CH_2Cl_2, RT, 1 h, 30%; (b) KOH, H_2O, HOSA, 70°C, 1 h, 40%; (c) acetic acid, RT, 18 h, 71%; (d) $NaBH_4$, CH_2Cl_2, MeOH, RT, 2 h, 76%

A

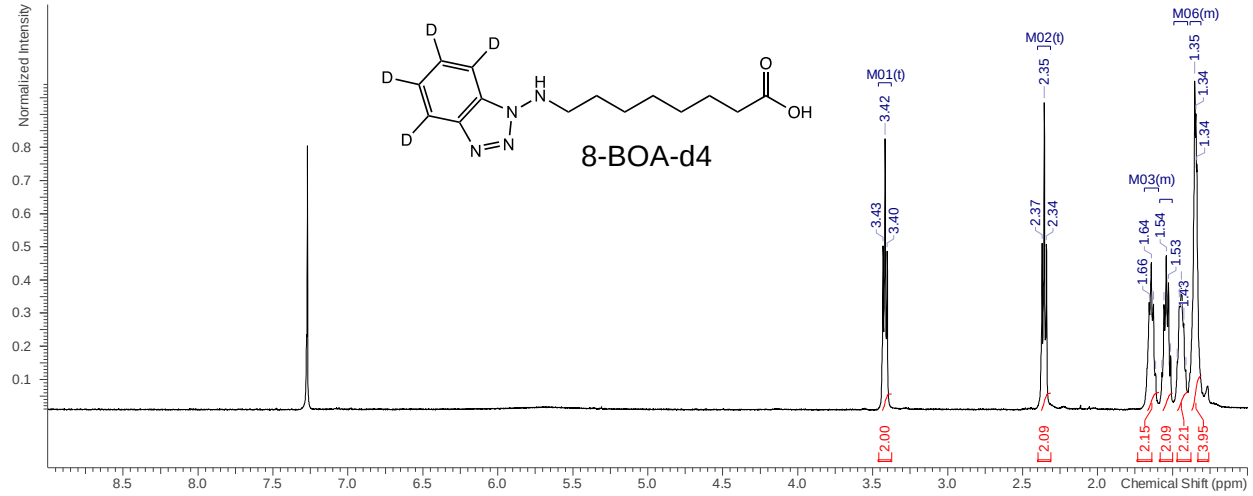

B

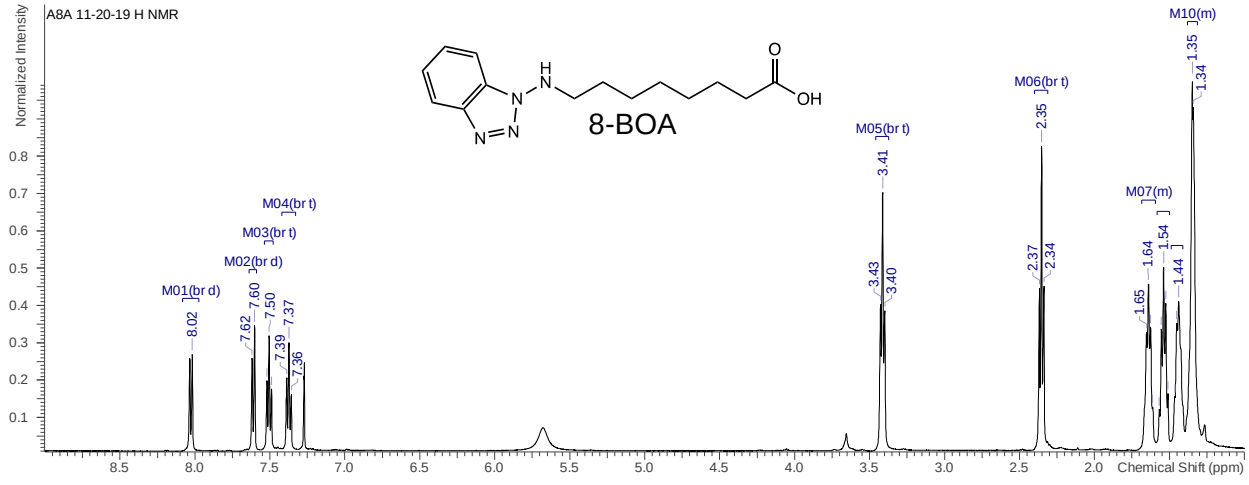

Figure S4.2. ^{1}H NMR spectra for 8-BOA-d4 (**A**) and 8-BOA (**B**). No signals were observed between 8.02 – 7.36 ppm for 8-BOA-d4**,** indicating a lack of any contaminating species without deuteration on the 1-aminobenzotriazole moiety. The residual chloroform solvent signal at 7.27 ppm is shown in both spectra. 8-BOA was synthesized previously, and the ^{1}H NMR spectra has been reproduced.

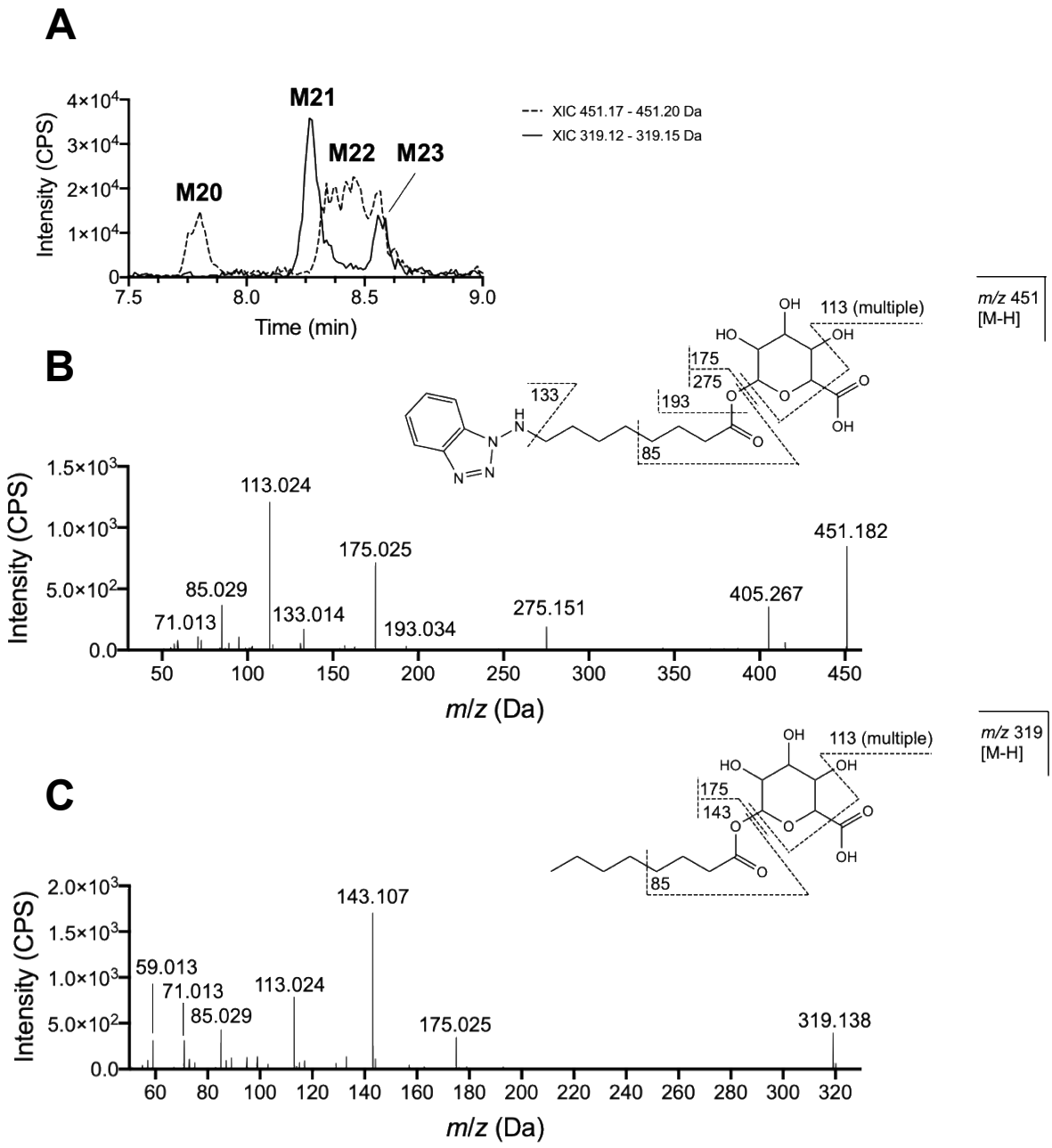

Figure S4.3. LC-MS/MS analysis, in ESI- mode, of glucuronides in pooled plasma. Extracted ion chromatograms (XIC) for *m/z* 451 (dashed line) and 319 Da (solid line) shows metabolites **M20** – **M23. M21** and **M23** have nearly overlapping retention times with the cluster denoting **M22** (**A**)**.** MS/MS spectra for the cluster corresponding to **M22** shows fragmentation characteristic to an acyl-glucuronide. Although only the 1-*β* anomer is depicted in the annotated scheme, the cluster likely represents a mix including the 2-, 3- and 4-*α/β* acyl-glucuronide anomers (**B**). MS/MS spectra for **M21**, with annotated fragmentation corresponding to a glucuronide-containing portion from the **Parent** where 1-aminobenzotriazole has been lost; only the 1-*β* anomer is shown (**C**).

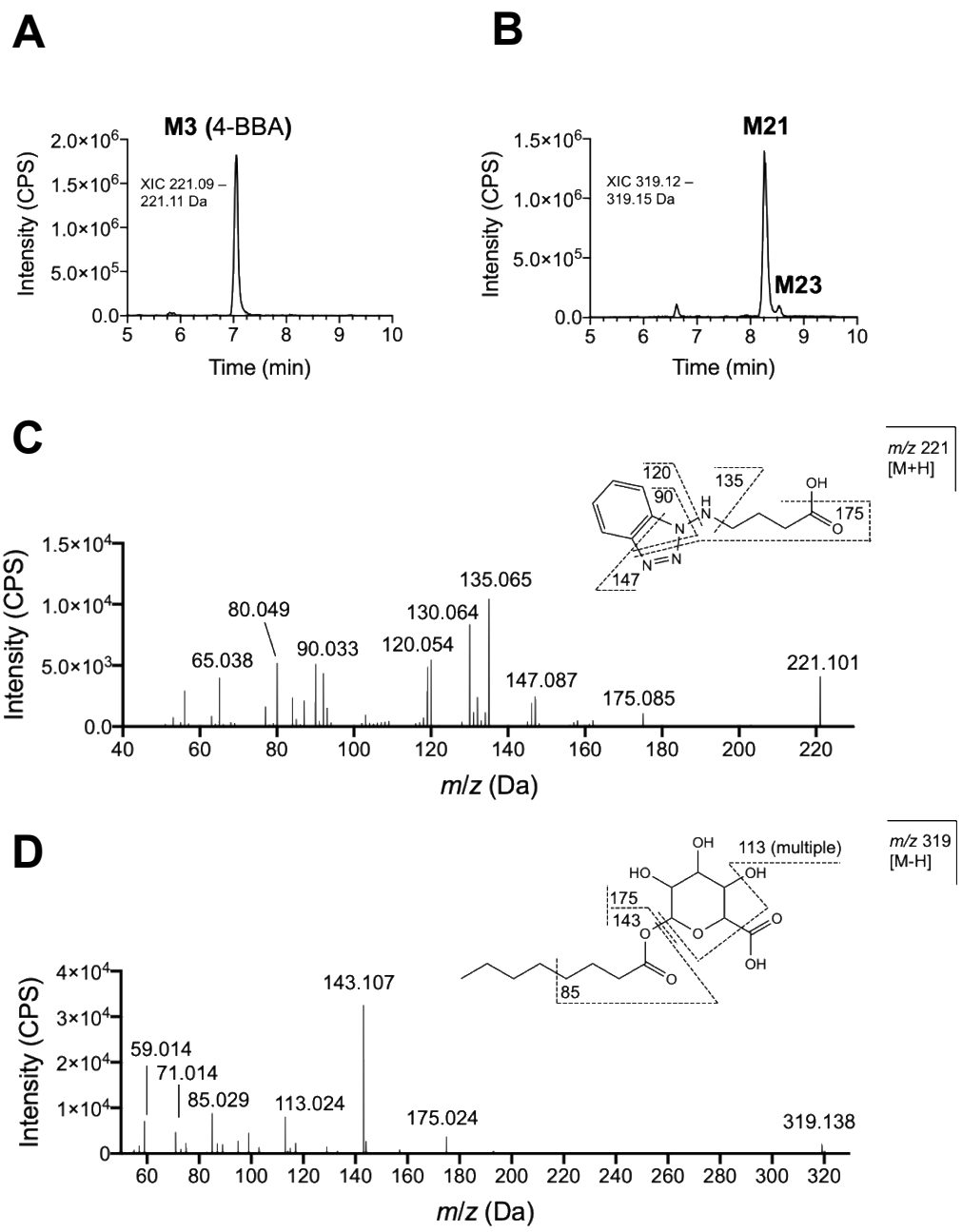

Figure S4.4. LC-MS/MS analysis of the major metabolites identified in urine collected from the bladders of rats at 24 hours post-infusion. XIC of *m/z* 221, the major metabolite identified in urine *via* ESI+ mode, which corresponded to the previously identified **M3** in plasma (**A**). XIC of *m/z* 319, the major metabolite identified in urine *via* ESI- mode, which corresponded to the previously identified **M21** in plasma, a trace amount of **M23** was also observed as well as an additional minor peak at 6.6 minutes (**B**). MS/MS spectra of **M3**, currently assigned as 4-BBA, in urine with annotated fragmentation that matched the same metabolite identified in plasma (**C**). MS/MS spectra of **M21** in urine, with annotated fragmentation that matched the same metabolite identified in plasma; only the 1-*β* anomer is shown (**D**).

Table S4.1. Clinical chemistries

Pre-infusion		
Analyte	[a]Treated	[a]Control
GLU (mg/dL)	375 ± 6.1	370 ± 9.2
BUN (mg/dL)	24.7 ± 1.2	24.0 ± 2.0
[b]CRE (mg/dL)	-	-
[b]PHOS (mg/dL)	-	-
TP (g/dL)	6.1 ± 0.1	6.1 ± 0.1
ALB (g/dL)	4.5 ± 0.1	4.3 ± 0.1
GLO (g/dL)	1.7 ± 0.1	1.7 ± 0.1
A/G	2.7 ± 0.3	2.5 ± 0.3
[b]TBIL (mg/dL)	-	-
[b]GGT (U/L)	-	-
ALT (U/L)	75.3 ± 4.2	74.7 ± 4.2
AST (U/L)	154 ± 8.7	143 ± 9.9
CHOL (mg/dL)	62.7 ± 1.2	62.7 ± 2.3
24-hour		
Analyte	[a]Treated	[a]Control
GLU (mg/dL)	138 ± 9.2	137 ± 6.5
BUN (mg/dL)	19.0	19.7 ± 3.1
CRE (mg/dL)	0.30	0.30
PHOS (mg/dL)	8.8 ± 0.6	8.2 ± 0.2
TP (g/dL)	5.7 ± 0.4	5.1 ± 0.5
ALB (g/dL)	3.9 ± 0.2	3.6 ± 0.3
GLO (g/dL)	1.7 ± 0.2	1.5 ± 0.2
A/G	2.3 ± 0.1	2.4 ± 0.1
TBIL (mg/dL)	<0.1	<0.1
GGT (U/L)	<7	<7
ALT (U/L)	79.3 ± 8.1	79.3 ± 17
AST (U/L)	257 ± 39.6	292 ± 96.1
CHOL (mg/dL)	63.3 ± 8.0	55.3 ± 7.1

[a]Average from three rats ± SD

[b]Due to sample dilution, these analytes could not be assessed

GLU, glucose; BUN, blood urea nitrogen; CRE, creatinine; PHOS, phosphate; TP, total protein; ALB, albumin; GLO, globulin; A/G, albumin/globulin ratio; TBIL, total bilirubin; GGT, gamma-glutamyl transferase; ALT, alanine aminotransferase; AST, aspartate aminotransferase; CHOL, cholesterol

Parent 8-BOA [M+H]+

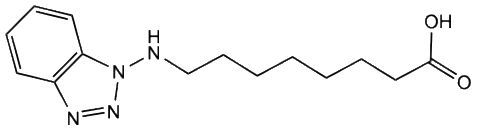

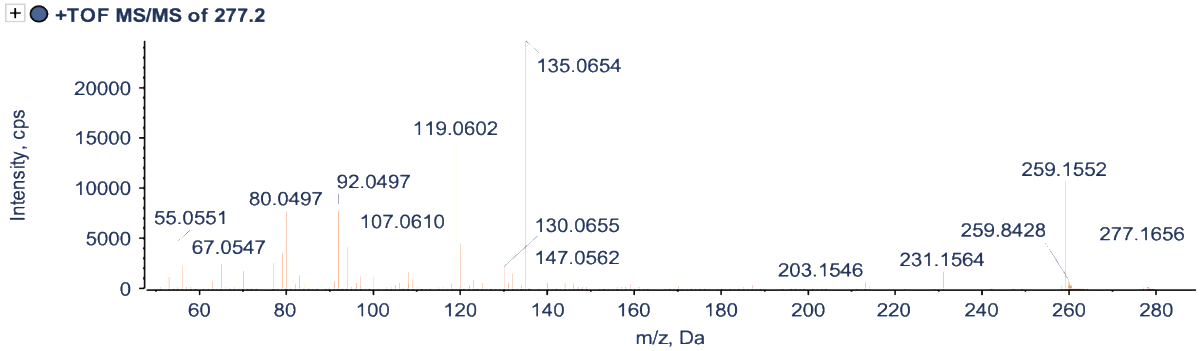

Mass (m/z)	Ion Formula	Error (mDa)	Intensity (cps)	RDB	Proposed Structures	Score
135.0654	C6H7N4	-1.1	24684.4	6	1	40.5
119.0602	C6H5N3	12.4	14796.8	6.5	1	37.5
259.1552	C14H19N4O	-0.2	10648.1	8	1	45
80.0497	C6H8	-12.3	7720.7	3.5	3	33.5
92.0497	C6H6N	0.2	7699.7	5	1	37.5
90.034	C6H4N	0.2	6250.2	6	1	37.5
107.061	C6H7N2	0.6	5466.9	5	2	36.5
55.0551	C4H7	0.8	4699.3	2	4	33
277.1656	C14H21N4O2	-0.4	4300.5	7	1	49
94.0654	C6H8N	0.3	4106.6	4	1	32.5
79.0546	C6H7	0.4	3538.2	4	1	36.5
121.0761	C7H9N2	0.1	3443.9	5	1	28.5
67.0547	C5H7	0.4	2971.4	3	3	30
77.0391	C6H5	0.5	2561.4	5	1	36.5
65.0391	C5H5	0.5	2464.5	4	0	3
130.0655	C8H6N2	12.9	2181.1	7.5	1	20
69.0704	C5H9	0.5	2064.9	2	3	33
147.0562	C7H7N4	-10.3	1836.6	7	1	28
231.1564	C14H19N2O	7.2	1721.5	7	1	32.5
124.1119	C7H12N2	12.4	1720.6	3.5	2	23
132.0687	C8H8N2	0.5	1477.2	6.5	1	20.5
83.0857	C6H11	0.2	1325.6	2	2	38
145.0767	C9H9N2	0.7	1247.4	7	1	23
97.1014	C7H13	0.3	1193.5	2	1	38
100.1126	C6H14N	0.5	1186.7	1	1	30.5
53.0392	C4H5	0.7	1159.3	3	4	30
112.112	C7H14N	-0.1	1049.2	2	1	35
123.0807	C8H11O	0.3	840.4	4	1	38

M1 Tetra-Demethylenation+Carnitine [M]+

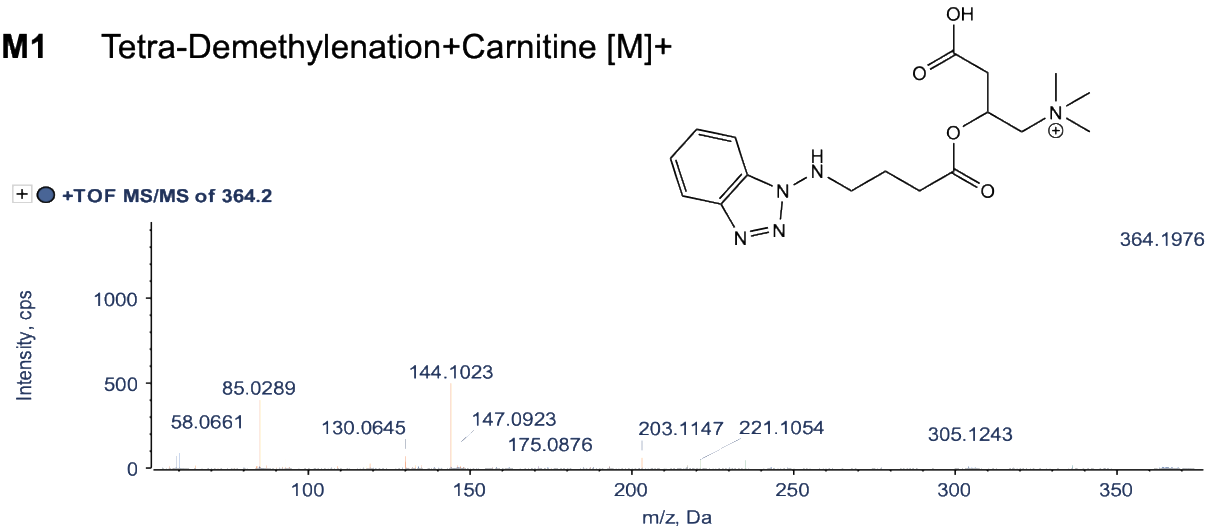

Mass (m/z)	Ion Formula	Error (mDa)	Intensity (cps)	RDB	Proposed Structures	Score
364.1976	C17H26N5O4	-0.3	1450.6	8	1	46
144.1023	C7H14NO2	0.4	502.1	2	11	37
85.0289	C4H5O2	0.5	403.7	3	7	36
147.0923	C6H13NO3	3.3	152.8	1.5	3	33.5
305.1243	C14H17N4O4	-0.1	135.3	9	1	45
157.0496	C7H9O4	0	115.7	4	2	38
59.0738	C3H9N	0.9	74.8	0.5	5	37.5
130.0645	C5H8NO3	14.6	71.5	3	3	32.5
175.0876	C8H15O4	-8.9	66.8	2	1	36.5
203.1147	C9H17NO4	-0.5	62.6	2.5	7	34.5
93.0578	C3H9O3	3.2	57.3	0	1	33.5
221.1054	C10H13N4O2	2.1	49.9	7	1	40.5
235.1196	C11H15N4O2	0.6	47.3	7	1	25
92.0494	C6H6N	-0.1	43.9	5	1	37.5
130.0872	C6H12NO2	1	37.2	2	15	36.5
216.1254	C10H18NO4	2.4	27.6	3	4	36.5
133.0769	C5H11NO3	3.6	20.7	1.5	3	29.5
135.0667	C6H7N4	0.2	20.7	6	1	45.5
336.1909	C17H26N3O4	-0.9	17.2	7	1	41.5
65.0408	C5H5	2.2	17	4	0	3
77.0382	C6H5	-0.4	16.7	5	1	36.5
87.0442	C4H7O2	0.1	16.4	2	7	41.5
118.0673	C5H12NO2	-18.9	15.7	1	7	32.5
171.0675	C8H11O4	2.3	15.4	4	1	36
84.0835	C5H10N	2.7	15.4	2	4	20.5
109.0781	C6H9N2	2.1	13	4	2	36.5
84.0443	C4H6NO	-0.1	12.7	3	4	41
57.0332	C3H5O	-0.3	12.6	2	3	33.5

M2 Loss of $C_8H_{14}O_2$ [M+H]+ 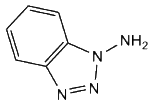

No MS/MS was acquired in pooled plasma (ESI+) mode for **M2**, however, it was assigned as ABT based on matching retention time to the chemical standard and accurate mass.

M3 Tetra-Demethylenation [M+H]+

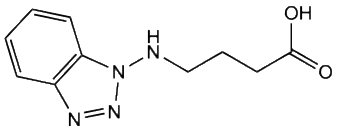

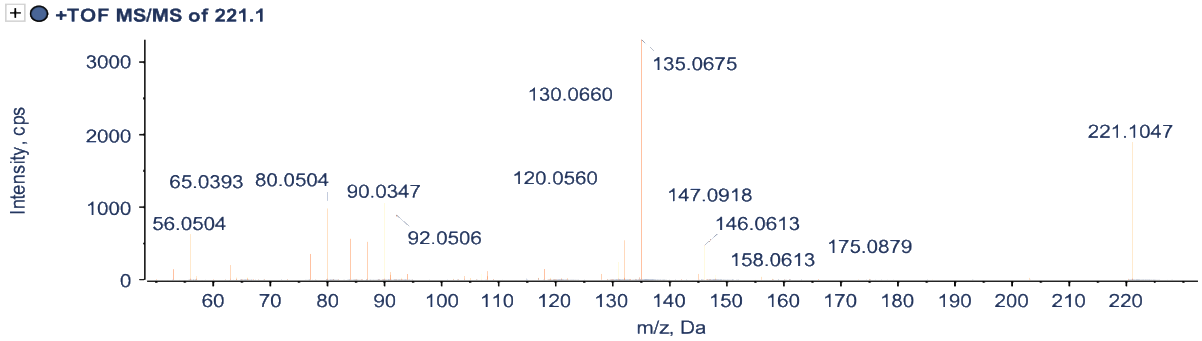

Mass (m/z)	Ion Formula	Error (mDa)	Intensity (cps)	RDB	Proposed Structures	Score
135.0675	C6H7N4	1	3307.5	6	1	40.5
130.066	C4H10N4O	-18.9	2167.3	2.5	1	29.5
221.1047	C10H13N4O2	1.4	1904.2	7	1	44
120.056	C6H6N3	0.3	1242.2	6	1	45.5
90.0347	C6H4N	0.9	1066.6	6	1	32.5
119.0609	C6H5N3	13.1	1043.4	6.5	1	37.5
147.0918	C4H11N4O2	4.1	1014.4	2	1	36.5
80.0504	C6H8	-11.7	987.8	3.5	1	33.5
65.0393	C5H5	0.7	965.4	4	0	3
92.0506	C6H6N	1.1	896	5	1	32.5
56.0504	C3H6N	0.9	632.8	2	1	30
84.0454	C4H6NO	1	566.9	3	1	36
132.0689	C8H8N2	0.7	548.8	6.5	1	20.5
87.0455	C4H7O2	1.4	527.4	2	1	40
146.0613	C4H10N4O2	-18.5	472.4	2.5	1	33.5
77.0393	C6H5	0.7	359.5	5	1	36.5
175.0879	C10H11N2O	1.3	291.6	7	1	32.5
63.0235	C5H3	0.6	210.7	5	0	3
103.0548	C4H9NO2	-8	187	1.5	1	37.5
118.0657	C4H10N2O2	-8	156.8	1.5	1	33.5
53.0393	C3H3N	13.3	148.6	3.5	1	24
108.0454	C6H6NO	1.1	123.3	5	0	3
158.0613	C8H6N4	2.6	118.2	8.5	1	22
128.0499	C4H8N4O	-19.4	84.6	3.5	1	29.5
107.0615	C6H7N2	1.1	83.9	5	2	36.5
157.077	C10H9N2	1	83	8	0	3
68.0508	C3H4N2	13.9	69.3	3.5	1	23

M4 Oxidation [M+H]+

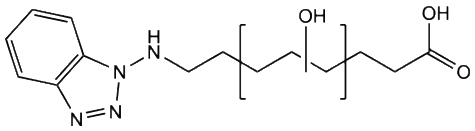

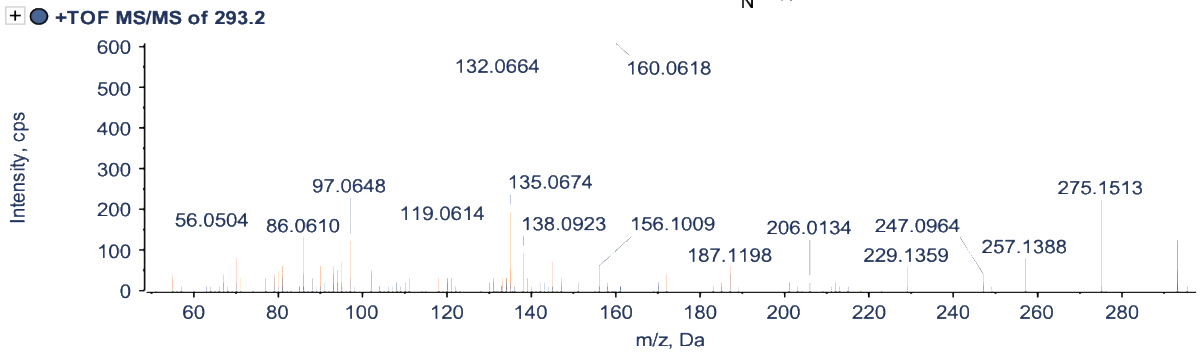

Mass (m/z)	Ion Formula	Error (mDa)	Intensity (cps)	RDB	Proposed Structures	Score
160.0618	C8H8N4	-12.6	608	7.5	1	25
132.0664	C6H12O3	-11.7	523	1.5	1	34.5
275.1513	C14H19N4O2	1	224	8	2	40
135.0674	C6H7N4	0.9	194	6	1	40.5
119.0614	C5H11O3	-8.9	163	1	1	37.5
86.061	C5H10O	-11.6	133	1.5	4	30.5
293.1642	C14H21N4O3	3.4	122	7	1	44
97.0648	C6H9O	0	122	3	3	35
114.0559	C6H10O2	-11.6	112	2.5	2	30.5
92.0509	C6H6N	1.5	112	5	1	32.5
56.0504	C3H6N	0.9	102	2	1	30
138.0923	C8H12NO	1	92	4	1	32
123.0826	C8H11O	2.2	92	4	1	32
74.0606	C4H10O	-12	92	0.5	5	30.5
257.1388	C14H17N4O	-0.9	82	9	1	36
70.0657	C4H8N	0.6	82	2	1	26.5
145.0761	C7H13O3	-9.8	71	2	1	37
95.0865	C6H9N	13.6	71	3.5	2	29.5
229.1359	C13H17N4	-8.9	61	8	1	24
187.1198	C8H15N2O3	12.1	61	3	1	36
156.1009	C8H14NO2	-1	61	3	2	36
90.0334	C6H4N	-0.4	61	6	1	32.5
81.0718	C6H9	1.9	61	3	3	36.5
60.0451	C3H8O	-11.9	61	0.5	4	30.5
159.088	C8H15O3	-13.6	51	2	1	40
102.0564	C5H10O2	-11.2	51	1.5	2	30.5
65.0395	C5H5	1	51	4	3	26

M5 Oxidation [M+H]+

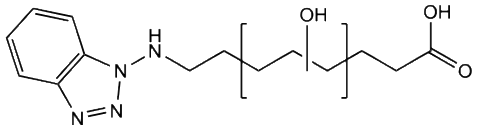

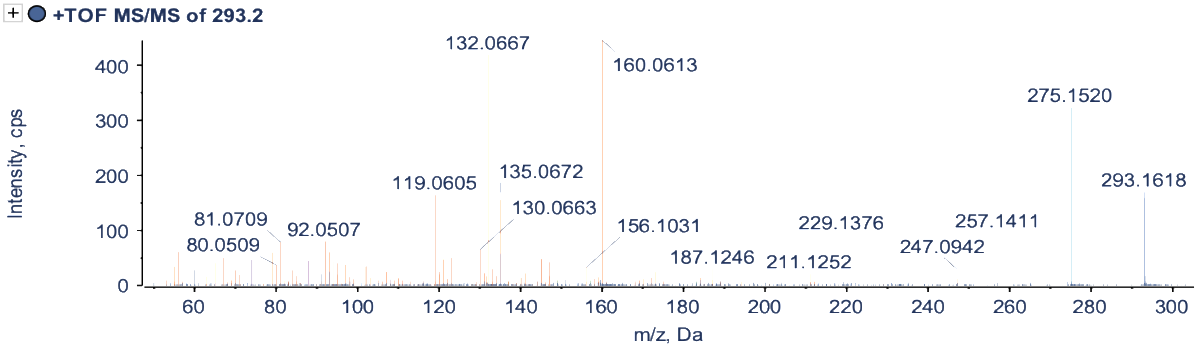

Mass (m/z)	Ion Formula	Error (mDa)	Intensity (cps)	RDB	Proposed Structures	Score
160.0613	C8H8N4	-13	445.3	7.5	1	25
132.0667	C6H12O3	-11.4	420.2	1.5	1	34.5
275.152	C14H19N4O2	1.7	323.2	8	2	40
293.1618	C14H21N4O3	0.9	170.1	7	1	44
119.0605	C5H11O3	-9.8	163.9	1	1	37.5
135.0672	C6H7N4	0.7	156.2	6	1	40.5
257.1411	C14H17N4O	1.4	96.2	9	1	36
92.0507	C6H6N	1.3	80.4	5	1	32.5
81.0709	C6H9	1	78.9	3	3	36.5
90.0346	C6H4N	0.7	66.4	6	1	32.5
130.0663	C6H10O3	3.8	65.8	2.5	1	34
86.0605	C5H10O	-12.1	63.3	1.5	4	30.5
138.0924	C8H12NO	1	62.8	4	1	32
114.0567	C6H10O2	-10.8	58.1	2.5	2	30.5
135.0921	C8H11N2	0.4	58	5	1	23.5
123.0818	C8H11O	1.3	50.4	4	1	32
67.0555	C5H7	1.2	50.4	3	3	29
145.0776	C7H13O3	-8.3	48.3	2	1	37
121.0764	C8H9O	11.6	47.9	5	1	29
147.0939	C7H15O3	-7.7	42.2	1	1	37.5
65.0389	C5H5	0.3	40.9	4	3	26
95.0867	C6H9N	13.7	40.3	3.5	2	29.5
97.066	C6H9O	1.2	38	3	3	30
80.0509	C6H8	-11.2	37.4	3.5	3	33.5
156.1031	C8H14NO2	1.1	33	3	2	36
187.1246	C8H15N2O3	16.9	30.8	3	1	36
247.0942	C11H11N4O3	11.6	29.5	9	0	3
118.065	C5H10O3	2.6	28.5	1.5	1	34.5
60.0448	C3H8O	-12.2	27.8	0.5	4	30.5

M6 Oxidation [M+H]+

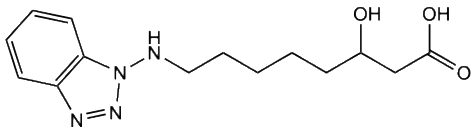

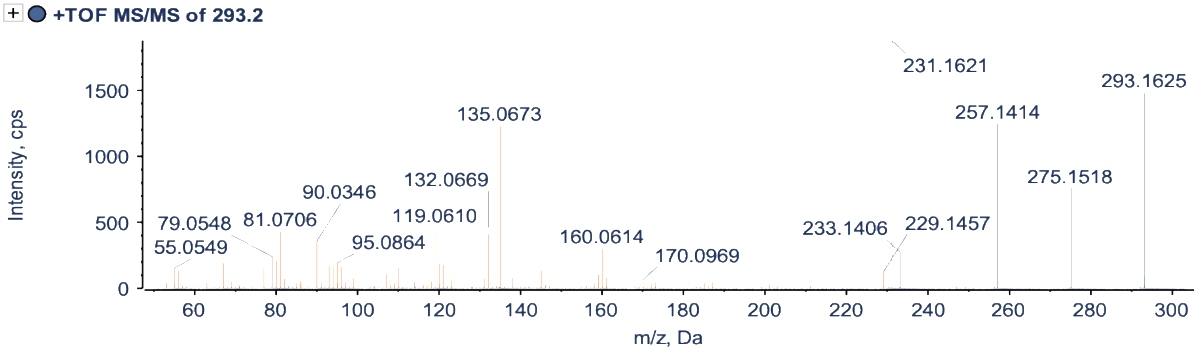

Mass (m/z)	Ion Formula	Error (mDa)	Intensity (cps)	RDB	Proposed Structures	Score
231.1621	C13H19N4	1.7	1876.1	7	1	24.5
293.1625	C14H21N4O3	1.7	1479.6	7	1	44
257.1414	C14H17N4O	1.7	1245.6	9	1	36
135.0673	C6H7N4	0.7	1228.4	6	1	40.5
275.1518	C14H19N4O2	1.5	760.8	8	2	40
119.061	C5H11O3	-9.3	458	1	1	37.5
81.0706	C6H9	0.7	430.2	3	3	36.5
132.0669	C6H12O3	-11.2	408.7	1.5	1	34.5
90.0346	C3H6O3	3.4	358.4	1.5	1	34.5
92.05	C6H6N	0.5	332.7	5	1	32.5
160.0614	C8H8N4	-13	299.8	7.5	1	25
233.1406	C12H17N4O	0.9	274	7	1	28
79.0548	C6H7	0.6	240.5	4	3	36.5
130.0659	C6H10O3	3.5	196	2.5	1	34
95.0864	C6H9N	13.4	195.5	3.5	2	29.5
67.0549	C5H7	0.6	191.6	3	3	30
110.0971	C6H10N2	13.3	155.3	3.5	1	29.5
55.0549	C4H7	0.7	155.1	2	4	33
77.0392	C6H5	0.7	151.3	5	1	36.5
70.0662	C5H10	-11.5	149.8	1.5	3	30.5
65.0393	C5H5	0.8	143.4	4	2	23
145.0767	C7H13O3	-9.3	132.1	2	1	37
229.1457	C13H17N4	1	128.9	8	1	24
159.0926	C8H15O3	-9	105.4	2	1	40

M7 Ketone Formation [M+H]+

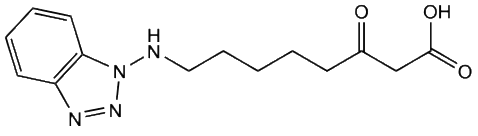

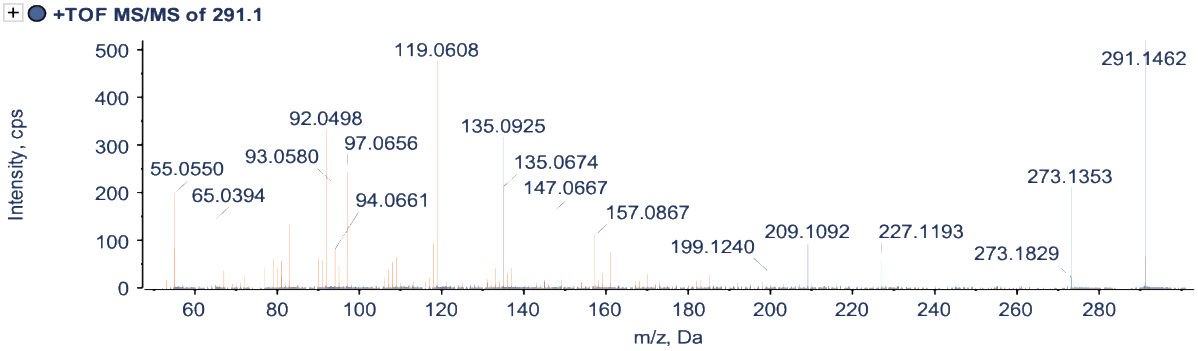

Mass (m/z)	Ion Formula	Error (mDa)	Intensity (cps)	RDB	Proposed Structures	Score
291.1462	C14H19N4O3	1	519.9	8	1	44
119.0608	C6H5N3	13	476.4	6.5	1	37.5
92.0498	C6H6N	0.4	332.6	5	1	32.5
135.0925	C8H11N2	0.9	317.8	5	1	23.5
97.0656	C6H9O	0.8	244.2	3	2	33
135.0674	C6H7N4	0.9	212.7	6	1	40.5
273.1353	C14H17N4O2	0.7	211.1	9	1	45
55.055	C4H7	0.8	199.5	2	1	33
147.0667	C7H7N4	0.2	158.3	7	1	33
65.0394	C5H5	0.8	144.3	4	0	3
83.0497	C5H7O	0.6	132.3	3	3	33
157.0867	C8H13O3	0.8	108.6	3	1	40
111.045	C6H7O2	1	100.6	4	1	33
139.0762	C8H11O2	0.8	98.3	4	1	36
118.0657	C7H6N2	13.1	94.2	6.5	1	20.5
209.1092	C14H13N2	1.8	93.2	10	0	3
101.0604	C5H9O2	0.7	91.7	2	1	33.5
55.0186	C3H3O	0.8	85.2	3	4	33
161.0718	C8H9N4	-10.4	75	7	1	28
111.0814	C7H11O	1	68.3	3	1	33
109.0705	C6H9N2	-5.5	65.6	4	2	36.5
90.0344	C6H4N	0.6	61.2	6	1	32.5
79.0553	C6H7	1.1	60.5	4	1	36.5
227.1193	C14H15N2O	1.5	58	9	0	3
81.0705	C6H9	0.7	57.9	3	1	36.5
108.0691	C6H8N2	0.9	55	4.5	2	33.5
95.05	C6H7O	0.8	46.2	4	2	30

M8 Oxidation [M+H]+

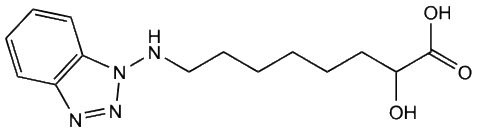

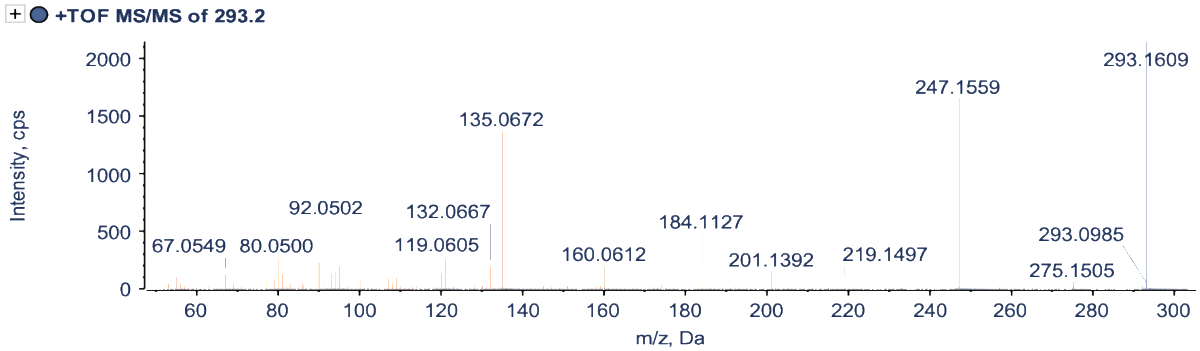

Mass (m/z)	Ion Formula	Error (mDa)	Intensity (cps)	RDB	Proposed Structures	Score
293.1609	C14H21N4O3	0.1	2147.7	7	1	49
247.1559	C13H19N4O	0.6	1659.2	7	1	33
135.0672	C6H7N4	0.7	1365.5	6	1	40.5
119.0605	C5H11O3	-9.8	281.4	1	1	37.5
80.05	C6H8	-12.1	265.7	3.5	3	33.5
121.0763	C8H9O	11.5	260.9	5	1	29
92.0502	C6H6N	0.7	231.2	5	1	32.5
90.0346	C6H4N	0.8	226.8	6	1	32.5
95.0858	C6H9N	12.9	196.1	3.5	2	29.5
132.0667	C6H12O3	-11.4	191.8	1.5	1	34.5
160.0612	C8H8N4	-13.1	190.2	7.5	1	25
94.0654	C6H8N	0.3	153.9	4	2	32.5
201.1392	C8H17N4O2	4.6	150.8	3	2	32.5
67.0549	C5H7	0.6	122.9	3	3	29
184.1127	C13H14N	0.6	109.5	8	0	3
55.0549	C4H7	0.7	105	2	4	29.5
77.0389	C6H5	0.3	100.3	5	1	36.5
109.0765	C6H9N2	0.4	99.5	4	2	36.5
65.039	C5H5	0.4	92.6	4	3	26
107.0607	C6H7N2	0.3	87.8	5	2	41.5
100.1129	C6H14N	0.8	85.8	1	1	26.5
79.0551	C6H7	0.9	76.7	4	3	36.5
275.1505	C14H19N4O2	0.3	58.9	8	2	45
86.0975	C5H12N	1	53	1	1	26.5
128.1076	C7H14NO	0.6	46.8	2	1	30
219.1497	C8H19N4O3	4.5	46.5	2	1	36.5

M9 Bis-Demethylenation [M+H]+

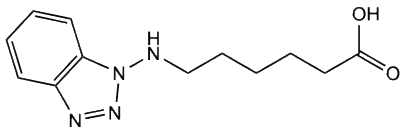

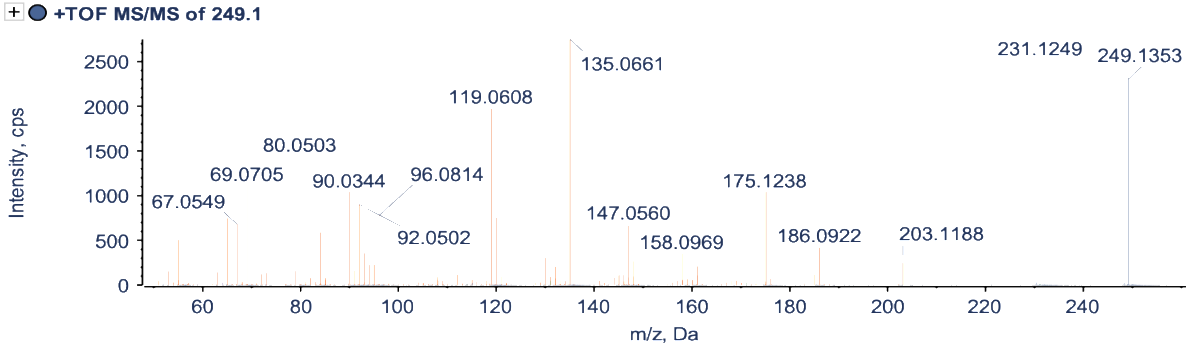

Mass (m/z)	Ion Formula	Error (mDa)	Intensity (cps)	RDB	Proposed Structures	Score
135.0661	C6H7N4	-0.4	2748.6	6	1	45.5
231.1249	C12H15N4O	0.8	2522.7	8	1	40
249.1353	C12H17N4O2	0.7	2303.8	7	1	49
119.0608	C6H5N3	13	1976.1	6.5	1	37.5
69.0705	C5H9	0.6	1113.7	2	1	33
90.0344	C6H4N	0.6	1044.8	6	1	32.5
175.1238	C6H15N4O2	4.8	1044	2	1	36.5
80.0503	C6H8	-11.8	959.1	3.5	1	33.5
92.0502	C6H6N	0.7	900.7	5	1	32.5
96.0814	C6H10N	0.6	779.6	3	1	32.5
65.0392	C5H5	0.6	747.1	4	0	3
67.0549	C5H7	0.7	681	3	1	30
147.056	C7H7N4	-10.5	667.3	7	1	28
56.0502	C4H8	-11.8	654.7	1.5	2	30.5
84.0816	C5H10N	0.8	588.8	2	1	30
55.0551	C4H7	0.8	505.9	2	2	33
186.0922	C10H10N4	2.2	422.8	8.5	1	22
77.0393	C6H5	0.7	406.6	5	1	36.5
158.0969	C6H14N4O	-19.3	350.4	2.5	1	29.5
107.0608	C6H7N2	0.4	310.1	5	2	36.5
130.0653	C8H6N2	12.8	305.7	7.5	1	20
203.1188	C12H15N2O	0.9	251.1	7	1	32.5
95.0497	C6H7O	0.6	231.6	4	1	33
161.1074	C10H13N2	0	209.8	6	1	28.5
132.0713	C8H8N2	3.1	205.9	6.5	1	20.5
79.055	C6H7	0.8	155.7	4	1	36.5
53.0392	C4H5	0.6	152.3	3	2	30
63.0236	C5H3	0.7	141	5	0	3

M10 Bis-Demethylenation+Methylation [M+H]+

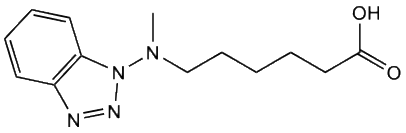

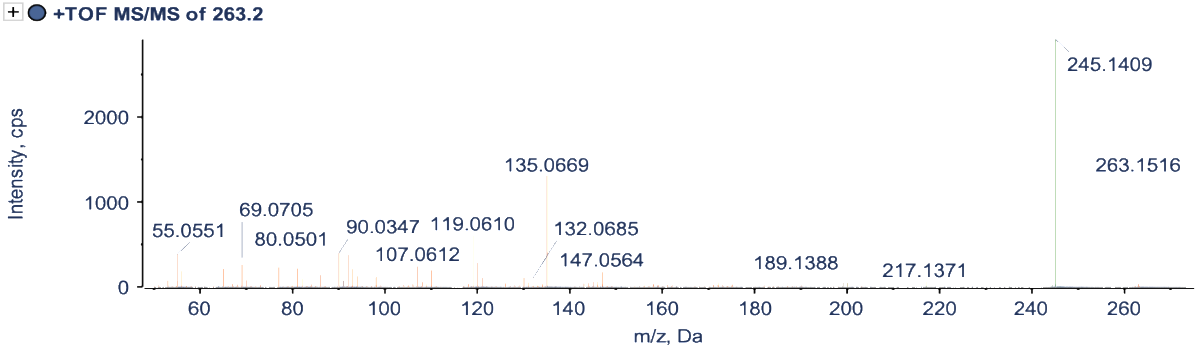

Mass (m/z)	Ion Formula	Error (mDa)	Intensity (cps)	RDB	Proposed Structures	Score
245.1409	C13H17N4O	1.2	2911.1	8	1	40
135.0669	C6H7N4	0.3	1310.4	6	1	41.5
263.1516	C13H19N4O2	1.4	1296.9	7	1	44
119.061	C6H5N3	13.2	609.2	6.5	1	37.5
80.0501	C6H8	-11.9	435.5	3.5	1	33.5
90.0347	C6H4N	0.9	395.9	6	1	32.5
55.0551	C4H7	0.9	386.5	2	2	33
92.0503	C6H6N	0.9	377.6	5	1	32.5
69.0705	C5H9	0.7	260	2	1	33
107.0612	C6H7N2	0.9	237.4	5	1	36.5
77.0393	C6H5	0.7	230	5	1	36.5
65.0394	C4H3N	13.4	212.6	4.5	1	20
110.0972	C6H10N2	13.3	194.3	3.5	1	20
83.0864	C5H9N	13.5	178.1	2.5	2	24
147.0564	C7H7N4	-10.1	175.4	7	2	40
79.0548	C6H7	0.6	151.1	4	1	36.5
189.1388	C7H17N4O2	4.2	140.8	2	1	36.5
86.0979	C5H12N	1.4	137.7	1	2	27.5
98.0975	C6H12N	1.1	122	2	1	27
130.0653	C8H6N2	12.8	111.9	7.5	1	17
121.0765	C7H9N2	0.5	108.9	5	1	32.5
132.0685	C8H8N2	0.3	105.1	6.5	1	22.5
67.0548	C5H7	0.6	82.8	3	1	30
53.0394	C4H5	0.9	75	3	2	30
55.0189	C3H3O	1	68.2	3	1	33

M11 Desaturation [M+H]+

(undefined olefin)

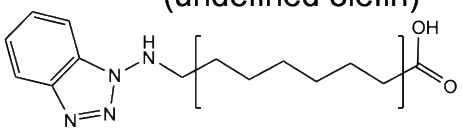

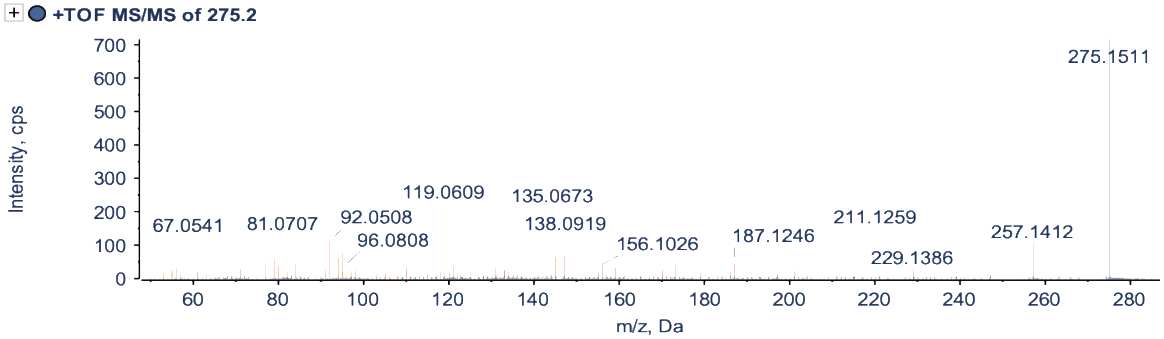

Mass (m/z)	Ion Formula	Error (mDa)	Intensity (cps)	RDB	Proposed Structures	Score
275.1511	C14H19N4O2	0.9	715.7	8	1	44
119.0609	C6H5N3	13.1	227	6.5	1	37.5
135.0673	C6H7N4	0.8	165.2	6	2	40.5
130.066	C8H6N2	13.4	150.2	7.5	1	20.5
81.0707	C6H9	0.8	130.1	3	2	36.5
92.0508	C6H6N	1.3	114.1	5	1	32.5
257.1412	C14H17N4O	1.5	106.6	9	1	40
90.0347	C6H4N	0.8	104.1	6	1	32.5
138.0919	C8H12NO	0.6	81.8	4	1	36
123.0817	C8H11O	1.3	81.7	4	1	36
95.0867	C7H11	1.1	76	3	1	33
147.0929	C9H11N2	1.2	68.7	6	1	23.5
145.077	C9H9N2	0.9	63.5	7	1	23.5
94.0658	C6H8N	0.7	61	4	2	32.5
79.0556	C6H7	1.4	58.6	4	2	36.5
132.0701	C8H8N2	1.9	53.6	6.5	1	20.5
70.0661	C4H8N	1	53.1	2	1	30.5
156.1026	C8H14NO2	0.7	43.5	3	1	40
141.092	C8H13O2	1	43.4	3	1	40
84.0809	C5H10N	0.1	43.2	2	1	35.5
187.1246	C12H15N2	1.6	43.2	7	1	23.5
173.1088	C8H17N2O2	-19.6	40.6	2	1	36.5
121.0756	C8H9O	10.9	38.1	5	1	33
140.1073	C8H14NO	0.4	38.1	3	1	41.5
110.0971	C7H12N	0.7	35.6	3	1	30
159.0929	C10H11N2	1.2	33.2	7	1	23.5
56.05	C3H6N	0.6	30.4	2	1	30.5
229.1386	C14H17N2O	5	29.9	8	1	32.5
107.0613	C6H7N2	1	28	5	3	36.5

M12 Desaturation [M+H]+

(undefined olefin)

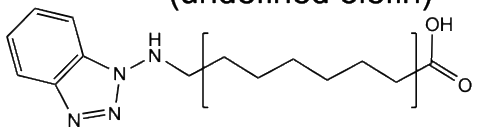

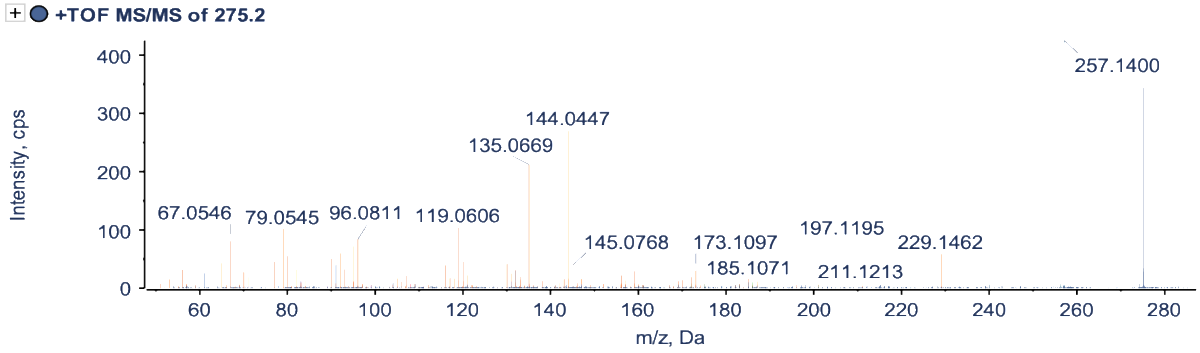

Mass (m/z)	Ion Formula	Error (mDa)	Intensity (cps)	RDB	Proposed Structures	Score
257.14	C14H17N4O	0.3	424.7	9	1	45
275.1513	C14H19N4O2	1	344.1	8	1	44
144.0447	C7H4N4	1.7	270	8.5	1	22
135.0669	C6H7N4	0.4	212	6	1	40.5
119.0606	C6H5N3	12.8	104.6	6.5	1	37.5
79.0545	C6H7	0.3	102	4	2	36.5
96.0811	C6H10N	0.3	83.9	3	1	32.5
67.0546	C5H7	0.4	80.4	3	2	30
81.0703	C6H9	0.5	78.8	3	2	36.5
95.0861	C7H11	0.5	72.1	3	1	33
110.0971	C7H12N	0.7	71.4	3	1	30
92.0503	C6H6N	0.8	60	5	1	32.5
229.1462	C14H17N2O	12.6	58.5	8	1	32.5
90.0349	C6H4N	1.1	50.7	6	1	32.5
77.0388	C6H5	0.3	45.7	5	1	36.5
65.0388	C5H5	0.3	43.6	4	1	27
130.0666	C8H6N2	14	41.8	7.5	1	20
116.049	C7H4N2	12.1	39.9	7.5	1	20
132.0702	C8H8N2	2	36.1	6.5	1	20.5
123.0795	C8H11O	-1	30.1	4	1	36
173.1097	C8H17N2O2	-18.8	30	2	1	36.5
159.0909	C10H11N2	-0.8	28.9	7	1	23
70.0657	C5H10	-12	27.3	1.5	2	30.5
156.0826	C8H14NO2	-19.3	21.7	3	1	40
172.1074	C8H16N2O2	-13.2	19	2.5	1	33.5
105.0697	C8H9	-0.2	17	5	0	8

(undefined ketone)

M13 Ketone Formation+Methylation [M+H]+

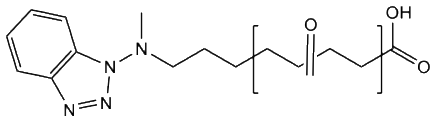

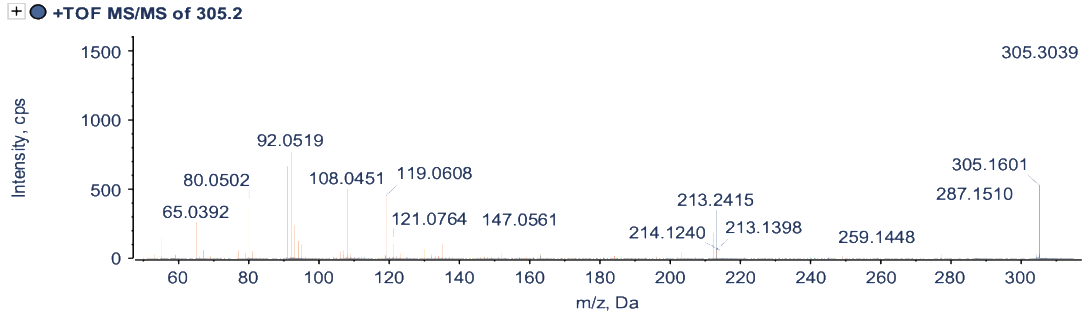

Mass (m/z)	Ion Formula	Error (mDa)	Intensity (cps)	RDB	Proposed Structures	Score
92.0519	C6H6N	2.4	771.6	5	1	32.5
91.0547	CH7N4O	-6.8	668.1	1	1	32.5
305.1601	C15H21N4O3	-0.8	527.5	8	1	49
108.0451	C7H8O	-11.8	504.5	4.5	1	27
119.0608	C6H5N3	13	455.7	6.5	1	37.5
287.151	C15H19N4O2	0.7	399.1	9	1	45
80.0502	C6H8	-11.9	384.7	3.5	3	33.5
65.0392	C4H3N	13.2	262.2	4.5	1	20
58.0661	C4H10	-11.6	192.2	0.5	4	30.5
55.055	C4H7	0.8	158.7	2	4	33
94.066	C6H8N	0.8	128.7	4	2	32.5
121.0764	C7H9N2	0.4	105.1	5	0	3
135.0574	C6H7N4	-9.1	104.5	6	1	36.5
147.0561	C7H7N4	-10.4	94.5	7	1	24.5
259.1448	C15H19N2O2	0.7	74.7	8	1	37.5
130.0662	C4H10N4O	-18.7	68	2.5	1	20.5
213.1398	C9H17N4O2	5.2	61.8	4	1	32.5
67.0549	C5H7	0.7	59.9	3	3	30
107.06	C6H7N2	-0.4	59.5	5	1	36.5
124.1122	C8H14N	0.1	56.6	3	0	8
77.0391	C6H5	0.5	56.4	5	1	36.5
106.0655	C6H6N2	12.9	52.2	5.5	1	33.5
97.1019	C7H13	0.7	50.7	2	1	33
203.1553	C9H19N2O3	16.2	43.6	2	1	36.5
123.0815	C8H11O	1	43.5	4	1	33
152.1089	C8H12N2O	14.5	41.5	4.5	2	20

M14 Methylation [M+H]+

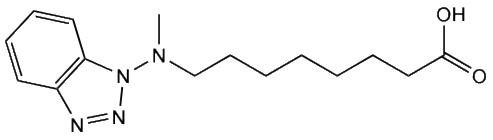

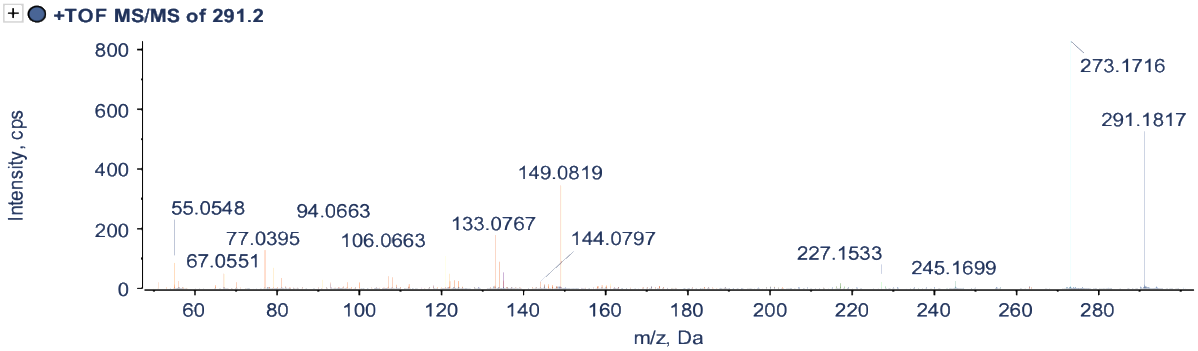

Mass (m/z)	Ion Formula	Error (mDa)	Intensity (cps)	RDB	Proposed Structures	Score
273.1716	C15H21N4O	0.7	828.8	8	1	45
291.1817	C15H23N4O2	0.1	526.7	7	1	49
149.0819	C7H9N4	-0.3	346.2	6	2	45.5
133.0767	C8H9N2	0.7	180.9	6	1	20.5
77.0395	C6H5	1	129.5	5	1	36.5
106.0663	C6H6N2	13.8	121.1	5.5	1	33.5
104.0503	C6H4N2	13.4	119.5	6.5	1	33.5
121.0759	C7H9N2	-0.1	110.1	5	1	37.5
55.0548	C4H7	0.6	86.6	2	4	33
94.0663	C6H8N	1.2	77.8	4	2	32.5
79.0551	C6H7	0.9	71.1	4	1	36.5
135.0932	C8H11N2	1.5	54.7	5	1	20.5
67.0551	C5H7	0.9	50.2	3	3	30
81.07	C6H9	0.1	36.2	3	3	41.5
91.0545	C6H5N	12.8	31.1	5.5	1	29.5
245.1699	C15H21N2O	5	26.6	7	1	32.5
135.0677	C6H7N4	1.1	25.5	6	1	36.5
227.1533	C15H19N2	-1	23.6	8	0	3
70.0663	C5H10	-11.4	21.9	1.5	3	30.5
97.1031	C7H13	1.9	21.8	2	1	33
51.0229	C3HN	12.6	21.6	4.5	1	20
93.0593	C6H7N	2	20.3	4.5	2	29.5
217.1723	C9H21N4O2	6.4	18.3	2	1	36.5
161.0724	C8H9N4	-9.8	18.2	7	2	25
83.0869	C6H11	1.4	16.4	2	2	33
146.0872	C9H10N2	3.4	16.3	6.5	1	17.5
112.1124	C7H14N	0.3	15.9	2	2	32

M15 Desaturation [M+H]+

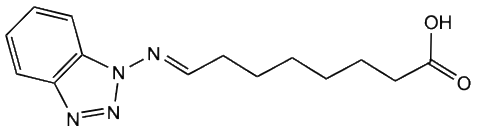

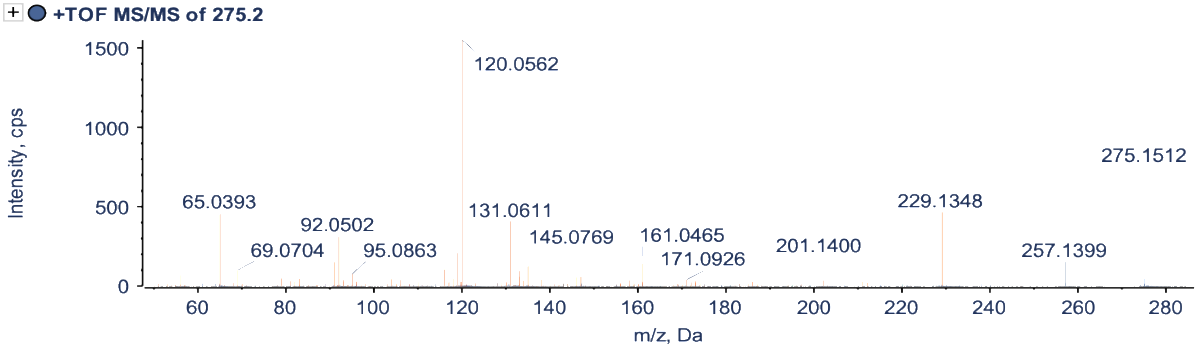

Mass (m/z)	Ion Formula	Error (mDa)	Intensity (cps)	RDB	Proposed Structures	Score
120.0562	C6H6N3	0.6	1551.3	6	1	40.5
275.1512	C14H19N4O2	1	750.7	8	1	44
229.1348	C14H17N2O	1.2	465.7	8	1	32.5
65.0393	C5H5	0.7	453.3	4	1	30
131.0611	C8H7N2	0.7	407.1	7	1	23.5
92.0502	C6H6N	0.8	309.9	5	1	32.5
145.0769	C9H9N2	0.8	234	7	1	23.5
119.0611	C6H5N3	13.3	207.1	6.5	1	37.5
201.14	C8H17N4O2	5.4	186.3	3	1	36.5
55.055	C4H7	0.8	185.3	2	3	33.5
257.1399	C14H17N4O	0.3	151.2	9	1	45
91.0418	C6H5N	0.1	151	5.5	1	34.5
161.0465	C7H5N4O	0.7	143.4	8	0	3
116.0502	C8H6N	0.7	106	7	0	3
69.0704	C5H9	0.5	101	2	2	33.5
77.0393	C6H5	0.7	95.5	5	1	36.5
95.0863	C7H11	0.8	77	3	1	33
90.0345	C6H4N	0.6	73.9	6	1	32.5
67.0552	C5H7	0.9	72.3	3	2	33
110.0974	C7H12N	1	60.1	3	1	30
79.0549	C6H7	0.7	47.9	4	2	36.5
83.0865	C6H11	1	45	2	1	33.5
104.05	C6H4N2	13.1	43.3	6.5	2	33.5
171.0926	C11H11N2	0.9	40.7	8	1	23
138.0921	C8H12NO	0.8	39.8	4	1	36

M16 Bis-Methylation [M+H]+

(undefined, may be ethylation)

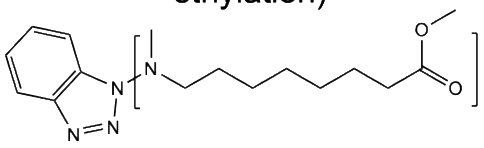

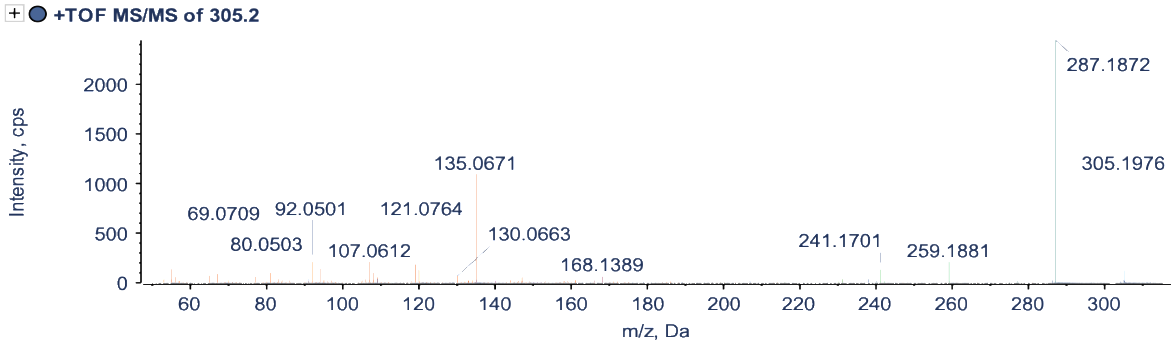

Mass (m/z)	Ion Formula	Error (mDa)	Intensity (cps)	RDB	Proposed Structures	Score
287.1872	C16H23N4O	0.6	2441.9	8	1	45
305.1976	C16H25N4O2	0.4	1095.8	7	1	49
135.0671	C6H7N4	0.6	1095.5	6	1	36.5
80.0503	C6H8	-11.7	277.6	3.5	3	33.5
107.0612	C6H7N2	0.8	213	5	1	36.5
92.0501	C6H6N	0.6	212.2	5	1	32.5
259.1881	C16H23N2O	7.6	210.5	7	1	32.5
121.0764	C8H11N	-12.2	210.3	4.5	1	14
119.0613	C6H5N3	13.5	181.5	6.5	1	37.5
90.0345	C6H4N	0.7	167.1	6	1	32.5
69.0709	C5H9	1	147.8	2	3	33
94.0653	C6H8N	0.1	142.3	4	3	37.5
55.0552	C4H7	1	136.2	2	4	33
241.1701	C16H21N2	0.1	133.4	8	0	8
67.0547	C5H7	0.5	91.5	3	3	30
65.0392	C4H3N	13.2	75	4.5	2	20
130.0663	C8H6N2	13.8	67.3	7.5	1	29
168.1389	C10H18NO	0.6	63.1	3	1	36
77.039	C6H5	0.5	60.4	5	1	36.5
146.0611	C7H6N4	2.4	59.4	7.5	2	21.5
132.0702	C8H8N2	2	53.6	6.5	1	29.5
230.153	C13H18N4	0.4	41.6	7.5	3	27

Parent 8-BAOA [M-H]-

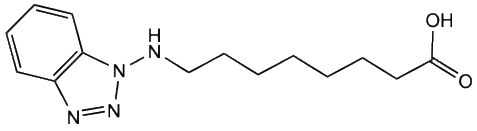

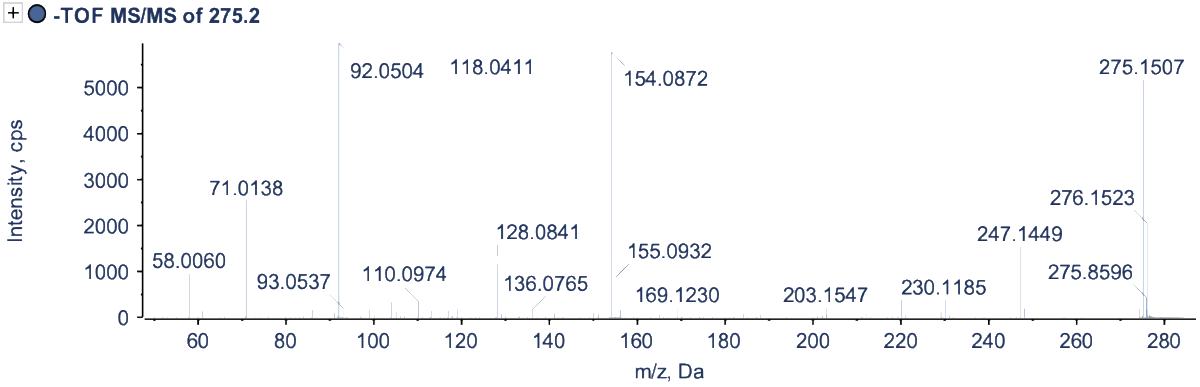

	Mass (m/z)	Ion Formula	Error (mDa)	Intensity (cps)	RDB	Proposed Structures	Score
1	92.0504	C6H6N	-0.2	5963.3	4.0	1	37.5
2	154.0872	C8H12NO2	-0.2	5777.0	3.0	1	42.0
3	275.1507	C14H19N4O2	-0.6	5173.0	7.0	1	49.0
4	118.0411	C6H4N3	0.0	4758.8	6.0	1	45.5
5	71.0138	C3H3O2	0.0	2555.9	2.0	1	42.0
6	247.1449	C14H19N2O2	-0.3	1542.6	6.0	1	41.5
7	128.0841	C7H12O2	-0.2	1158.8	1.5	1	39.0
8	58.0060	C2H2O2	0.0	947.2	1.5	1	39.0
9	230.1185	C14H16NO2	-0.2	394.1	7.0	0	8.0
10	220.1341	C13H18NO2	-0.2	389.9	5.0	0	8.0
11	110.0974	C7H12N	-0.1	358.4	2.0	1	35.0
12	104.0378	C6H4N2	-0.2	331.1	5.5	2	38.5
13	169.1230	C10H17O2	-0.4	221.9	2.0	0	8.0
14	203.1547	C8H19N4O2	3.4	206.3	1.0	1	36.5
15	136.0765	C8H10NO	-0.3	169.4	4.0	1	38.0
16	99.0451	C5H7O2	0.0	166.1	2.0	1	42.0
17	86.0372	C4H6O2	-0.1	163.4	1.5	1	39.0
18	117.0456	C7H5N2	-0.3	147.6	6.0	1	28.5
19	113.0606	C6H9O2	-0.2	147.6	2.0	1	42.0
20	108.0815	C7H10N	-0.3	144.2	3.0	1	27.0
21	61.0292	C2H5O2	-0.3	131.1	0.0	0	3.0
22	52.0192	C3H2N	-0.1	126.1	3.0	1	32.0
23	176.1441	C12H18N	-0.4	125.0	4.0	0	8.0
24	229.1339	C14H17N2O	-0.7	109.6	7.0	1	32.5
25	150.0316	C6H4N3O2	0.7	96.0	6.0	0	3.0
26	141.0917	C8H13O2	-0.4	92.1	2.0	1	40.0
27	90.0346	C6H4N	-0.3	90.7	5.0	1	32.5
28	186.1287	C13H16N	-0.1	83.2	6.0	0	8.0

M17 Unassigned Gain of 16.9885

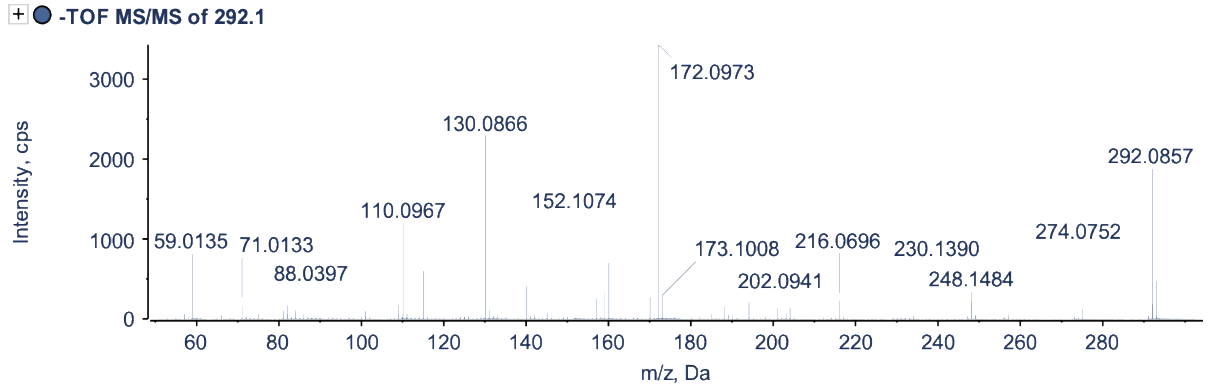

M18 Unassigned Gain of 272.9481

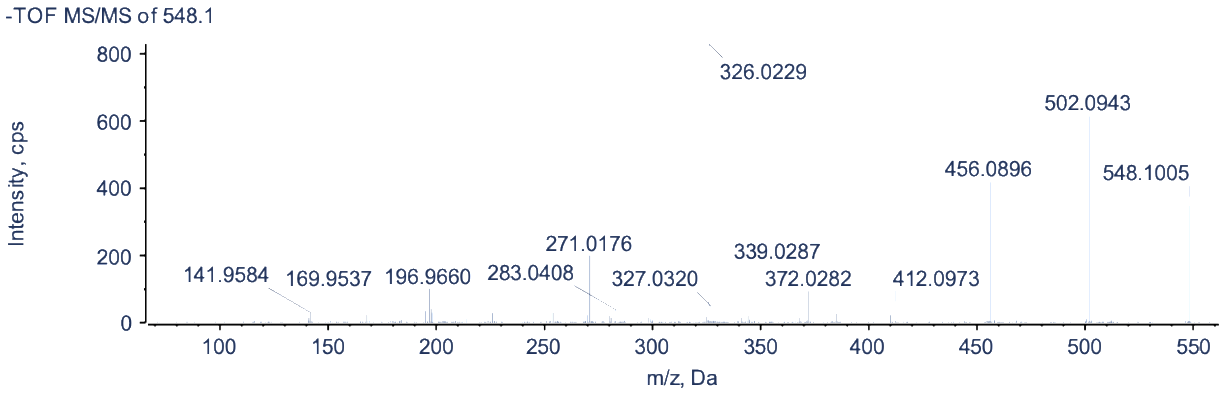

M19 Bis-Demethylenation+Oxidation [M-H]-

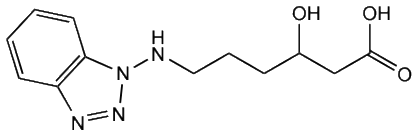

-TOF MS/MS of 263.1

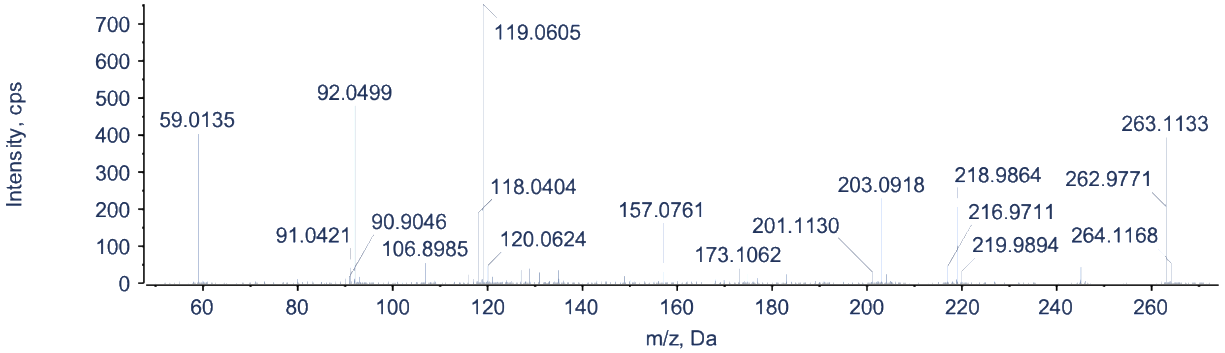

	Mass (m/z)	Ion Formula	Error (mDa)	Intensity (cps)	RDB	Proposed Structures	Score
1	119.0605	C7H7N2	-1.0	753.4	5.0	1	23.5
2	92.0499	C6H6N	-0.6	479.3	4.0	1	32.5
3	59.0135	C2H3O2	-0.4	403.6	1.0	1	37.5
4	203.0918	C10H11N4O	-2.0	231.7	7.0	1	28.0
5	118.0404	C6H4N3	-0.6	190.0	6.0	1	40.5
6	245.1029	C12H13N4O2	-1.5	44.7	8.0	2	40.0
7	131.0598	C8H7N2	-1.7	40.7	6.0	1	23.5
8	173.1062	C6H13N4O2	1.8	40.0	2.0	2	32.5
9	127.0755	C5H9N3O	0.4	35.7	2.5	0	5.0
10	157.0761	C10H9N2	-1.0	32.7	7.0	0	3.0
11	201.1130	C11H13N4	-1.6	30.5	7.0	1	24.5
12	183.0646	C10H7N4	-3.0	24.8	9.0	1	21.0
13	116.0500	C5H8O3	2.1	23.3	1.5	1	34.0
14	104.0369	C6H4N2	-1.1	19.6	5.5	2	33.5
15	123.0444	C7H7O2	-0.7	17.4	4.0	0	3.0
16	195.0618	C8H9N3O3	-3.2	14.6	5.5	0	0.0
17	90.0345	C3H6O3	2.3	12.6	0.5	1	34.5

M3 Tetra-Demethylenation [M-H]-

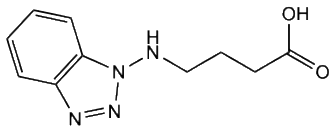

No MS/MS spectra were recorded for **M3** in ESI- mode in pooled plasma.

M4 Oxidation [M-H]-

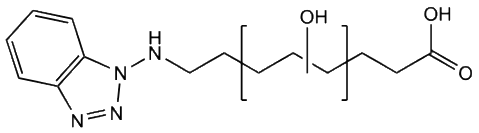

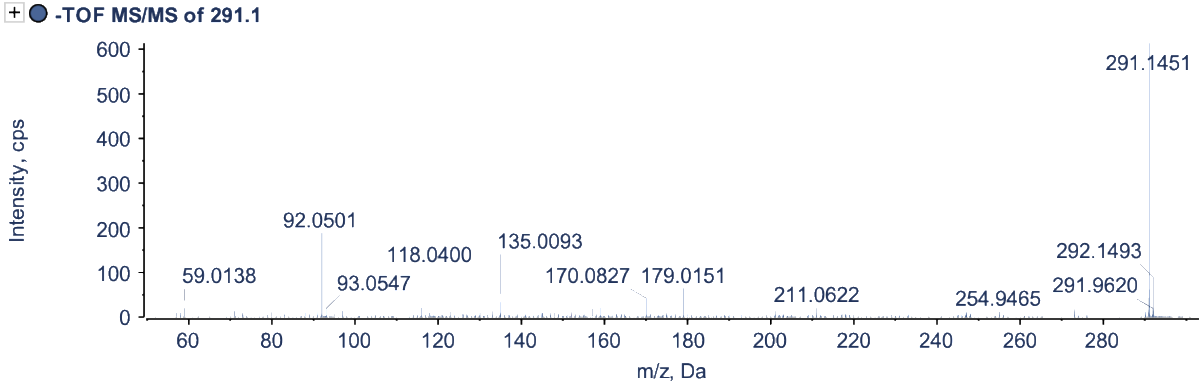

	Mass (m/z)	Ion Formula	Error (mDa)	Intensity (cps)	RDB	Proposed Structures	Score
1	291.1451	C14H19N4O3	-1.2	613.8	7.0	1	44.0
2	92.0501	C6H6N	-0.5	188.9	4.0	2	32.5
3	118.0400	C6H4N3	-1.0	112.5	6.0	1	40.5
4	170.0827	C8H12NO3	0.4	42.5	3.0	1	42.0
5	115.0397	C5H7O3	-0.3	35.9	2.0	1	42.0
6	135.0093	C7H3O3	0.5	33.8	6.0	0	3.0
7	211.0622	C11H7N4O	-0.3	20.0	10.0	0	8.0
8	59.0138	C2H3O2	0.0	20.0	1.0	1	42.5
9	157.0956	C7H13N2O2	-2.6	20.0	2.0	0	3.0
10	273.1317	C14H17N4O2	-4.0	17.0	8.0	2	40.0
11	71.0139	C3H3O2	0.1	13.6	2.0	1	42.0
12	201.0883	C13H13O2	-3.8	13.3	7.0	0	3.0
13	91.0160	C6H3O	-2.9	13.1	5.0	1	26.0
14	71.0481	C4H7O	-2.1	12.9	1.0	4	29.5
15	133.0726	C8H9N2	-4.5	12.7	5.0	1	23.5
16	263.1393	C14H19N2O3	-0.8	12.7	6.0	1	36.5
17	123.0439	C7H7O2	-1.2	12.2	4.0	2	30.0
18	85.0290	C4H5O2	-0.5	10.4	2.0	2	33.5
19	135.0469	C8H7O2	1.7	10.3	5.0	0	3.0

M5 Oxidation [M-H]-

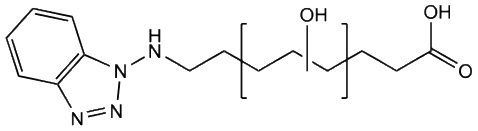

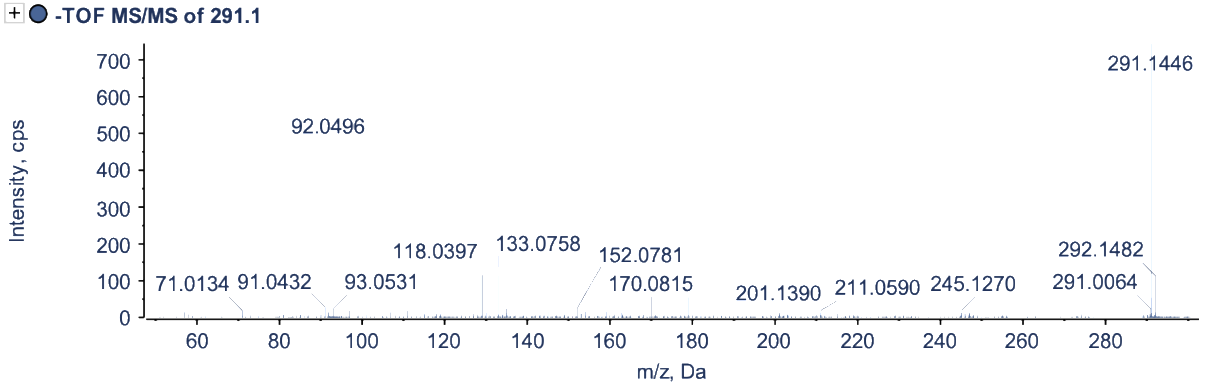

	Mass (m/z)	Ion Formula	Error (mDa)	Intensity (cps)	RDB	Proposed Structures	Score
1	291.1446	C14H19N4O3	-1.7	744.2	7.0	1	44.0
2	92.0496	C6H6N	-1.0	482.2	4.0	0	3.0
3	118.0397	C6H4N3	-1.3	144.4	6.0	1	36.5
4	133.0758	C8H9N2	-1.3	115.8	5.0	0	3.0
5	129.0544	C4H7N3O2	0.0	115.0	2.5	0	5.0
6	170.0815	C8H12NO3	-0.8	56.1	3.0	0	3.0
7	201.1390	C8H17N4O2	3.3	29.9	2.0	1	36.5
8	91.0432	C3H7O3	3.2	27.9	0.0	0	3.0
9	152.0781	C7H10N3O	-4.8	25.4	4.0	0	3.0
10	135.0079	C7H3O3	-0.9	25.1	6.0	0	3.0
11	273.1330	C14H17N4O2	-2.7	23.1	8.0	2	40.0
12	113.0229	C3H3N3O2	-0.2	22.1	3.5	0	5.0
13	83.0504	C5H7O	0.2	21.2	2.0	1	38.5
14	211.0590	C11H7N4O	-3.5	19.8	10.0	0	3.0
15	245.1270	C14H17N2O2	-2.6	19.5	7.0	2	32.5
16	71.0134	C3H3O2	-0.4	18.8	2.0	1	37.0
17	111.0457	C6H7O2	0.5	17.8	3.0	1	34.0
18	154.0861	C8H12NO2	-1.2	15.3	3.0	1	37.0
19	159.1122	C7H15N2O2	-1.7	15.2	1.0	0	3.0
20	57.0339	C3H5O	-0.7	14.8	1.0	1	33.5
21	116.0505	C8H6N	-0.1	12.6	6.0	0	8.0
22	135.0432	C6H5N3O	-0.6	12.6	5.5	1	37.5
23	211.0986	C12H11N4	-0.3	12.3	9.0	1	26.0

M6 Oxidation [M-H]-

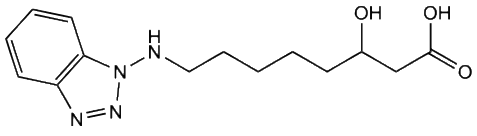

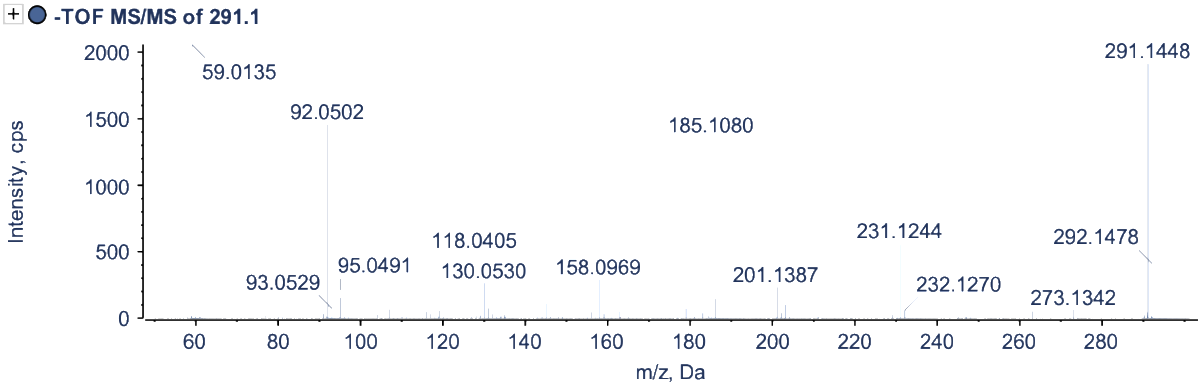

	Mass (m/z)	Ion Formula	Error (mDa)	Intensity (cps)	RDB	Proposed Structures	Score
1	59.0135	C2H3O2	-0.3	2058.1	1.0	1	37.5
2	291.1448	C14H19N4O3	-1.5	1910.7	7.0	1	44.0
3	92.0502	C6H6N	-0.4	1455.8	4.0	0	3.0
4	185.1080	C12H13N2	-0.4	1360.2	7.0	0	8.0
5	231.1244	C12H15N4O	-0.7	555.1	7.0	1	28.0
6	158.0969	C11H12N	-0.7	292.7	6.0	0	3.0
7	130.0530	C5H8NO3	2.0	265.2	2.0	0	3.0
8	201.1387	C8H17N4O2	3.0	231.6	2.0	1	36.5
9	95.0491	C6H7O	-1.1	154.7	3.0	2	36.5
10	133.0767	C8H9N2	-0.4	149.1	5.0	0	3.0
11	118.0405	C6H4N3	-0.5	129.8	6.0	1	36.5
12	145.0768	C9H9N2	-0.3	111.9	6.0	0	8.0
13	203.1175	C12H15N2O	-1.4	103.1	6.0	1	23.5
14	273.1342	C14H17N4O2	-1.5	64.3	8.0	2	40.0
15	107.0599	C6H7N2	-1.6	63.0	4.0	2	32.5
16	263.1392	C14H19N2O3	-0.9	48.7	6.0	1	36.5
17	116.0491	C8H6N	-1.5	46.9	6.0	0	3.0
18	156.0693	C10H8N2	0.0	43.6	7.5	0	5.0
19	183.0930	C12H11N2	0.2	38.2	8.0	0	8.0
20	143.0640	C9H7N2	2.5	34.2	7.0	0	3.0
21	91.0419	C3H7O3	1.8	31.8	0.0	0	3.0
22	211.0598	C11H7N4O	-2.7	30.7	10.0	0	3.0
23	104.0371	C6H4N2	-0.9	26.5	5.5	1	29.5
24	135.0087	C7H3O3	0.0	25.6	6.0	0	8.0
25	229.1451	C13H17N4	-0.8	25.0	7.0	1	24.5

M7 Ketone Formation [M-H]-

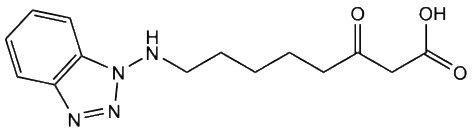

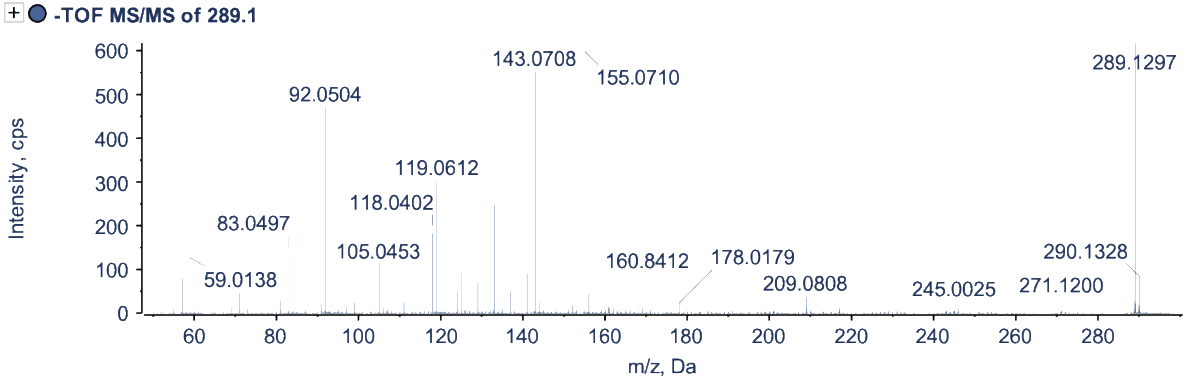

	Mass (m/z)	Ion Formula	Error (mDa)	Intensity (cps)	RDB	Proposed Structures	Score
1	289.1297	C14H17N4O3	-0.9	618.1	8.0	1	44.0
2	155.0710	C8H11O3	-0.4	598.4	3.0	1	45.0
3	143.0708	C7H11O3	-0.5	552.4	2.0	1	37.5
4	92.0504	C6H6N	-0.2	472.5	4.0	1	37.5
5	119.0612	C7H7N2	-0.3	301.6	5.0	1	28.5
6	133.0511	C6H5N4	-0.8	247.9	6.0	1	40.5
7	118.0402	C6H4N3	-0.9	182.6	6.0	1	40.5
8	83.0497	C5H7O	-0.5	133.1	2.0	3	33.5
9	59.0138	C2H3O2	0.0	126.9	1.0	1	42.5
10	105.0453	C6H5N2	-0.6	114.7	5.0	2	36.5
11	125.0598	C7H9O2	-1.0	91.2	3.0	1	33.5
12	141.0553	C7H9O3	-0.4	90.8	3.0	1	37.0
13	57.0344	C3H5O	-0.2	79.2	1.0	4	33.5
14	129.0551	C6H9O3	-0.6	71.2	2.0	1	37.5
15	137.0594	C8H9O2	-1.4	50.4	4.0	1	36.0
16	124.0759	C7H10NO	-0.9	49.9	3.0	1	30.0
17	71.0139	C3H3O2	0.0	44.8	2.0	1	42.0
18	209.0808	C9H11N3O3	0.2	37.5	5.5	0	5.0
19	150.0556	C8H8NO2	-0.5	35.2	5.0	1	33.0
20	271.1200	C14H15N4O2	0.0	34.1	9.0	1	45.0
21	82.0290	C4H4NO	-0.9	33.4	3.0	1	30.0
22	111.0810	C7H11O	-0.5	31.2	2.0	1	33.5
23	81.0341	C5H5O	-0.5	29.6	3.0	3	33.0
24	77.0393	C6H5	-0.4	29.1	4.0	1	36.5
25	168.0658	C8H10NO3	-0.8	27.0	4.0	1	37.0
26	99.0805	C6H11O	-1.0	24.4	1.0	2	33.5
27	178.0179	C6H2N4O3	4.7	23.0	7.5	0	0.0
28	165.1290	C11H17O	0.5	21.5	3.0	0	8.0

M20 Glucuronidation [M-H]-

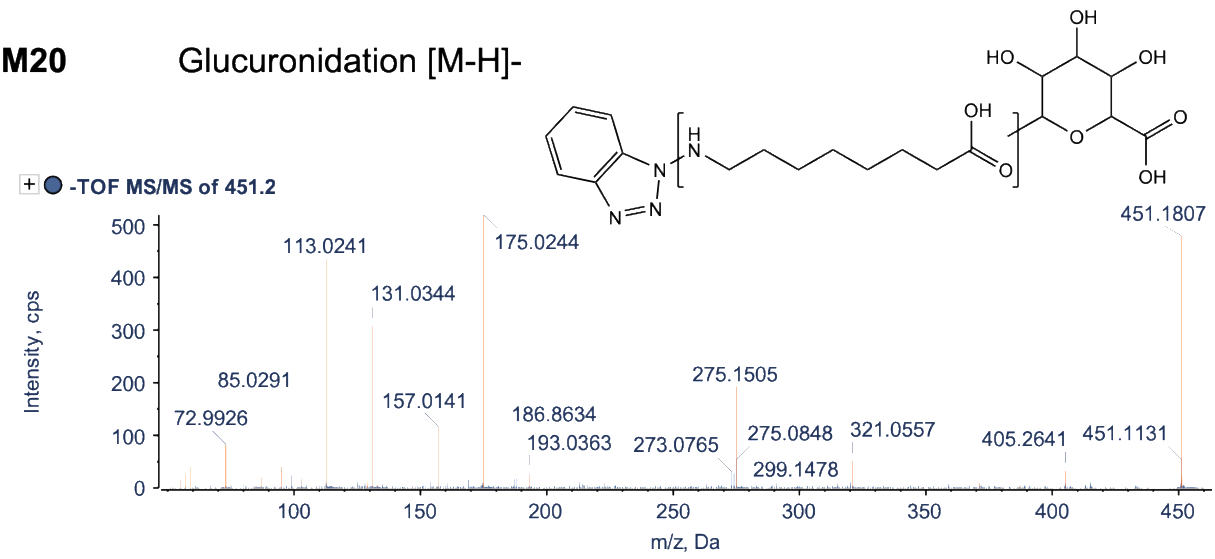

	Mass (m/z)	Ion Formula	Error (mDa)	Intensity (cps)	RDB	Proposed Structures	Score
1	175.0244	C6H7O6	-0.4	519.3	3.0	10	45.0
2	451.1807	C20H27N4O8	-2.7	479.1	9.0	1	44.0
3	113.0241	C5H5O3	-0.4	434.2	3.0	5	29.5
4	131.0344	C6H3N4	-1.9	307.2	7.0	1	40.0
5	275.1505	C14H19N4O2	-0.8	193.1	7.0	1	45.5
6	85.0291	C4H5O2	-0.4	181.4	2.0	2	33.5
7	157.0141	C6H5O5	-0.1	117.5	4.0	17	41.0
8	72.9926	C6H	-15.8	83.0	6.0	1	36.0
9	73.0293	C3H5O2	-0.2	80.2	1.0	9	38.5
10	71.0135	C3H3O2	-0.4	73.6	2.0	9	33.5
11	101.0240	C6HN2	9.5	67.5	7.0	2	36.0
12	275.0848	C11H15O8	7.6	54.2	4.0	1	37.0
13	321.0557	C15H13O8	-5.9	51.7	9.0	0	3.0
14	59.0138	C2H3O2	0.0	40.8	1.0	9	38.5
15	95.0137	C5H3O2	-0.1	40.6	4.0	2	35.0
16	273.0765	C11H13O8	14.9	31.8	5.0	1	34.0
17	193.0363	C6H9O7	0.9	27.0	2.0	4	40.5
18	57.0347	C3H5O	0.1	26.6	1.0	1	38.5
19	99.0079	C4H3O3	-0.9	23.7	3.0	7	29.5
20	188.0141	C7H8O6	-18.5	20.1	3.5	10	26.5
21	168.9886	C6HO6	10.7	17.1	6.0	2	18.5
22	187.0958	C10H11N4	-3.1	16.2	7.0	1	28.0
23	103.0412	C6H3N2	11.1	16.1	6.0	2	36.5
24	55.0195	C3H3O	0.6	16.1	2.0	1	33.5
25	118.0404	C6H4N3	-0.7	15.5	6.0	1	40.5

M8 Oxidation [M-H]-

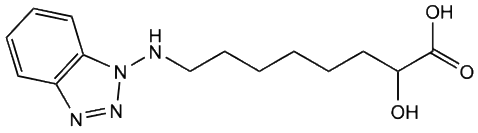

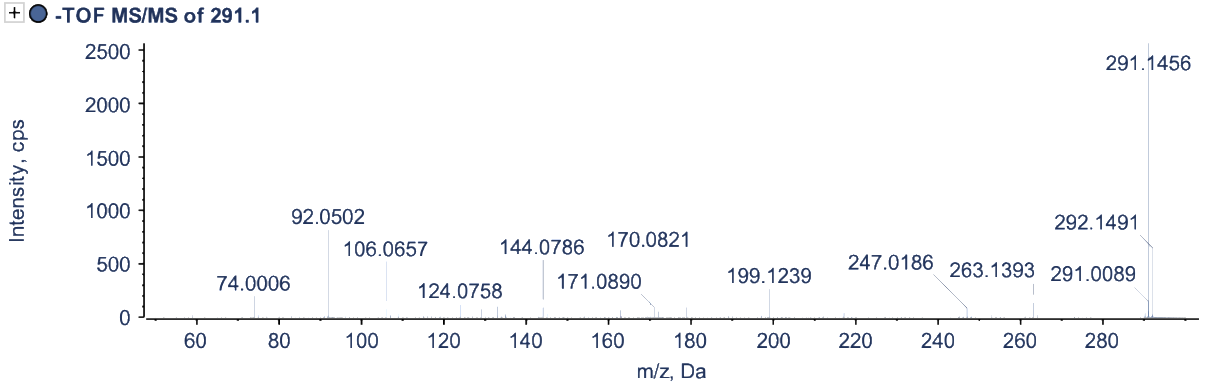

	Mass (m/z)	Ion Formula	Error (mDa)	Intensity (cps)	RDB	Proposed Structures	Score
1	291.1456	C14H19N4O3	-0.6	2563.5	7.0	1	49.0
2	92.0502	C6H6N	-0.4	817.2	4.0	2	32.5
3	170.0821	C8H12NO3	-0.2	610.0	3.0	1	42.0
4	199.1239	C8H15N4O2	3.8	264.1	3.0	2	32.5
5	74.0006	N3O2	1.0	199.9	2.0	0	3.0
6	263.1393	C14H19N2O3	-0.8	139.1	6.0	1	41.5
7	124.0758	C7H10NO	-0.9	121.7	3.0	1	27.0
8	133.0277	C8H5O2	-1.8	101.6	6.0	0	3.0
9	144.0786	C7H12O3	-0.6	92.6	1.5	1	34.0
10	118.0406	C6H4N3	-0.5	89.3	6.0	1	40.5
11	106.0657	C7H8N	-0.6	77.4	4.0	1	23.0
12	129.0552	C6H9O3	-0.5	74.2	2.0	1	37.0
13	172.1060	C7H14N3O2	-3.2	51.6	2.0	0	3.0
14	211.0611	C11H7N4O	-1.5	50.5	10.0	0	3.0
15	217.1335	C8H17N4O3	2.9	41.1	2.0	1	36.5
16	109.0657	C7H9O	-0.2	39.6	3.0	2	35.0
17	135.0070	C5HN3O2	-0.4	27.9	6.5	0	5.0
18	59.0135	C2H3O2	-0.4	19.5	1.0	1	37.5
19	83.0502	C5H7O	-0.1	17.9	2.0	4	38.0
20	197.1097	C13H13N2	1.2	16.9	8.0	0	3.0
21	87.0083	C6HN	-3.2	16.5	6.5	1	29.0
22	91.0416	C6H5N	-1.1	16.4	4.5	1	29.5
23	155.1072	C9H15O2	-0.5	14.5	2.0	0	3.0
24	157.0862	C8H13O3	-0.8	12.9	2.0	1	40.0

M9 Bis-Demethylenation [M-H]-

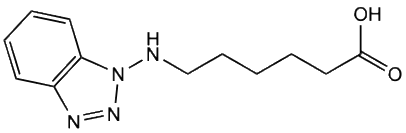

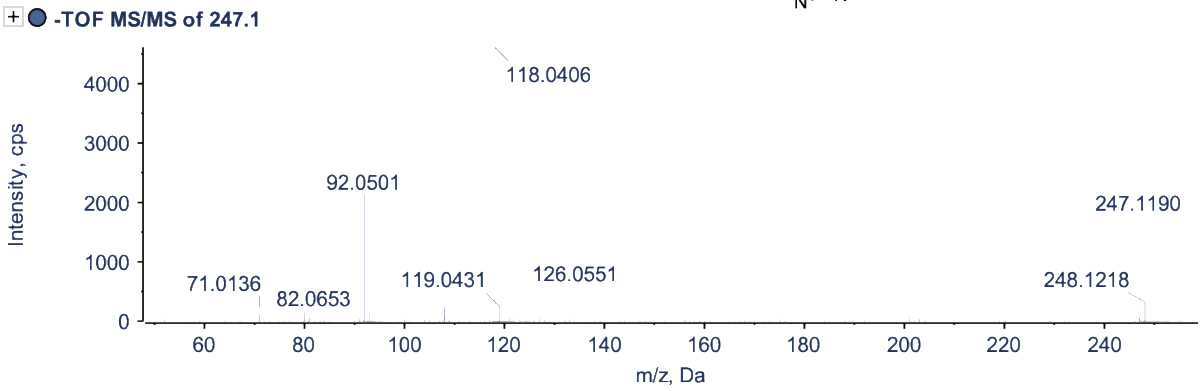

	Mass (m/z)	Ion Formula	Error (mDa)	Intensity (cps)	RDB	Proposed Structures	Score
1	118.0406	C6H4N3	-0.5	4612.3	6.0	1	40.5
2	92.0501	C6H6N	-0.5	2131.0	4.0	1	32.5
3	247.1190	C12H15N4O2	-1.0	1763.7	7.0	1	44.0
4	126.0551	C6H8NO2	-1.0	263.8	3.0	1	37.0
5	108.0445	C6H6NO	-1.0	243.6	4.0	1	33.0
6	82.0653	C5H8N	-0.9	164.1	2.0	1	30.0
7	80.0499	C5H6N	-0.6	146.1	3.0	1	27.0
8	90.0345	C6H4N	-0.4	116.2	5.0	1	32.5
9	71.0136	C3H3O2	-0.3	108.1	2.0	1	37.0
10	108.0214	C4H2N3O	1.0	106.3	5.0	0	3.0
11	201.1026	C12H13N2O	-0.7	70.4	7.0	1	32.5
12	121.0286	C7H5O2	-0.9	47.1	5.0	0	3.0
13	175.1238	C6H15N4O2	3.7	39.7	1.0	1	36.5
14	167.0352	C9H3N4	-1.1	37.2	10.0	0	3.0
15	133.0505	C6H5N4	-1.5	33.4	6.0	1	40.5
16	123.0453	C7H7O2	0.1	32.2	4.0	0	8.0
17	52.0189	C3H2N	-0.4	31.8	3.0	1	27.0
18	100.0513	C5H8O2	-1.7	31.4	1.5	1	34.0
19	104.0362	C6H4N2	-1.8	26.4	5.5	2	33.5
20	128.0689	C6H10NO2	-2.8	20.9	2.0	1	40.0
21	50.0039	C3N	0.3	20.5	4.0	0	3.0
22	158.0959	C11H12N	-1.7	18.7	6.0	0	3.0
23	156.0819	C11H10N	0.0	18.7	7.0	0	8.0
24	77.0395	C6H5	-0.2	17.7	4.0	1	41.5
25	113.0607	C6H9O2	-0.1	17.3	2.0	1	45.0

M21 Loss of $C_6H_4N_4$+Glucuronidation [M-H]-

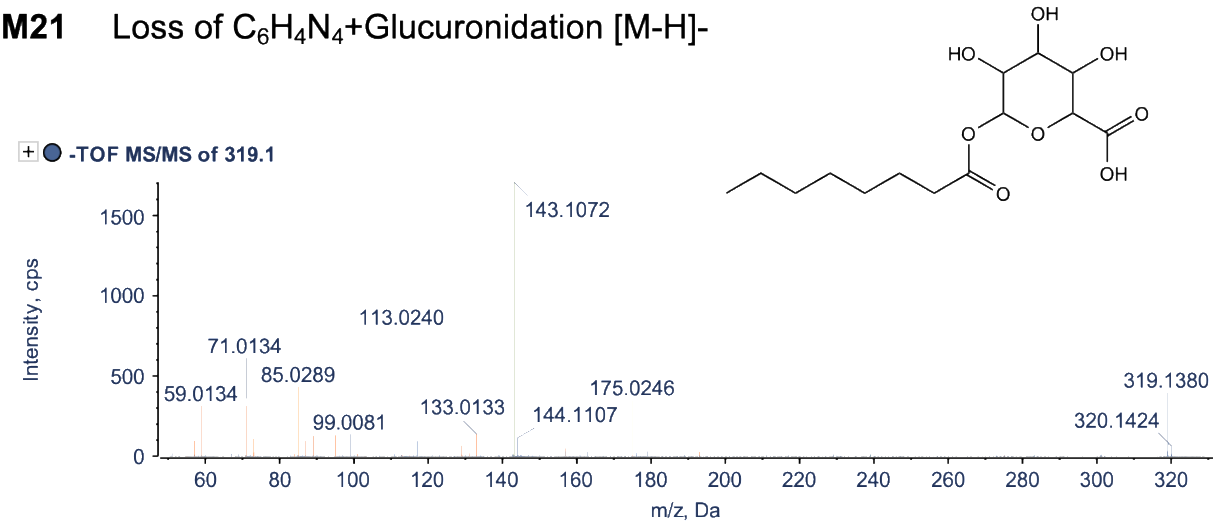

	Mass (m/z)	Ion Formula	Error (mDa)	Intensity (cps)	RDB	Proposed Structures	Score
1	143.1072	C8H15O2	-0.6	1706.7	1.0	2	40.5
2	113.0240	C5H5O3	-0.4	788.7	3.0	5	29.5
3	85.0289	C4H5O2	-0.6	432.2	2.0	2	33.5
4	319.1380	C14H23O8	-1.8	397.1	3.0	1	44.0
5	175.0246	C6H7O6	-0.2	349.7	3.0	10	45.0
6	59.0134	C2H3O2	-0.4	313.4	1.0	9	33.5
7	71.0134	C3H3O2	-0.4	312.8	2.0	9	33.5
8	133.0133	C4H5O5	-1.0	138.0	2.0	6	33.5
9	99.0081	C4H3O3	-0.7	137.6	3.0	7	29.5
10	95.0137	C5H3O2	-0.2	131.4	4.0	2	35.0
11	89.0240	C3H5O3	-0.4	127.6	1.0	10	33.5
12	72.9929	C2HO3	-0.2	111.5	2.0	3	33.5
13	57.0341	C3H5O	-0.5	99.7	1.0	1	33.5
14	87.0079	C3H3O3	-0.8	98.2	2.0	10	33.5
15	117.0190	C4H5O4	-0.4	94.0	2.0	11	33.5
16	115.0033	C4H3O4	-0.4	74.6	3.0	11	33.0
17	75.0080	C2H3O3	-0.8	72.4	1.0	3	33.5
18	129.0182	C5H5O4	-1.1	66.4	3.0	10	33.0
19	103.0023	C3H3O4	-1.4	57.2	2.0	4	33.5
20	179.0152	C5H7O7	-4.5	29.0	2.0	0	3.0
21	193.0343	C6H9O7	-1.0	27.7	2.0	4	40.5
22	67.0183	C4H3O	-0.7	18.3	3.0	1	33.0
23	51.0237	C4H3	-0.3	16.8	3.0	3	27.0
24	111.0088	C5H3O3	0.0	15.9	4.0	5	34.0
25	84.0216	C4H4O2	-0.1	15.2	2.5	2	35.0
26	68.9974	C3HO2	-0.8	13.0	3.0	9	33.0
27	239.0934	C12H15O5	0.9	11.9	5.0	13	26.0

M22 Glucuronidation [M-H]-

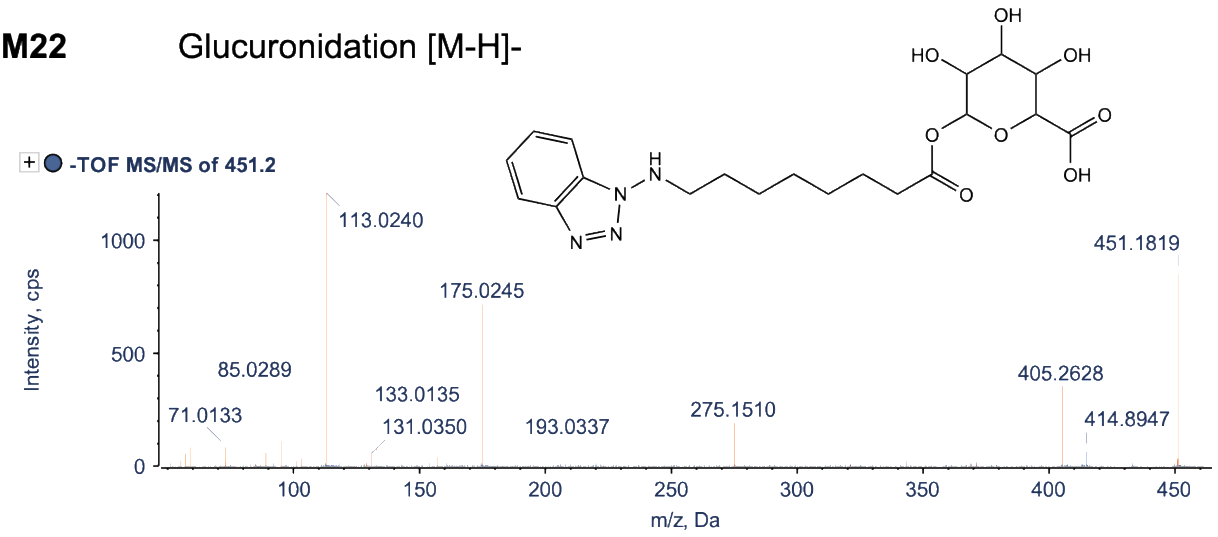

	Mass (m/z)	Ion Formula	Error (mDa)	Intensity (cps)	RDB	Proposed Structures	Score
1	113.0240	C5H5O3	-0.4	1210.9	3.0	5	29.5
2	451.1819	C20H27N4O8	-1.5	851.5	9.0	1	44.0
3	175.0245	C6H7O6	-0.3	716.8	3.0	10	45.0
4	85.0289	C4H5O2	-0.6	369.5	2.0	2	33.5
5	275.1510	C14H19N4O2	-0.4	192.0	7.0	1	45.5
6	133.0135	C4H5O5	-0.7	174.3	2.0	6	33.5
7	71.0133	C3H3O2	-0.5	112.2	2.0	9	33.5
8	95.0135	C5H3O2	-0.4	110.0	4.0	2	30.0
9	59.0134	C2H3O2	-0.5	84.1	1.0	9	33.5
10	72.9925	C6H	-15.8	83.9	6.0	1	36.0
11	89.0237	C3H5O3	-0.7	59.8	1.0	10	33.5
12	131.0350	C6H3N4	-1.3	57.4	7.0	1	40.0
13	115.0033	C6HN3	-14.3	48.1	7.5	1	34.0
14	157.0138	C6H5O5	-0.4	38.7	4.0	17	41.0
15	193.0337	C6H9O7	-1.7	34.6	2.0	4	40.5
16	103.0035	C3H3O4	-0.2	34.1	2.0	4	38.5
17	101.0232	C6HN2	8.7	24.5	7.0	2	36.0
18	55.0187	C3H3O	-0.3	23.8	2.0	1	33.5
19	343.2147	C19H27N4O2	0.8	23.0	8.0	0	8.0
20	84.0214	C4H4O2	-0.3	21.2	2.5	2	30.0
21	379.1861	C14H27N4O8	2.7	18.2	3.0	1	36.5
22	99.0077	C4H3O3	-1.1	18.1	3.0	7	29.5
23	371.1679	C19H23N4O4	-4.5	17.0	10.0	3	20.5
24	247.1429	C14H19N2O2	-2.3	16.0	6.0	1	32.5
25	129.0186	C6HN4	-2.1	15.4	8.0	1	37.0

M23 Loss of $C_6H_4N_4$+Glucuronidation [M-H]-

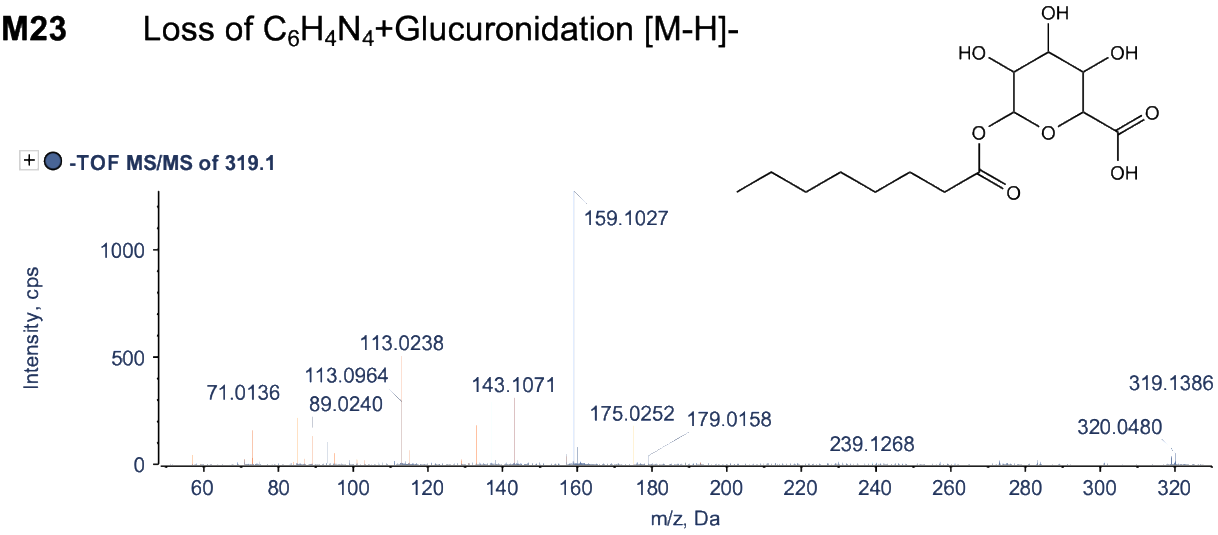

	Mass (m/z)	Ion Formula	Error (mDa)	Intensity (cps)	RDB	Proposed Structures	Score
1	159.1027	C8H15O3	0.0	1274.8	1.0	2	30.0
2	113.0238	C5H5O3	-0.6	507.8	3.0	5	29.5
3	319.1386	C14H23O8	-1.3	318.2	3.0	1	44.0
4	143.1071	C8H15O2	-0.7	311.3	1.0	2	40.5
5	137.0238	C7H5O3	-0.6	292.6	5.0	2	21.5
6	113.0964	C7H13O	-0.8	291.1	1.0	1	33.5
7	71.0136	C3H3O2	-0.2	274.3	2.0	9	33.5
8	85.0286	C4H5O2	-0.9	219.1	2.0	2	33.5
9	133.0137	C4H5O5	-0.6	183.8	2.0	6	33.5
10	175.0252	C6H7O6	0.4	182.8	3.0	10	45.0
11	72.9929	C2HO3	-0.2	159.5	2.0	3	33.5
12	59.0134	C2H3O2	-0.4	145.4	1.0	9	33.5
13	89.0240	C3H5O3	-0.5	135.7	1.0	10	33.5
14	93.0337	C6H5O	-0.9	106.6	4.0	1	30.0
15	115.0035	C4H3O4	-0.1	67.7	3.0	11	38.0
16	157.1221	C9H17O2	-1.3	50.2	1.0	1	33.5
17	57.0342	C3H5O	-0.4	47.5	1.0	1	33.5
18	157.0150	C6H5O5	0.8	37.6	4.0	17	36.0
19	239.1268	C13H19O4	-2.1	33.2	4.0	3	29.5
20	87.0069	C3H3O3	-1.9	27.2	2.0	10	33.5
21	131.0344	C5H7O4	-0.6	23.9	2.0	10	33.5
22	173.1167	C9H17O3	-1.6	23.8	1.0	2	33.5
23	101.0254	C4H5O3	1.0	23.4	2.0	7	29.5
24	55.0192	C3H3O	0.3	23.4	2.0	1	33.5
25	283.1555	C11H23O8	15.6	20.2	0.0	0	3.0

M10 Bis-Demethylenation+Methylation [M-H]-

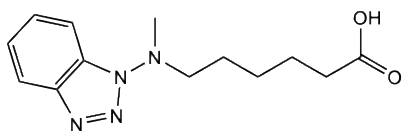

-TOF MS/MS of 261.1

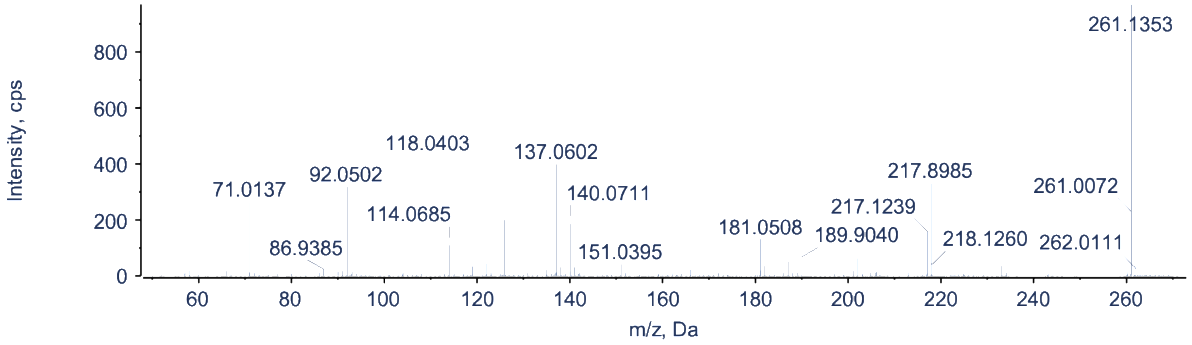

	Mass (m/z)	Ion Formula	Error (mDa)	Intensity (cps)	RDB	Proposed Structures	Score
1	261.1353	C13H17N4O2	-0.4	969.7	7.0	1	49.0
2	137.0602	C8H9O2	-0.6	397.6	4.0	0	3.0
3	118.0403	C6H4N3	-0.8	361.5	6.0	1	40.5
4	92.0502	C6H6N	-0.4	318.5	4.0	1	32.5
5	71.0137	C3H3O2	-0.2	265.0	2.0	1	42.0
6	140.0711	C7H10NO2	-0.6	186.0	3.0	1	37.0
7	217.1239	C12H15N3O	1.8	157.8	6.5	0	0.0
8	181.0508	C10H5N4	-1.2	131.9	10.0	0	3.0
9	114.0685	C6H10O2	-0.2	109.3	1.5	1	42.0
10	95.0498	C6H7O	-0.5	87.9	3.0	1	36.0
11	202.1001	C13H14O2	0.2	63.6	6.5	0	5.0
12	187.0758	C12H11O2	-0.7	50.4	7.0	0	3.0
13	122.0608	C7H8NO	-0.3	43.4	4.0	1	38.0
14	151.0395	C6H5N3O2	0.8	39.9	5.5	0	0.0
15	233.1298	C13H17N2O2	0.2	35.5	6.0	1	41.5
16	166.0269	C11H4NO	-2.9	22.8	10.0	0	3.0
17	135.0439	C6H5N3O	0.1	21.5	5.5	0	5.0
18	181.0874	C8H11N3O2	1.7	19.9	4.5	0	0.0
19	58.0059	C2H2O2	-0.1	19.5	1.5	1	39.0
20	117.0438	C7H5N2	-2.0	17.3	6.0	1	32.5
21	187.0964	C10H11N4	-2.5	17.1	7.0	2	25.0
22	66.0335	C4H4N	-1.4	16.8	3.0	2	26.0
23	90.0335	C6H4N	-1.4	15.0	5.0	1	32.5

M24 Bis-Methylation+Oxidation [M-H]-

(undefined hydroxylation)

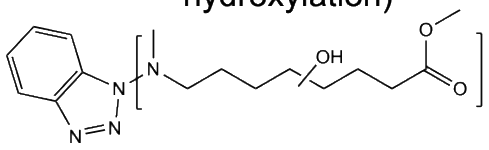

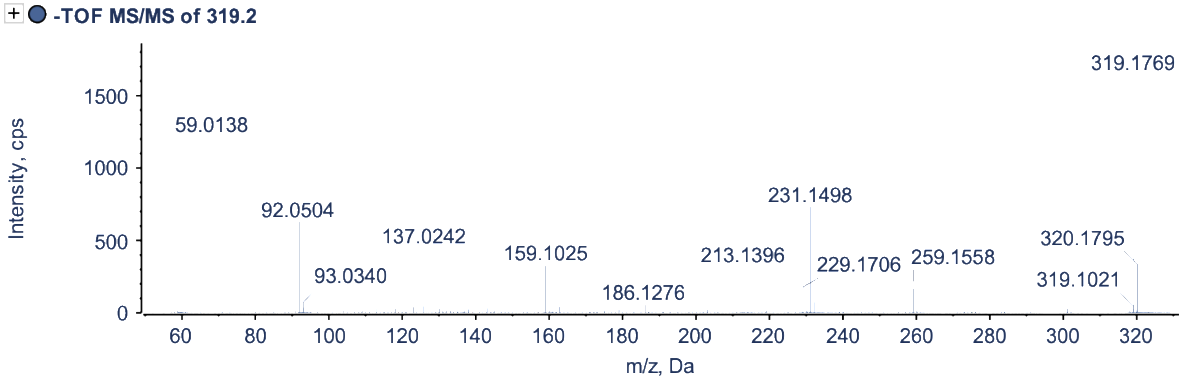

	Mass (m/z)	Ion Formula	Error (mDa)	Intensity (cps)	RDB	Proposed Structures	Score
1	319.1769	C16H23N4O3	-0.7	1861.0	7.0	1	49.0
2	59.0138	C2H3O2	0.0	1087.3	1.0	1	42.5
3	231.1498	C14H19N2O	-0.5	730.5	6.0	1	25.5
4	92.0504	C6H6N	-0.2	628.2	4.0	3	41.5
5	159.1025	C8H15O3	-0.1	322.7	1.0	0	8.0
6	213.1396	C14H17N2	-0.2	316.4	7.0	0	8.0
7	137.0242	C7H5O3	-0.2	309.0	5.0	0	8.0
8	229.1706	C10H21N4O2	3.6	179.1	2.0	1	32.5
9	259.1558	C14H19N4O	-0.6	166.6	7.0	3	41.5
10	113.0965	C7H13O	-0.7	62.6	1.0	1	33.5
11	186.1276	C8H16N3O2	2.8	52.9	2.0	1	32.5
12	123.0810	C8H11O	-0.5	37.4	3.0	1	36.0
13	143.1074	C8H15O2	-0.3	33.1	1.0	1	45.5
14	301.1673	C16H21N4O2	0.3	29.9	8.0	1	45.0
15	130.0530	C5H8NO3	2.1	28.6	2.0	0	3.0
16	113.0246	C5H5O3	0.1	27.7	3.0	0	8.0
17	203.1555	C8H19N4O2	4.2	21.6	1.0	1	32.5
18	91.0425	C6H5N	-0.2	21.3	4.5	2	38.5
19	291.1715	C16H23N2O3	0.1	21.2	6.0	1	41.5
20	85.0290	C4H5O2	-0.5	19.1	2.0	1	37.0
21	132.0687	C5H10NO3	2.1	17.3	1.0	0	3.0

M13 Ketone Formation+Methylation [M-H]-

(undefined ketone)

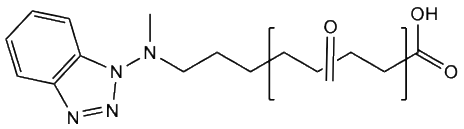

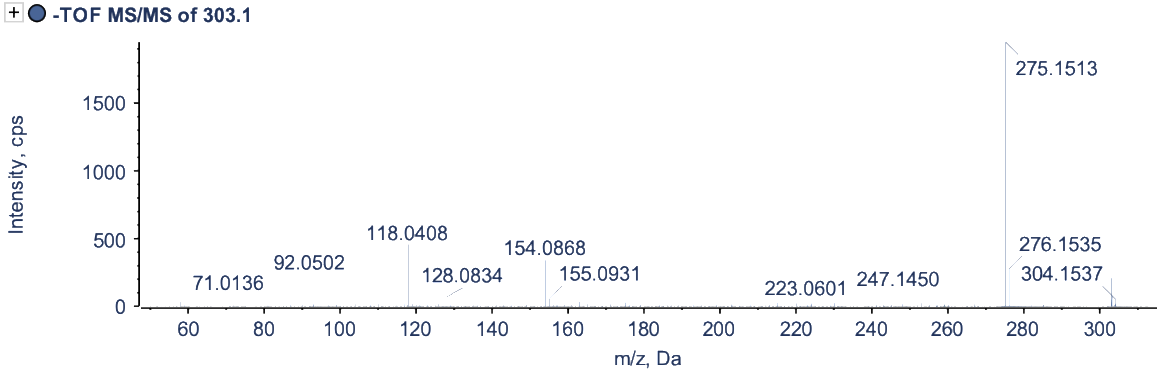

	Mass (m/z)	Ion Formula	Error (mDa)	Intensity (cps)	RDB	Proposed Structures	Score
1	275.1513	C14H19N4O2	0.0	1951.9	7.0	1	45.5
2	118.0408	C6H4N3	-0.2	454.7	6.0	1	45.5
3	154.0868	C8H12NO2	-0.5	340.9	3.0	1	36.0
4	92.0502	C6H6N	-0.3	226.0	4.0	2	32.5
5	303.1466	C15H19N4O3	0.4	209.0	8.0	1	49.0
6	247.1450	C14H19N2O2	-0.2	114.8	6.0	1	37.5
7	71.0136	C3H3O2	-0.3	84.6	2.0	1	37.0
8	128.0834	C7H12O2	-0.9	69.3	1.5	1	34.0
9	223.0601	C12H7N4O	-2.4	45.2	11.0	0	3.0
10	163.0219	C12H3O	3.0	32.3	11.0	0	3.0
11	175.1162	C12H15O	3.4	27.3	5.0	0	3.0
12	215.1243	C9H17N3O3	-3.3	25.7	2.5	0	0.0
13	230.1182	C12H14N4O	0.9	24.5	7.5	1	22.0
14	208.0385	C13H6NO2	-1.9	21.5	11.0	0	3.0
15	117.0439	C7H5N2	-1.9	20.9	6.0	0	3.0
16	220.1331	C11H16N4O	0.2	20.2	5.5	0	5.0
17	123.0437	C5H5N3O	-0.1	16.6	4.5	0	5.0
18	229.1354	C9H17N4O3	4.8	16.3	3.0	1	36.5
19	267.1225	C15H15N4O	-2.6	15.9	10.0	0	3.0
20	110.0979	C7H12N	0.4	15.9	2.0	1	26.5
21	203.1552	C8H19N4O2	3.8	14.3	1.0	1	32.5
22	104.0375	C6H4N2	-0.5	14.3	5.5	1	33.5
23	171.1015	C7H13N3O2	0.2	14.1	2.5	0	5.0

M15 Desaturation [M-H]-

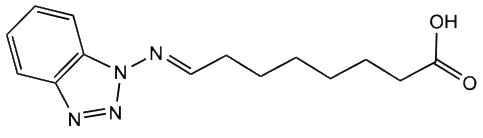

No MS/MS spectra were recorded for **M15** in ESI- mode in pooled plasma.

M25 Unassigned Gain of 102.0212

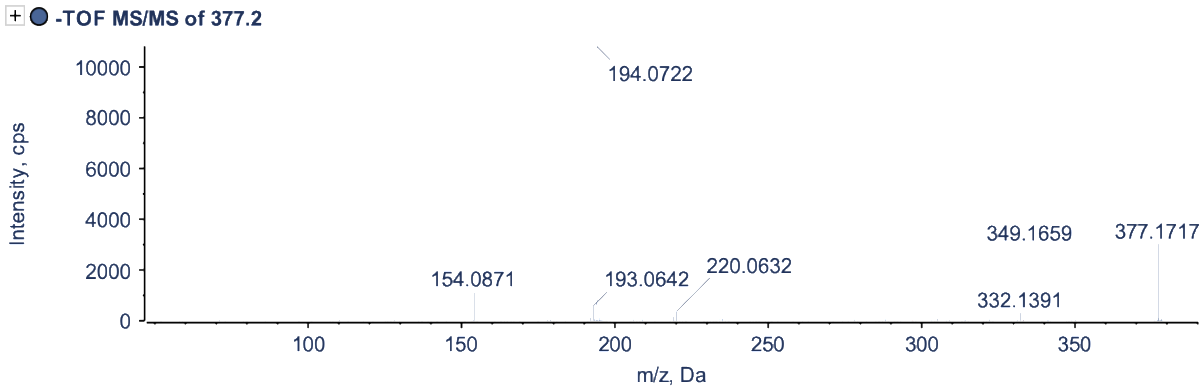

M16 Bis-Methylation [M-H]- (undefined, may be ethylation)

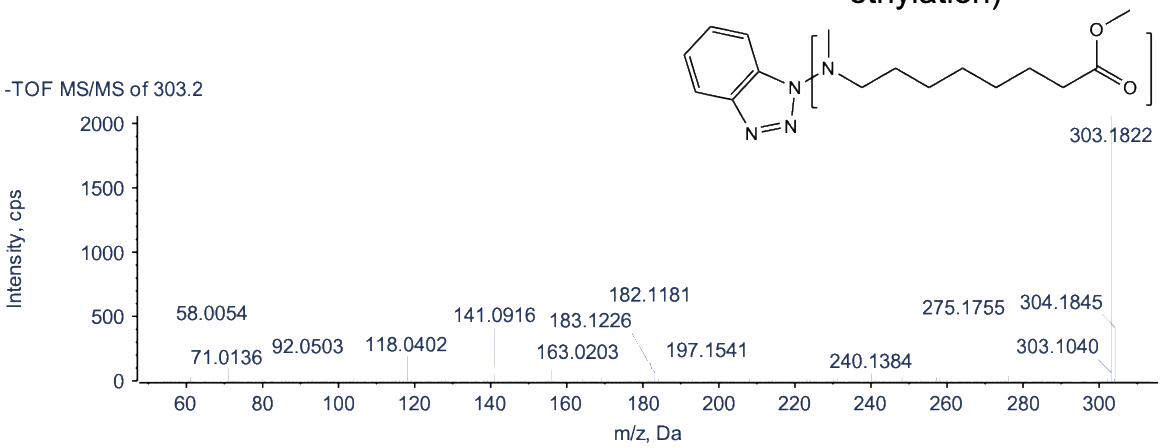

	Mass (m/z)	Ion Formula	Error (mDa)	Intensity (cps)	RDB	Proposed Structures	Score
1	303.1822	C16H23N4O2	-0.5	2059.6	7.0	1	49.0
2	182.1181	C10H16NO2	-0.5	576.4	3.0	1	42.0
3	275.1755	C16H23N2O2	-1.0	333.4	6.0	1	36.5
4	118.0402	C6H4N3	-0.9	193.1	6.0	1	40.5
5	92.0503	C6H6N	-0.2	173.0	4.0	2	37.5
6	127.0757	C7H11O2	-0.7	158.9	2.0	2	37.0
7	197.1541	C12H21O2	-0.6	142.9	2.0	0	3.0
8	71.0136	C3H3O2	-0.2	94.4	2.0	2	37.0
9	156.1149	C9H16O2	-0.6	91.6	1.5	1	37.0
10	113.0603	C6H9O2	-0.5	81.8	2.0	2	37.0
11	58.0054	C2H2O2	-0.6	79.6	1.5	2	34.0
12	240.1384	C14H16N4	0.3	56.6	8.5	0	5.0
13	141.0916	C8H13O2	-0.5	52.9	2.0	2	37.0
14	248.1649	C15H22NO2	-0.7	33.5	5.0	0	8.0
15	61.0291	C2H5O2	-0.4	31.9	0.0	1	33.5
16	257.1650	C16H21N2O	-0.9	28.9	7.0	0	3.0
17	104.0380	C6H4N2	0.0	23.4	5.5	1	38.5
18	169.1587	C9H19N3	0.3	22.1	1.5	0	5.0
19	99.0442	C5H7O2	-0.9	20.3	2.0	2	37.0
20	231.1859	C10H23N4O2	3.2	13.4	1.0	1	36.5

References

Al-Esawi NSE, Geeran ARM, Alajeely MHJ, Al-Isawi AOJ. (2020). Expression of CYT4Z1 in breast carcinoma; Correlating with clinicopathological parameters. Biomed Pharmacol J, 13, 1.

Campbell CD, Rees CW. (1969). Reactive intermediates. Part I. Synthesis and oxidation of 1- and 2-aminobenzotriazole. Journal of the Chemical Society C: Organic, 742-7.

Capper CP, Rae JM, Auchus RJ. (2016). The Metabolism, Analysis, and Targeting of Steroid Hormones in Breast and Prostate Cancer. Horm Cancer, 7, 149-64.

Chovan JP, Ring SC, Yu E, Baldino JP. (2007). Cytochrome P450 probe substrate metabolism kinetics in Sprague Dawley rats. Xenobiotica, 37, 459-73.

Darnell M, Weidolf L. (2013). Metabolism of xenobiotic carboxylic acids: focus on coenzyme A conjugation, reactivity, and interference with lipid metabolism. Chem Res Toxicol, 26, 1139-55.

Davies B, Morris T. (1993). Physiological parameters in laboratory animals and humans. Pharm Res, 10, 1093-5.

DeSantis CE, Ma J, Gaudet MM, Newman LA, Miller KD, Goding Sauer A, Jemal A, Siegel RL. (2019). Breast cancer statistics, 2019. CA Cancer J Clin, 69, 438-51.

Faed EM. (1984). Properties of acyl glucuronides: implications for studies of the pharmacokinetics and metabolism of acidic drugs. Drug Metab Rev, 15, 1213-49.

Guengerich FP, Martin MV, Sohl CD, Cheng Q. (2009). Measurement of cytochrome P450 and NADPH-cytochrome P450 reductase. Nat Protoc, 4, 1245-51.

He D, Zhang J, Wu W, Yi N, He W, Lu P, Li B, Yang N, Wang D, Xue Z and others. (2019). A novel immunodeficient rat model supports human lung cancer xenografts. Faseb j, 33, 140-50.

Iannaccone PM, Jacob HJ, (2009). Rats! Dis Model Mech. 206-10.

Kobayashi K, Urashima K, Shimada N, Chiba K. (2002). Substrate specificity for rat cytochrome P450 (CYP) isoforms: screening with cDNA-expressed systems of the rat. Biochem Pharmacol, 63, 889-96.

Kowalski JP, McDonald MG, Pelletier RD, Hanenberg H, Wiek C, Rettie AE. (2020). Design and Characterization of the First Selective and Potent Mechanism-Based Inhibitor of Cytochrome P450 4Z1. Journal of Medicinal Chemistry.

Li C, Subramanian R, Yu S, Prueksaritanont T. (2006). Acyl-coenzyme a formation of simvastatin in mouse liver preparations. Drug Metab Dispos, 34, 102-10.

Li Y, Steppi A, Zhou Y, Mao F, Miller PC, He MM, Zhao T, Sun Q, Zhang J. (2017). Tumoral

expression of drug and xenobiotic metabolizing enzymes in breast cancer patients of different ethnicities with implications to personalized medicine. Sci Rep, 7, 4747.

Loi CM, Smith DA, Dalvie D. (2013). Which metabolites circulate? Drug Metab Dispos, 41, 933-51.

McDonald MG, Ray S, Amorosi CJ, Sitko KA, Kowalski JP, Paco L, Nath A, Gallis B, Totah RA, Dunham MJ and others. (2017). Expression and Functional Characterization of Breast Cancer-Associated Cytochrome P450 4Z1 in Saccharomyces cerevisiae. Drug Metab Dispos, 45, 1364-71.

Mollard S, Mousseau Y, Baaj Y, Richard L, Cook-Moreau J, Monteil J, Funalot B, Sturtz FG. (2011). How can grafted breast cancer models be optimized? Cancer Biol Ther, 12, 855-64.

Murayama T, Gotoh N. (2019). Patient-Derived Xenograft Models of Breast Cancer and Their Application. Cells, 8.

Murray GI, Patimalla S, Stewart KN, Miller ID, Heys SD. (2010). Profiling the expression of cytochrome P450 in breast cancer. Histopathology, 57, 202-11.

Noto FK, Adjan-Steffey V, Tong M, Ravichandran K, Zhang W, Arey A, McClain CB, Ostertag E, Mazhar S, Sangodkar J and others. (2018). Sprague Dawley Rag2-Null Rats Created from Engineered Spermatogonial Stem Cells Are Immunodeficient and Permissive to Human Xenografts. Mol Cancer Ther, 17, 2481-9.

Obach RS, Walsky RL, Venkatakrishnan K. (2007). Mechanism-based inactivation of human cytochrome p450 enzymes and the prediction of drug-drug interactions. Drug Metab Dispos, 35, 246-55.

Ortiz de Montellano PR. (2018). 1-Aminobenzotriazole: A Mechanism-Based Cytochrome P450 Inhibitor and Probe of Cytochrome P450 Biology. Med Chem (Los Angeles), 8.

Radvanyi L, Singh-Sandhu D, Gallichan S, Lovitt C, Pedyczak A, Mallo G, Gish K, Kwok K, Hanna W, Zubovits J and others. (2005). The gene associated with trichorhinophalangeal syndrome in humans is overexpressed in breast cancer. Proc Natl Acad Sci U S A, 102, 11005-10.

Regan SL, Maggs JL, Hammond TG, Lambert C, Williams DP, Park BK. (2010). Acyl glucuronides: the good, the bad and the ugly. Biopharm Drug Dispos, 31, 367-95.

Rieger MA, Ebner R, Bell DR, Kiessling A, Rohayem J, Schmitz M, Temme A, Rieber EP, Weigle B. (2004). Identification of a novel mammary-restricted cytochrome P450, CYP4Z1, with overexpression in breast carcinoma. Cancer Res, 64, 2357-64.

Rowland M, Tozer T. (2011). Clinical pharmacokinetics and pharmacodynamics: Concepts and Applications. 4th ed. Philadelphia: Wolters Kluwer Health/Lippincott Williams & Wilkins.

Sadeque AJ, Eddy AC, Meier GP, Rettie AE. (1992). Stereoselective sulfoxidation by human

flavin-containing monooxygenase. Evidence for catalytic diversity between hepatic, renal, and fetal forms. Drug Metab Dispos, 20, 832-9.

Sarda S, Page C, Pickup K, Schulz-Utermoehl T, Wilson I. (2012). Diclofenac metabolism in the mouse: novel in vivo metabolites identified by high performance liquid chromatography coupled to linear ion trap mass spectrometry. Xenobiotica, 42, 179-94.

Smits BM, Cotroneo MS, Haag JD, Gould MN. (2007). Genetically engineered rat models for breast cancer. Breast Dis, 28, 53-61.

Stanley KK, Tubbs PK. (1975). The role of intermediates in mitochondrial fatty acid oxidation. Biochem J, 150, 77-88.

Stewart HB, Tubbs PK, Stanley KK. (1973). Intermediates in fatty acid oxidation. Biochem J, 132, 61-76.

Suga T. (2003). Drug metabolism in peroxisomes: involvement of peroxisomal beta-oxidation system in the oxidative chain-shortening of xenobiotic acyl compounds. Drug Metab Pharmacokinet, 18, 155-62.

Vyas KP, Kari PH, Pitzenberger SM, Halpin RA, Ramjit HG, Arison B, Murphy JS, Hoffman WF, Schwartz MS, Ulm EH and others. (1990). Biotransformation of lovastatin. I. Structure elucidation of in vitro and in vivo metabolites in the rat and mouse. Drug Metab Dispos, 18, 203-11.

Yang J, Liao M, Shou M, Jamei M, Yeo KR, Tucker GT, Rostami-Hodjegan A. (2008). Cytochrome p450 turnover: regulation of synthesis and degradation, methods for determining rates, and implications for the prediction of drug interactions. Curr Drug Metab, 9, 384-94.

Yang X, Hutter M, Goh WWB, Bureik M. (2017). CYP4Z1 - A Human Cytochrome P450 Enzyme that Might Hold the Key to Curing Breast Cancer. Curr Pharm Des, 23, 2060-4.

Zhang ZY, Wong YN. (2005). Enzyme kinetics for clinically relevant CYP inhibition. Curr Drug Metab, 6, 241-57.

Chapter 5

Future directions

5.1 Off-target CYP-mediated bioactivation of 3-furancarboximides and further analog generation

One of the motivations to assess the structure-activity relationships (SAR) for new furan-containing congeners as substrates for CYP4B1-mediated bioactivation was the undesired off-target CYP bioactivation that can occur. For example, human CYP1A2 also effectively bioactivates 4-ipomeanol, and therefore its administration may lead to unintended hepatoxicity. In preliminary experiments with an expanded library of 30 furan-containing congeners, the cytotoxicity resulting from CYP1A2-mediated bioactivation in HepG2 cells modified to express this enzyme was assessed. We observed that, in general, smaller and branched substrates showed a higher preference for CYP4B1, whereas large and hydrophilic end-capped substrates exhibited a preference for CYP1A2. Therefore, future analog generation should certainly take this structural insight into consideration and utilize counter-screening for CYP1A2-mediated bioactivation.

Secondly, to better understand the effect of CYP4B1-mediated ω-hydroxylation on reducing the desired bioactivation pathway, the addition of a terminal trifluoromethyl moiety on pro-toxicants was assessed. In a pilot study, a terminal trifluoromethyl variant of compound **C4** (**C4-F$_3$**) was synthesized and evaluated for potency in the CYP4B1-expressing HepG2 cell line. The LD_{50} of **C4-F$_3$** was nearly equivalent to that determined for **C4**, indicating no immediately discernable detriment from the addition of this functional group. Unfortunately, the necessary building blocks to synthesize the terminal trifluoromethyl variants of **C5** and **C8** were not readily available at the time. Therefore, direct SAR comparisons surrounding ω-hydroxylation and cytotoxic potency could not be made for congeners of this type. However, these preliminary

results indicate this would be a feasible strategy to pursue to generate novel furan-containing pro-toxicants for CYP4B1-mediated bioactivation moving forward.

5.2 Interrogate CYP4Z1-mediated cellular proliferation and migration in breast cancer cell lines

While there are certainly translational limitations to using immortalized cell lines for investigating potential new molecular drivers of breast cancer, the assessment of CYP4Z1-mediated effects on breast cancer cells *in vitro* is an important foundational study that requires completion. To this end, the following cell lines have been modified *via* lentivirus by our collaborators from Heinrich-Heine University, Germany to express CYP4Z1, or a control vector: T47D, MDA, SKBR3, and MCF7. These cell lines will be instrumental in future studies that interrogate CYP4Z1-mediated proliferation and migration.

We extensively characterized the selective and mechanism-based inhibition of CYP4Z1 with 8-[(1H-benzotriazol-1-yl)amino]octanoic acid (8-BOA) in both membrane and whole cell settings. In T47D breast cancer cells, preliminary studies revealed that CYP4Z1-mediated metabolism of arachidonic acid to generate the preferential metabolite 14,15-epoxyeicosatrienoic acid (14,15-EET) could be reduced by ~80% with 3 μM of 8-BOA. The low micromolar potency for substantial reduction in formation of pro-tumorigenic 14,15-EET in CYP4Z1-expressing whole cells indicates 8-BOA will be an effective chemical tool for future mechanistic studies in the afore-mentioned cell lines.

5.3 Further examine the mechanism of CYP4Z1 inactivation from 8-BOA with purified enzyme in a reconstituted system

Our initial studies showed that while the canonical pathway of heme alkylation was observed during 1-aminobenzotriazole (ABT) inactivation of CYP4Z1, this does not occur for 8-BOA mediated inactivation of CYP4Z1. The HepG2-CYP4Z1 membrane system used for most

studies reported here proved to be a robust and effective enzyme source, however, purified CYP4Z1 in a reconstituted system would enable further mechanistic probing of any covalent interactions of 8-BOA with the apoprotein of CYP4Z1.

Although not detailed in the prior chapters, significant efforts were undertaken to purify CYP4Z1 to homogeneity, so this has been summarized briefly below. Initial expression results utilizing a proprietary yeast expression construct with a 6-histine (His) tag affixed to the C-terminus of CYP4Z1 that was generated by collaborators from the University of Washington Department of Genome Sciences were promising. We used a hybrid protocol consisting of methodology adapted for generation of yeast microsomes and solubilization techniques frequently used for heterologous CYP expression. Although continually plagued by extremely low yield, we were successful in isolating a small amount of highly pure CYP4Z1 (**Figure 5.1A, B**) that provided carbon-monoxide binding spectra indicative of mostly holo-enzyme*, i.e* with functional heme (**Figure 5.1C**). Using a reconstituted system and semi-quantitative LC-MS/MS detection, an assessment of the capability of purified CYP4Z1 to metabolize arachidonic acid was undertaken. We definitively confirmed that CYP4Z1-dependent metabolism of arachidonic acid generates 14,15-EET preferentially and not 20-hydroxyeicosatetraenoic acid (**Figure 5.2**). This metabolite preference matched what our group has observed in CYP4Z1-expressing yeast microsomes, HepG2 membranes, T47D membranes, and T47D whole cells. Unfortunately, the concentration and amount of purified CYP4Z1 was so low that any mechanistic work was not technically feasible at this time.

In attempts to address the yield concerns, we identified that poor solubilization resulted in ineffective extraction of CYP4Z1 from the yeast membranes (~2-5%). Furthermore, the 6His-tagged CYP4Z1 bound poorly to the nickel nitrilotriacetic acid affinity column, leaving little on-column to affinity purify. Lastly, purification attempts that resulted in a low, albeit acceptable, amount of enzyme bound to the column frequently precipitated during loading/washing or during

dialysis to remove components of the elution buffer. To trouble-shoot these latter issues, yeast membrane extraction optimization studies were performed by screening numerous detergents. We found that membrane extraction efficiency was markedly increased by using 5-cyclohexyl-1-pentyl-β-D-maltoside (CYMAL-5). Also, solubilized CYP4Z1 was subjected to strong denaturing conditions (*ie* 6 M guanidinium chloride) prior to loading on the Ni-column. This resulted in a substantial increase in enzyme bound to the column as assessed by western blot, indicating that the His-tag was either buried in the natively folded enzyme or was engaging in intra-protein electrostatic interactions that inhibited binding to the column.

Therefore, it was determined critical that any further enzyme expression be attempted with a new vector construct. To this end, efforts are underway by collaborators at the University of Washington Department of Genome Sciences and the University of Michigan Departments of Medicinal Chemistry and Pharmacology to clone new expression vectors with truncated (N-terminus) CYP4Z1 variants to improve solubilization, Ni-column binding, and help to prevent enzyme precipitation. Additionally, an extended 10His-tag has been added in an effort to further improve binding to the Ni-column. Alternatively, a glutathione S-transferase tag with glutathione resin for chromatography might be more effective for column binding and aid in solubility, potentially resulting in more effective enzyme purification. Therefore, a more efficient method for the purification of CYP4Z1 appears tractable and is essential for future studies to illuminate the mechanism of enzyme inactivation and further biochemical characterization of this enzyme *via* experiments with a purified reconstituted enzyme system.

5.4 Probe the *β*-oxidation pathway for 8-BOA metabolism *in vitro* and further characterize the resultant major products

Substantial evidence for the primacy of the *β*-oxidation pathway in the metabolism of 8-BOA was observed *in vivo*. Therefore, *in vitro* experiments using appropriate subcellular fractions should be performed to confirm this in an orthogonal setting. Both mitochondrial and

peroxisomal settings should be probed for their *β*-oxidation propensity towards this substrate, along with the attendant cofactor dependency. In addition to analyzing the formation rates of the -C_2H_4- chain-shortened metabolite (already synthesized), the -C_4H_8- chain-shortened metabolite should be synthesized as synthetic methods are in place to achieve this goal. This ABT-analog should be assessed for its ability to cause both on-target CYP4Z1 and off-target CYP inactivation. Furthermore, upcoming *in vivo* studies should quantify the amounts of both *β*-oxidation products in plasma. In total, this will be beneficial for future modeling of target inactivation if K_I and k_{inact} values for these metabolites are known and it is determined that unbound circulating concentrations are substantial enough to contribute as active metabolites to CYP4Z1 inactivation.

5.5 Test the efficacy of 8-BOA in CYP4Z1-expressing xenograft tumor models of breast cancer in the rat

The objective of much of the research presented herein was to develop a chemical tool that would be effective in interrogating the role of CYP4Z1 in breast cancer. Both *in vitro* and *in vivo* studies indicate that 8-BOA would be useful for this purpose. The ultimate goal would now be to test the efficacy of 8-BOA in CYP4Z1-expressing xenograft tumor models of breast cancer in the rat. Both cell- and patient-derived xenografts would be effective options to pursue, and with the improved generation of immunocompromised rat models these are now feasible for this species. Such studies will enable significant strides to be made in confirming or rejecting the hypothesis that increased expression of CYP4Z1 is a driver of breast cancer malignancy. If the administration of 8-BOA is effective in knocking out a majority of active CYP4Z1 and the attendant production of pro-tumorigenic signaling ligands, this would very significantly advance the validity of CYP4Z1 as a drug target in breast cancer.

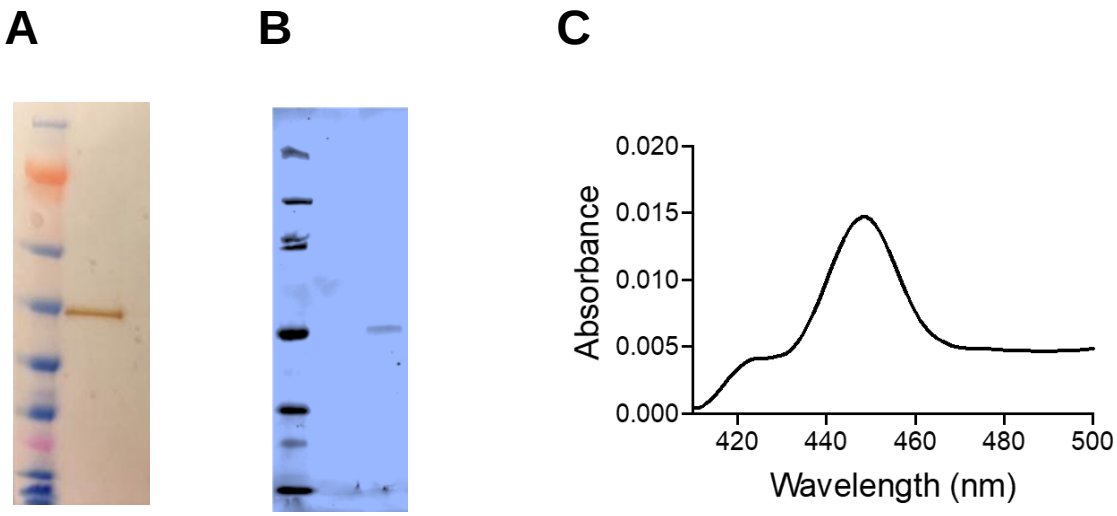

Figure 5.1. Characterization of recombinantly expressed and isolated CYP4Z1. CYP4Z1 was expressed in *Saccharomyces cerevisiae* (Y12) and purified using affinity chromatography (Ni-NTA). In SDS-PAGE (silver stain detection) analysis of the purified enzyme no contaminating proteins were observed, only CYP4Z1 migrating at ~ 55 kDa (**A**). Western blot of the isolated enzyme with anti-CYP4Z1 (Atlas Antibodies) (**B**). Carbon-monoxide binding spectra obtained with purified CYP4Z1, a λ_{max} of 448 nm was observed (**C**).

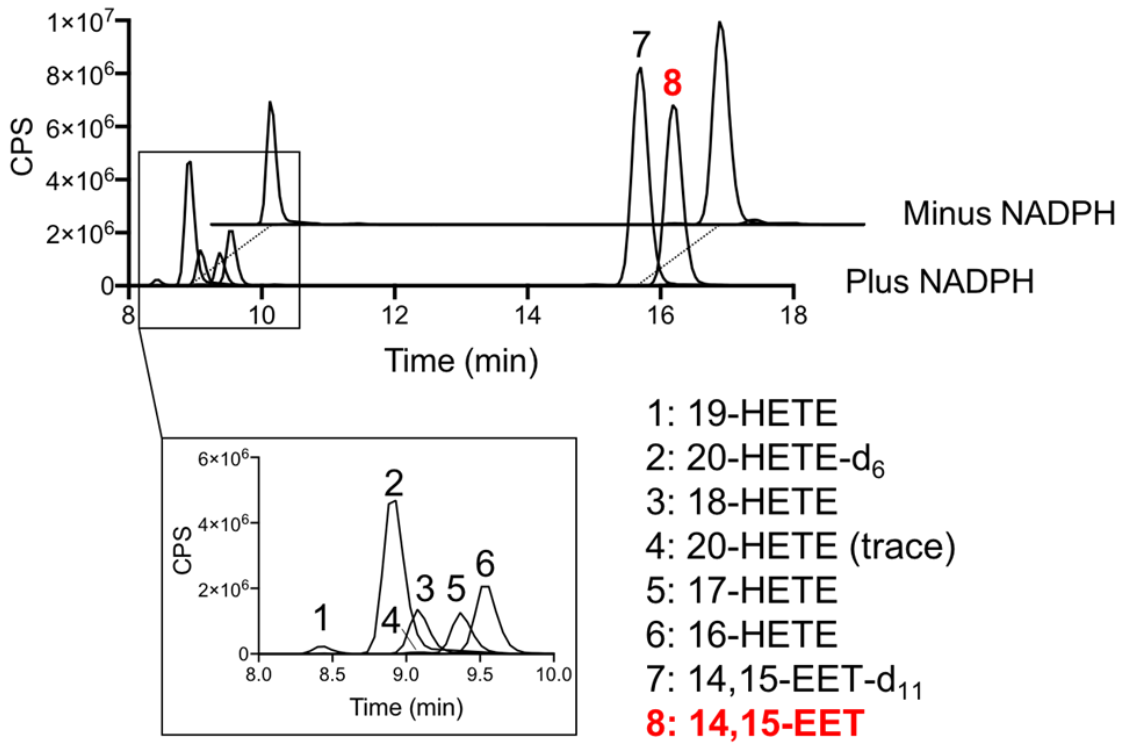

Figure 5.2. LC-MS/MS analysis of CYP4Z1 metabolism of arachidonic acid. The metabolism of arachidonic acid in a reconstituted system with recombinantly expressed and purified CYP4Z1 was NADPH-dependent and preferentially produced 14,15-EET (highlighted in red). Equal amounts of the internal standards 20-HETE-d_6 and 14,15-EET-d_{11} (100 ng) were added during sample workup to enable semi-quantitative comparisons of metabolite formation for these two analytes. Note, due to lack of chemical standards for 16 – 19-HETE, the assignments presented here for these metabolites are tentative.